The Development of a Field-Portable MEMS Gravimeter

Steven George Bramsiepe

Schools of Physics & Astronomy and Engineering
University of Glasgow

Presented as a thesis for the degree of Ph.D in the University of Glasgow,
University Avenue, Glasgow, G12 8QQ

January 2020

Summary

Gravimetry is a technique that has existed since the 17th and 18th century and involves the measurement of the acceleration due to gravity. The technique can be used to measure changes in density below the ground where conventional methods cannot. This is because gravity cannot be shielded, and therefore, can always be measured. It has many useful applications, particularly in surveying for oil, gas and minerals but can also be used to detect the precursors to volcanic eruptions and earthquakes, the density contrast of buried walls for archaeology and the detection of subsurface voids. Typically, however, gravimeters can cost in excess of £70k and weight over 8 kg. This cost and weight has prohibited some applications of gravimeters where either many of the devices would be required or if weight was prohibitive.

In the winter of 2014, an important step forward to a lightweight, low-cost and portable MEMS gravimeter was made. This was the first time that a MEMS based gravimeter had measured the Earth Tides as reported by R. P. Middlemiss et al. The device, however, still required a large array of electronics and vacuum equipment which made it impossible to be able to be taken into the field. Clearly, if the device was to ever become a disruptive technology within the gravimeter industry, significant effort would be required to obtain a device with sufficient sensitivity that was also portable. This thesis highlights the work that was required to bring the MEMS that was a lab-bound device, and make successful measurements of the change in acceleration due to gravity in the field.

In this thesis, a miniaturised MEMS gravimeter is presented with an RMS of 13 μGal when averaged to 1000 s, a factor three better than the original set-up from R. P. Middlemiss et al. The system went from a set-up with the approximate dimensions of a typical fridge-freezer (including the array of electronic equipment) to a portable platform of dimensions 30 cm wide by 30 cm deep by 15 cm high. The platform used a small steel cube as a vacuum container for the device, three micrometer legs for precision levelling, batteries and a custom electronics board. This custom electronics board was designed, tested and improved during the course of this thesis. The board was controlled by a microcontroller from Microchip (the

dsPIC33EP512MU810) and is shown to be capable of a large amount of digital filtering that was required for this application, including the use of a decimator and digital based lock-in amplifier. The board measured displacements, temperatures (which were also controlled) and tilts, all of which the microcontroller digitally filtered and downsampled so that they could be sent to a computer for data logging.

Declaration

I certify that the thesis presented here is solely my own work other than where I have clearly indicated. The work was carried out in the Institute for Gravitational Research at the University of Glasgow between July 2015 and March 2019, under the supervision of Prof. Giles Hammond. Any work carried out by someone other than myself has been clearly stated. Though not exclusively, mainly includes the work carried out by my supervisor Prof. Giles Hammond, my colleague Dr. Richard Middlemiss and Mr. David Loomes. I declare that the thesis does not include work forming part of a thesis presented successfully for another degree. I declare that this thesis has been produced in accordance with the University of Glasgow's Code of Good Practice in Research. Parts of this work have been published in the following peer-reviewed papers:

- S. G. Bramsiepe, D. Loomes, R. P. Middlemiss, D. J. Paul, and G. D. Hammond. A high stability optical shadow sensor with applications for precision accelerometers. IEEE Sensors Journal, 18(10):4108–4116, 2018.
- R. P. Middlemiss, S. G. Bramsiepe, R. Douglas, S. Hild, J. Hough, D. J. Paul, A. Samarelli, S. Rowan, and G. D. Hammond. Microelectromechanical system gravimeters as a new tool for gravity imaging. pages 1–15, 2018.
- R. P. Middlemiss, S. G. Bramsiepe, R. Douglas, J. Hough, D. J. Paul, S. Rowan, and G. D. Hammond. Field tests of a portable MEMS gravimeter. Sensors (Switzerland), 17(11):1–12, 2017.
- A. Prasad, S. G. Bramsiepe, R. P. Middlemiss, J. Hough, S. Rowan, G. D. Hammond, and D. J. Paul. A portable MEMS gravimeter for the detection of the earth tides. In 2018 IEEE SENSORS. IEEE, oct 2018.

Steven George Bramsiepe
January 2020

Acknowledgements

I would first like to thank my parents, Sheelagh and Paul, as well as my brother, Michael for the continued love and support throughout my life. If it wasn't for this support, I would more than likely not be where I am now. It was also this love and support that helped me develop the passion for science, mathematics and critical thinking that has allowed me to get to the stage of submitting a PhD thesis in physics.

I would also have to thank my supervisor, Prof. Giles Hammond, who has been patient throughout the learning process. My supervisor has further instilled an obsessive nature in regards to critically thinking about how processes function, and whether any changes have made sense. The question "How does the data look?" will no doubt stay with me for the rest of my life. The behaviours and thought processes obtained during my time as a PhD student will continue to develop, helping me as I go forward into academia and beyond. It is here I would also like to thank my unofficial supervisor, Dr Richard Middlemiss, who has 'shown me the ropes' since I first started as a newly born researcher. I would also like to thank him for his continued support throughout the PhD and the writing of the thesis. It is here I also want to thank Dr. Abhinav Prasad for his help with the writing of this thesis.

I also have to thank my friends and office mates who have made working a joyful experience, a statement that not many can say. I should apologise for the times I distract everyone, however, I am sure we will all be quite even on this. I am sure all the talented individuals I have had the pleasure of talking to will achieve what they want going into the future.

Finally I will finish with a closing quote.

"Live long and prosper"
- Leonard Nimoy as Spock

Preface

In this thesis, the miniaturisation of a microelectromechanical system (MEMS) based gravimeter, named "wee-g", is discussed. The thesis outlines the work carried out to move what was a lab-bound device into the field for successful gravimeter field measurements. Chapter 1 outlines the history behind gravimetry, followed by typical applications, the different gravimetry methods that exist nowadays as well as specifics on a few commercially available devices. These details are followed by information on the development of the MEMS-based gravimeter that had been carried out by Prof. Giles Hammond and Dr Richard Middlemiss up until the start of this project. These details include information on the fabrication techniques used to produce a MEMS device. Details on how the system was operated are then described, which includes discussion on the optical shadow sensor and lock-in amplifier. Towards the end of chapter 1, details of the performance obtained by R. P. Middlemiss et al during their Earth-tide detection are highlighted. This was the first time a MEMS-based gravimeter had measured the Earth Tides. Finally, the possible applications of a low-cost, lightweight MEMS-based gravimeter are highlighted.

Chapter 2 sets the scene for what was required of the project, including a simulation on the temperature sensitivity of the MEMS. The simulation was obtained by editing ANSYS and Solidworks models that had originally been created by Prof. Giles Hammond and Dr. Richard Middlemiss. The chapter also outlines other sensitivities of the device, such as changes in tilt, and also estimates to what order these effects are seen. This estimate allows values to be set for each of the components that will be required for the systems function. These sub-systems include the displacement sensor, temperature sensors and actuators, and tilt sensing. The final sections of the chapter summarise all of the requirements by detailing the plan of the system including the need for a custom electronics board and the use of a microcontroller.

Chapter 3 starts by introducing how temperature measurements can be made as well as how a proportional integral differential (PID) controller functions. This outline is then followed by the noise model of the planned system that was used to obtain an estimate on the

final temperature sensor noise. Details of the digital-based filters and decimation are also described to obtain this estimate. A great deal of work was carried out by Mr. David Loomes to design and code a microcontroller based electronics board that allowed the testing of the system. This includes work carried out in future chapters as well as chapter 3. These details are then followed by the performance of the final system, including, to what level the PID controller was able to control the system's temperatures. A conclusion of this chapter is then outlined at the end to summarise.

Chapter 4 highlights the necessary steps to create a digital based lock-in amplifier utilising a one dimensional shadow sensor. The chapter starts by describing the function of a shadow-sensor and a lock-in amplifier. This description is then followed by details on the differences of a digital-based lock-in amplifier relative to the analogue version. The chapter then gives details of the noise model of the circuitry developed. As with the previous chapter, the noise model is then compared to the performance of the final system. This comparison includes a displacement sensitivity as well as the acceleration sensitivity. Finally, the chapter is summarised in a conclusion.

Chapter 5 outlines the work that was carried out on the tilt sensors. After introducing the reasons why tilt is a variable that has to be monitored, a description of how electrolytic tilt sensors function is given. This description includes details on the circuits involved for different set-ups that were used. Each of these set-ups then have separate noise models that is outlined. These noise models are then be compared to the final performance of each of the different set-ups used, with the aid of Dr. Abhinav Prasad. This comparison allows the lower noise set-up to be chosen for final field use. These details are then summarised in a conclusion of the chapter.

Chapter 6 collects the sub-systems described in the previous three chapters into a complete custom electronics board. The chapter highlights the layout of the board as well as the work carried out to create a platform in which the board and MEMS could be taken into the field. These highlights are followed by details of two successful field tests of the miniaturised platform which were carried out with the help of Dr. Richard Middlemiss, Rebecca Douglas and Prof. Giles Hammond. The first test was a measurement of the change in gravity between the top and bottom of a building. The second test involved a field test measuring the change in gravity while ascending a local hill range. Both of these tests showed the device, now miniaturised, could be taken out of the lab and successfully measure changes of gravity, allowing for further development of the MEMS-based gravimeter. The final section of the chapter shows a confirmation measurement of the Earth-tides. This detection showed

that, although the system had undergone significant changes, the sensitivity of the device remained.

Chapter 7 summarises the entire project in a final conclusion. This summary is then followed by a discussion on how the final system could have been improved given additional time. The improvements are followed by a section on future work that is, or may be, funded due to the progress of the ‘wee-g” device made in this project.

Table of contents

List of figures

List of tables

Chapter 1

Gravimetry

1.1 Gravimetry

Newton's Universal Law of Gravity states that there is a mutual force that acts between two bodies that is proportional to their mass and inversely proportional to their separation [7]. The apple falling from the tree feels a force, F_g acting on it that accelerates it towards the Earth and likewise the Earth feels that same force, F_g acting towards the apple. In reality, since the Earth is so massive, the effect on the Earth is negligible whereas the apple very noticeably accelerates at approximately 9.81 m s^{-2}. Gravity is not a static value everywhere but dependent on the local distribution of mass caused by local topography and ground densities. These local variations cause changes in the gravitational acceleration felt by an object/observer and so, by measuring changes in this acceleration, information on the local subterranean structure can be inferred. This capability facilitates useful applications such as: finding the location of underground voids [8, 9], finding oil/gas/mineral deposits [10–12], investigating sinkholes [13, 14], whether magma is intruding into a chamber (which is a precursor sign of a volcanic eruption) [15–19], and finding lost crypts for archaeological purposes [20, 21]. Since the gravitational constant, $G = 6.67 \times 10^{-11}$ m^3 kg^{-1} s^{-2} is much smaller than the other coupling constants (such as Coulomb's constant, $k_e = 9 \times 10^9$ N m^2 C^{-2}), the forces involved and therefore the accelerations are very small making measurements more difficult. A benefit of gravity measurements however, is that since there are no known ways to shield gravity, measurements can provide information about hidden regions that other sensors cannot. The science of measuring changes in gravity is known as gravimetry, and its origins go as far back as the 1700s. Over the centuries, gravity measurements have increased in accuracy and number; increasing the global coverage around the world on the land, sea, and air.

Historically, these measurements have been carried out using large, heavy and high-cost gravimeters. The need for these high-cost gravimeters, however, could soon come to an end. In the last five years, a Microelectromechanical System (MEMS) gravimeter was designed and successfully tested at the University of Glasgow [1]; showing that low-cost, portable gravimeters are achievable. This chapter will summarise the history of gravimeters. Details will be provided on: the performance and cost of commercial devices; the uses of gravimeters and the required sensitivities for certain applications; and a discussion of the development of the aforementioned Glasgow MEMS gravimeter.

1.1.1 History

Wolfgang Torge [22] reasons the first gravity measurements made in the 17th and 18th centuries were triggered by the development of the mathematics necessary to describe the mechanics of rigid and deformable bodies. This new understanding drove the desire to map the geoid which were made with using pendula. These measurements would play a role in developing a further understanding of the Earth's shape and structure. The development of gravimeters since these early innovations can be split into four distinct phases.

The first phase was the theoretical foundation of gravimetry, which had its roots in work carried out by S. Stevin (1548-1620) and Galileo Galilei (1564-1642) where they disproved Aristotle's (384-322 BC) theory that gravitational acceleration was proportional to the object's weight. The first gravimeters were pendula-based, constructed by Christian Huygens (1629-1695); who also developed the mathematical equations that allowed its motion to be understood. Measurements of gravity require the understanding that Isaac Newton (1643-1727) gave in 1687 in his "Philosophiae Naturalis Principia Mathematica". One of the equations that he derived was his Universal Law of Gravitation seen in equation 1.1 [7].

$$F_g = G\frac{m_1\, m_2}{r^2}\,, \tag{1.1}$$

where F_g [in N] is the mutual force of gravity between two masses m_1 and m_2 [in kg] at a separation of r [in m]. G is the gravitational constant equal to 6.67×10^{-11} m^3 kg^{-1} s^{-2}. The equation is an essential relationship for gravimetry as it shows that the gravitational force between two objects is proportional to their masses, and inversely proportional to their separation. The equation also contains the gravitational constant which can be thought of as a coupling constant between two objects. By changing the mass and the separation of the object, the force of gravity will change; and therefore the mutual acceleration felt between

the two masses. This acceleration can be calculated using Newton's second law of motion, seen in equation 1.2.

$$\vec{F} = m\,\vec{a}\,, \tag{1.2}$$

where m is the mass with an acceleration of a. Given that the force of gravity is the equivalent force of motion, the resulting expression can be rearranged for acceleration. This results in a relationship for the acceleration of a given object from the force of gravity. If the mass of the Earth is used, m_E and the radius, R, equation 1.3 is obtained:

$$a = \frac{G\,m_E}{R^2}\,. \tag{1.3}$$

Note that the acceleration of an object is independent of its own mass, i.e. 1 kg of lead will accelerate at the same rate that 5 kg of grain does due to gravity. Given the mass of the Earth is approximately 5.972×10^{24} kg and a radius of approximately 6371 km, an estimate of the acceleration due to gravity can be calculated to be 9.8136 m s^{-2} (the approximate accepted value at the surface of the Earth). The work carried out by A. C. Clairaut (1713-1765) was important for the geodetic utilisation of gravity measurements in his "Théorie de la Figure de la Terre". Geodesy is the mapping of the Earth's gravity field. A map of equipotential values of gravity is called the geoid (for greater detail see section 1.1.2.7). The final mathematical foundation of this phase was provided by the French mathematicians J. L. Lagrange (1736-1813), P. S. Laplace (1749-1827), A. M. Legendre (1752-1833) and S. D. Poisson (1741-1840).

The second phase saw the global usage of pendulum-based apparatus for geodesy and geophysics in the 18th and 19th century. An experiment funded by the Royal Society to find the mean density of the Earth was undertaken in the 18th century at Schiehallion, a mountain in Scotland. The aim of the Schiehallion experiment was to derive the mean density of the Earth and the mountain's relative gravitational attraction [23]. As the Earth is not a perfect sphere but an oblate spheroid (meaning it is wider at the equator than the between the poles); one would expect a latitude dependency for gravitational acceleration. This thought was confirmed by taking arc measurements at Lapland (1736/37, P. L. Maupertuis) and comparing that to measurements in Peru (1735/44, P. Bouguer and C. M. La Condamine). An altitude dependency had already been proven using measurements in the Andes Mountains. This understanding also allowed for a sea level reduction of gravity. A sea level reduction of gravity is a value for the acceleration of gravity at sea level which should match that of the geoid. Half a century later in 1792, a precision measurement boasting an accuracy of

$\pm 100\ \mu\text{m s}^{-2}$, or, 10 mGal was performed by J. D. Cassini de Thury *. The measurement was made using a wire pendulum of length 3.8 m. By 1818, H. Kater had constructed the first reversible pendulum with an error of approximately 35 mGal. This pendulum, however, had a length of only 1 m. Measurements with wire-based pendula such as those used by J. D. Cassini De Thury in 1792 were continued up until 1830 with a similar performance. These measurements were stopped, only to be resumed 32 years later in 1862. Measurements up to 1799 were used by Laplace to compute the flattening of the Earth. This calculation was done using 15 gravity points to obtain a ratio of 1:330 (the currently accepted value is 1:298.257223563 [24]). The flattening ratio is defined as the difference between each of the semiaxis of the spheroid divided by the long axis. For a sphere both the major and minor axes are identical, so the flattening ratio would be zero. In 1828 Gauss (1777-1855) suggested that the mathematical model of Earth for gravimetry should be an equipotential surface at sea level. This equipotential surface was later called a surface geoid by J. B. Listing in 1873. Not long after this, an essential problem in geophysics was confirmed by G. G. Stokes (1819-1903), stating that there was no unique solution for the mass distribution for a given potential (inversion problem). Stokes integral formula allowed the computation of the geoid from gravity values a century after its formulation, after sufficient globally distributed gravity data had been acquired. Experiments such as the ones above allowed calculations of the Earth's mass and the Gravitational constant to be made. Further refinement of this allowed the use of local terrain corrections, such as mass deficits (ocean) and mass surpluses (mountains). At the end of 19th century, brass pendula accuracy increased from the previous $\pm(10 \rightarrow 20)$ mGal using a wire pendula, to ± 5 mGal, with an observation time of half a day to a full day. By this time, observations were also being carried out on the ocean and were necessary for geodetic and geophysical applications. By 1901, Helmert calculated an ellipsoid flattening of 1:298.3 (closer to the accepted value of 1:298.257223563).

The third development phase consisted of the further refinement of current pendula based gravimeters, as well as the use of torsion balance and spring based gravimeters for applied geophysics. It was here, at the start of the 20th century, that relative pendulum gravimeters made a jump in performance, obtaining an accuracy of $\pm(1 \rightarrow 2)$ mGal due to the use of invar and quartz pendula in a vacuum with astronomical timings. Alongside these, torsion balance gravimeter methods were developed by W. Schweydar in 1918, allowing the first salt dome to be confirmed in the Gulf Coast of the USA in 1922 [25]. Despite these developments, both

*The unit Gal, named after Galileo Galilei, is equal to 1 cm s^{-2}. It is used instead of SI units in the field of commercial gravimetry. The unit g (9.81 m s^{-2}) is sometimes used but is not static (as the value can change based upon the variables aforementioned), and is therefore a poor choice for a standard unit

types of gravimeters continued to be costly with observation times ranging from one to six hours.

In order to generate faster survey times, static gravimeters were developed that observed the equilibrium position of a mass on a spring system. Though Herschel had proposed the construction of a spring balance for gravimetry in 1833, it was not until between 1930 and 1950 that any such device was created. Devices such as the level spring balance developed by O. H. Truman in 1930 could obtain accuracies of $0.2 \rightarrow 0.5$ mGal. This sensitivity would be improved to $0.05 \rightarrow 0.2$ mGal by A. Hoyt [26] in 1960. The observation times for such devices was now between 10 and 30 minutes and they had almost entirely replaced the torsion balance by 1939. Though ocean measurements had been carried out before the 20th century, it was not until the work of F. A. Vening-Meinesz in 1921 that a more extensive survey of the oceans could be carried out. Vening-Meinesz developed a two-pendulum system for measurements taken on moving platforms. The use of this system on submarines allowed for over 5000 measurements to be taken by several countries; however, they were limited to an accuracy of $\pm(3 \rightarrow 10)$ mGal. With the addition of these submarine measurements, the initial catalogue of 15 gravity values used by Laplace in 1799 for the calculation of the Earth's flattening ratio had grown to more than 10000.

The final development phase in the story of gravimeters was the establishment of gravity networks during the 20th century. Between 1930 and 1950, more than 30 different types of spring-based gravimeters were in use, however the most successful was that of Lucien LaCoste in 1939 and manufactured by LaCoste & Romberg (L&R). It was during this development that the zero-length spring was introduced by LaCoste; another relative spring-based measurement that was easier to make, calibrate and use. These gravimeters obtained an accuracy of about 20 μGal, reduced to $1 \rightarrow 5$ μGal once corrections for internal and external errors were taken into account. Zero-length spring gravimeters dominated the industry until Scrintrex Ltd developed a fused quartz gravimeter in 1989. This device used both capacitive sensing and electrostatic feedback and allowed the device to largely dominate the gravimetry market. During the second half of the 20th century, static gravimeters could be constructed with an accuracy of ± 1 μGal for stationary systems, and ± 10 μGal for field use. This period also saw the construction of the first free-fall absolute gravimeters. The falling rods were timed with enough precision to obtain an accuracy of $\pm(1 \rightarrow 2)$ mGal by Volet (1946). However, by 1963, Sakuma and Faller obtained an accuracy of ± 10 μGal through the introduction of a Michelson interferometer [27]. The latter half of the 20th century also welcomed the construction of sea and bore-hole gravimeters and their accompanying measurements (Sea, Graf 1957, and LaCoste 1959) and included the first aerial surveys. The

first gravity gradiometers were also developed around this time. These gradiometers measure the spatial derivative of gravity, providing information on how the acceleration of gravity changes with spatial position (and thus are in units of s^{-2}). Given that the value of gravity is given by the expression, $g = {}^{GM_E}/_{r^2}$, it would stand that the gradient is given by the following:

$$\frac{\mathrm{d}g}{\mathrm{d}r} = \frac{-2GM_E}{r^3} = -2\frac{g}{r}\,, \tag{1.4}$$

where M_E denotes the mass of the earth [kg], assumed to be a point mass measured at radius r [m]. The late 20th to early 21st century has seen the use of gravimeters and gradiometers on satellites [28–33], providing further information on the terrestrial gravity field. By 1987, over 11 million gravity values were stored, many that are publicly accessible, whilst others are overseen by military organisations. In 1999, a team lead by Mark Andler who utilised an onboard microprocessor and capacitive force feedback negated some of the reasons zero-length springs were used. Rather than measuring the movement of the spring, the system measures the amount of capacitive force required to keep it in the zero position.

Following the four phases highlighted by Wolfgang Torge, gravimetry and gradiometry has continued to improve in accuracy and coverage. Measurements have now been taken using space-based satellites such as the Gravity Field and Steady-State Ocean Circulation Explorer (GOCE) [30, 34, 35] and the Gravity Recovery and Climate Experiment (GRACE) [32, 36, 37]. GRACE was launched in March of 2002 to map the Earth's gravity field and consists of two satellites. The mission is still running under an extended mission phase as it was designed to have a lifetime of five years. GOCE on the other hand, was launched on the 17th March 2009 and mapped the Earth's geoid. GOCE, however, ran out of fuel on the 21st October 2013 followed by a planned disintegration in the lower atmosphere. This map has since been used in oceanography and climate change amongst others and continues to be exploited. It is worth noting that although, both GOCE and GRACE measure gravity, GRACE measures temporal variations whereas GOCE measured the static gravity field.

1.1.2 Applications

The first use of gravimetry was in calculating the gravitational acceleration of the Earth, followed by the Earth's flattening ratio [22]. Following its first use, it has since been applied to the measurement of: the Earth's geoids (positions around the Earth with the same gravitational potential [38]); local topographies such as the location of exploitable minerals like oil and gas; and looking for the location of sinkholes within the field of civil engineering. Gravimetry has also had useful environmental applications by furthering the predictions of

precursor signals that indicate volcanic eruptions assisting early warning systems [17][18]. Other environmental applications include: monitoring the sequestration of nuclear material, and monitoring the draining of subsurface water deposits caused by massive consumption of water within the agricultural sector [37][36]. Gravimetry can also boast a useful position within the field of archaeology, unearthing underground ruins and tunnels.

1.1.2.1 Subsurface Voids

Throughout history, it has been common practice to hide and tunnel underground, whether to build command facilities as Germany and the UK did during World War 2, or to dig underground tunnels like those traversed by the Viet Cong or even by medieval soldiers to bypass the opposition's defences [39–43]. Nowadays, modern underground facilities could include intercontinental missile bases that house the more traditional explosives as well as nuclear payloads, tunnels concealing human trafficking, and the smuggling of contraband. These problems in modern society have generated a significant interest in the tools and techniques that can measure (or at least be used to infer) what is below the ground. To image areas of interest, several different measurement techniques are used and combined for the greatest accuracy.

As the gravitational acceleration felt by an object will depend on the mass distribution around the object, information on subsurface anomalies can be obtained, including that of any mass void like tunnels or holes. The change in gravity in the vertical direction (g_z), expected from a cylindrical tunnel of length (L), and radius (r), is given by equation 1.5 [8].

$$g_z = \frac{\pi \rho G r^2 z}{x^2 + z^2} \times \left(\frac{y + L}{[(y+L)^2 + x^2 + z^2]^{1/2}} - \frac{y - L}{[(y-L) + x^2 + z^2]^{1/2}} \right) , \tag{1.5}$$

where ρ [kg m^{-3}] is the average density around the tunnel at a depth of z, x and y are the respective axes away from the centre of the cylinder. G is the gravitational constant $= 6.67 \times 10^{-11}$ m^3 kg^{-1} s^{-2}. This equation can be simplified by noting that the largest signal is along the centreline of the cylinder, i.e. $x = y = 0$. By also setting $L >> z$, equation 1.6 below can be obtained:

$$g_z = \frac{2\pi \rho G r^2}{z} . \tag{1.6}$$

For example, using equation 1.6, a 1 m radius tunnel at a depth of 5 m would induce a change in gravitational signal of ≈ 23 μGal if the tunnel were surrounded by granite ($\rho = 2750$ kg m^{-3}). This equation can also be redefined by replacing g_z with the noise of a given system

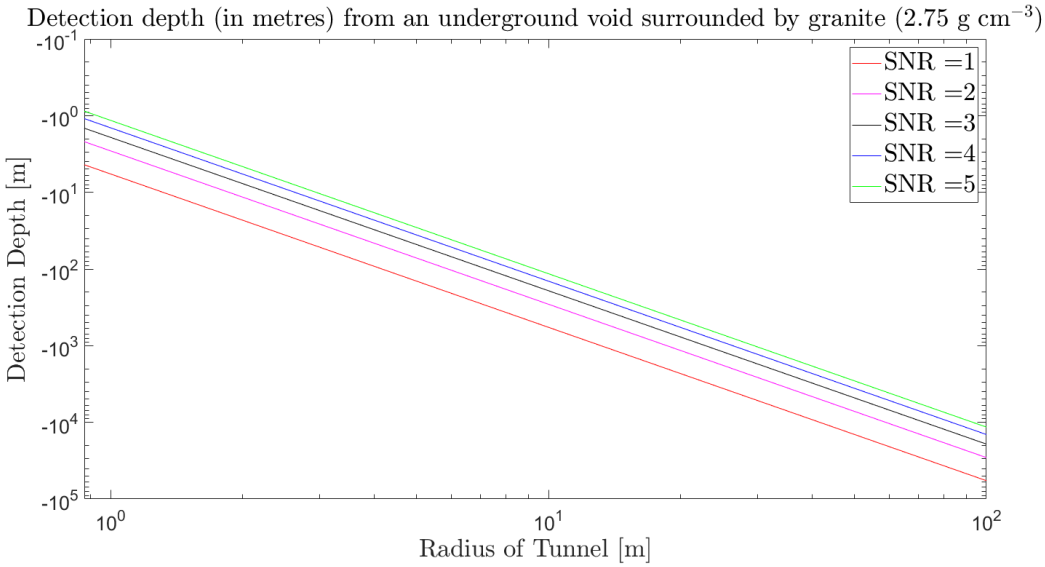

Fig. 1.1 Graph showing the detection depth for a given radius of a tunnel for a system sensitivity of 20 μGal with differing SNRs. This calculation used the density of granite (2.75 g cm^{-3}) as the surrounding rock.

(g_n) and the signal to noise ratio of the measurement (N) required. By rearranging for z, equation 1.7 is obtained and shows the detection depth given the SNR required and system noise.

$$z = \frac{2\pi\rho G r^2}{N g_n} \,. \tag{1.7}$$

As an example, a system with a noise of 20 μGal could detect a 5 m radius tunnel as far down as 70 m with an SNR of 2. As the SNR requirement increases, the detection depth comes closer to the surface, i.e. becomes shallower, due to needing a larger signal for a given system noise. Figure 1.1 shows the detection depth for a system with a noise of 20 μGal for different tunnel radii and SNR values (this assumes that the noise is white).

1.1.2.2 Volcanology

Particular fields of study focus their attention on identifying the precursors to volcanic eruptions, otherwise known as volcanology, within which gravimetry has useful applications. The Mogi Model is a mathematical tool which allows an estimation of the Earth's deformation as magma intrudes into a chamber [44]. The model relates a change in volume of a sphere buried at depth, z beneath the surface to changes in the elevation of the surface, dz at a total

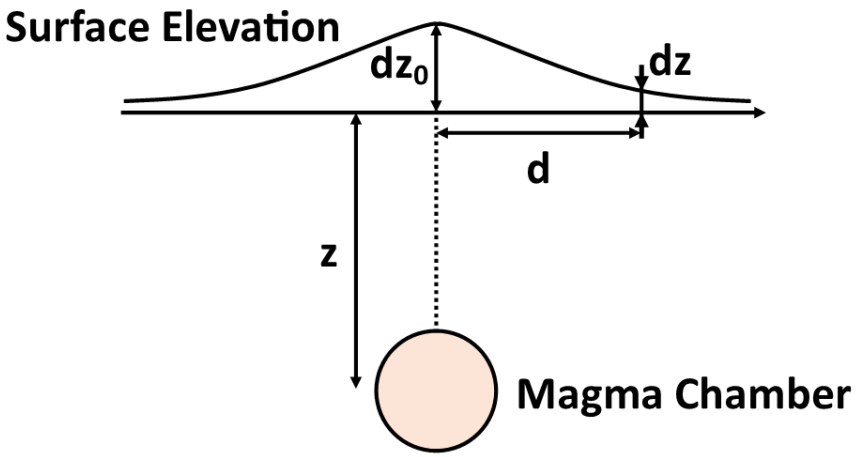

Fig. 1.2 Depiction of the variables used in modelling Mogi Model. The model considers the effect of magma filling a subterranean chamber which results in a protrusion on the surface.

distance from the centre of uplift, d. The magma chamber can be simplistically thought of as a balloon that is repeatedly inflated and let down and is depicted in figure 1.2. An estimate of the gravitational signal, g_m, obtained from such a movement of magma with mass, ΔM_m [kg] is shown in equation 1.8 [16].

$$g_m = \frac{\Delta M_m \, G \, z}{(x^2 + z^2)^{3/2}} \, . \tag{1.8}$$

Here, x and z represent the surface distance and the depth to the centre of the magma source, both in metres, m. As an example, a cylindrical flow of magma with a mass of 1×10^{11} kg (an estimate of a smaller magma flow) can be detected as far as 3.2 km horizontally from the source at a depth of 4 km (total distance of 5.12 km from source) with an SNR of 1 using a system with noise of 20 μGal. Similarly, an intrusion of magma with a mass of $= 1 \times 10^{12}$ kg could be detected up to 10 km horizontally away at a depth of 4 km (total distance of 10.7 km from source) with an SNR of 1, using the same system. Figure 1.3 shows the gravity signal from moving magma of mass 10^{11} kg and 10^{12} kg. Measurements of the signals expected before volcanic eruptions have been been carried out. Carbone et al. [18] discusses a series of gravity measurements while highlighting that time variable gravity has a benefit over other

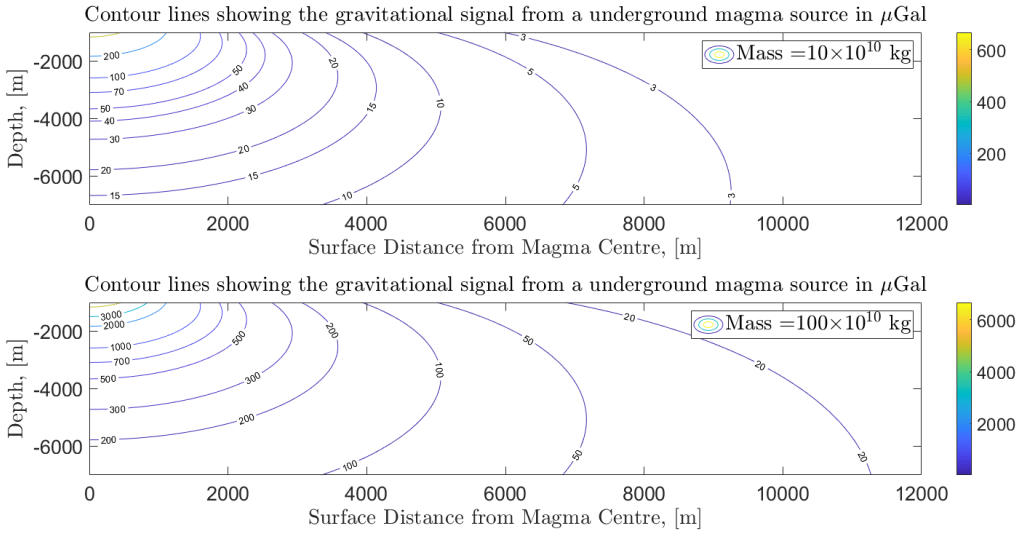

Fig. 1.3 The expected gravity signal from an intrusion of magma of two different masses (top $\Delta M = 10^{11}$ kg, bottom $\Delta M = 10^{12}$ kg). Several gravity contours are shown on each for a given depth and distance of the magma. This result is using equation 1.8 with the Mogi Model.

methods during volcanic observations. It has been shown that gravity signals from volcanoes could vary from tens to hundreds of μGal depending on proximity to source and its size. For example, gravity measurements at Mt. Etna during 1990-1991 showed changes up to 450 μGal when taking a cross section through the summit and fracture whereas measurements at the Piton de la Fournaise volcano (an island approximately 750 km east of Madagascar in the Indian Ocean) showed signals up to a maximum of 100 μGal.

1.1.2.3 Carbon Capture Monitoring

Recently, there has been a desire to store large amounts of excess CO_2 underground to reduce the effect of climate change. This method does not come without consequence. If the CO_2 leaks, it would be to the detriment of local wildlife [45] and render the attempt to capture the CO_2 an expensive failure. M. Sugihara et al. modelled the expected change in gravity over time while continuously pumping 10^9 kg each year 2250 m into the earth [46]. They showed that one would require a measurement accuracy of less than the 100 nGal level over several years. The change in signal was estimated to be around 1000 nGal per 1000 days, i.e. 1 nGal per day. This level of change a day is incredibly tiny and is not achievable using the most modern and expensive absolute gravimeters (see discussion on the FG-5 in section 1.1.4.1).

At best, the most accurate gravimeters could be used to remove trends after monitoring over extended periods.

1.1.2.4 Earthquake Precursors

Earthquakes can happen almost anywhere in the world, yet are much more likely to occur near tectonic plate boundaries. They are capable of causing devastating damage to buildings and infrastructure, claiming lives and putting financial strain on communities. Before an Earthquake strikes, there is pre-seismic activity leading up to the event [47]. Depending on the distance from the epicentre and magnitude of the earthquake, the size of the pre-seismic signature can vary. Data taken before and during an earthquake, with a surface-wave magnitude of 6.4, displayed pre-seismic data leading up the event. The seismic signal varied from 50 to 250 μGal, while the seismic sensors varied from 4612 km to 1402 km from the epicentre [47].

It has also been noted that monitoring for gravity signals could increase the speed at which an estimate for an upcoming Earthquake can be obtained. As an example, the US Geological Survey (USGS) took 40 minutes to update its initial estimate of magnitude 7.9 to 8.8 compared to 3 hours for the Japan Meteorological Agency [48]. Another study [49] looked into the prompt gravity signals, a gravity signal observed before an earthquake, induced by the 2011 Tohoku-Oki earthquake. They found a signal with an amplitude of 0.10 μGal $\rightarrow$ 0.15 μGal with a significance of 99%. This signal was between the rupture onset time and the arrival of the p-wave. This study amongst others could help reduce the time required to issue warnings and help with faster estimation of its magnitude (which currently takes up to several minutes).

1.1.2.5 Civil Engineering

In many parts of the world, cities have been built on top of a class of rock that is water-soluble known as evaporite [50]. It is estimated that 35% to 40% of the USA is built upon evaporite. As the minerals dissolve in groundwater, large voids start to form underground until, eventually, the thin crust at the top gives way, taking anything above with it. These features are known as “sinkholes”. The water can be from rain but can also have unnatural causes, e.g. drilling works above ground or broken water pipes. Sinkholes can be a few hundred metres wide and vary in depth from just a few, to tens of metres [14][51]. Statistics show that the probability of death due to sinkholes is small (approximately one hundred deaths or injuries per year [52]), yet they can still cause severe damage to property. The

devastation caused, combined with their lack of predictability, has created a demand by residents, government officials, and property investors to advance the technology that can measure and predict sinkholes. Gravimetry can be applied to measure the cavities forming and so certainly has its place within this research. A measurement near the location of the two sinkholes formed at Wink, Texas (named as Wink Sink 1 and Wink Sink 2), showed a -170 μGal change [14]. This anomaly was also highlighted by an interferometric synthetic-aperture radar (InSAR) onboard a satellite.

1.1.2.6 Oil and Gas

It is common practice in oil and gas exploration to look for the gravity signals of salt domes [53]. Salt domes are vertical intrusions of evaporite rock (mainly salt) into surrounding rock strata. These are significant, as they can form a stratigraphic trap which serves as a reservoir of petroleum, oil, or gas. These signals can vary in strength and shape when plotted against distance. Signals from salt domes, for example, can vary wildly from hundreds of μGal to tens of mGal. This variation is due to the variety of sizes, shapes, depths/distances and the density contrasts occurring within the surrounding earth. A simple model similar to that of the magma calculation in section 1.1.2.2 can be used to estimate the signal from a particular density contrast, as shown in equation 1.9 [53].

$$\Delta g_0 = 2\pi G \int_a^0 \int_{Z_1}^{Z_2} \rho(r,z) r (r^2+p^2)^{-3/2} z \, \mathrm{d}z \, \mathrm{d}r \,, \tag{1.9}$$

where the gravity signal, Δg_0, is the first order term in a fast converging series. ρ is the density of the salt as a function of r (the distance from the centre of the dome to the current position) and z (the distance from the centre of the dome to the current height). G is, as usual, the gravitational constant $= 6.67 \times 10^{-11}$ m^3 kg^{-1} s^{-2}. a is the total radius of the dome, Z_1 is the depth to the centre of the dome, Z_2 is the depth of the total anomaly and p is the total distance from the observer to the centre of the dome. These terms are visualised in figure 1.4. To simplify this, only the first order term is will be used, and the density is assumed to be constant. By then integrating, the previous equation simplifies to:

$$\Delta g_0 = \pi G \rho (Z_2^2 - Z_1^2) \int_0^a r (r^2+p^2)^{-3/2} \mathrm{d}r \,. \tag{1.10}$$

The final integral can be obtained using a simple integration by substitution. Letting $u = r^2 + p^2$ with $\mathrm{d}u = 2r\mathrm{d}r$, the integration becomes $\frac{1}{2}\int u^{-3/2} du = \left[u^{-1/2}\right]$. By resubstituting u the equation finally becomes:

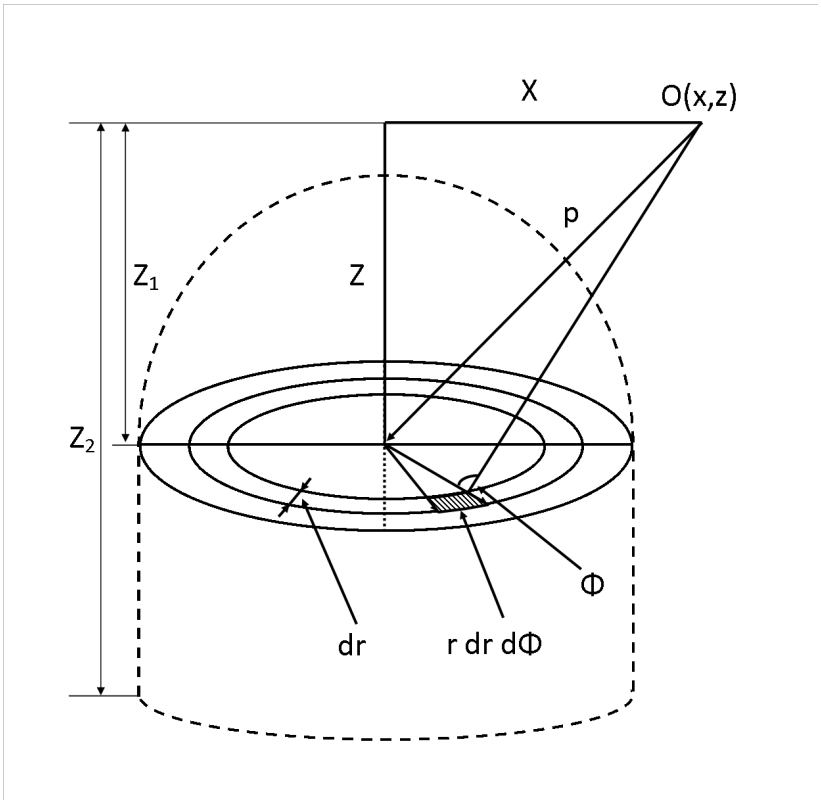

Fig. 1.4 Diagram depicting the variables used to model a salt dome made up of a hemisphere and cylinder. Key variables of the dome are its: density, radius, height, depth, and distance from observer.

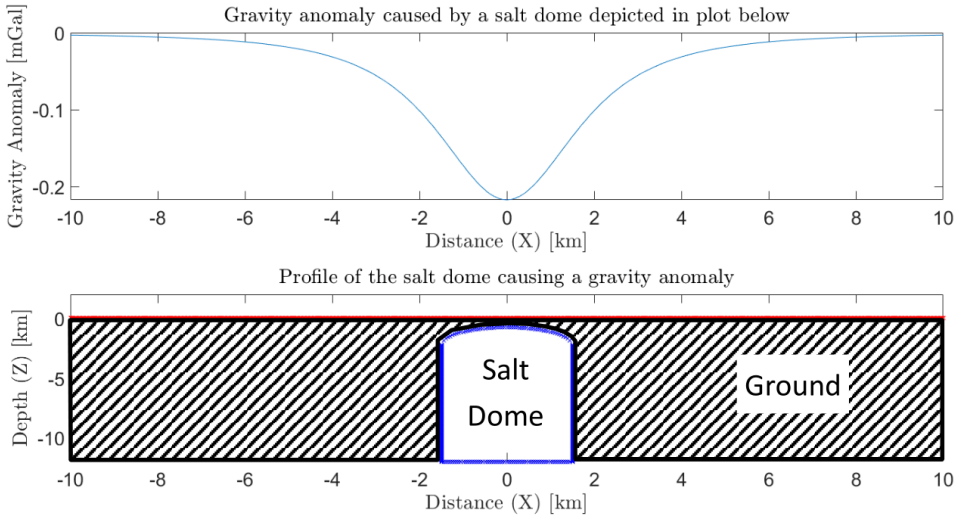

Fig. 1.5 Diagram of the gravity anomaly caused by an underground salt dome. Here the density contrast was assumed to be 0.3 g cm^{-3} for a dome radius of 1.5 km at a depth of 1.5 times the radius (2.25 km). The salt dome extends down to 12 km. The graph shows how the gravity anomaly varies as the distance from the center line of the anomaly.

$$\Delta g_0 = \pi G \rho (Z_2^2 - Z_1^2)\left(\frac{1}{\sqrt{a^2 + p^2}} - \frac{1}{p}\right) . \tag{1.11}$$

As an example, a salt dome with an average density contrast of 0.3 g cm^{-3}, with a radius of 1.5 km and at a depth of 1.5, times the radius (2.25 km), could have a gravity signal of up to 0.21 mGal. The gravity signal from this anomaly is seen in figure 1.5 with horizontal distance from the centreline. The lower figure shows the 2D profile of the salt dome with it reaching as far down as 12 km.

1.1.2.7 Planetary Geodesy

Geodesy comes from an Ancient Greek word which literally translates to “Division of the Earth”. The classical definition of Geodesy is the ‘mapping of the Earth’s Surface and gravity field’, normally referred to in terms of gravitational acceleration [38]. Related to geodesy is the discipline of geodesics, involving the determination of Earth’s field of gravity and of many other celestial bodies. Measurements can highlight changes in both position and time. For space-borne applications, a gradiometer is generally used. As mentioned

previously, gradiometers measure the derivatives of the gravity potential with respect to spatial position, which is in units of s^{-2}. The second derivative of gravity diminishes with the radial distance to the third order (see equation 1.4) and thus requires accurate timing measurements alongside an accurate separation distance and common mode rejection. The Gravity Field and Steady-State Ocean Circulation Explorer (GOCE), used three precision accelerometer pairs (precision of an order 10^{-12} m $s^{-2}/\sqrt{\text{Hz}}$ at a 1 s sampling rate) to measure changes of order 10^{-11} s^{-2}. These changes were sufficient to measure changes in the melting of the polar icecaps and were a comparison of the work undertaken originally by the Gravity Recovery and Climate Experiment (GRACE) [54, 32, 36]. There was, however, one distinct difference which was mentioned previously, GRACE was measuring the temporal changes and GOCE the static field. The geoid, a surface with the same gravity potential, is useful in fields like climate science and is measurable by mapping the horizontal and vertical displacements of land via the use of a satellite continuous monitoring system. An example of such a monitoring system is the combination of the Very Long Baseline Interferometer (VLBI), Satellite Laser Ranging (SLR), Global Navigation Satellite System/Global Position Satellite (GNSS/GPS) and Doppler Orbitography and Radiopositioning Integrated by Satellite (DORIS) networks world wide [55]. This array of systems monitor the movement of the tectonic plates showing varying speeds of drift, from a few mm, to more than a cm per year [56, 57].

1.1.2.8 Archaeology

As mentioned previously, the signal seen from a gravity anomaly depends on the density contrast and the distance from the sensor. These variables make archaeology through gravimetry extremely difficult. Buildings and ruins, for example, could be quite small and have a very similar density to nearby rock/sediment, resulting in too small a signal. The same issue would arise with collapsed old mines or voids that have been filled with nearby rock/sediment/water (making the density contrast poor). Measurements made of a Byzantine Church in Iznik/Nicea, Turkey, showed a gravity anomaly of -5 μGal to $+5$ μGal while only being a few metres underground [21]. This small signal was used to begin mapping the unseen structure of the church, including the wall, foundations and voids. For these measurements, a range of other methods were used, such as ground-penetrating radar, magnetic mapping, and electric resistivity tomography to improve the knowledge of the underground structure. As a comparison, a study at the St. Nicolas Church in Pukanec, Slovakia found a signal as large as -30 μGal, inferring the location of a crypt just 1 m underneath the church apse [20].

1.1.3 Gravimetry Methods

1.1.3.1 Absolute Gravimeters

Pendulum Gravimeters

Pendula were the basis of the first gravimeters to be used. To make a pendulum-based observation of gravity, the oscillation time and length of said pendulum must be known. This oscillation time is then used to calculate the acceleration of gravity. Figure 1.6 shows an example of a pendulum with a length of L and a mass of m.

Appendix D provides a derivation of equation 1.12 and 1.14. Equation 1.12 gives the equation used for calculating the acceleration due to gravity acting on a pendulum of length L with an oscillation period, t_o.

$$g = \frac{4\pi^2 L}{t_o^2}\left(1 + \frac{1}{16}\theta^2 + \frac{11}{3042}\theta^4 + ...\right) . \tag{1.12}$$

If equation 1.12 is taken to first order, i.e. for small angles then the equation simplifies to have no θ terms as seen in equation 1.13.

$$g = \frac{4\pi^2 L}{t_o^2} . \tag{1.13}$$

Equation 1.12 can be used to derive equation 1.14. The equation shows the relationship to calculate the error in a gravity measurement for a given error in length of the pendulum and oscillation period.

$$\left(\frac{\Delta g}{g}\right) = \left(\frac{\Delta L}{L}\right) - \left(\frac{2\,\Delta t_o}{t_o}\right) . \tag{1.14}$$

If an accuracy of 100 μGal is required of a gravity measurement using a pendulum of length 1 m, the length of the pendulum has to be measured to within ± 0.1 μm and its oscillation known to within ± 0.1 μs.

A consideration would also need to be made regarding temperature changes on the pendulum. A clear parameter that varies with temperature is the length of the pendulum, due to its non-zero thermal expansion coefficient as well as the change in Young's modulus (see section 2.2.1.1 for more information). If we take the derivative of equation 1.12 with respect to temperature (T), equation 1.15 can be obtained. Remembering that the measured quantity during experimentation is the oscillation period, a change in temperature would result in an error in the timing measurement which would in turn cause an error in the gravity measurement. This is why is why the equation has the variable dT, the change in period

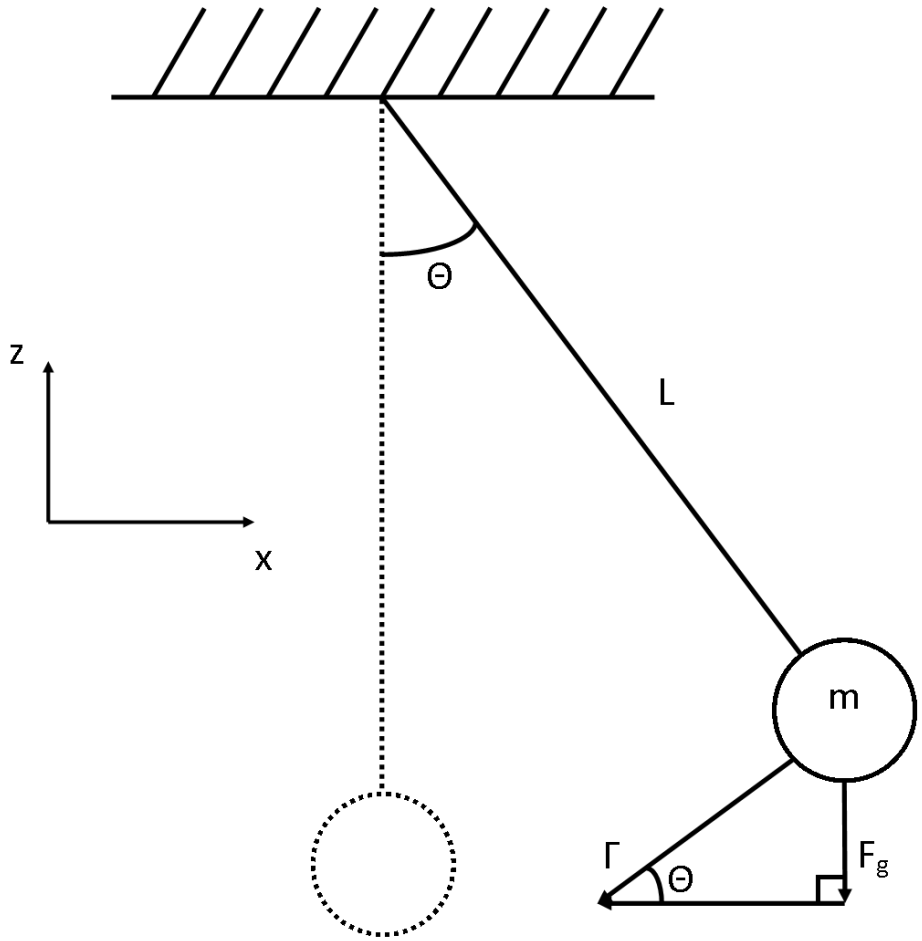

Fig. 1.6 Diagram showing gravity acting on a pendulum and the resulting torque that results in an oscillation dependent on the acceleration due to gravity and the length of the pendulum. *L*

given by the expression, $\mathrm{d}t_o = \frac{\alpha L_0}{2TL}\mathrm{d}T$. Given the thermal expansion of quartz (a material that has commonly been used to create high quality gravimeters), $\alpha = 5.5 \times 10^{-7}$ K^{-1} for a pendulum of length $L = 1$ m at standard Earth gravity equal to 9.81 m s^{-2}, a 10 K change in temperature would result in an error of $\mathrm{d}g = 1.3$ mGal. This shows why it is important to have such a device under temperature control.

$$\frac{\mathrm{d}g}{g} = \frac{4\,\pi^2\,L\left(\frac{1}{(T+dT)^2} - \frac{1}{T^2}\right)}{g}\,. \tag{1.15}$$

A worthwhile note is that pendula can be used in a semi-absolute arrangement. This only requires the acceleration of gravity to be known at some starting position (g_1) and the two oscillation periods, T_1 and T_2 relating to positions 1 and 2. Note that this does not require the length of the pendulum or any other factors (except for the initial measurement of g_1). Equation 1.16 shows the relationship that governs the difference in gravity between points 1 and 2 ($\Delta g_{1,2}$).

$$\Delta g_{1,2} = g_2 - g_1 = g_1\left(-2\,\frac{T_2 - T_1}{T_2} + (\frac{T_2 - T_1}{T_2})^2\right)\,. \tag{1.16}$$

The equation shows that once a single point of gravity is measured, only a series of oscillation periods is required to find the surrounding values of gravity.

Free Fall Gravimeters

By dropping a mass and measuring its position, z_n after a time interval, t_n, the acceleration due to gravity, g, can be measured. Equation 1.17 shows that for three positions and times; the absolute value of gravity can be measured. In reality, many more than just three points would be required to optimise accuracy. It is also necessary to perform the free fall in a vacuum to reduce air friction effects that would consequently alter the measured acceleration. These new measures necessitated an advance in glass making and vacuum systems that allowed free fall gravimeters to achieve optimum accuracy. Advances in distance measurements and timing measurements were also crucial, particularly the invention of the interferometer that allowed these gravimeters to become the most accurate on the market. The relationship used to calculate the acceleration of gravity from three separate spatial and temporal measurements is seen in equation 1.17, the derivation of which is in appendix D.

$$g = 2\,\frac{(z_3 - z_1)(t_2 - t_1) - (z_2 - z_1)(t_3 - t_1)}{(t_3 - t_1)(t_2 - t_1)(t_3 - t_2)}\,. \tag{1.17}$$

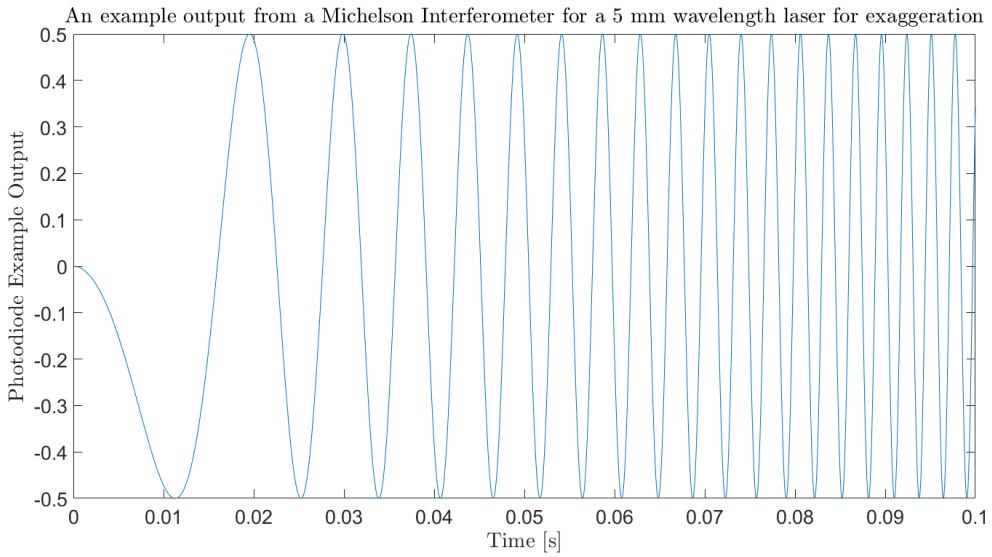

Fig. 1.7 Graph showing an example of the output from a Michelson Interferometer for a falling mass. For exaggeration, the wavelength of the laser was set to 5 mm to better highlight the trend. The fringes become closer together as mass gets closer to the bottom of the cavity. The fringes are separated by $\frac{\lambda}{2}$.

The terms z_{th}, and t_{th} are the nth position and time measurement of the mass. Figure 1.7 shows an exaggerated output from a free fall gravimeter being measured using a Michelson Interferometer. A Michelson Interferometer consists of a laser aimed at a beam splitter [58]. One of the light beams is directed at a stationary mirror and the other at the moving mass. After reflecting off of both mirrors, the beam paths reunite and travel towards a photodiode. If the waves are in phase, then they add (constructive interference), however, if in anti-phase, they cancel (destructive interference). This design is shown in figure 1.8 and figure 1.7 shows an example of the output from a Michelson Interferometer for a mass dropped from an arbitrary height. The fringes are separated by $\frac{\lambda}{2}$, showing an increasing speed of the mass as time passes. Figure 1.7 shows a decrease in the time taken for the laser to return to the sensor as the mass falls at an increasing speed. Using figure 1.7, the peak positions are used to obtain the corresponding times. Note that as gravity changes by approximately 0.3 mGal m^{-1}, to obtain a resolution better than $0.3 \times L$, where L is the length of the gravimeter, the non-homogeneous gravity field must be taken into account.

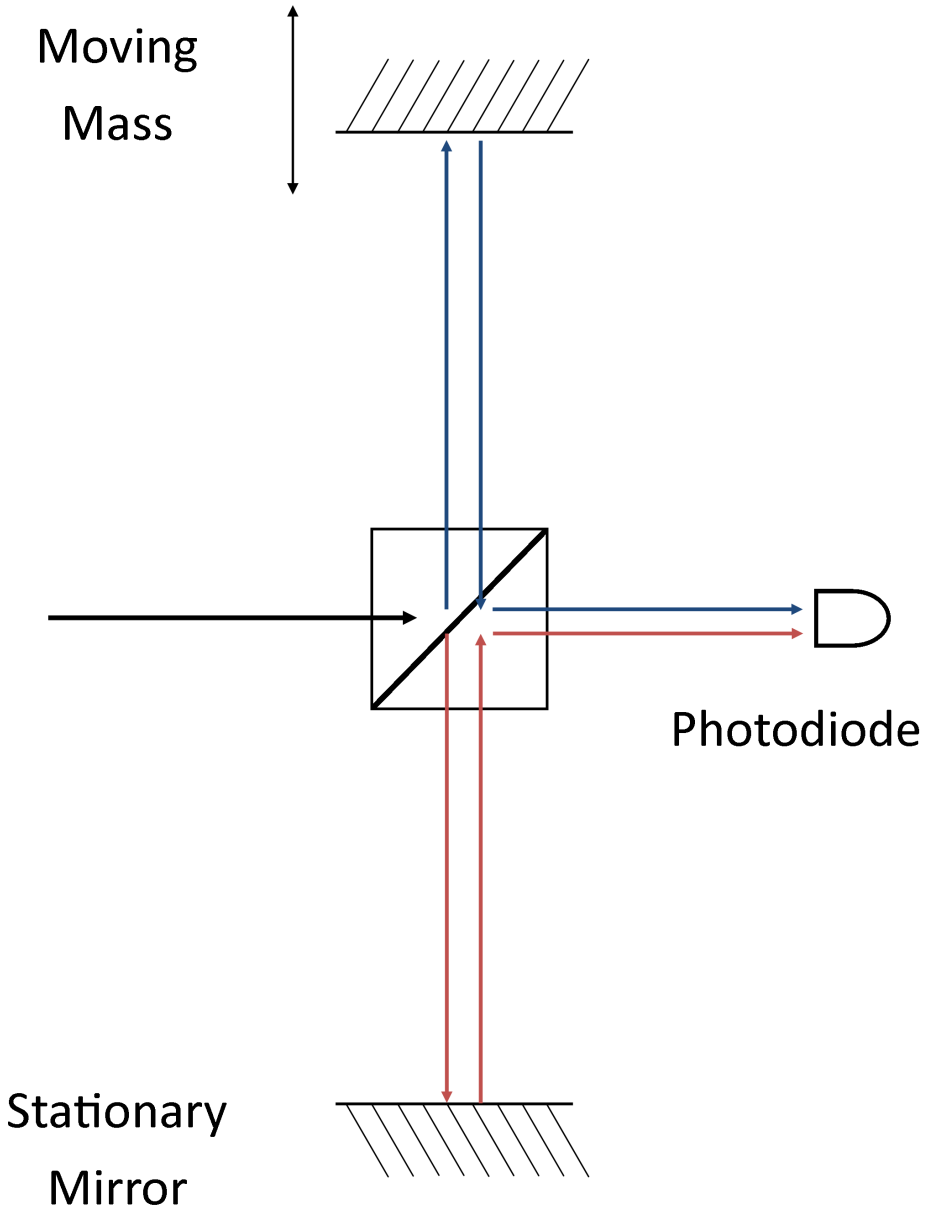

Fig. 1.8 Diagram showing the Michelson Interferometer Scheme as used in a Micro-g LaCoste FG-5. A laser beam travels to a beam splitter, resulting in two beams being redirected. One to a stationary mirror, and the other to a moving mass. By recombining, and reaching a photodiode, constructive/destructive interference occurs.

Symmetric Rise and Fall Gravimeter

A rise and fall gravimeter is similar to a free fall gravimeter, but with one significant difference. Rather than measuring the position and time as a mass falls, it throws the mass upwards, where its position z_n is measured at time t_n constantly. This vertical displacement is then measured at the same level on the other side of the apex creating pairs of data points. Strictly speaking, only two pairs of data points is required for the calculation of the acceleration due to gravity but more are used for accuracy. See figure 1.7 for the depiction of the measured data points. Equation 1.18 (derived in appendix D) shows that the acceleration of gravity can be calculated given the difference in vertical displacement, Δz, between two measuring positions and the time taken for the mass to return to displacement at the other side of the apex, Δt_1 and Δt_2. These variables are depicted in the figure showing the masses trajectory in terms of height and time.

$$g = \frac{8\Delta z}{\Delta t_2^2 - \Delta t_1^2} \,. \tag{1.18}$$

As with the free fall gravimeter, the non-homogeneous gravity field has to be taken into account for sensitivities < 0.3 mGal. The rise and fall gravimeter was developed after the free fall gravimeter. One such gravimeter was the IMGC designed in 1976 and realised in cooperation with the Bureau International des Poids et Mesures [59]. Rise and fall gravimeters are used as they have an advantage of reducing the errors associated with free fall gravimeters.

1.1.3.2 Relative Gravimeters

Balance and Zero Length Spring

A zero length spring is a spring with zero load for zero displacement. Most springs have zero-restoring force at a finite displacement. These springs have the advantage of being insensitive to longitudinal and transverse vibrations. The gravimeter consists of a spring acting against the torque produced by gravity acting on a suspended mass. The suspended mass is moved to a zero position either via a biasing lever connected to the spring or by use of another weaker “measuring” spring connected to the suspended mass system. Figure 1.10 depicts the fundamentals of the described system above. Either a lever or screw can be moved to bring the system to a balanced position, allowing a value to be noted as the measurement.

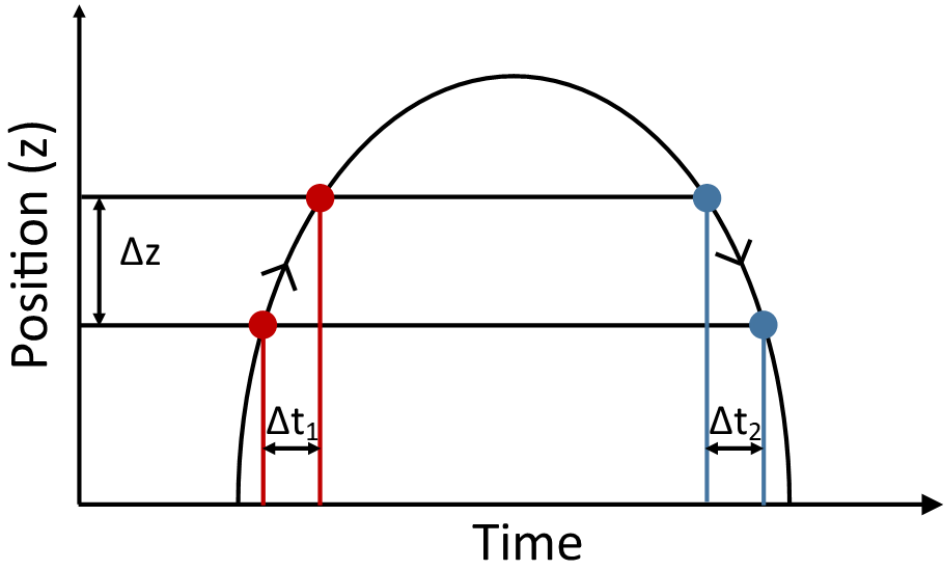

Fig. 1.9 Diagram showing the measurement points of a rise and fall gravimeter. The system measures the time at 4 positions, and as two pairs of heights at either side of the apex. The difference between these points on the same side allows for the calculation of the acceleration due to gravity. The position and times can be measured using a Michelson Interferometer as shown in figure 1.7.

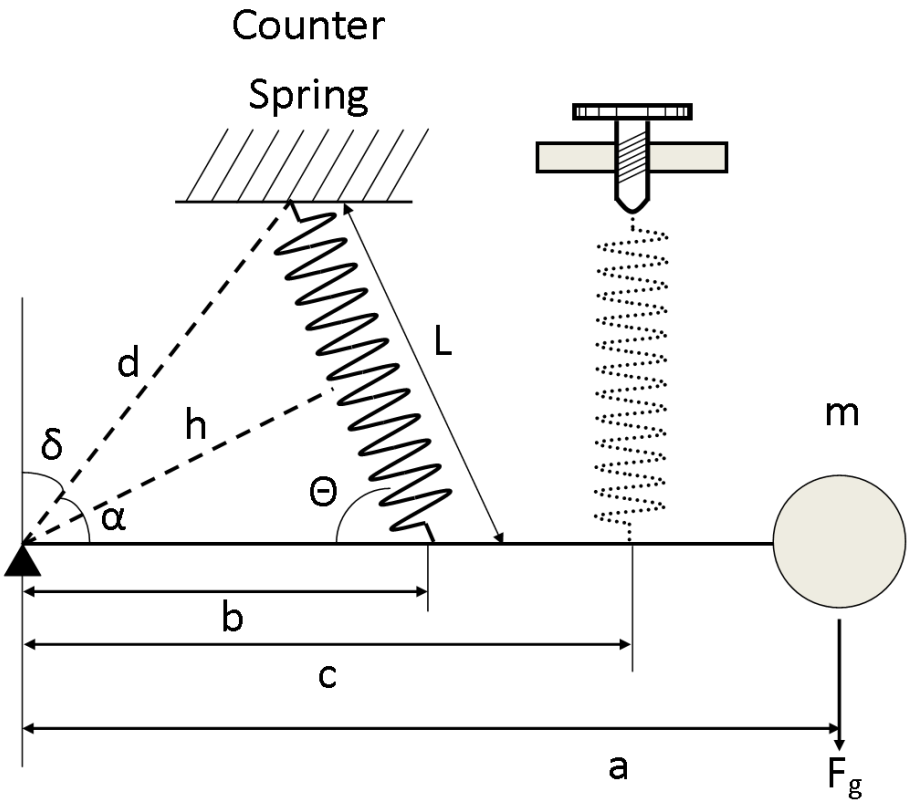

Fig. 1.10 Diagram showing the forces and variables involved in a zero length spring. A mass of m is suspended a distance away from a pivot point, with a spring countering this torque at a distance (b) from the pivot. The measuring spring can be used to adjust where the mass sits, allowing relative measurements from previous zero positions.

Equation 1.19 shows the relation of the system shown in figure 1.10 utilising the zero length spring, the derivation of which is in appendix D. It can be seen that the sensitivity (a change in angle α for a given change in gravity dg, $\frac{\mathrm{d}\alpha}{\mathrm{d}g}$) is highest when $\alpha+\delta=90°$ (where δ is the angle the vector makes from origin to the top of the counter spring), whilst minimising δ, and maximising α, i.e. the mass is suspended horizontally (seen in figure 1.10). If a system with $\alpha+\delta=90°$, $\alpha=\delta=45°$, a change in gravity of 100 μGal would produce a change in angle of 102 nRad, which, if the measuring spring is 20 cm from the pivot point, results in a change in displacement of 20.4 nm. If instead $\delta=10°$ and $\alpha=80°$, the displacement would be 116 nm. In reality this technique is calibrated using a known signal.

$$\frac{\mathrm{d}\alpha}{\mathrm{d}g}=\frac{\sin(\alpha+\delta)\sin(\alpha)}{\sin(\delta)}\frac{1}{g}\,. \tag{1.19}$$

1.1.4 Current Leading Commerical Gravimeters

1.1.4.1 Micro-g LaCoste FG-5

An example of a modern **absolute** gravimeter is the FG-5 [60, 61], manufactured by Micro-g LaCoste. It utilises the superspring: a long-period, active, seismic-isolation device. The superspring consists of a short (20 cm) mainspring with a a natural period of about one second which is contained inside a support housing. This housing also has springs which are servo-controlled to track the Superspring mass (that is attached to the end of the mainspring). This spring acts to isolate against ground (vertical) motions with a frequency higher than that of the mainspring. The design of the superspring gives an inertial reference for the gravity measurements. To measure the displacement of the mass (and therefore acceleration), a Mach-Zender type interferometer is used. The interferometer uses a fixed (reference) arm and a variable (test) arm with a length kept via use of the Superspring mass. Isolation in the vertical direction results in any change of the beam length (measured by the interferometer) is solely due to the acceleration of the dropped object, i.e. gravity. Using a time of flight method, the system drops a mass in a non-drag chamber using the interferometer to continuously monitor its position. The FG-5 uses a 633 nm He-Ne laser. After obtaining times and positions of a series of peaks, equation 1.20 is fitted to the data:

$$x_i=x_0+v_0\tilde{t}_i+\frac{g_0\tilde{t}_i^2}{2}\frac{\gamma x_0\tilde{t}_i^2}{2}+\frac{1}{6}\gamma v_0\tilde{t}_i^3+\frac{1}{24}\gamma g_0\tilde{t}_i^4\,, \tag{1.20}$$

where:

Fig. 1.11 Picture of the FG-5 from Micro-g LaCoste. It boasts a sensitivity of 15 μGal/$\sqrt{\text{Hz}}$ at 10 s, but is prohibitively large and immovable, consuming 500 W.

$$\tilde{t}_i = t_i - \frac{(x - x_0)}{c} \,. \tag{1.21}$$

x_0, v_0 and g_0 are the initial position, velocity and gravitational acceleration for a measured peak position and time, x_i and t_i. γ is the gravity gradient $= 0.3$ mGal m^{-1}, and c is the speed of light $= 3 \times 10^8$ m s^{-1}. This equation is the result of taking into consideration a non-homogeneous gravity field when using a free fall gravimeter.

The FG-5 boasts an absolute sensitivity of 2 μGal, with a precision of 15 μGal/$\sqrt{\text{Hz}}$ at 10 s. This precision is capable of 1 μGal in 3.75 minutes, or 0.1 μGal in 6.25 hours. The drawbacks, however, are that it requires a floor space of 3 m^2, a total volume of 1.5 m^3, and has a total mass of 150 kg. The device also only operates at $20 \rightarrow 30$ degC, has a power consumption of ≈ 500 W, and can cost into the millions of British pounds [61]. Since the FG-5 is costly, heavy, large and power-hungry, it is not used for field measurements but for static measurements that require the utmost precision and accuracy. Figure 1.11 shows the FG-5 as taken from its brochure [60].

1.1.4.2 Micro-g LaCoste A-10 Portable Gravimeter

The A-10 is a portable absolute gravimeter that also incorporates the Superspring (same as the FG-5). The system uses the Superspring similar to the FG-5 by maintaining the position of a reference corner cube used in the interferometer setup by suspending it from the mainspring. Again, the inner support assembly is actively servo-controlled by tracking of the mass suspended from the Superspring. In this application, by ensuring the length of the mainspring is constant a period of approximately 30 s is obtained. The system must be prepared before use, allowing the thermal control to regulate the system to the target temperature. This process can take more than 4 hours and is ideally undertaken the day before the measurements. It is also recommended that the laser is switched on the day before the acquisition. Once these tasks are completed, the atomic clock can lock within 5-10 minutes, so a vehicle battery is recommended to be charged, as the system can pull 25 A from a 12 V source (300 W) during the warming phase, reducing to 16 A (192 W) when operating. i.e. if operated from a vehicle, the engine will have to be left on to maintain a charge. The system typically takes 30 minutes to acquire data in the field. The gravimeter boasts a precision down to 10 μGal in 10 minutes (stated for a quiet site), and an absolute accuracy of 10 μGal. This accuracy does, however, come at a cost; the system has a mass of 105 kg, a 50 cm diameter and a height of 90 cm.

1.1.4.3 Scintrex CG-6 Autograv™Gravity Meter

The CG-6[62] (seen in figure 1.12[63]) is a relative gravimeter from Scintrex, and is the latest iteration of the widely used CG [64] series of relative gravimeters. The previous model, the CG-5, has been used extensively in the field due to its lower price point in comparison to gravimeters like the FG-5, while still retaining sufficient accuracy and the portability required to be useful in the field. The CG-6 is approximately 24cm $\times$ 21cm $\times$ 21.5cm, with a mass of 5.2 kg. In comparison to the 500 W consumption of the FG-5, the CG-6 only consumes 5.2 W. Though the device states a resolution of 1 μGal, it can drift up to 20 μGal day^{-1} after compensation (200 μGal day^{-1} without). In order to compensate, the system can make automatic corrections using the Earth tides, the instrument tilt, the temperature, the noisy sample filter, the seismic noise filter, and drift data. It works by using a fused quartz zero length spring, similar to that described in section 1.1.3.2. The device can be remotely controlled using Bluetooth and a tablet so as not to disturb the sensor. It can auto-compensate for the tilt with a range of $\pm$200 arcseconds ($\pm$0.056 degrees).

Fig. 1.12 A picture of the CG-6 from Scintrex, a relative gravimeter utilising a quartz zero length spring to obtain resolutions of 1 μGal with compensated drifts of 20 μGal day^{-1}. It measures 24cm $\times$ 21cm $\times$ 21.5cm, weighs 5.2 kg, and consumes 5.2 W of power.

1.2 Development of a MEMS Gravimeter

1.2.1 Introduction

The field of absolute gravimetry was dominated by pendulum measurements up until the invention of the free fall gravimeter. Relative gravimeters such as the initial torsion balances, and relative pendula measurements have largely been replaced with spring-based devices. These, however, are still large, costly and heavy (though certainly not as large as modern absolute free fall gravimeters that can require a room to keep operational). The modern field gravimeter (such as the CG-5/6 mentioned previously) still cost up to one million British pounds and weigh 5 kg each. If a device could be created that was at least an order magnitude smaller in size, weight and cost, it could become the next gravimeter to be commercialised, given it had sufficient sensitivity and stability. Micro-Electro-Mechanical Systems (MEMS) can be made for a range of applications including: biomedical purposes (BioMEMS [65–67]), radio frequency (RF) MEMS [68–71] and inertial MEMS. As the device discussed here is an accelerometer, this section will focus on inertial MEMS. The MEMS accelerometer, a type of inertial MEMS device that can measure inertial accelerations, was developed in 1975 by Vaganov [72], followed shortly by Roylance and Angell in 1979 [73]. Arguably, two of the most critical drivers for superior, lower cost accelerometers was the deployment of airbag systems in cars [74] (100 million MEMS were sold per year by 2007 [72]); and modern smart-phones. Smart-phones have three-axis system MEMS accelerometers and gyroscopes allowing the phone to interpret which way the screen should be aligned (by detecting the direction of the acceleration due to gravity). As of yet, none of these accelerometers have the sensitivities, or perhaps more appropriately, the stability over long periods to be used as gravimeters. The first MEMS accelerometers developed in 1975 had a resonant frequency of over 1 kHz. For example, the LSM6DSL [75] included in the Samsung Galaxy S9, has an RMS noise of 1.8 Gal $\rightarrow$ 3 Gal. Such a device is unusable for gravimetry which require sensitivities of order 10's μGal, typically for periods of several hours and days. There were no such MEMS-based device that had demonstrated sufficient sensitivity over these time scales until a device capable of measuring down to frequencies of 10^{-6} Hz was published from The University of Glasgow [1]. This was the first demonstration that MEMS could be stable and sensitive enough to be called a gravimeter. It was here that the device was named "Wee-g". A MEMS-based gravimeter could prove to be a disruptive technology, possibly reducing the price and size of relative gravimeters by more than an order of magnitude — more details on the design and fabrication will come later in this section.

1.2.1.1 Inertial MEMS

Inertial MEMS has expanded with the proliferation of mobile phones as well as tablets, gaming systems, TV remotes and wearable sensors [76–81]. This type of MEMS are micromachined devices, that are used to measure forms of motion, such as an accelerometer (measuring accelerations) or gyroscopes (measuring angular velocities). Accelerometers are devices that measure accelerations, typically in units of g ($= 9.81$ m s^{-2}). These devices typically consist of a mass on a spring system that, under an acceleration, becomes displaced by a measurable amount, allowing a change in gravity to be calculated. The MEMS device discussed in this thesis falls into this category. These mass on a spring accelerometers are generally only sensitive to one dimension but can be used in unison to obtain information on multiple axes at once (tri-axial). Linear measurements of acceleration can also be made using a torsional mass system which has an asymmetric mass and therefore rotates under linear accelerations which can be measured. Following linear measurements of acceleration, angular acceleration can also be measured but using torsional springs on a circular piece of silicon with comb-like fingers on the outside. These fingers then rotate under angular accelerations resulting in a change in overlap between the comb-like fingers on the rotating component and stationary read-off fingers.

1.2.1.2 MEMS Gravimeter Background Theory

To understand accelerometers, and therefore the MEMS Gravimeter developed at the University of Glasgow, a derivation of the transfer function of such systems must first be made. Let us therefore consider the dynamics of a spring-based system that follows Hooke's Law. Equation 1.22 shows the relationship for driven harmonic motion for a mass on a spring system with mass m, spring constant k, damping ratio λ, position z, velocity $\mathrm{d}z/\mathrm{d}t$, acceleration $\mathrm{d}^2z/\mathrm{d}t^2$ and resonant frequency w_0. The system is driven by the oscillating force $F_0e^{i\omega t}$. These variables are also depicted in figure 1.13.

$$m\frac{\mathrm{d}^2z}{\mathrm{d}t^2} = -kx - b\frac{\mathrm{d}z}{\mathrm{d}t} + F_0e^{i\omega t}\ , \tag{1.22}$$

where b is the damping coefficient. This equation can be rearranged to the form:

$$\frac{\mathrm{d}^2z}{\mathrm{d}t^2} + \frac{b}{m}\frac{\mathrm{d}z}{\mathrm{d}t} + \omega_0^2 z = F_0e^{i\omega t}\ . \tag{1.23}$$

If we now consider that the solution to equation 1.23 has the form $z = Ae^{i(\omega t-\psi)}$, equation 1.24 can be obtained.

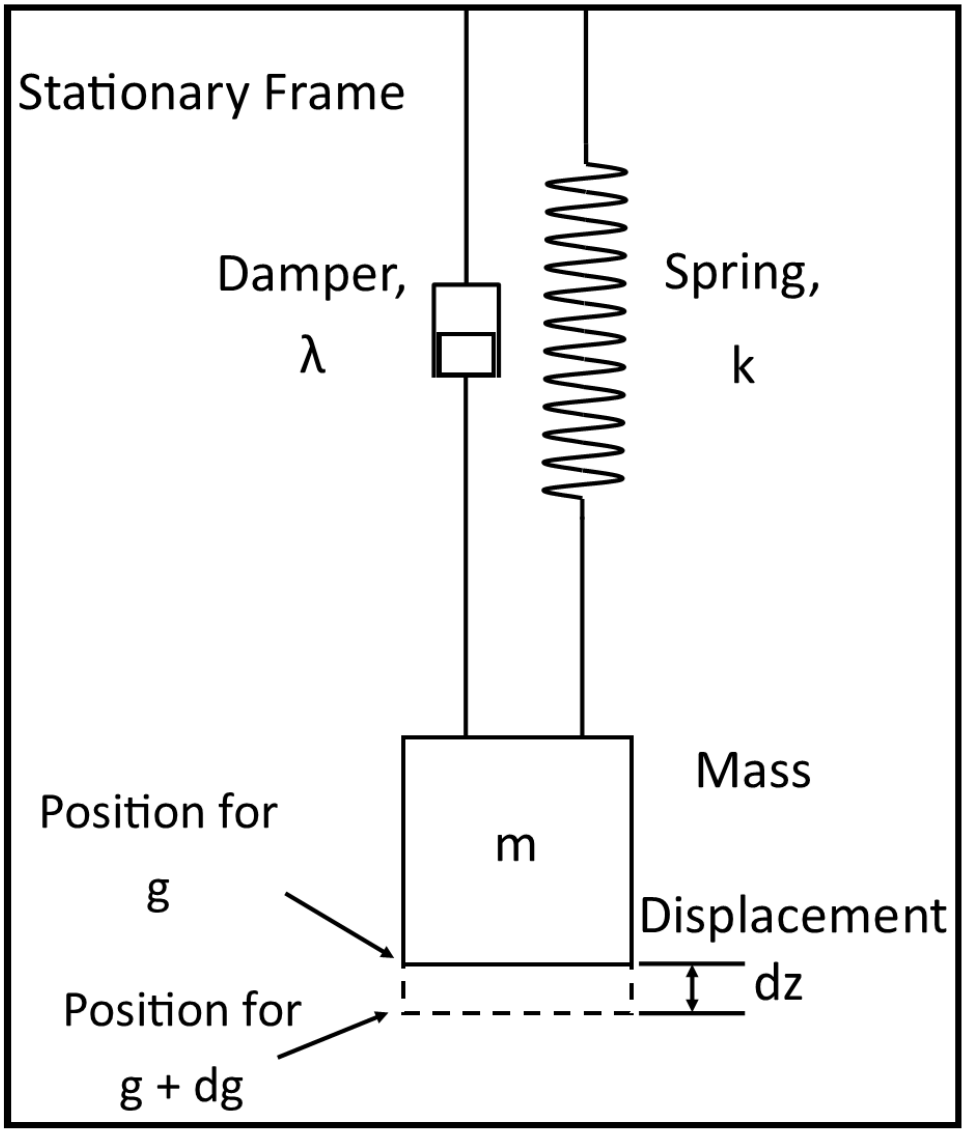

Fig. 1.13 Diagram depicting a mass on a spring system with a stationary frame. With spring constant, k, mass, m, change in position of dz, damping coefficient b and acceleration from gravity of g.

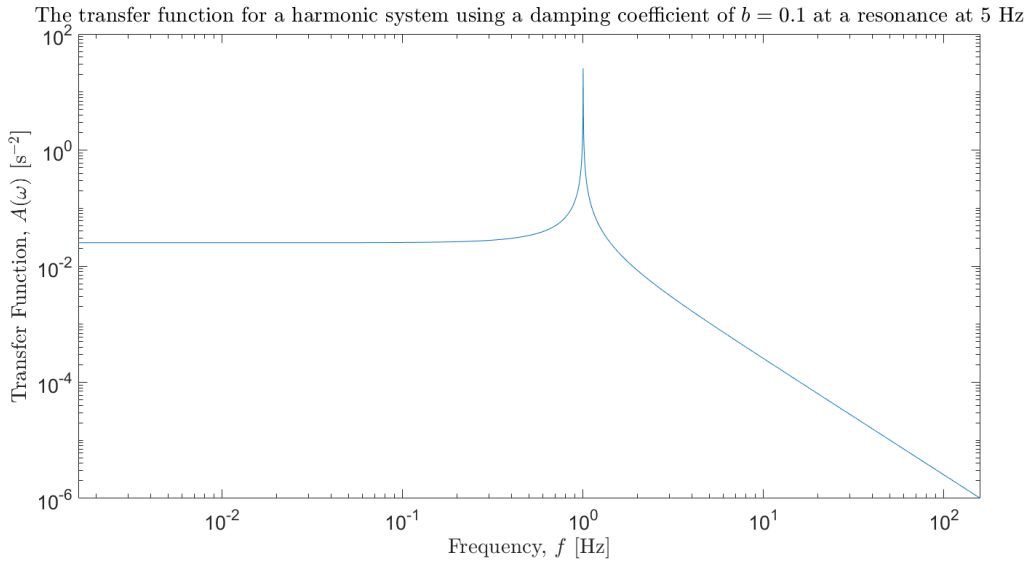

Fig. 1.14 A graph depicting the general shape of the transfer function in harmonic oscillators. It can be seen that the system has a peak at the angular resonant frequency of 5 Hz. At zero frequency, the system approaches $1/(\omega_0^2)$. At the other side of resonance the system approaches zero. Note the constant region at low frequencies below resonance.

$$-\omega^2 z + ib\omega z + \omega_0^2 z = \frac{F_0}{m} e^{i\omega t} \,. \tag{1.24}$$

Equation 1.24 can be used to find the transfer function ($A(\omega)$) of the harmonic system. For an accelerometer, the transfer function is defined as the ratio of the displacement over acceleration. Equation 1.25 can be obtained by dividing z by equation 1.24. Noting that the transfer function is the displacement [in m] per acceleration [in m s^{-2}] at the angular frequency ω.

$$A(\omega) = \frac{z}{\frac{\mathrm{d}^2 z}{\mathrm{d}t^2}} = \frac{1}{-\omega^2 + \omega_0^2 + ib\omega} \,. \tag{1.25}$$

This equation shows how the mass is displaced given an acceleration at some angular frequency. An example plot of the magnitude of the transfer functions can be seen in figure 1.14.

Figure 1.14 shows as the system approaches the angular resonant frequency (here $f_0 = 5$ Hz), a peak is seen. This peak changes in amplitude depending on the damping ratio of the system (here $b = 0.1$). The system also approaches $1/(\omega_0^2)$ at a frequency of zero. This figure also shows that at a frequency lower than the resonance peak, there is a constant relationship

between acceleration and displacement. This is region in which the oscillator can be used as an accelerometer. A MEMS with a low resonant frequency means that the system must be applied for frequency regimes even lower. This low resonant frequency, however, offers the advantage of an increased displacement for a given acceleration relative to higher resonant frequencies.

Equation 1.26 (derived in appendix D)) shows the equation that governs the MEMS-based gravimeter where k is the spring constant, m is the mass on the spring that has a change in displacement of dz because of a change in gravity of dg. These terms are also seen in figure 1.13 from before. Note that k/m is equal to the square of the resonant frequency, ω_0^2.

$$\mathrm{d}g = \frac{k}{m}\,\mathrm{d}z = \omega_0^2 \mathrm{d}z\,. \tag{1.26}$$

If a spring with a resonant frequency of 2 Hz moved by 10 nm, then this would imply a change in gravity of 158 μGal . Using equation 1.26, equation 1.27 can be obtained (also derived in appendix D).

$$\frac{\mathrm{d}g}{g} = \frac{\mathrm{d}z}{z}\,. \tag{1.27}$$

From equation 1.27, to get an uncertainty of a 100 μGal, an accuracy of 200 pm is required.

1.2.2 Design and Fabrication

1.2.2.1 Design

The MEMS Gravimeter was fabricated in the James Watt Nanofabrication Centre at The Unversity of Glasgow. The MEMS Gravimeter consists of a mass on a spring system suspended by three anti-spring flexures [1, 82, 83] [†]. These Geometric Anti-Springs (GAS) are inspired by work carried out by the Gravitational Wave community on projects such as the VIRGO Laser Interferometer [84]. The GAS was designed for seismic isolation in the gravitational-wave community and helped to increase the vertical attenuation as well as thermal stability of the isolation. The anti-spring is mirrored to limit the proof mass in one dimension, also having the effect of lowering the spring constant as the geometry produces a negative restoring force. They are referred to as geometric anti-springs due to the negative spring component's creation solely from geometry. A single spring can be summarised with the following variables: thickness (d), total length (L), launch angle (θ_0) and constrained angle θ_L as depicted in figure 1.15. A single flexure like that in the figure will deflect with a

[†]The system has changed design since this. Now, the device uses four flexures.

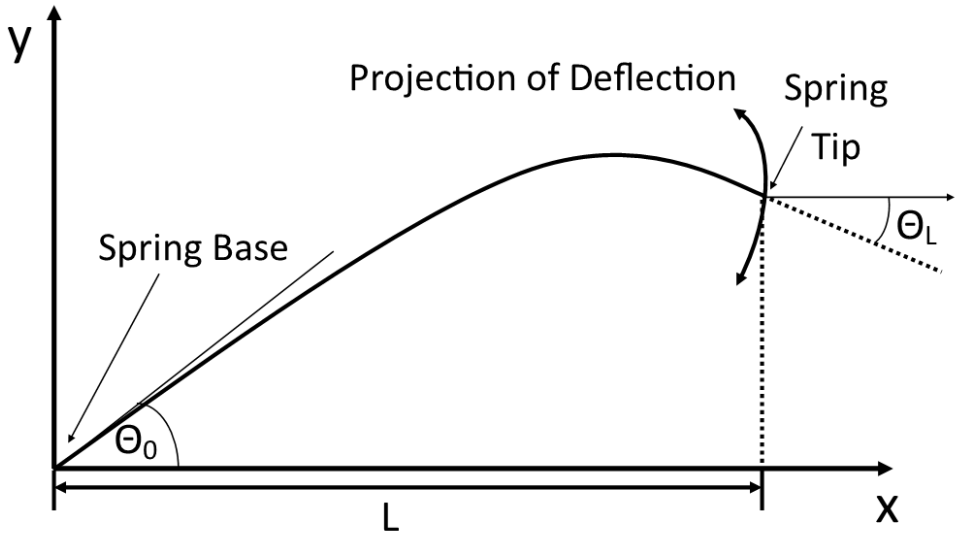

Fig. 1.15 A diagram of a Geometric Anti-Spring (GAS) showing its key variables. It has maximum width L with a launch angle of θ_0 and constrained angle θ_L. The flexure has a constant thickness of d.

curved response, however, if two that were the mirror image of each other were joined at the tip then the system would then deflect linearly down and up.

To help understand how a fabricated MEMS would function, different geometries can be modelled using a finite element analysis (FEA) program such as, "ANSYS Structural Analysis Release v18.1". ANSYS solves a set of equations by iteratively increasing the component of gravity acting on the system until the forces acting on the system is within a given tolerance. This component of gravity is then increased and the process repeated. ANSYS is discussed further in section 2.2.1.1.

1.2.2.2 Fabrication Process

Processing silicon has become commonplace in a society where most people are in possession of smartphones, computers/laptops and tablets. We are also seeing an increase in cars and household appliances becoming "smart", requiring a myriad of sensors (based on silicon) allowing them to be connected to and send information to the internet. Even though silicon processing is widely undertaken, it still takes a long time to develop a new technology that

is based in silicon. It took a PhD and three years of work to develop a reliable process to produce a working MEMS gravimeter [83]. First, a 220 μm thick, <100> crystal structure silicon wafer is patterned using a process known as photo-lithography. Photo-lithography involves taking a substance known as a photo-resist and spinning it in a liquid state onto the top of a wafer, making sure to remove the non-flat edge around the wafer. After the photo-resist has been spun, it is baked to make it solid and ready for the next step. The resist is then exposed to 435.8 nm ultra-violet (UV) light that has passed through a pattern that exposes only the desired areas. These photo-resists can be negative or positive. Negative resists are where areas exposed to light are 'hardened': the molecules that make up the resist cross-link increase their resistance to solvents. Positive resits break down when exposed to light, and thus the exposed areas can be removed with solvents. The process for the MEMS uses an AZ4562 positive resist. After exposure, the undesired resist that was exposed to UV is washed away using an AZ400K developing solution, leaving the desired pattern. The areas that are left act to protect the silicon below, while the unprotected areas are etched by whichever etching process that is chosen. A summary of the process thus far is summed up in figure 1.16.

Here, the etching of the silicon was carried out using the Bosch Process [85]: a patented form of deep reactive ion etching. This process allows for a highly uniform etch profile for deep etch depths, which is not necessarily the case for other forms of etching, such a 'wet' etching. The Bosch process begins by exposing the silicon to an etching plasma, Sulphur Hexafluoride (SF_6), that etches in all directions (isotropically). This stage is followed by a passivation stage that uses a chemical like Octafluorocyclobutane (C_4F_8) to make the newly exposed silicon inert, halting any further etching. To etch further, the process requires removal of the passivation layer at the bottom of the etched areas. Removal of this layer is carried out by bombarding it with ions, de-passifying the bottom of the etched areas and leaving the side walls still inert. Now the cycle can be repeated by exposing the bottom layer with the etching chemical SF_6, and so on. The etching process is summarised in figure 1.17.

1.2.3 Optical Sensor

For a given acceleration acting on the MEMS, the proof mass will displace proportionally to the magnitude of the acceleration. As the MEMS will only displace in a single dimension, a one dimensional displacement sensor was required. R. P. Middlemiss et al. [83] chose to use an optical shadow sensor akin to that used by Lockerbie et al. [86]. An optical shadow sensor uses a light source (in this case, an off-the-shelf, red light emitting diode (LED)) to cast a shadow of the proof mass over two photo-diodes. Rather than being separately amplified and

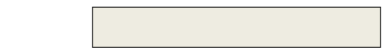

(a) Clean silicon wafer

(b) Silicon wafer with AZ4562 photo-resist including edge bead

(c) Silicon wafer with edge bead removed

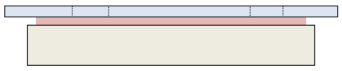

(d) Photo mask placed onto resist

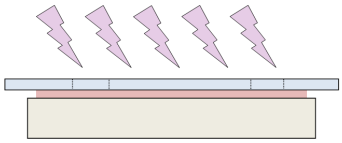

(e) Exposed resist is illuminated using ultra violet light (435.8 nm)

(f) Exposed resist is cleaned away using a AZ400K developer

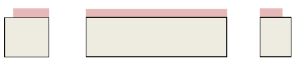

(g) The exposed silicon is etched.

Fig. 1.16 A series of diagrams showing the processes required to have a patterned etch-mask ready for the silicon to be etched. Starting with a clean wafer (a) and ending in the exposed silicon being etched (g).

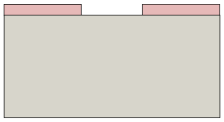

(a) Sample with etch mask ready for etching.

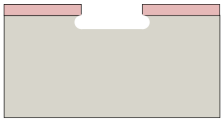

(b) Isotroptically etch the sample using SF_6

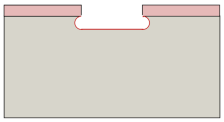

(c) Passify newly exposed silicon using C_4F_8.

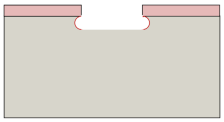

(d) Bombard bottom layer with ions to de-passify ready for further etching.

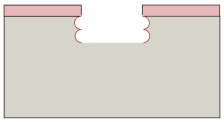

(e) Again SF_6 etching places that are no long passified.

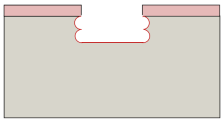

(f) Passify all of the silicon using C_4F_8 again.

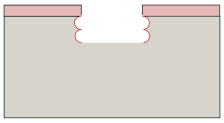

(g) Again bombard bottom with ions

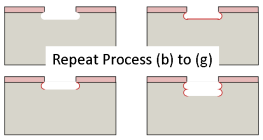

(h) Repeat the processing steps (b) to (g).

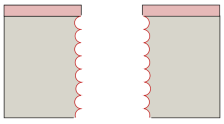

(i) After a several cycles, sample is etched all the way through.

Fig. 1.17 A summary of the deep reactive ion etch process known as the Bosch Process. The sample with the etch-mask is etched, passified, bombarded with ions and the process repeated until the sample is etched all the way through seen in (i).

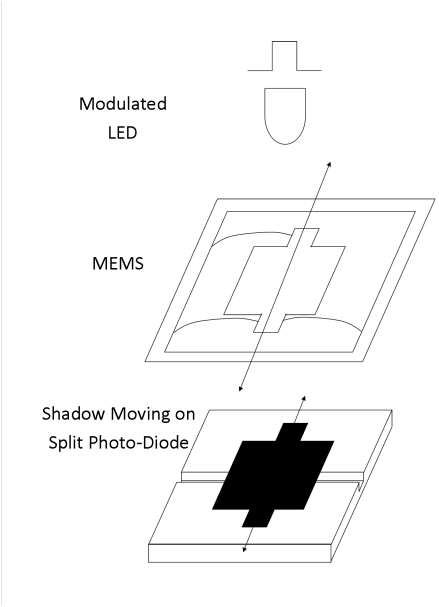

Fig. 1.18 A diagram depicting the schematic diagram of a one dimensional optical shadow sensor. As the MEMS moves, the shadow (cast on the photo-diodes with the LED) moves. This changes the relative amount of current from each diode, which is then amplified.

subtracted, these photo-diodes are arranged such that the anode of one diode is connected to the cathode of the other, and vice versa. This arrangement results in the difference between the two photo-diodes being output directly as a current, allowing for higher current to voltage gains without saturation. The arrangement of the LED, MEMS and photo-diodes are shown in figure 1.18. The Lock-in technique [87] was also chosen with the shadow sensor due to its superior ability to pick out a signal from noise by modulating the signal at a chosen (preferably high) modulation frequency [87], to eliminate as much low-frequency (1/f) noise as possible. The lock-in technique involves modulation and demodulation: in this case, the LED was dimmed and brightened at a chosen frequency, f_M. After the light passed onto the photo-diode, creating a photo-current, the output was converted into a voltage using a current to voltage converter. This output voltage was connected to an analogue Femto Lock-in Amplifier (the LIA-MVD-200-L [88]). The lock-in device also takes a reference signal (a signal that has the same phase and frequency of the original modulated signal drive for the LED), and uses this to demodulate the signal, outputting either an: in-phase component (X), out of phase component (Y) or the total magnitude ($R = \sqrt{X^2 + Y^2}$). The principles of lock-in amplifiers are further discussed in section 4.2.

Material	Fused Silica	Silicon	Copper	Aluminium
Thermal Expansion (K^{-1})	4.5×10^{-7}	2.6×10^{-6}	17×10^{-6}	23×10^{-6}

Table 1.1 A table showing some common materials and their value of linear thermal expansion. Metals generally have quite high thermal expansion coefficients where a crystal such as fused silica has a low thermal expansion ($1 \rightarrow 2$ orders of magnitude lower) [4, 5]

.

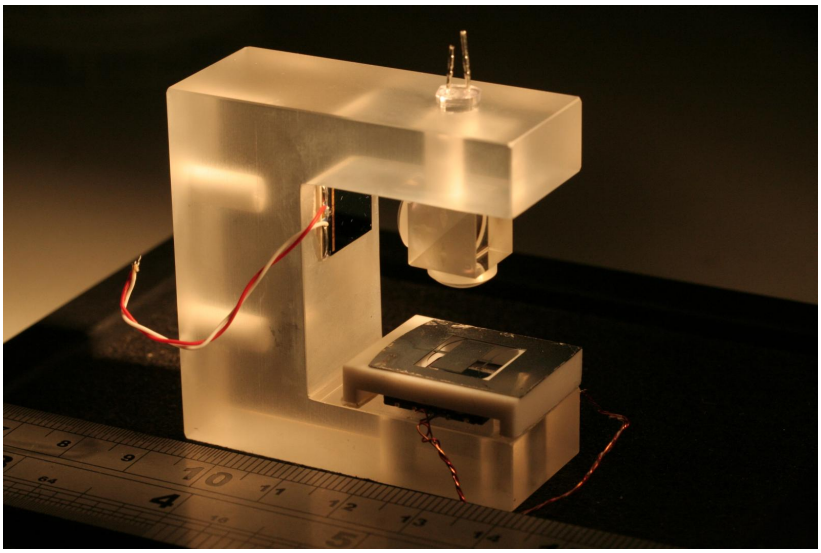

Fig. 1.19 A picture of the piece of fused silica. This piece is colloquially known as the "Silica C". The Silica C can be seen with the split photo-diodes on the bottom, LED at the top, beamsplitter below the LED, and a MEMS on a mount above the photo-diodes. The mount was made from MACOR, a trademarked machinable glass ceramic.

1.2.4 System Setup

The system was set up on a piece of fused silica in the shape of the letter 'C', colloquially referred to as a "Silica C". This Silica C can be seen in figure 1.19 and was approximately 4.5 cm $\times$4.5 cm $\times$1.5 cm in size. Fused silica was chosen due largely to its low thermal expansion relative to other materials. Table 1.1 shows the thermal expansions for fused silica, silicon, and two metals (copper and aluminium).

It can be seen from table 1.1 that fused silica expands around 50 times less than that of common metals used in construction. If the system used a piece of aluminium, for example, and there was a change in temperature of one kelvin, a change in length of $\Delta l = 230$ nm for a 1 cm piece would be observed. The size of signals in the system are expected to be of order of a few nanometres and thus, aluminium, and similarly copper, would not be suitable.

Though the system used active temperature control (discussed in more detail in the next section), even if the aluminium was controlled to a milliKelvin, there would still be changes of order 0.23 nm, too close to the size of the expected signals. For the same 1 mK variation on a fused silica system, a change of only 4.52 pm would be seen, far below the system noise. The 'Silica C' was surrounded by a copper shield that helped isolate the system from temperature fluctuations by creating a barrier that could also be temperature controlled. The system was then housed in a large vacuum tank available in the department, as seen in figure 1.20. All the electronics used to run the device were commercial devices, each costing upwards of several thousand pounds, connected to a computer and run using a LabVIEW programme. To measure the temperatures, a Keithley 2000 [89] was used for each, utilising a 4-wire measurement method. This 4-wire measurement (also known as Kelvin measurement) involves attaching two wires at each side of a thermometer. One side of the thermometer is connected to the excitation and the resistance measurement input. The other side of the thermometer is connected to the remaining side of the excitation and input of the resistance measurement.

Measuring a resistor using the 4-wire method has several advantages over using two. One such advantage is that the four wires measure the voltage drop over the resistor to ensure there is no offset from the lead resistance. To carry out a four-wire measurement, a bias resistor is in series with the thermometer. The system then takes the ratio of the thermometer to the bias resistance (dimensionless) which can be multiplied by the bias resistance (assumed constant) to obtain a resistance. This resistance value can then be converted into a temperature (more information on the four-wire measurement in chapter 3). Transferring these temperatures into LabVIEW, an output can be automated to control the temperature to a particular value by passing a current through a resistor near the position of the thermometer. The output to control the temperature was calculated using a control system called a Proportional Integral Differential (PID) controller. The controller calculates an output based on the difference between the current temperature, and the set point (proportional), then the current rate of change of the temperature (differential), and what is effectively a term relating to the weighted time spent above and below the set point (integral).

The modulation of the LED was achieved using an HP 33120A square-wave signal generator [90] to have the LED drive and a reference signal for demodulation both at a frequency of 107 Hz (50:50 duty cycle). The current from the photo-diodes was then converted to a voltage using the Stanford Research Systems SR570 current to voltage converter [91] with a bandpass of 3 Hz to 100 Hz and a gain of 10^6 V A^{-1}. The signal was then demodulated using the Femto lock-in amplifier, LIA-MVD-200-L with a gain of

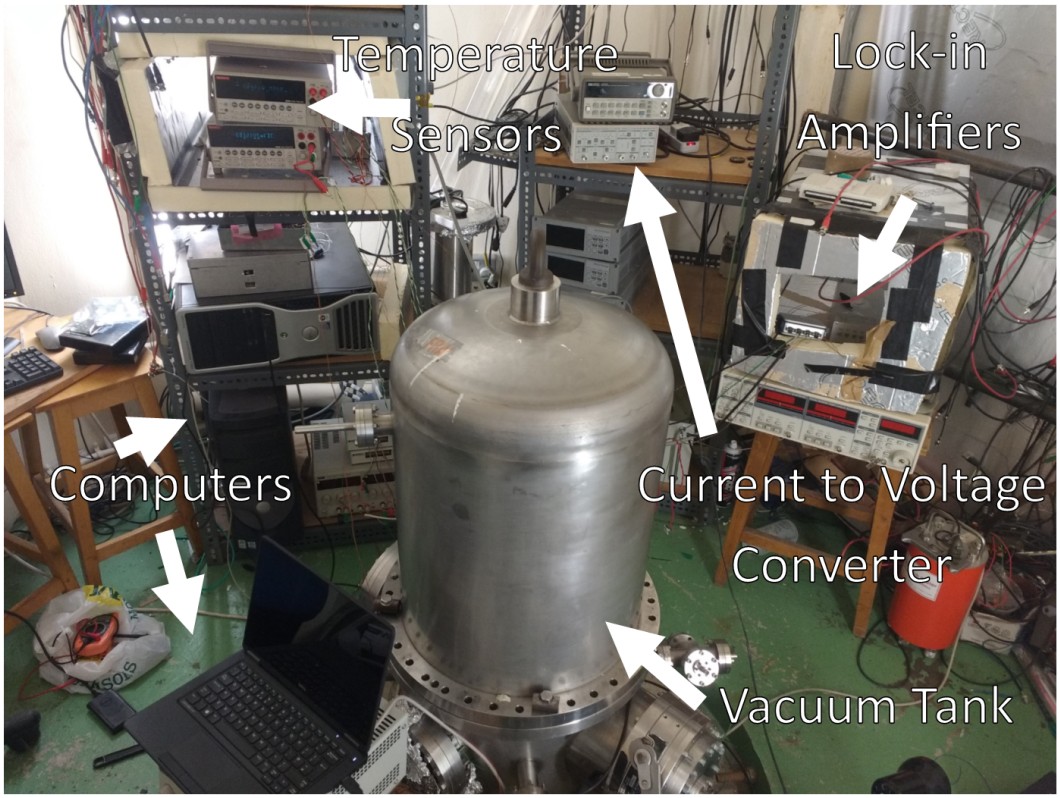

Fig. 1.20 A picture of the vacuum tank that housed the original MEMS gravimeter. The bulky and costly electronics can be seen around the vacuum tank in the background.

10, and a time constant of 3 s. The demodulated signal was then low pass filtered using a Stanford Research System SR560[92], with a cutoff at 0.03 Hz and -12 dB per octave. Post filtering, the signal was sampled using a 16-bit analogue-to-digital converter from National Instruments (M Series 6229 [93]) connected to the LabVIEW programme. Finally, the LabVIEW programme saved each of the inputs, including temperatures and the signal, with a time constant of 24 s. After the measurements, post-processing could then be carried out including regression, a technique that allows multiple variables to be correlated and removed from the data. A flow diagram of the setup can be seen in figure 1.21. The device's sensitivity to tilt warranted the use of tilt sensors. The tilt sensor was a commercial product, the Model 755-Series miniature tilt sensor, from Jewell Instruments. The 755-Series is a dual axis sensor that required the use of the Model 83162 Dual-Channel Signal Conditioning Card. The output from the conditioning card was then sampled by the computer.

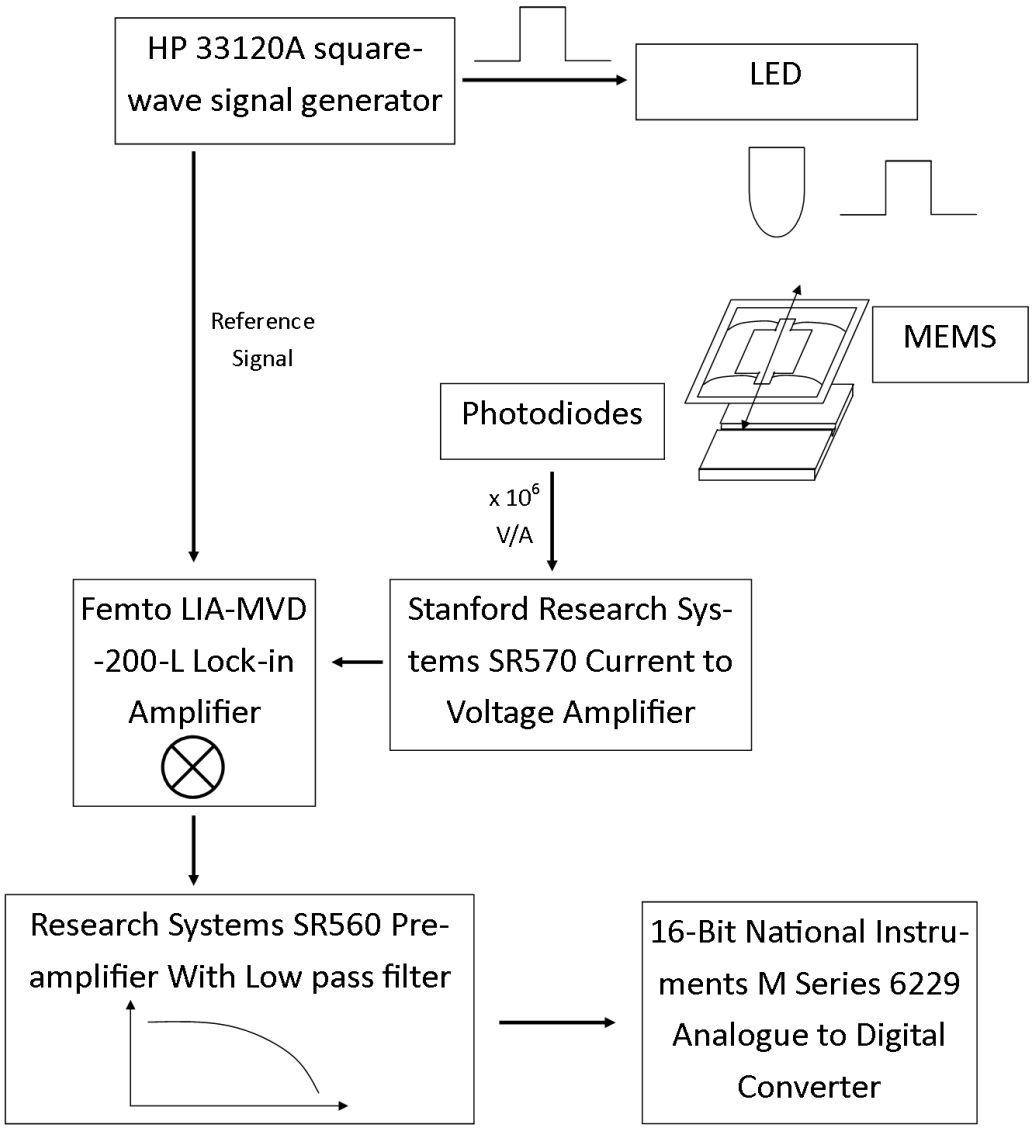

Fig. 1.21 A schematic diagram for the initial setup using to measure the Earth tides in the Nature paper "Measurement of the Earth tides with a MEMS gravimeter" by R. P. Middlemiss et al [1]. The signal generator modulates an LED which causes a shadow on the photo-diodes. These photo-diodes are arranged in a split photo-diode arrangement such that the difference in the current from each diode is taken to allow for a larger amplification. This difference in current is then converted to a voltage using a current to voltage amplifier, then demodulated in the lock-in amplifier using the reference signal from the signal generator. This output is low pass filtered and, finally, digitised to the computer.

1.2.5 Performance

The shadow sensor obtained a sensitivity of ≈ 0.8 mV, that, with a calibration of 1.13 MV/m, resulted in a sensitivity of just under 1 nm. The data of the displacement sensitivity can be seen in figure 1.22a and was taken with a time constant of 44 s. Figure 1.22b shows the amplitude spectral density of the time series data. It shows that even with the lock-in amplifier, there is still remaining 1/f noise with a sensitivity of 7 nm/$\sqrt{\text{Hz}}$ at 100s, and 50 nm/$\sqrt{\text{Hz}}$ at 1000 s.

1.2.6 Measurement of the Earth Tides

It is common knowledge that Ocean tides are due to the gravitational pull as a result of our Sun and Moon's orbit. There does, however, also exist an Earth tide, also known as a crustal tide. This Earth tide results in the displacement of the Earth's crust due to the gravitational pull of the Moon and the Sun. Figure 1.23 shows an exaggerated demonstration of how the deformation works at different positions of the Moon (The sun also affects the Earth's deformation by about a half of the effect than that of the moon). When the Sun and the Moon are aligned on one side of the Earth, then a maximum deformation is observed. If the Sun and Moon are aligned in opposing sides from the Earth, a minimum is observed. The average displacement for the Earth tides is around 25 cm in Glasgow, United Kingdom. As the crust displaces, the distance from the centre of the Earth also changes, altering the average gravitational acceleration at that point by approximately $100 \rightarrow 300$ μGal. This signal is usually greater than the changes in gravitational acceleration obtained during searches for oil, gas and minerals and so needs to be corrected in the data. An Earth tide measurement is considered a standard test for gravimeters.

In the winter of 2016, at the James Watt Nanofabrication Centre in the University of Glasgow, a MEMS gravimeter was fabricated, but one of the 4-flexures accidentally broken. Over the festive period, the device was still set up to test the system noise, as it was stable and noted to have a low frequency of 2.2 Hz. This device went on to successfully measure the Earth Tide signal in the Kelvin Building, University of Glasgow. The creation of a MEMS gravimeter was an essential step in producing a working device that could disrupt the gravimetry sector. The data obtained showed a clear signal of the Earth tides, with a confidence of 114σ [1], including visible signs of the Sun's gravitational effect. To see the Earth tides in the data, a regression against temperature was required. This regression checked the correlation coefficient between multiple variables that could be dependent or independent. During these measurements, the temperatures of the MEMS, LED, room and

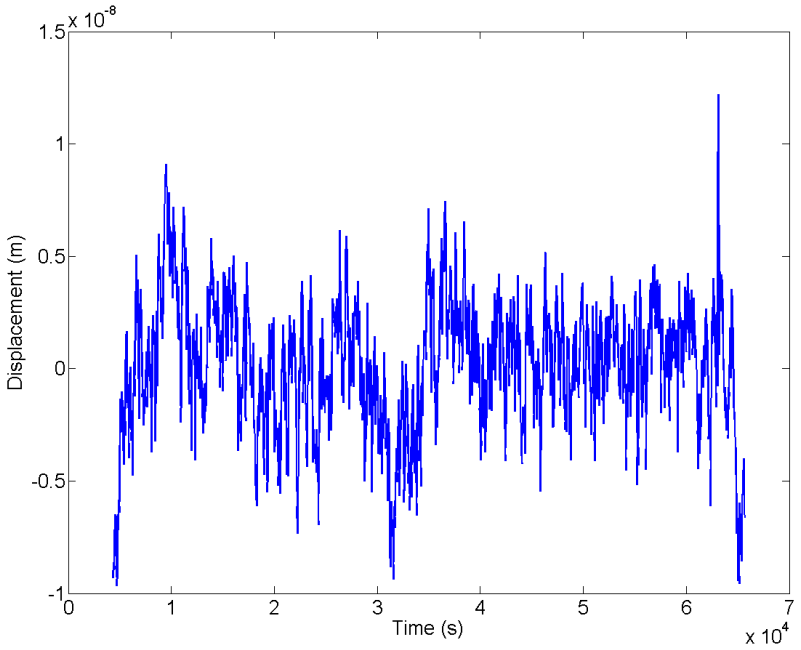

(a) Figure of the typical time series data from the shadow sensor showing a displacement, peak to peak, of just less than 10 nm. This data was taken over a period of approximately 12 hours. Taken from the thesis of R. P. Middlemiss [83].

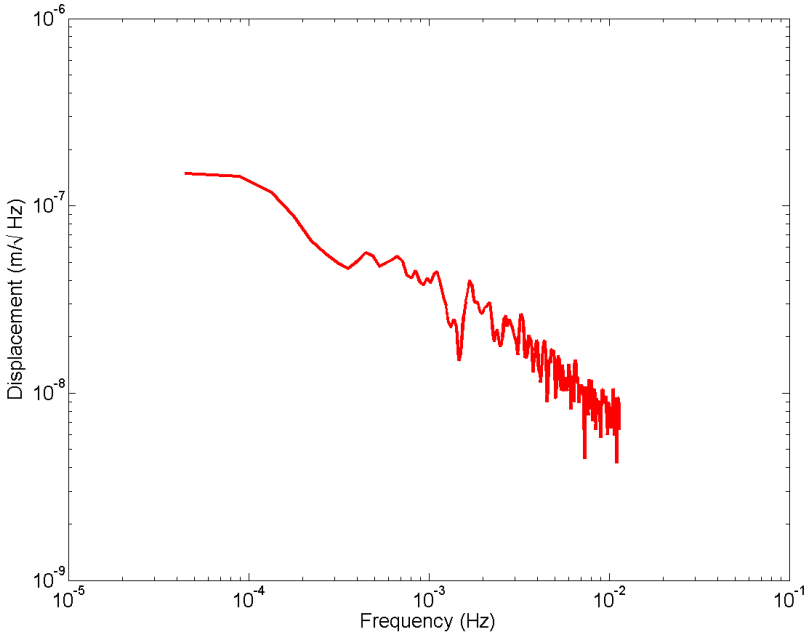

(b) The amplitude spectral density plot of the data seen in figure 1.22a. It can be seen that the sensor has a sensitivity of approximately 50 nm/$\sqrt{\text{Hz}}$ at 1000 s. Taken from the thesis of R. P. Middlemiss [83].

Fig. 1.22 Graphs showing the performance of the shadow optical sensor in both time and frequency. The top figure shows the time series with peak to peak noise approximately 10 nm which corresponds to a amplitude spectral density of 50 nm/$\sqrt{\text{Hz}}$ at 1000 s.

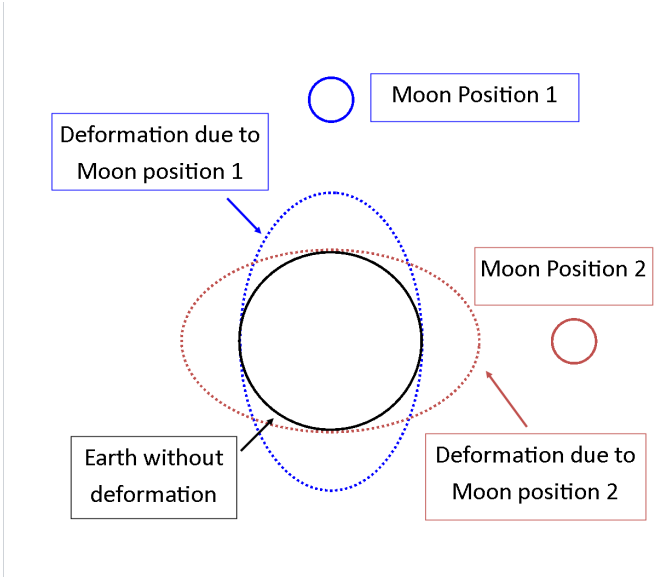

Fig. 1.23 Diagram showing the exaggerated deformation of the Earth due to the moon's gravity at different positions of its phase. In position 1, the moon is closest to the top of the circle (the Earth), and so experiences a larger pull than the rest of the Earth. Similarly, at position 2, the pull is felt the strongest on the right side of the Earth. In reality, the Earth's crust moves up and down around 1 m or so due to the moon's gravity. The sun can still effect this by about a half of that of the moon. A maximum Earth tide is seen when the sun and the moon are in phase in the same direction. A minimum is seen when they are in anti-phase, causing the sun's effect to reduce that of the moon's.

copper shield were monitored. The regression against these temperatures was carried out using a MATLAB script. Figure 1.24 shows the data post-regression, which correlates with an R-value of 0.86 between the expected Earth Tide (in red), and the regressed data (blue). This R-value was obtained by correlating the data sets by, again, using MATLAB's "corrcoeff" function. The correlation can be stated with a confidence of 114 σ.

1.2.7 Possible Applications

Due to a MEMS-based gravimeter being able to be lightweight, low-cost and mass fabricated, new avenues for gravimetry could be opened due to the previously prohibitive costs, size and weight.

One such avenue is that of gravimetry on drones. Currently, if gravimetry were to be carried out in the air, it would require an experienced pilot in a small plane such as a Cessna to fly as close as possible to the ground to maximise the signal. Experiments involving a plane and a skilled pilot are a costly, time-consuming and ultimately dangerous venture. However,

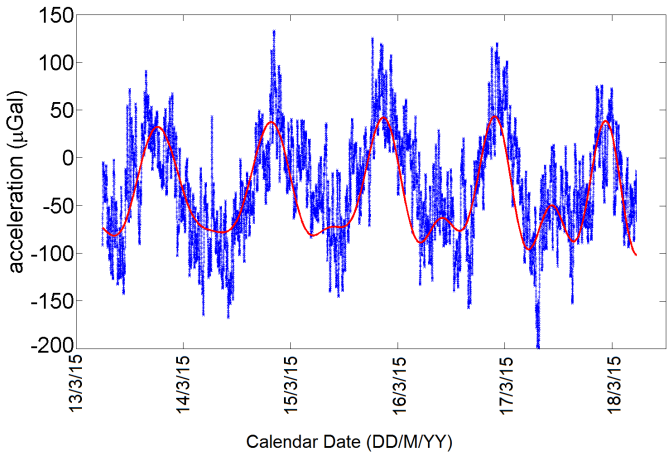

Fig. 1.24 A graph of the regressed data from R. P. Middlemiss et al. showing the detection of the Earth Tides with a MEMS Gravimeter. Tide signals here are approximately 120 μGal, and were detected with R value that is 114σ.

if a gravimeter was sufficiently small, with the necessary sensitivity, then an unmanned drone could be used, negating the risk and a considerable portion of the cost. There would, however, arise an issue in using a gravimeter on a moving platform as it would be necessary to to distinguish between an acceleration due to gravity and one due to inertial accelerations. This, however, could be minimised by utilising vibration isolation and further isolation stages if necessary. It is also worth noting that two sensors could be used together to cancel inertial effects, i.e. a Gradiometer. If the sensors were placed vertically relative to the ground, this arrangement can make a measurement of the g_{zz} component, that is the differential of the vertical component of gravity with vertical displacement ($\frac{\partial g_z}{\partial z}$). Of course more sensors can be used to obtain information on the other axes. Note that the SI unit of gradiometry is s^{-2} but is often stated in the unit, Eotvos where 1 E is the equivalent of 10^{-9} s^{-2}. Stated in terms of Gal, 1 E = 10^{-4} mGal m^{-1}. One point is effectively subtracted from the other, so any accelerations observed are due to gravity alone. Another possible method would be to use a gravimeter with stable enough isolation from the vehicle's acceleration spectrum. Due to the possible reduction in price by at least an order of magnitude, gravimeter networks become a lot more plausible. Currently, a gravimeter like the CG-5 would cost upwards of £70k. However, if the cost is significantly reduced, it could become affordable to have networks of gravimeters that can increase the SNR of a measurement, and create a multi-pixel gravimeter network. A network could be useful for continuously monitoring for events like volcanic eruptions, potentially saving lives. Another advantage is that the system can offer real time

information on the activity of a volcano that other methods cannot currently offer such as magma accumulation in void space, distinguish mechanisms for volcanic uplift and recognise formation of bulk fracture zones (as well as others) [18].

1.2.7.1 Summary

The gravimeter described thus far has been lab-bound due to the bulky and expensive electronics and vacuum system required for its operation. Considerable work would have to be carried out to reduce the overall size of the device. Reducing the size of the electronics/vacuum system also required the construction of a portable platform that would allow the MEMS gravimeter to be taken out into the field to prove its usefulness to industrial companies and partners. This thesis will provide details on the processes involved in creating a field-testable prototype MEMS gravimeter. This miniaturisation will require the miniaturisation of several components, such as the electronics (LED drive, current to voltage converters, lock-in amplifiers, thermal control, tilt monitoring and filters amongst others), as well as the physical equipment used for transport. A custom electronics board would also have to be designed and tested to obtain the necessary performance allowing for acceleration sensitivities at the tens of μGal level. This feat would be one more necessary stepping stone producing a commercially viable MEMS gravimeter that has multiple applications, as opposed to the current expensive and bulky products. A MEMS Gravimeter could open up new avenues of commercial interest, prompting investigation into “disposable” networks of gravimeters and drone-based measurements. The success of this project could lead to a bright future for the gravimetry community and market, one with low-cost, small and lightweight gravimeters.

Chapter 2

System Requirements

2.1 Introduction

The system developed by R. P. Middlemiss et al. [1] is a promising candidate for a portable, low-cost MEMS gravimeter capable of disrupting the gravimetry industry. The technology can be simply described as a mass on a spring system that is highly sensitive to accelerations, both inertial and gravitational in origin. It is, however, also sensitive to temperature variations and changes in tilt (as are all commercial gravimeters). This chapter will discuss the key requirements of a system that is capable of measuring accelerations down to the target sensitivity of tens of μGal. The system can be broken down into three sub-systems: the temperature sensor and actuation, the displacement sensor (which is used to detect changes in acceleration), and the tilt sensor. The required performance of these components will be estimated and discussed. Since there was no off-the-shelf system that combined the functionality to the required precision, a custom electronics board had to be designed and tested. The custom electronics board would require a micro-controller to communicate between the components, as well as be able to compute a significant number of digital filters in real-time.

2.2 Sensitivity Requirements

2.2.1 Temperature Sensitivity

It was discovered during previous work [83] that the system was susceptible to changes in temperature. ANSYS modelling was carried out to assess the thermal sensitivity of the device due to the thermal expansion coefficient (α), and the change in Young's modulus with

temperature, β. β is defined as the thermal coefficient of the Young's Modulus (Y) with $\beta = \frac{1}{Y}\frac{dY}{dT}$.

2.2.1.1 Finite Element Analysis (FEA) - ANSYS

FEA functions by first splitting a geometry into a series of elements called a mesh. Load steps, in this case increments of acceleration or temperature, are applied to the system whereupon a series of equations are solved to calculate the stress at each element. If the stress (or force) is below a certain convergence criteria, the next load step is applied. In the case of the MEMS device, the model can be configured to output the displacement of the proof mass as the acceleration due to gravity and/or temperature of the MEMS changes.

To understand how ANSYS models the displacement of the MEMS, an understanding of stress, strain, and the resulting deformation must be obtained. Stress, σ, is defined as the ratio of force, F, and area, A, i.e. $\sigma = \frac{F}{A}$. Strain, ε, is defined as the ratio of deformation, ΔL, and total length, L, i.e. $\varepsilon = \frac{\Delta L}{L}$, which is dimensionless. A useful property in material science is the Young's Modulus, Y. This is defined as the ratio of stress to strain,

$$Y = \frac{\sigma}{\varepsilon} = \frac{F}{A}\frac{L}{\Delta L}\,. \tag{2.1}$$

It can be seen that the Young's Modulus has the units of $\frac{F}{A}$, the same as stress, which are also the units of pressure. The Young's Modulus of materials are generally in units of MPa or GPa. The Young's modulus of a material can also be thought of as how stiff it is, with a higher number requiring a large force to stretch/squeeze an object. It can be seen from equation 2.1 that if a known force is acting on an area of an object, the proportional change in length can be obtained, given its Young's Modulus.

One assumption made when using the Young's modulus is that the material is *isotropic*, that is, the relationship between stress and strain is the same in all directions; meaning the deformation will not depend on which axis a force is applied. Metals are an example of isotropic materials, and are therefore specified with a scalar value of the Young's modulus, e.g. copper has a Young's modulus of $Y = 117$ GPa. Silicon, however, is an anisotropic material. This means that the resulting deformation from a given force depends on the crystal orientation so a scalar value is not sufficient to describe its elastic behaviour. It is more common to discuss the elasticity tensor of the material for anisotropic materials. This is effectively a tensor version of the Young's Modulus. For the purposes of this project, a simple isotropic value of the Young's Modulus for silicon was used. It is known that this

assumption should produce a result that is within 30% of the anisotropic value, which was deemed sufficient for this modelling work [5].

Two models were carried out, each exploring the effect of gravity (g), linear thermal expansion (α) and the change in Young's Modulus due to temperature (β). Both of these models used an isotropic value for silicon, with the first simulating a pendulum and the second simulating the actual MEMS geometry. The pendulum model allowed a comparison with analytical expressions, ensuring that ANSYS obtained the expected result.

Case 1 - Isotropic Silicon Pendulum

The geometry of a pendulum with a point mass was created using a 3D Computer Aided Design (CAD) package built into ANSYS, seen in figure 2.1. The pendulum was designed with the following dimensions: a length of $L = 7$ mm, a width of $w = 7$ μm, and a thickness of $h = 240$ μm. The bob suspended from the pendulum had a mass equal to 0.7 g. A Young's modulus of $Y = 160$ GPa was used while the change in temperature was 5 K (unless otherwise stated).

Thermal Expansion, α

The first model studied only considered the effect of the thermal expansion coefficient. An analytical estimate was calculated using the equation $\Delta L = \alpha \, \Delta T \, L_0$. The value for the linear thermal expansion was calculated to be $\Delta L = 85.75$ nm using $\Delta T = 5$ K, $L_0 = 7 \times 10^{-3}$ m and $\alpha = 2.45 \times 10^{-6}$ K^{-1} [4]. The extension was found to be 85.87 nm using the ANSYS models, a value very close to the analytical solution.

Gravity, g

The acceleration of gravity, and the resulting deformation, was the next stage to be modelled. If the pendulum has a length of L_0, with a mass of m, the resulting extension can be calculated by rearranging equation 2.1 and substituting $F = mg$ to obtain:

$$\Delta L = \frac{m \, g \, L_0}{A \, Y} \tag{2.2}$$

where g is the acceleration due to gravity, A is the cross-sectional area of the pendulum, and Y is the Young's modulus of silicon. The extension due to gravity was calculated to be 178.83 nm, where ANSYS obtained a result of 178.71 nm. Again, these are similar results.

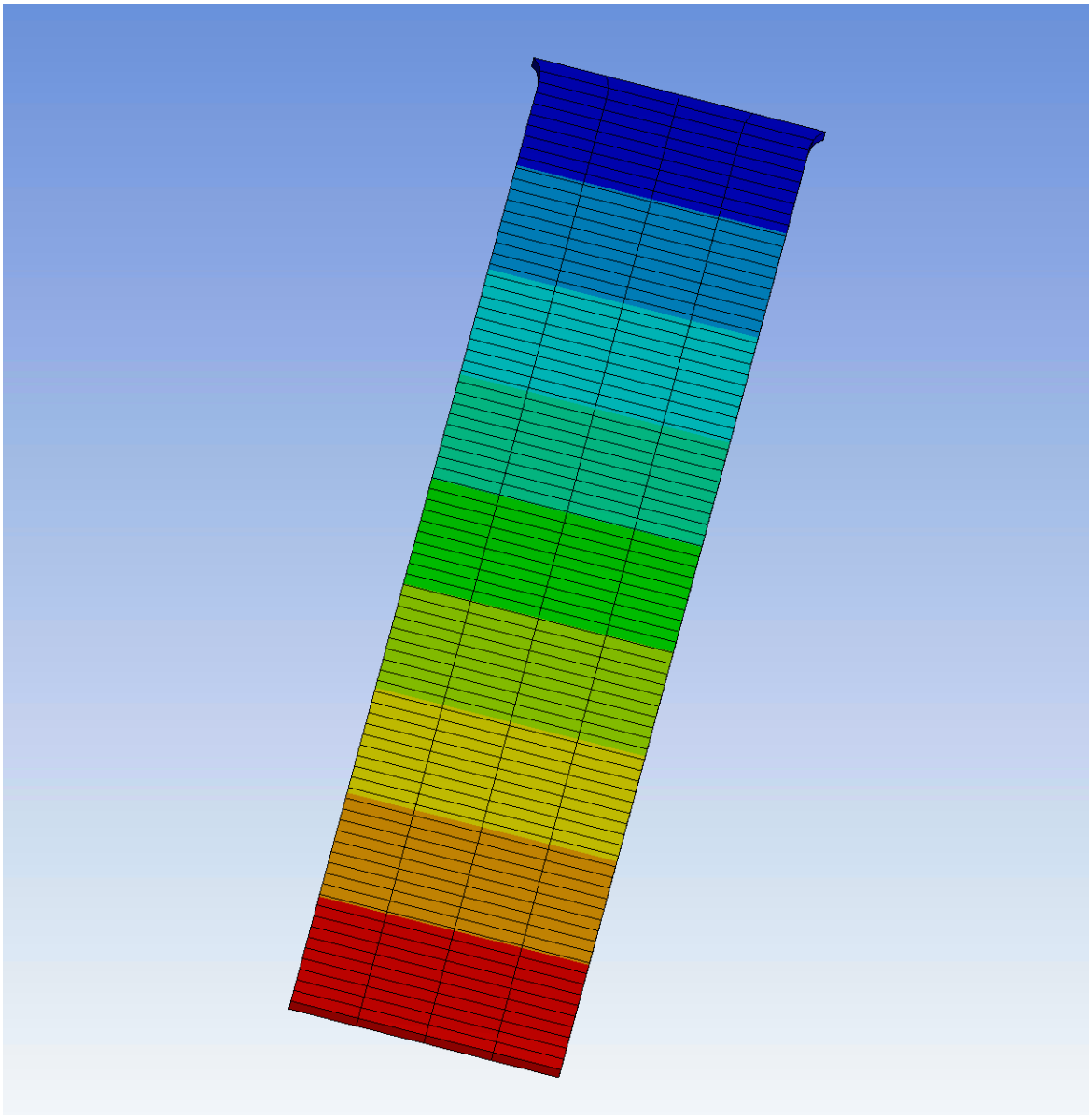

Fig. 2.1 A diagram showing the ANSYS model used to simulate the extension in an isotropic silicon pendulum. Here, a gradient can be seen on the beam that relates to the total deformation of those elements. As the pendulum utilises a point mass, no pendulum bob can be seen.

Effect	Extension [nm] (Analytical)	Extension [nm] (ANSYS)
Gravity (g)	178.83	178.71
Thermal Expansion (α)	86	85.9
Thermal coefficient of Youngs Modulus (β)	0.054	0.05
Total	265	264

Table 2.1 A table showing the effect of thermal changes on isotropic silicon. The resulting deformation from the linear thermal expansion, acceleration of gravity, and a temperature dependant Young's modulus can be seen. The analytical values closely match with ANSYS. It is clear that gravity has the largest effect, followed by the linear thermal expansion of silicon.

Gravity and Temperature Dependant Young's Modulus, $g+\beta$

Next, the effect of a temperature dependant Young's modulus was modelled. To model this, the effect from the acceleration of gravity had to be applied first, followed by a temperature change. The Young's modulus was made temperature dependent using the relationship of $Y = Y_0(1+\beta\Delta T)$, where Y_0 is the Youngs Modulus before the change in temperature and β is the temperature coefficient of the Young's modulus ($\beta = \frac{1}{Y_0}\frac{\mathrm{d}Y}{\mathrm{d}T}$ [94]). The net extension can be calculated given the strain in the material ($\varepsilon = \frac{Y}{\sigma}$) to obtain,

$$\Delta L = \frac{m\,g\,L_0}{A\,Y_0(1+\beta\,\Delta T)}\,. \tag{2.3}$$

Note that $[1+\beta\,\Delta T]^{-1} \approx [1-\beta\,\Delta T]$, assuming the Binomial approximation. Given that the first order coefficient is approximately $\beta = -60$ ppm/K [5], then the change in length is $\Delta L = 178.88$ nm, a 54 pm difference to the analytical calculation for just gravity. Again, ANSYS matched up closely to what was estimated, modelling a difference of 50 pm.

Gravity, the linear thermal expansion, and a temperature dependant Young's modulus, $g+\alpha+\beta$

Finally, all three parameters were modelled. For the isotropic pendulum, the estimated values of extension closely matched the results from ANSYS. The summary of these can be seen in table 2.1. Clearly the dominant effect here is the acceleration due to gravity, followed by the linear thermal expansion.

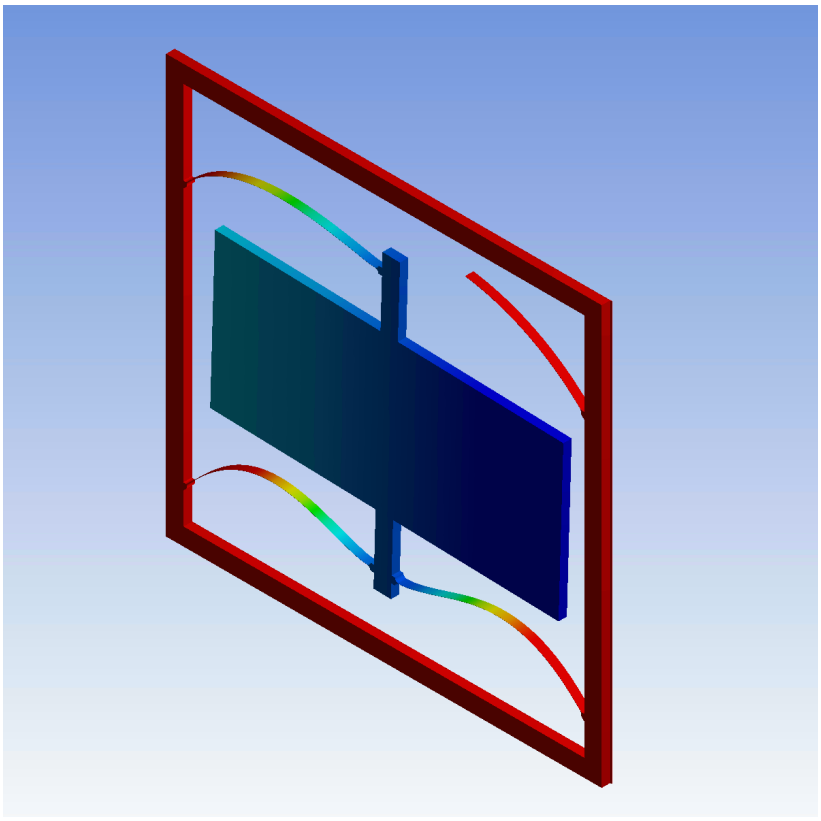

Fig. 2.2 A picture showing the geometry of the MEMS used for simulating stress and the resulting deformation of the proof mass using ANSYS. The image shows a colour map of the deformation due to gravity in the vertical axis.

Case 2 - Isotropic Silicon MEMS

Since the isotropic silicon pendulum matched closely to the analytical solutions, a model was created by editing a pre-existing three flexure MEMS ANSYS file. The geometry used is shown in figure 2.2 and uses a flexure thickness of 240 μm (which is the silicon wafer thickness) and a width of 6 μm. The system assumes a Young's modulus of $Y = 169$ GPa and a temperature change of 10 K.

Gravity, g

Using the aforementioned variables, ANSYS obtained a displacement of the proof mass relative to the frame equal to 1.4584 mm, a value not too different from physically tested MEMS devices.

Gravity + Thermal Expansion, $g + \alpha$

By introducing the linear thermal expansion of silicon to the model, a total displacement of 1.466 mm was obtained. i.e. the introduction of the thermal expansion only resulted in a change in displacement of 7.6 μm compared to just gravity. Next, the resonant frequency was calculated. To obtain this, the force was calculated for each step, using the equation $F = m\,a$, where m is the mass of the MEMS, and a is the acceleration at that load step. The spring constant (k) was calculated using the equation $k = \frac{\mathrm{d}F}{\mathrm{d}z}$, where $\mathrm{d}F$ is the change in force between steps, and $\mathrm{d}z$ is the change in displacement between steps. Now the resonant frequency was obtained by taking the square root of the spring constant divided by the mass of the spring, followed by dividing the result by $2\,\pi$, i.e. $f_0 = \frac{1}{2\,\pi}\sqrt{\frac{k}{m}}$. Before converting into a temperature sensitivity, the displacement was converted into an acceleration. This can be done by simply multiplying the displacement difference by the square of the angular resonant frequency. This gave, $\mathrm{d}a = 123$ mGal for a 10 K change or, $\frac{\mathrm{d}a}{\mathrm{d}T} = 12.3$ μGal mK^{-1}, both calculated using a resonant frequency of 2.025 Hz. Figure 2.3 shows two graphs. The top graph shows how the MEMS displaces under an increasing acceleration load. The lower graph shows the resonant frequency of the MEMS with the same acceleration load. It can be seen that the displacement does not follow a simple straight line relationship. As the acceleration increases, the resonant frequency of the device approaches a minimum. Since changes in displacement get larger with a lower frequency, the top graph shows an increasing gradient until the device passes the minimum frequency.

Gravity and a Temperature Dependant Young's Modulus, $g + \beta$

Running the model with a temperature dependent Young's Modulus gives a change in displacement of 73.1 μm (which is the equivalent of 1.15 Gal) for a 10 K change in temperature. Given a resonant frequency of 1.99 Hz, a temperature sensitivity of 114 μGal mK^{-1} was obtained, almost ten times larger than the thermal expansion effect.

Combined Effect of Gravity, Linear Thermal Expansion and a Temperature Dependant Young's Modulus, $g + \alpha + \beta$

When the effect of a temperature dependent Young's Modulus was combined with the linear thermal expansion, the total change in displacement decreased slightly. A change in displacement of 72 μm was obtained. Here, the resonant frequency was 1.99 Hz, which gives a temperature sensitivity of 113 μGal mK^{-1}. All of the effects described for the isotropic

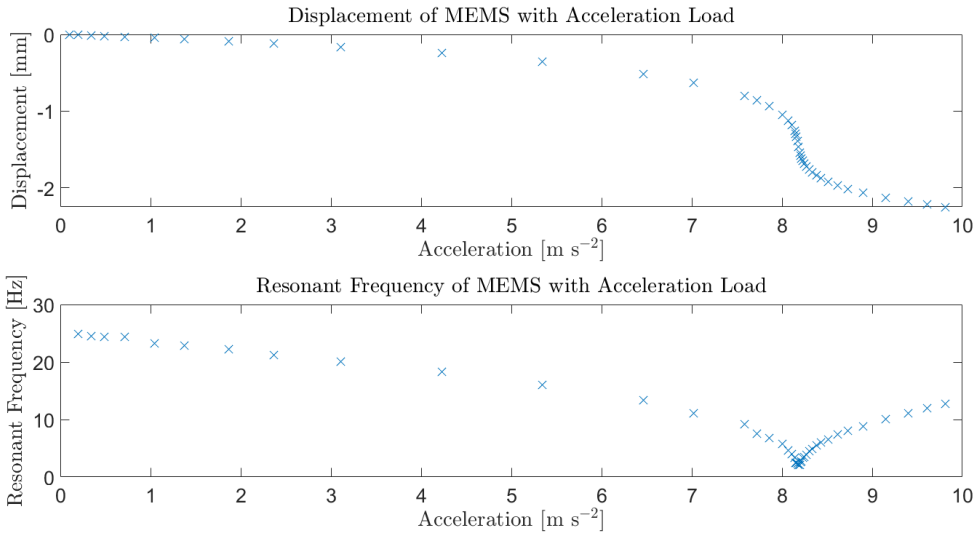

Fig. 2.3 Two graphs showing how the MEMS displaces (upper graph) and how the resonant frequency changes (lower graph) as the device is loaded under an increasing acceleration. The displacement steps increase as acceleration increases due to a decrease in the resonant frequency until a point where both trends flip.

MEMS are summarised in table 2.2. It is clear that the dominant thermal effect is from a temperature dependent Young's modulus (β).

Summary

By using ANSYS to model the geometry shown in figure 2.2, a temperature sensitivity of $\approx$ 113 μGal mK^{-1} was calculated. This value is over four times higher than the 25 μGal mK^{-1} value as reported [1]. The difference between the modelled value and physical measurements could be due to not using an anisotropic silicon model or possibly due to variations in the etching of the MEMS geometry. Considering both values, a temperature sensor would be required that had sub-milliKelvin accuracy to achieve acceleration measurements stable to tens of μGal.

2.2.1.2 Further Temperature Sensitivities

Thermal Expansion of Proof Mass

The temperature sensitivity of the flexures is not the only temperature effect in the system. If the proof mass were to change in temperature, then it would expand in all directions. Since

Effect	Extension [μm] (ANSYS)
Gravity (g)	1458
Thermal Expansion (α)	7.6
Thermal effect of Young's Modulus (β)	73.1
Thermal Expansion + Young's Modulus ($\alpha+\beta$)	72

Table 2.2 A table showing the displacement of the MEMS using isotropic silicon. The table shows the extension for gravity, linear thermal expansion, a temperature dependant Young's modulus, and their combined effect. After gravity, the displacement (and therefore the acceleration sensitivity) is most sensitive to the temperature dependant Young's modulus term.

the system uses a shadow sensor (described in chapter 4), an expansion in all directions would cancel out, but only if the device was perfectly centred. First consider a MEMS device with a proof mass of length L_0 that is off-centre by x, relative to the photodiode centre. If the proof mass changes in temperature by ΔT, then the new length of the proof mass becomes $L_T = L_0(1+\alpha_T \Delta T)$, where α_T is the linear thermal expansion coefficient. The difference in the area of the shadow cast from the proof mass between either side of the centre of the photodiode (of width w) is equal to $w(\frac{L_T}{2}-x) - w(\frac{L_T}{2}+x) = 2\,x\,w$, i.e. independent of the length of the proof mass. Therefore, the system should be independent of the thermal expansion of the proof mass, even with an offset. However, this is only the case if the light intensity is assumed to be uniform across the proof mass. This assumption cannot be made and thus if the proof mass is off-centre, then the device is temperature sensitive.

To obtain an idea of the sensitivity for an off-centre proof mass, a Gaussian distribution for the light intensity was considered. As the output from a split photodiode is proportional to the difference in total light between either side, a further assumption can be made that the output is also proportional to the difference in shadow between either side. Figure 2.4 shows the light intensity relative to the intensity at an angle of zero, i.e. straight on. The datasheet defines the viewing angle ($\theta_{1/2}$) as the angle at which the luminous intensity is half relative to the intensity at an angle of zero. Figure 2.4a shows a system with a perfectly centred MEMS and photodiode that would have zero signal output due to the equal amount of light on either side of the MEMS. In contrast to this, figure 2.4b shows the case where the MEMS is offset. This offset would mean that a temperature change results in a signal as the expansion of silicon covers a different amount of light on either side.

To estimate the sensitivity due to a non-uniform light intensity, first consider the general equation for a Gaussian, $a\exp(-\frac{(x)^2}{2\sigma^2})$, where a is the peak output from the LED, x is the

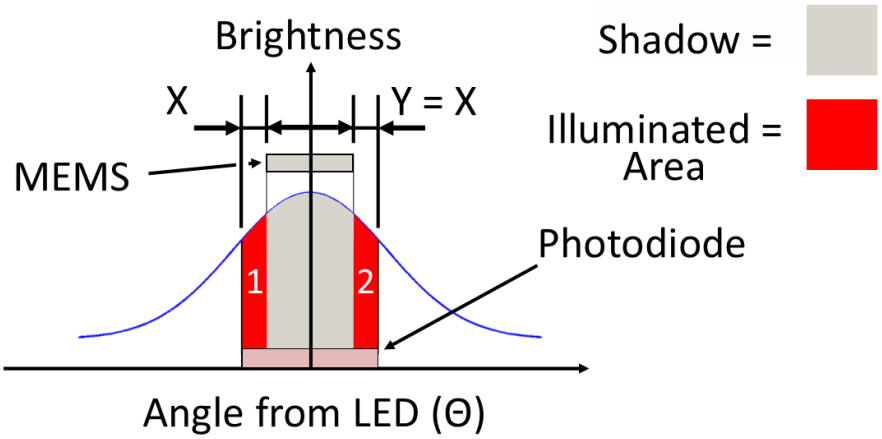

(a)

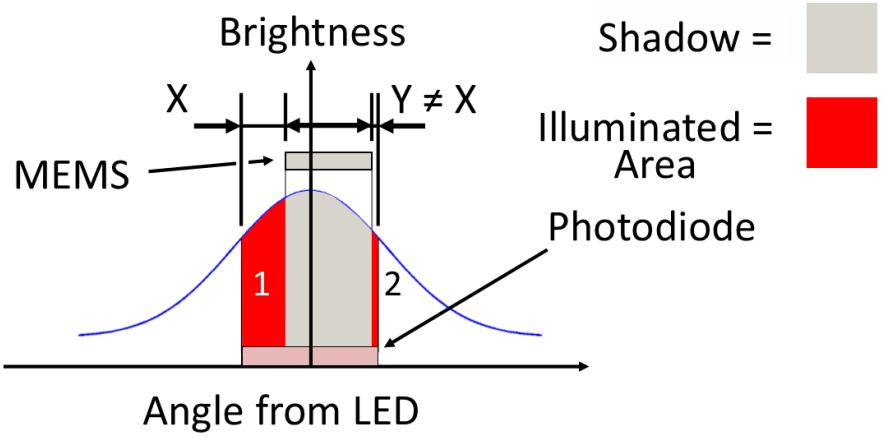

(b)

Fig. 2.4 A comparison between having a centred MEMS (top pane) and offset MEMS (bottom pane) on the displacement sensor output due to temperature fluctuations. For the centred MEMS, the uniform expansion/contraction would result in equal amounts of light being covered, so no change in signal would be seen. However, the uniform expansion/contraction would result in a different amount of light being covered on either side of the photodiode for the non-centred case, and would result in a change in signal.

distance from the LED centre line (assumed to be the same as the centre line of the photodiodes) and σ is the standard deviation of the intensity with respect to distance. Generally for an LED, the spatial distribution is given as a viewing angle. It is therefore better to consider the angle that is made from the centre line to the displacement along the proof mass. If we assume the LED is approximately 1 cm from the proof mass, the angle (θ) is equal to $\tan^{-1}(\frac{l}{1\times10^{-2}})$, where l is the displacement along the proof mass. With the Gaussian $f(\theta) = a\exp(-\frac{\theta^2}{2\sigma^2})$ (where σ is now the standard deviation with respect to angle and $f(\theta)$ is the light intensity of the Gaussian at an angle θ from the centre-line) an estimate of the total difference of light on either side of the photodiode centre line can be made. Since $2\theta_{1/2}$ is simply the full width half maximum (FWHM), the standard deviation is therefore equal to $\sigma = \frac{\text{FWHM}}{2\sqrt{2\ln 2}} = \frac{2\theta_{1/2}}{2\sqrt{2\ln 2}}$.

To obtain an idea of the change in total light intensity, two pairs of integrals must be considered. The first set of integrals use an initial length L_0 that is offset by x, while the second set use the expanded length $L_T = L_0(1+\alpha\Delta T)$ with the same offset as the first. The first set can be seen in equation 2.4 and the second set in equation 2.5.

$$\begin{aligned} F(\theta)_0 &= \int_{\theta_{s0}}^{\theta_x} a\exp(-\frac{\theta^2}{2\sigma^2})\,\mathrm{d}\theta \\ F(\theta)_1 &= \int_{\theta x}^{\theta_{f0}} a\exp(-\frac{\theta^2}{2\sigma^2})\,\mathrm{d}\theta\ . \end{aligned} \tag{2.4}$$

$$\begin{aligned} F(\theta)_2 &= \int_{\theta_{s1}}^{\theta x} a\exp(-\frac{\theta^2}{2\sigma^2})\,\mathrm{d}\theta \\ F(\theta)_3 &= \int_{\theta x}^{\theta_{f1}} a\exp(-\frac{\theta^2}{2\sigma^2})\,\mathrm{d}\theta\ , \end{aligned} \tag{2.5}$$

where θ_{s0}, θ_{s1}, θ_{f0}, and θ_{f1} are the angles subtended from the LED to the displacements along the proof mass of $-\frac{L_0}{2}+x$, $-\frac{L_T}{2}+x$, $\frac{L_0}{2}+x$, and $\frac{L_T}{2}+x$. $F(\theta)$ is the integral of $f(\theta)$. An estimate of the total change in intensity can be made, given a change in temperature of of ΔT and the integrals $F(\theta)_0 - F(\theta)_1$ and $F(\theta)_2 - F(\theta)_3$. The indefinite integral of a Gaussian function is given by $\sqrt{\frac{\pi}{2}}\,a\,\sigma\,\mathrm{erf}(\frac{x}{\sqrt{2}\sigma})$, where erf is the error function. Therefore, the difference between the terms in each set is given by:

$$\mathrm{d}F_1 = F(\theta)_0 - F(\theta)_1 = \sqrt{\frac{\pi}{2}}\sigma\left[2\theta_x\,\mathrm{erf}(\frac{\theta_x}{\sqrt{2}\sigma}) - \theta_{f0}\,\mathrm{erf}(\frac{\theta_{f0}}{\sqrt{2}\sigma}) - \theta_{s0}\,\mathrm{erf}(\frac{\theta_{s0}}{\sqrt{2}\sigma})\right] \quad (2.6)$$

$$\mathrm{d}F_2 = F(\theta)_2 - F(\theta)_3 = \sqrt{\frac{\pi}{2}}\sigma\left[2\theta_x\,\mathrm{erf}(\frac{\theta_x}{\sqrt{2}\sigma}) - \theta_{f1}\,\mathrm{erf}(\frac{\theta_{f1}}{\sqrt{2}\sigma}) - \theta_{s1}\,\mathrm{erf}(\frac{\theta_{s1}}{\sqrt{2}\sigma})\right]. \quad (2.7)$$

By calculating the difference between equations 2.6 and 2.7 (as seen in equation 2.8), an estimate of the temperature sensitivity can be made given, $\theta_{s0} = \tan^{-1}(\frac{-L_0/2+x}{\times 10^{-2}})$, $\theta_{f0} = \tan^{-1}(\frac{L_0/2+x}{2\times 10^{-2}})$, $\theta_{s1} = \tan^{-1}(\frac{-L/2+x}{\times 10^{-2}})$, and $\theta_{f1} = \tan^{-1}(\frac{L/2+x}{\times 10^{-2}})$.

$$\mathrm{d}F_2 - \mathrm{d}F_1 = \sqrt{\frac{\pi}{2}}\,\sigma\left[\theta_{f0}\,\mathrm{erf}(\frac{\theta_{f0}}{\sqrt{2}\sigma}) + \theta_{s0}\,\mathrm{erf}(\frac{\theta_{s0}}{\sqrt{2}\sigma}) - \theta_{f1}\,\mathrm{erf}(\frac{\theta_{f1}}{\sqrt{2}\sigma}) - \theta_{s1}\,\mathrm{erf}(\frac{\theta_{s1}}{\sqrt{2}\sigma})\right]. \quad (2.8)$$

Note that by dividing $\mathrm{d}F_1 - \mathrm{d}F_2$ by the initial difference in light before the thermal expansion ($\mathrm{d}F_1$), the relative sensitivity is obtained. This division also cancels the variable a, which is therefore not needed. Assuming the proof mass is approximately 8 mm in length and is offset by 100 μm, the relative change of $R = \frac{\mathrm{d}F_1 - \mathrm{d}F_2}{\mathrm{d}F_1} = -2.4$ ppm K^{-1} can be calculated. This value is obtained given the linear thermal expansion coefficient of silicon $\sigma_T = 2.45$ ppm K^{-1} [4]. Therefore, a change in temperature of 1 K would change the output from the photodiodes by 2.4 ppm. This would take effect as the relative change in signal and can be assumed to be the equivalent of a change in the offset. A coefficient of -2.4 ppm K^{-1} is the equivalent to a displacement sensitivity of 240 pm K^{-1} if a typical offset of 100 μm is assumed. For a 2 Hz device this displacement would be an acceleration sensitivity of 3.8 μGal K^{-1} or 0.0038 μGal mK^{-1}. This is an incredibly small effect relative to the result from ANSYS.

LED Intensity Variations

Another component in the system that is sensitive to temperature variations is the LED, which is used to illuminate the photodiodes. Several characteristics can change as the temperature changes in an LED. Fundamentally, as the temperature of the LED changes, the bandgap involved in the production of the emitted photons also changes (an increase in temperature acts to increase the width of the band gap [95]). A change in the width of the bandgap results in a change of the wavelength of the photons, i.e a larger wavelength for an increase in temperature. As well as the wavelength, the intensity of photons can change with temperature, resulting in an even larger effect. A paper from K. A. Vinogradova et al. [96] outlines several

of the effects from a change in temperature. The paper shows a large difference between LEDs of different colours, where blue LEDs (455 nm) were amongst the most stable, at 1.6 ppm mK^{-1} power loss. In contrast, red LEDs (660 nm) and far-red LEDs (730 nm) were among the worst at 2.8 ppm $mK^{-1} \rightarrow 4.4$ ppm mK^{-1}. Another study [97] showed the temperature sensitivity of red LEDs to be as high as ≈ 7.6 ppm mK^{-1}.

Assuming that the output from the photodiodes, and therefore the signal, is proportional to the luminous flux, then the temperature stability of the signal due to the LED is also the same, i.e. 2.8 ppm $mK^{-1} \rightarrow 7.6$ ppm mK^{-1}. As an example, if the temperature sensitivity was assumed to be $\sigma_T = 5$ ppm mK^{-1}, a sensitivity can be obtained if a few other assumptions are made. Mainly, it is assumed that the output from the photodiodes (i.e. the photocurrent and therefore signal) is directly proportional to the change in power of the LED. This would mean that a sensitivity of σ_T is also the sensitivity of the output current. Continuing from this assumption, the output current should be directly proportional to the displacement of the MEMS (ignoring offsets from electronic components). If the MEMS was centred to 100 μm, a temperature sensitivity of 5×10^{-10} m mK^{-1} can be calculated (simply the displacement multiplied by the LED sensitivity). This displacement sensitivity would be the equivalent of 7.9 μGal mK^{-1} for a 2 Hz device. This is not an insignificant effect for a target sensitivity of order tens of μGal and shows that the temperature control would have to be at the order of milliKelvin.

LED Central Wavelength Shift

Photodiodes are similar to LEDs, in that they are fabricated using a semiconductor (created from silicon). Photodiodes (PDs) absorb photons of sufficient energy to create an electron-hole pair. These pairs occur when the electron transitions from the valence band to the conduction band. The electron in the conduction band then travels towards the cathode resulting in current. However, the absorption response with respect to wavelength can vary in shape depending on the type of photo-diode, and whether they have been made to suppress the absorption of particular wavelengths. Figure 2.5 shows an example of the spectral output for a red LED and the IR-suppressed PD response. Any changes in the central wavelength of the LED would result in a change of the photodiode output. The rate of change of the output from the photodiode, i.e. the change in current, is proportional to the rate of change of the spectral response (which is a function of wavelength). That is, $\mathrm{d}I \propto \frac{\mathrm{d}R(\lambda)}{\mathrm{d}\lambda}$, where I is the current, R is the spectral response, and λ is the wavelength. This change in current would then be observed as a change in displacement.

To obtain an estimate of the effect of a temperature change on the wavelength (and therefore current), a temperature coefficient for the central wavelength must first be obtained. Malik et al. [95] studied the effect of temperature on the bandgap, and therefore, the central wavelength. They found for a change in temperature of 400 K, the central wavelength moved from 5007 nm to 5208.5 nm. This is a shift of 201.5 nm per 400 K, i.e. 0.504 nm K^{-1} (this is the equivalent of 101 ppm K^{-1}). Note that the spectral response of the photodiodes is linear around the the LED's central wavelength, and the current is proportional to the integral of the spectral response of the PD's times the LED output spectrum with respect to wavelength. It would follow that the current is equal to the integral of a Gaussian (LED output) multiplied by the straight line response of the photodiodes with respect to wavelength, i.e. $I \propto \int_{-\text{inf}}^{+\text{inf}} f(\lambda) \times R(\lambda) \text{d}\lambda$, where $f(\lambda)$ is the spectral output of the LED, and $R(\lambda)$ is as before. $R(\lambda)$ is of the form $k\lambda + c$ between the wavelengths 500 nm and 800 nm with the responses 0.25 A/W and 0.6 A/W respectively. $f(\lambda)$ has the form, $a \exp - \frac{(\lambda-\mu)^2}{2\sigma^2}$, where a is the peak output from the LED, μ is the central wavelength, and σ is the standard deviation. The values: $a = 10.2$ mcd, $\mu = 700$ nm, and $\sigma = 35$ nm can be obtained from the datasheet [98] for a typical off-the-shelf red LED. The next question that needs to be addressed is the value of the integral before and after a shift in wavelength of the central peak (assuming the same standard deviation). It is easiest to do this numerically. First, for the Gaussian of the form described, the integral is equal to $a\sigma\sqrt{2\pi}$. This can then be confirmed by using a simple MATLAB script to manually integrate a Gaussian equation. Both numerical and analytical results obtained a value of $8.7544 \times 10^{-08}\, a$ (the units are not important). However, the integral of a Gaussian multiplied by the straight line response of the photodiodes, within the limits specified, is not so easy to integrate analytically. Using MATLAB, the result of $4.24 \times 10^{-8} a$ was calculated. The change from $8.7544 \times 10^{-8} a$ to $4.24 \times 10^{-8} a$ is reasonable as the straight line response of the photodiodes is defined from 0.25 A/W to 0.6 A/W, where the central peak is located at approximately 0.486 A/W. The ratio of the integrals is $\frac{4.24 \times 10^{-8}}{8.7544 \times 10^{-8}} = .4833$ (close to the LED's central peak wavelength response on the PDs). Now the resulting change in the integral from a shift in temperature, and therefore, central wavelength can be calculated. The integral was recalculated using a change of 10 nm to obtain $4.343 \times 10^{-8} a$. This is a difference of $0.1 \times 10^{-8} a$, i.e. a 2.4 ppt per 10 nm shift. Remembering that the thermal spectral coefficient of the LED is 0.5 nm K^{-1}, the value 120 ppm K^{-1} can be calculated. Using a further assumption that the current is proportional to the absolute displacement of the MEMS, a sensitivity in terms of a displacement (and therefore an acceleration) can be calculated. If we use an absolute displacement of the MEMS equal to 100 μm, the result of 12 pm K^{-1} can be calculated

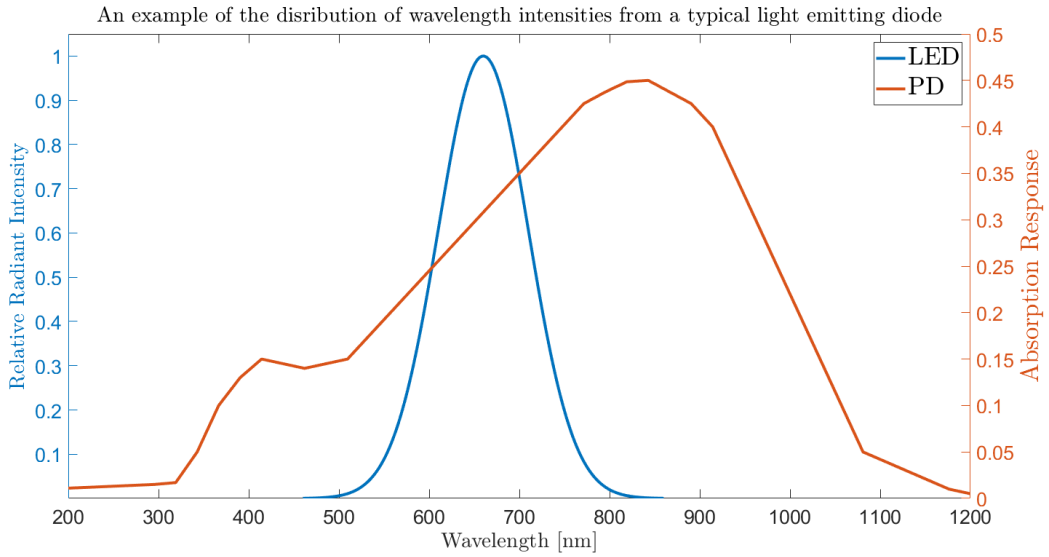

Fig. 2.5 A plot showing an example of the wavelength absorption response of an infra-red suppressed photo-diode. It can be seen that the response shape is not a simple normal distribution. If the LED were to change or drift in its output wavelength, a change in the signal would be seen.

which is approximately equal to 0.2 μGal K^{-1} (0.2 nGal mK^{-1}). This effect is negligible for the target sensitivity.

Summary

Several temperature effects have been discussed, including the contribution from temperature changes in the MEMS, LED, and PDs. The summary of these results can be seen in table 2.3. The table shows a need for temperature control that is within 1 mK or less. A 1 mK change could cause a spurious gravity reading as high as 115 μGal for a 2 Hz MEMS device (though previously published values of this were closer to 25 μGal/mK).

2.2.2 Tilt Sensitivity

2.2.2.1 Out-of-Plane Sensitivity

As gravimeters are devices which measure the acceleration due to gravity, it is quite apparent that if they tilt relative to the direction of gravity, the measured output will also change. If the MEMS device is at an angle of θ from the gravity field vector (vertical), then the component

Source	Sensitivity [μGal mK^{-1}]
ANSYS	115
Thermal Expansion of Proof Mass	0.0038
LED Intensity Variations	7.9
LED Central Wavelength Shift	0.0002

Table 2.3 A table showing a summary of estimated and modelled temperature sensitivities for multiple components including the MEMS ANSYS modelling, LED, and photodiodes. The total effect is clearly dominated by the results from ANSYS. The ANSYS model showed that the variation due to a temperature sensitive Young's modulus of silicon would likely be the largest effect.

of gravity (a) measured by the device is equal to $g\cos\theta$. Taking the derivative with respect to θ gives equation 2.9.

$$\mathrm{d}a = -g\sin\theta\,\mathrm{d}\theta\ . \tag{2.9}$$

Equation 2.9 shows that, for very small values of θ, $\sin\theta \approx 0$. Therefore, $\mathrm{d}a \approx 0$, i.e the device should be insensitive to tilt. If we assume that the device can be levelled within 333 μRad, the equivalent of a vertical alignment of 100 μm over a baseline of 30 cm, then a change in tilt of 10 μRad would result in:

$$\begin{aligned}\mathrm{d}a &= 9.81 \times \sin(333 \times 10^{-6}) \times 10 \times 10^{-6} \\ \mathrm{d}a &= 3.3\ \mu\mathrm{Gal}\ .\end{aligned} \tag{2.10a}$$

Equation 2.10a shows that, for a change in angle of 10 μRad from the starting angle of 333 μRad, a change in acceleration of 3.3 μGal could be measured. This is the equivalent of 0.33 μGal μRad^{-1}. This estimated sensitivity is for the out-of-plane axis (as shown in figure 2.6) and is the less sensitive axis for a three-flexure MEMS device.

In-Plane Sensitivity

Changes caused by variations in tilt were shown to be larger in the in-plane direction (shown in figure 2.6). This effect is at least an order of magnitude larger than the simple $g\cos(\theta)$ estimation. The difference between these axes is due to the design of this MEMS only having three flexures. Having an asymmetric geometry causes the flexures to have an uneven

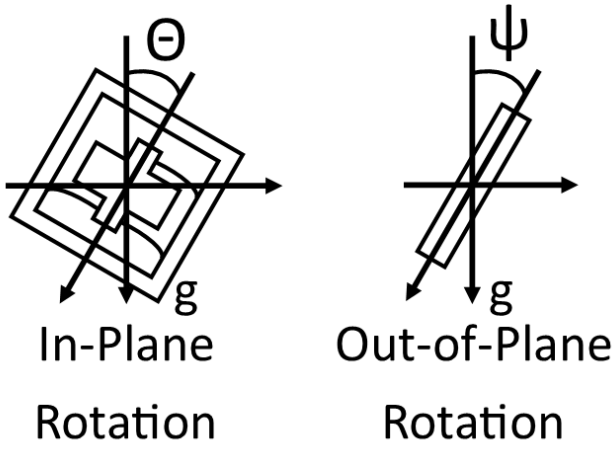

Fig. 2.6 A diagram showing the in and out-of-plane rotations for the MEMS, the most sensitive axis being θ (in-plane rotation). For $\theta = 0$ the sensitivity becomes zero for the out-of-plane axis. The out-of-plane rotation shows a simple $g\sin(\theta)$ behaviour, where the in-plane rotation shows a sensitivity that is an order of magnitude larger.

restoring force, and therefore an increased tilt sensitivity. Since the writing of this thesis, the effect of tilt has been modelled on a four flexure system that also follows the parabolic $g\cos(\theta)$ behaviour seen in the out-of-plane axis.

R. P. Middlemiss et al. [83] quotes a measured tilt sensitivity of 4.4 μGal μRad^{-1} (in-plane), and 0.12 μGal μRad^{-1} (out-of-plane). Assuming the larger sensitivity, a tilt sensor would be required to measure better than 1 μRad. Table 2.4 shows the summary of the tilt sensitivities of the device.

Source	Tilt Sensitivity [μGal μRad^{-1}]
$g\sin\theta$	0.33
Out-of-Plane	0.12
In-Plane	4.4

Table 2.4 A table showing the tilt sensitivity of the MEMS. It is apparent that, with a sensitivity of 4.4 μGal μRad^{-1}, a sensor with an RMS noise of the order 1 μRad is required.

2.3 Proposed System

As the system needed to be portable and lightweight, it was necessary to design a custom electronics board that included all the requirements aforementioned. The system would require current-to-voltage converters, analogue-to-digital converters (ADCs), temperature sensors, tilt sensors, digital-to-analogue converters (DACs), as well as to be able to compute a series of digital filters and calculations. The top-level design of the system can be seen in figure 2.7. At its centre is a microcontroller, the dsPIC33E from Microchip, which can compute all the necessary filters and calculations required to run the system. The microcontroller also communicates with the other components in the system to: sense and control several temperatures, modulate the shadow sensor and implement the lock-in-amplifier, and monitor the tilt.

To produce the LED drive, a DAC would be used to create an alternating current (AC) signal. The DAC would be updated with voltage values that followed a sinusoidal pattern, which, with a resistor, would dictate the amount of current being supplied to the LED.

Due to the total temperature sensitivity possibly being as high as 115 μGal mK^{-1}, an ADC would be required that could measure temperatures to within a milliKelvin over long periods. To obtain sufficient sensitivity, the ADC used a four-wire resistance measurement and compared the sensor to a stable reference in a ratiometric technique. The sensing resistor was a temperature sensitive resistor, such as a PT100, which has a resistance of 100 Ω at 0 $^{\circ}$C.

A control system such as a proportional integral differential (PID) controller would be required to control temperatures to within a milliKelvin. Initially, the PID would be part of the computer user interface, but ultimately had to be hard-coded into the board to make it fully autonomous. The PID would output a value representing a voltage that would be output by a digital-to-analogue converter (DAC). This voltage would drive a heater, attached close to where that temperature sensor was measuring, causing heat to be generated. Given that DACs are generally not made for sourcing or sinking much current, an op-amp would be required on its output, acting as a buffer. As three temperatures are required to be controlled at the same time, an ADC, a DAC and buffers would be required for each channel.

Two tilt sensors would also be required, with a sensitivity down to microradian levels. Typically, commercially available tilt sensors are electrolytic and require alternating currents, at a frequency of at least 1 kilohertz. An AC signal could be outputted using the spare DACs. One sensor would be required for both the in-plane and the out-of-plane axis of the MEMS.

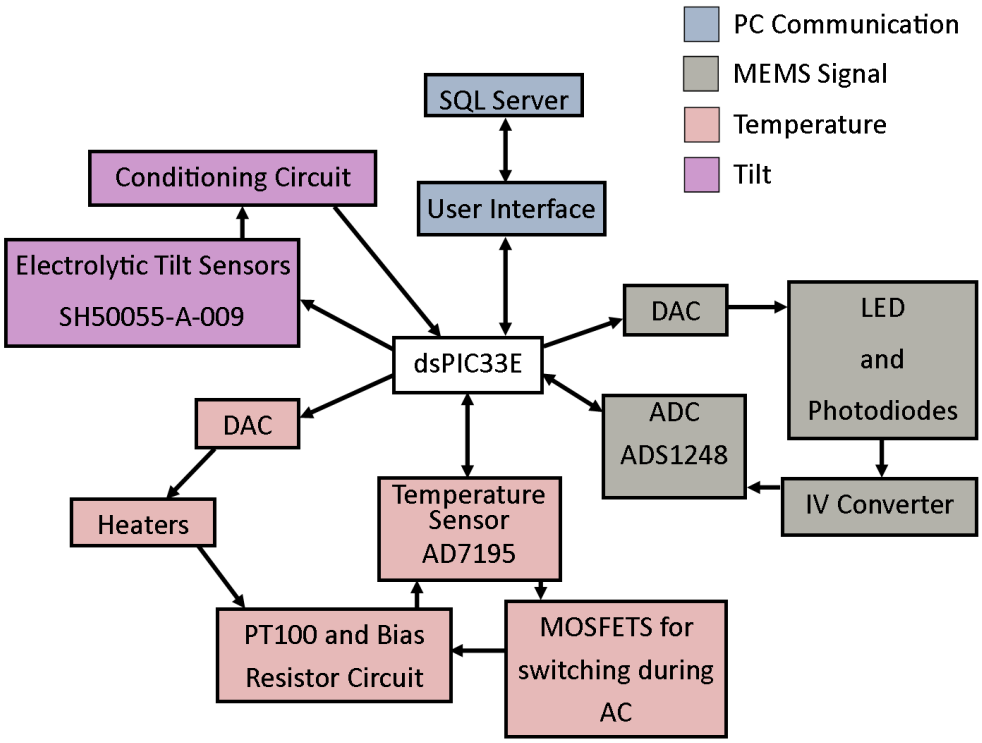

Fig. 2.7 A block diagram of the system planned for getting the MEMS gravimeter into the field. It would have a microcontroller, the dsPIC33E, at its core that communicates with each of the components involved in making a high stability measurement. The system would require: temperature control and actuation, a shadow sensor and digital lock-in amplifier, and a tilt sensor.

The values obtained here can then be used in regression models to remove their effects (if necessary) from the data.

Finally, there would be a need for a component that communicates to a computer (via a USB and FTDI interface), retrieve settings from the computer and communicate these to the rest of the board. Communication would be achieved using the dsPIC33E microcontroller. The microcontroller would also need the ability to compute a large number of filters including the digital lock-in amplifier.

2.3.1 dsPIC

At the heart of the custom electronics board is the dsPIC33EP512MU810 (shortened to DSPIC33E), a digital signal controller (DSC) from Microchip. As stated, the microcontroller would communicate with all the components present on the board, taking the data from each of them and sending it to a connected computer. An essential aspect of the board's design was to have the ability to condition data using filters, e.g. a low-pass filter. The dsPIC33E is not a typical microcontroller, as it contains a specific digital signal processing (DSP) block used to compute digital filters efficiently. This efficient architecture in a small microcontroller would allow for the large number of multiplications, additions, and divisions required in filtering real-time data with high sampling rates. The reason the lock-in amplifier (phase sensitive detection) and filtering is to be computed on a microcontroller is to reduce the price and cost of the combined electronics as well as to increase flexibility. Filtering using analogue electronics would require components to be physically changed via soldering, whereas, in a digital filter, it is as simple as changing an array of numbers. "MPLAB X IDE" is the software from Microchip used to program the company's microcontrollers, as well as to debug them.

2.3.1.1 Digital Signal Processing (DSP) Engine Block

The chosen dsPIC33E is a microcontroller that has a specialised architecture for digital signal processing. This functionality comes in the form of a digital signal processing engine block. Effectively, the system is built to compute a series of instructions from arrays without using extra CPU cycles, proving perfect for digital filters. To compute these instructions, the microcontroller also contains a set of data accumulators, which are simply a piece of memory that is larger than the standard bit size which allow multiplication of numbers without overflow (the term used to describe when a stored value in binary goes above the bit limit which "wraps" the number back around to 0.).

2.4 Conclusion

To conclude, a portable, low-cost and lightweight system would have to be designed, tested and improved. The system would have to be able to: convert currents into voltages, sample those voltages into digital signals, create analogue signals for the LED, measure and control temperatures to within a few milliKelvin, measure tilts with a sensitivity of μRads and, finally, compute digital filters requiring a large number of multiplications and summations. The system would have to measure a displacement of approximately 0.6 nm over periods of days in order to deliver a MEMS with a sensitivity of the order of tens of μGal. To obtain these sensitivities, a microcontroller (dsPIC33E), and a custom electronics board would be required. The following chapters, namely chapters 3, 4 and 5, detail the circuits, components and performance of the electronics board created.

Chapter 3

Temperature Control

3.1 Introduction

Sensitivities to temperature are found throughout the system, from the LED and photodiodes, to the electronics, as well as the MEMS itself. According to R. P. Middlemiss [83], the temperature sensitivity was measured to be approximately $\approx 25\ \mu\text{Gal mK}^{-1}$. As outlined in the previous chapter, the effect of the temperature dependency of the Young's Modulus on the flexures is the dominant thermal effect. With the target of tens of μGal, clearly temperature control is required at the level of milliKevlin or below. The original set-up utilised the Keithley 2000, a $6\frac{1}{2}$-Digit Multimeter. Due to its size (2.1 cm high $\times$7.2 cm wide $\times$22.1 cm deep) and cost (approximately £1000), an alternative was required. As already outlined, the alternative was fit onto a custom electronics board. A technique that allowed for precision resistance sensing was the four-wire measurement, also known as the Kelvin measurement. This is what the Keithley 2000 uses for its resistance sensing, although a two-wire measurement was also available. The sensor also had to be robust enough for use in the field. After values of the temperature were taken, a technique would also be required to control the temperature to a given set point. This temperature control was achieved with a simple Proportional Integral Differential (PID) control loop using a DAC to output current through resistors to heat the surrounding area. As a heater was implemented and not a Peltier, the system could not be actively cooled, therefore the temperature was always maintained at slightly above ambient.

3.1.1 4-Wire Measurement

The Keithley 2000 that was used in the original system utilised the 4-wire measurement technique (named for its four leads). Two of the four leads are connected at either side of a temperature sensitive resistor. The thermistor was a Pt100 (as with original set-up used by R. P. Middlemiss). Pt100's have a resistance of a 100 Ω at 0 °C with a temperature coefficient that increases by 0.385 Ω K^{-1}. There are two ways of measuring resistances: a half-bridge or a full-bridge (which is also known as a Wheatstone bridge).

Half-Bridge

A half-bridge uses two resistors in series, one of which is the sensing resistor, and the other a bias resistor (seen in figure 3.1). A full-bridge contains four resistors in a diamond arrangement, which is also shown in figure 3.1. The half-bridge is used to measure the ratio of $R_{\text{sens}}/R_{\text{bias}}$ (the equivalent of the voltage drop over these resistors), whereas the full bridge is used to measure the ratio of the difference in potential between points B and D, and the potential difference at A and C. The use of the half-bridge allows for noise cancellation. A cancellation occurs because the current through both of the resistors is the same, and therefore, cancels, i.e. $\frac{V_{\text{pt100}}}{V_{\text{bias}}} = \frac{I R_{\text{pt100}}}{I R_{\text{bias}}} = \frac{R_{\text{pt100}}}{R_{\text{bias}}}$. This is also known as a ratiometric measurement. It can also be seen from figure 3.1 that the half-bridge has two wires extending from either side of the sensing resistor, i.e. a four-wire measurement. This arrangement allows the cancellation of the resistance of the wires, obtaining a more accurate measurement.

Full-Bridge

The full-bridge, though more complex, allows a high gain to be used. This is due to the fact that the output of the bridge is zero when all resistances are balanced (because points D and B will have the same potential). As with the half-bridge, any potential changes across A and C (due to voltage reference drifts for example) will also be observed between B and D. Since the ratio of these differences in potential are taken, any changes in the supply voltage should cancel.

For this project, a half-bridge configuration was implemented due to its more simplistic nature. When considering the ratio of the voltages (V_{Pt100} and V_{bias} from figure 3.1) and given that the current (I) is flowing through both of these resistors, equation 3.1 is obtained.

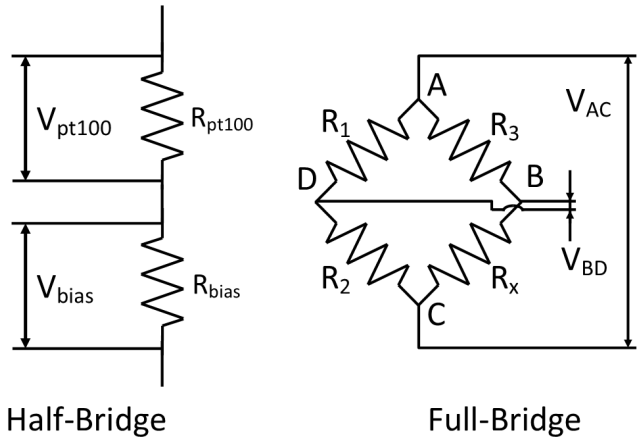

Fig. 3.1 A diagram showing the differences between a half-bridge and a full-bridge resistance measurement. The half-bridge (left) has two resistors, allowing the ratio of the voltage across the resistors to be measured. The ratio of the voltage is equal to the ratio of the resistances, since both resistors experience the same current. For the full-bridge, there are four resistors, with a voltage applied between two sets of two resistors. When balanced, the output (the difference between B and D) is zero, and so allows for high gains.

$$\begin{aligned}\frac{V_{\text{Pt100}}}{V_{\text{bias}}} &= \frac{I\,R_{\text{Pt100}}}{I\,R_{\text{bias}}} \\ &= \frac{R_{\text{Pt100}}}{R_{\text{bias}}} \\ \therefore R_{\text{Pt100}} &= \frac{V_{\text{Pt100}}}{V_{\text{bias}}} R_{\text{bias}}\ .\end{aligned}$$

Equation 3.1 shows that if the bias resistance is known, and the ratio of the voltages across each resistor is measured, a value of the sensing resistor can be calculated. Since the value of the bias resistor is assumed to be constant during the calculation, this resistor must be as thermally stable as possible, otherwise it will appear as a change in the measured resistance.

The ADC "AD7195" from Analog Devices was used to measure the resistances using the four-wire technique [99]. This ADC was chosen since it is a strain gauge amplifier, which has many features useful for a resistance bridge measurement. The ADC contains four analogue inputs for up to two differential measurements (non-simultaneous sampling), but, more importantly, also includes an input for using an external reference. The device also has four logic outputs that are used to control an alternating bridge, which reverses the direction of the current through the resistors at a set frequency. The logic is connected to the gates of four MOSFETs that dictate what side of the resistor bridge is connected to which voltage potential. The schematic used to control the bridge potentials can be seen later in this chapter.

Since the AD7195 uses an external reference from either side of the bias resistor, the output value obtained from the ADC is a 24-bit number that represents a value from $-\frac{R_{\text{bias}}}{\text{Gain}} \rightarrow +\frac{R_{\text{bias}}}{\text{Gain}}$, if in bipolar mode. The decimal value, N_{dec}, needs to be converted to a value of resistance using the equation:

$$R_{\text{measured}} = \left[\frac{N_{\text{dec}} - 2^{23}}{2^{23} - 1}\right] \frac{R_{\text{bias}}}{\text{Gain}}\ . \tag{3.1}$$

Negative values are represented by a decimal value below 2^{23}, while positive values are above 2^{23} in decimal. The subtraction of 2^{23} shifts the decimal values from $-(2^{23}) \rightarrow +(2^{23}-1)$, and thus, when divided by $2^{23}-1$, scales from $-1 \rightarrow +1$. By multiplying by $\frac{R_{\text{bias}}}{\text{Gain}}$, the result now scales as required. For example, a 107 Ω resistor being measured by the AD7195, with a bias resistor of 10 kΩ, would return a decimal value of $8,478,400$ in bipolar mode (which is the term used when negative voltages are allowed within the sampling range), and $179,520$ in the unipolar mode (when negative voltages are not allowed in the sampling range).

Using Pt100's, a resistance of 109.625 Ω at 25 °C would be expected (the calculation of which can be seen in the equation 3.2).

$$R_{\text{pt100}} = 100 + (25)(0.385)$$
$$R_{\text{pt100}} = 109.625\ \Omega\ .$$

Once the resistance of the Pt100 is obtained, a value for the temperature can be calculated using equation 3.2.

$$T_{\text{pt100}} = \frac{R_{\text{pt100}} - 100}{0.385}\ . \tag{3.2}$$

3.1.2 PID Controller

To control the system to within a few mK, a proportional, integral and differential (PID) controller was required. A PID takes input data points, such as the current value of the temperature, and outputs a value that is used to control the temperature. For actuation, a buffered DAC output was used to heat a resistor. A PID outputs a value based upon three factors: how far the current temperature is from the setpoint (proportional), how long the system has spent above and below the setpoint (integral), and the current rate of change of the temperature (differential, over a set time constant).

A PID controller's output, $u(t)$, can be mathematically expressed using the current error, $e(t) = P - T$, where P is the setpoint, and T is the current temperature. Equation 3.3 shows one of the relationships used to calculate the output.

$$u(t) = K_p \left(e(t) + \frac{1}{K_i} \int_0^t e(t')\mathrm{d}t' + K_d \frac{\mathrm{d}e(t)}{\mathrm{d}t} \right)\ , \tag{3.3}$$

where K_p is the proportional coefficient, K_i is the integral coefficient, K_d is the differential coefficient, and t_i is the instantaneous time. Using the Laplace transform, equation 3.3 can be represented in the s-domain to get equation 3.4:

$$\mathscr{L}(u(t)) = U(s) = K_p \left(X(s) + \frac{X(s)}{K_i\, s} + K_d\, s\, X(s) \right)\ , \tag{3.4}$$

where s is the complex variable, $s = \sigma + i\,\omega$, with real numbers σ and ω, and $X(s)$ is the input in the s-domain. This representation is useful because the transfer function, $H(s)$ of the system can be calculated using the equation:

Control Type	K_p	K_i	K_d
PID	$0.6K_c$	$0.5T_c$	$T_c/8$

Table 3.1 A table of the rules used as part of the Ziegler-Nichols tuning method [6]. Once the critical coefficient (K_c) and oscillation period (T_c) have been noted, values for each of the coefficients can be estimated.

$$H(s) = \frac{\text{Output}}{\text{Input}} = \frac{U(s)}{X(s)} = K_p \left(1 + \frac{1}{s K_i} + s K_d\right) . \tag{3.5}$$

When implemented practically, the coefficients for each of the terms can be obtained using the Ziegler-Nichols tuning method [6]. First, the system's integral and differential contributions are reduced to zero (i.e. $K_i = \infty$ and $K_d = 0$), and the proportional gain is increased until the system oscillates around the set point. The period of this oscillation (T_c), and the critical proportional coefficient (K_c), are noted, allowing the terms to be set using the rules in table 3.1.

3.2 Noise Model

3.2.1 Noise Sources

Noise exists everywhere, whether it be pickup from the mains, or long-term drifting in electronics due to varying potentials. Any measurement for low-frequency applications contains noise categorised under two types, short-term noise and long-term noise. Short-term noise (typically noise down to 100s or 1000s of seconds) can be averaged, and therefore, is considered less of an issue given that the noise is "white". This treatment of the short-term noise is a general rule because if the noise was high enough that even after averaging it was above the target, then it would limit the functionality and need to be reduced by other means. The second and more significant problem for long-term measurements is noise over the large time scales, in this case over the course of many days or weeks. All electronics have some level of low-frequency noise (⅟f noise), that is noise that increases in amplitude at lower frequencies. Sometimes components can drift for a known reason, i.e. due to temperature variations, and at other times, it is not so easy to pin-point. Given that the drifts are predictable, their effects can be removed. For example, the AD7195 has a linear drift equal to 10 ppm per 1000 hours. With these specified values, a measurement of 25 °C would only drift 2.8 mK in 1000 hours (= 41.7 days), i.e. an average of 68 μK per day. An example

of drift in an electronic component is the LED, where a study [100] showed that the output from LEDs decreases exponentially and not linearly.

An example of short-term noise is Johnson-Nyquist noise, also known as thermal noise [101]. It is commonly called thermal noise as it originates from random fluctuations and thermal agitation of charge carriers. Johnson noise is a form of 'white' noise, as it has a constant amplitude at all frequencies (a flat spectral density). Thermal noise can be calculated for the planned system using equations 3.6a and 3.6b.

$$V_{\text{ASD}} = \sqrt{4\,k_B\,T\,R} \tag{3.6a}$$

$$V_{\text{rms}} = \sqrt{4\,k_B\,T\,R\,\Delta f}\,. \tag{3.6b}$$

A thermal noise of 1.33 nV/$\sqrt{\text{Hz}}$ and 12.9 nV/$\sqrt{\text{Hz}}$ can be calculated, given the resistances of 107 Ω for the Pt100 and 10 kΩ for the bias resistor. It should be noted that equation 3.6b assumes that there are not further amplitudes above the bandwidth value, however, given that filters are not ideal and attenuate with a roll-off, it is more common to multiply the resulting RMS by $\sqrt{\frac{\pi}{2}}$. i.e. the equation gives an estimate on the lower end of what the real value would be. The sampling rate of the AD7195 can be calculated using the equation:

$$\text{Sampling Rate} = \frac{\text{M}_{\text{clk}}}{N \times F_s \times 1024}\,, \tag{3.7}$$

where N is the order of the sinc filter used in the AD7195 ($N = 4$ for a sinc^4 filter), M_{clk} is the frequency of the master clock (= 4.92 MHz), and F_s is the selected bit value (assume = 49). A sinc filter is an idealistic filter where all frequencies above the specified value are removed, leaving only those below. It is so named because the shape of the frequency response (a top hat) becomes a sinc function when brought into the time domain via Fourier transform. Using the equation and the specified values, an output rate of 24.5 Hz can be calculated. If we use this as an estimate to the bandwidth, an RMS noise of 6.58 nV and 63.9 nV can be calculated for the resistances above.

Of course, the circuitry used for measuring the resistances does not just have Johnson noise. Another source of noise is the voltage reference (MAX6177 [102]). The noise of the voltage reference should be at the level of 100s of nV. However, as the voltage across the bridge causes a current that is common in both the bias resistor and sensing resistor, the noise can be ignored since the output is ratiometric.

The conversion from an analogue signal is made using an analogue-to-digital converter. This step introduces input referred noise and quantisation noise. Quantisation occurs due

to there being a finite number of bits that can represent an analogue signal during sampling. The smallest change in voltage, or, quantisation step (q) in an n bit digitised signal is given by equation 3.8. The quantisation step, also known as the least significant bit (LSB), is the peak-to-peak error in the range $-\frac{\text{LSB}}{2} \rightarrow +\frac{\text{LSB}}{2}$. As an example, a 24-bit ADC has a quantisation error of 59.6 nV for a voltage range of 1 V.

$$q = \frac{V_{\text{range}}}{(2^n - 1)} \,. \tag{3.8}$$

Input referred noise is caused by components inside the sampling stage of the ADC, such as Johnson noise from resistors as well as thermal capacitor noise ($\frac{k_B T}{C}$), which is typically referred to as "k-T-C" noise [101]. The input noise of devices is typically stated, if relevant, on the ADC datasheets, but can be measured by grounding both inputs to the ADC and measuring the noise. In some ADCs, the quantisation noise is higher than the input referred noise, and so no input noise is specified due to its limitation from the quantisation. The input noise of ADCs is dependent on both the gain and the sampling rate. The values for all data rates and gains can be seen in table 3.2. The table shows the effective resolution of the AD7195 when chopping is enabled and the Sinc^4 filter is being used. Chopping is a technique commonly used on the input of ADCs to cancel low frequency noise and offsets. This is achieved by switching the the polarity of the input pins and averaging every two samples. The overall trend is an increase in noise (or decrease in effective resolution) as the sampling rate increases. On top of this, as the programmable gain amplifier (PGA) is increased, the effective resolution still decreases. However, as the voltage range has been reduced by a factor more than the resolution reduction, there is an overall decrease in noise. As an example, going from a gain of 1 to 8 for a sampling rate of 15 Hz, decreases the peak to peak resolution in bits from 20.9 to 20.6. Since the range changes from V_{ref} to $\frac{V_{\text{ref}}}{2^3}$, the resolution goes from $\frac{V_{\text{ref}}}{2^{20.9}}$ to $\frac{V_{\text{ref}}}{2^{20.6+3}}$, i.e. a 2.8 bit improvement in resolution (a factor of 6.96).

A peak-to-peak resolution of 21.7 bits for a gain of 64 at 1.175 Hz (Sinc^4 filter enabled) can be seen from table 3.2. Equation 3.9 can be used to calculate that 2.3 bits, peak-to-peak, is the equivalent of 45.9 $\mu\Omega$. This resistance is the equivalent of 0.12 mK of noise on the input.

$$R_{\text{noise}} = \left\lceil \frac{2^{\text{bits}_{\text{noise}}}}{2^{24} - 1} \right\rceil \frac{R_{\text{bias}}}{\text{gain}} \,. \tag{3.9}$$

Sampling Rate	Gain of 1	Gain of 8	Gain of 16	Gain of 32	Gain of 64
1.175	24 (23.1)	24 (21.8)	24 (21.8)	24 (21.7)	24 (21.7)
1.875	24 (22.6)	23.9 (21.4)	23.9 (21.4)	23.9 (21.4)	23.9 (21.4)
2.5	24 (22.2)	23.8 (21.3)	23.8 (21.3)	23.8 (21.3)	23.8 (21.1)
12.5	23.8 (21.2)	23.5 (20.9)	23.4 (20.9)	23.2 (20.6)	22.7 (20.2)
15	23.6 (20.9)	23.3 (20.6)	23.3 (20.5)	23 (20.5)	22.6 (19.9)
37.5	23.2 (20.7)	22.9 (20.2)	22.8 (20.2)	22.5 (20)	22 (19.3)
75	22.8 (20.3)	22.6 (20)	22.3 (19.8)	22.1 (19.5)	21.5 (18.9)
240	22.2 (19.4)	21.8 (19.2)	21.6 (18.9)	21.3 (18.6)	20.7 (18.1)
600	21.4 (18.8)	21.1 (18.4)	20.9 (18.2)	20.6 (18)	20 (17.3)
1200	19.9 (17.3)	19.8 (17.1)	19.8 (16.9)	19.6 (16.9)	19.3 (16.5)

Table 3.2 A table of the effective resolution, in bits, of the AD7195 while using chopping and the Sinc^4 filter. The numbers shown are the effective resolution (Peak-to-Peak resolution). It can be seen that noise generally gets worse as the sampling rate increases. Also note that when increasing the gain, it would appear as if the resolution is decreasing. However, as the system now has a smaller voltage range, there is still an overall decrease in noise.

3.2.2 Model

3.2.2.1 Short Term Noise

Figure 3.2 shows the full circuit diagram for the temperature sensing, including the key noise sources. Both the resistors and the MOSFETs exhibit thermal noise. The reference introduces voltage noise (both short term and drift), while the input of the ADC introduces both quantisation noise and input referred noise. The buffer stage included on the reference inputs stops current from leaking into or out of the input that would cause noise and drifting. The buffers, however, also then introduce additional voltage and current noise.

Table 3.3 shows the sources of noises and their values. It can be seen that the thermal noise is among the lowest contribution to noise, and therefore can be ignored. To transform the voltage noise into a temperature noise, the voltage must first be divided by the nominal reference voltage (3 V). This result is then multiplied by the bias resistance (10 kΩ), before being divided by the coefficient for the PT100 (0.385 Ω K^{-1}).

It can be seen from table 3.3 that the digitisation noise is at least an order of magnitude below the input noise, and thus can be ignored. The largest noise contributor other than the input noise is the reference. However, the noise from this source will be correlated between the input and reference, and therefore cancel out. This correlation is one of the advantages of using a ratiometric measurement, and here results in the noise being limited by the input

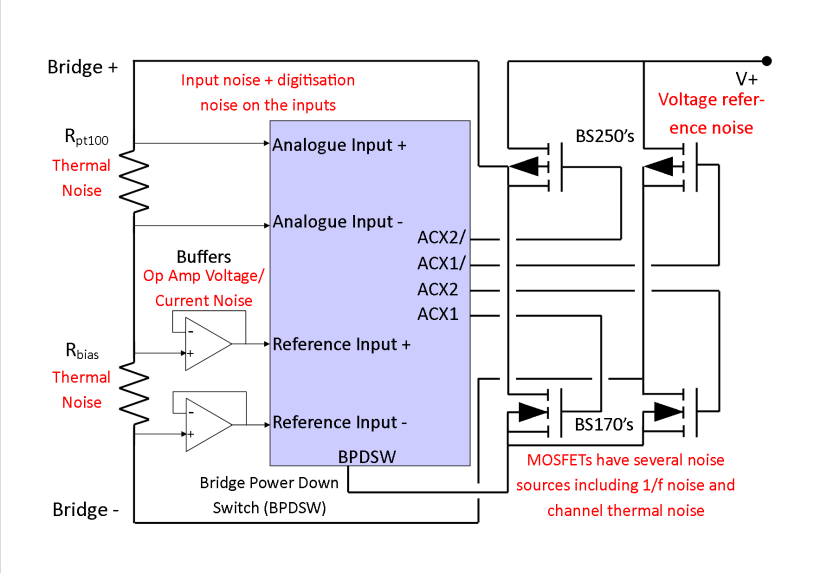

Fig. 3.2 A circuit diagram showing the full temperature sensing circuit (with noise sources stated). The voltage source causes current noise in both resistors, however, because it is a ratiometric measurement, it should cancel. Thermal agitation in the resistors causes uncorrelated 'white' noise. Upon sampling, the ADC introduces input referred noise and digitisation noise. However, since the input noise is the dominant effect, digitisation can be ignored. The MOSFETs also introduce several noise types, including, 1/f and 'white' noise. The reference input requires buffering, otherwise current can leak into or out of these pins, causing offsets.

Noise Type	Noise Source	RMS Noise [nV]	RMS Noise [μK]
Thermal Noise	Pt100	5.75	49.7
	Bias Resistor - PGA = 1	55.6	481
	Bias Resistor - PGA = 64	0.87	7.52
	OPA2277 (x2)	38	329
	OPA2277 (x2) - PGA = 64	0.59	5.11
	BS170 (x2)	0.75	6.45
	BS250 (x2)	1.57	13.6
Digitisation Noise	AD7195 - PGA = 1	69.7	547
	AD7195 - PGA = 64	1.09	8.56
Input Noise	AD7195 - PGA = 1	687	5400
(37.5 Hz)	AD7195 - PGA = 64	28.3	221
Reference Noise	MAX6177	210	1800

Table 3.3 A table of the short term noise contribution in the temperature sensor circuitry. At high gains, the system would be dominated by the reference noise, however, as it is utilising a ratiometric measurement, the noise should cancel. Therefore, at both high and low gain, the system should be dominated by the ADC input noise and nothing external.

noise of the AD7195. It should be noted that, as the gain of the system increases, the input noise decreases relative to the input signal, offering an advantage. However, as the gain increases, if the system was limited by external noise, it would offer no advantage as the signal to noise ratio remains constant. The system should theoretically always be limited by the input noise at all gains. Figure 3.3 shows simulated data from the AD7195 for several gains at the lowest data rate (4.7 Hz), and a higher data rate (100 Hz). Since the dominant noise source is the input noise, only this source can really be observed. The noise plots appear to not be white. This asymmetry is due to the limited bit-depth of the sampling. If a number in-between two bits is sampled, the device would sample and obtain one of the bit values more often as it "spends" more time closer to the voltage represented by that bit. If many samples were taken, they could be averaged to get below the bit-depth. If the noise was upwards of 100s of bits or more, the digitised pattern would be less visible. The graph was produced using a MATLAB script that generated a Gaussian distribution of bits similar to what was observed in the datasheet before being digitised (rounded to the nearest digitised value).

Self-heating is the phenomenon where the power dissipation from a resistive element results in a change of resistance due to the element changing in temperature. This effect is generally given as a coefficient in units of W K^{-1}, corresponding to the relative temperature

Simulated Noise Data for different PGA values for the AD7195. The higher the output data rate, the larger the noise.

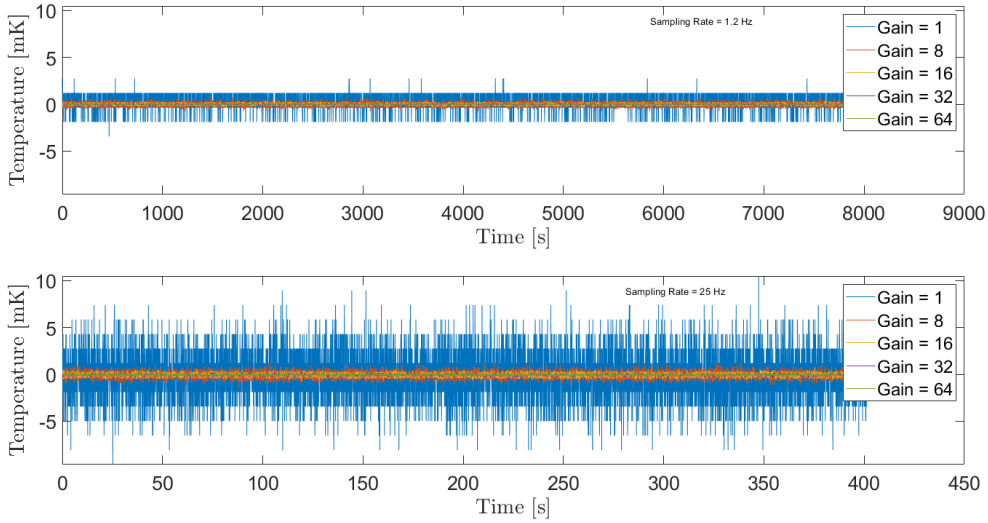

Fig. 3.3 A plot of simulated data from the AD7195 at two sampling rates and multiple gains. The dominant noise source is the input noise at all gains, hence the reduction in noise as the gain is increased. To obtain a resistance, the decimal value is multiplied by the bias resistance and divided by the gain of the PGA. This resistance can then be divided by the thermal coefficient of the Pt100 to obtain a temperature. The two data rates, 100 Hz and 4.7 Hz, show an increase in noise as the sampling rate increases.

change, given the power dissipation. In the circuit used here, the total resistance from source to ground is $R_{\text{pt100}} + R_{\text{bias}} = 107 + 10 \times 10^3\ \Omega = 10.107\ \text{k}\Omega$. With a source voltage of approximately 3.3 V, this results in a current of 327 μA. Given that the expression for the power dissipation is $P = IV = I^2 R$, a value of 11.4 μW can be calculated. If the typical Pt_{100} has a self-heating coefficient of $\alpha_{\text{self-heating}} = 40\ \text{mW K}^{-1}$, a temperature change of $\text{d}T = P/\alpha_{\text{self-heating}} = 0.285$ mK is obtained. This self-heating effect could be observed when using a high gain since the effect would normally be buried in noise.

3.2.2.2 Low Frequency Noise (Drift)

Aside from short-term noise, the system can also drift over long periods, this can be thought of as low-frequency noise. Low-frequency noise could be caused by changes in the temperature, but could also originate from the intrinsic drift in electronics. For applications of gravimetry, this low-frequency drift, or 1/f noise, is the most crucial type of noise to consider.

The voltage reference chip used in the readout (MAX6177) drifts by 50 ppm over 1000 hours, however, as the voltage reference drifts, the voltages over each of the resistors also change, and so the ratio between them should remain constant. After the reference, the only component that should drift is the ADC (the AD7195).

The AD7195 datasheet specifies two values for drift versus time. One has a coefficient of 10 ppm over 1000 hours, while the offset has a coefficient of 25 nV over 1000 hours. As these values are stated per 1000 hours, it would imply the measurement for these values showed a constant drift in one direction. This drift should, therefore, be able to be removed using regression methods. Since datasheets don't specify drift over the course of days and weeks, building a detailed long term noise model is almost impossible.

3.2.2.3 Temperature Sensitivity

So far, temperature sensitivities have been discussed at length. However, the assumption that the Pt100 resistors change by exactly $0.385\ \Omega\ \text{K}^{-1}$ has been used. Firstly, this coefficient has a tolerance of $\pm 8.5 \times 10^{-3}\ \Omega\ \text{K}^{-1}$ [103]. This tolerance could mean a difference of 212.5 mΩ (552 mK) at room temperature. Though this uncertainty is large, the coefficient should be constant, therefore it can be ignored as it is just an offset. For a Class B Pt100, the resistance R_{Pt100} at temperature T is seen in equation 3.10.

$$R_{\text{Pt100}} = R_0 \left(1 + \alpha_a T + \alpha_b T^2\right), \tag{3.10}$$

where R_0 is the resistance of the Pt100 at 0 °C, with a linear and second order polynomial thermal coefficient of $\alpha_a = 3.9083 \times 10^{-3}$ K^{-1}, and $\alpha_b = -5.7750 \times 10^{-7}$ K^{-2} respectively. For the range of 0 °C to 100 °C, this averages to the previously mentioned 0.385 Ω K^{-1}. However, more accurately, a change from 25 °C to 26 °C would be:

$$\begin{aligned} \Delta R_{\Delta T=1} &= R_0 \left(\alpha_a \left(T_{26} - T_{25} \right) + \alpha_b \left(T_{26} - T_{25} \right)^2 \right) \\ &= 100 \left(3.9083 \times 10^{-3} + -5.7750 \times 10^{-7} \right) \\ &= 0.3908 \ \Omega \ . \end{aligned} \tag{3.11a}$$

From equation 3.11a, it can be seen that the assumption of 0.385 Ω K^{-1} for a 1 K change would actually result in a difference of 0.0058 Ω. This resistance is the equivalent of a 15.1 mK error. Repeating this calculation for a few milliKelvin, equation 3.11a gives a change of 390.8 $\mu\Omega$. Taking the difference of this and the expected 385 $\mu\Omega$ change results in an error of 15 μK, well below the target error.

One of the assumptions made in calculating the temperature is that the value of the bias resistor remains constant. However, if there are changes to this value due to temperature, the measurement will also appear to change. This effect would be assumed to have been a real change in the Pt100, and would cause excess drift (the drift would occur as the system is being controlled based on the measured value of the Pt100). By rearranging equation 3.1, equation 3.12 can be obtained, which shows the relative error in the measured resistance.

$$\frac{\mathrm{d}R_{pt}}{R_{pt}} = \frac{\mathrm{d}R_{bias}}{R_{bias}} \ . \tag{3.12}$$

Combining equation 3.12 with equation 3.2 results in equation 3.13. This equation shows what relative error of the bias resistor is required for a given change in temperature of the Pt100.

$$\frac{\mathrm{d}R_{bias}}{R_{bias}} = \frac{0.385}{R_{pt}} \mathrm{d}T_{pt} \ , \tag{3.13}$$

where $\mathrm{d}T_{pt}$ is the equivalent change in temperature of the Pt100. For example, a relative error of 3.6 ppm is required of the bias resistor for a change in temperature of 1 mK of the Pt100. This calculation uses the value of $R_{pt} = 107$ Ω for the Pt100. If the temperature requirement meant that the Pt100 could vary up to 5 K, a relative error of 1.8 ppt on the bias resistor would be needed. Because milliKelvin control is required, a Vishay Ultra High Precision, Z-Foil resistor was chosen (Y070610K0000T9L). The resistor boasts a thermal coefficient of

± 50 ppb/K, between the range of 0 °C $\rightarrow$ 60 °C. A thermal coefficient of ± 50 ppb/K is the equivalent of ± 14 μK/K, far better than what was required.

The AD7195 datasheet specifies two thermal coefficients: an offset error of ± 5 nV/K and a gain error of ± 1 ppm/K. The effect of these errors can be shown using equations 3.14a and 3.14b. The given values result in an error of 39 μK/K and 278 μK/K for the offset and gain error respectively. The offset error is negligible, whereas the gain error could be significant over changes of a few Kelvin.

$$\mathrm{d}T_{\text{offset}} = \frac{\left(\left(\frac{\frac{R_{pt}}{R_b}V_{ref}+V_\sigma}{V_{ref}}\right)R_b - R_{pt}\right)}{0.385} \tag{3.14a}$$

$$\mathrm{d}T_{\text{gain}} = \frac{\sigma_{\text{gain}}}{\text{Gain}}\frac{R_{pt}}{0.385}, \tag{3.14b}$$

where R_{pt} and R_b are the resistances of the Pt100 and Bias resistor respectively, V_{ref} is the reference voltage, V_σ is the offset error, and $\mathrm{d}T$ is the temperature error.

3.2.3 Decimator

As discussed previously, a finite impulse response (FIR) filter was required to reduce the noise and data rate [101]. The filter utilised the DSP Engine Block described in section 2.3.1.1. The filter was designed to be a low-pass filter (to remove higher frequencies with a zero at $1/8^{\text{th}}$ of the sampling frequency). An FIR filter is so named, as the impulse response, or output, using a Dirac delta settles in a finite time. This settling behaviour is not the case for an infinite impulse response (IIR) filter [101], due to the feedback term. An example of the impulse response for an FIR and IIR filter can be seen in figure 3.4.

An FIR filter can be visualised as a series of delay stages, also known as 'Taps', with a multiplier from each of these stages connected to a summation stage (a "summer"). This description can be seen in figure 3.5. As the FIR filter is a digital system, time is discretised, meaning that it is not one continuous 'stream', but quantised moments for a particular sample. Each instance a new input is generated, the remaining values in the system move along one. The values are then multiplied by the coefficients for that stage, b_m (for $m = 1 \rightarrow n$), and

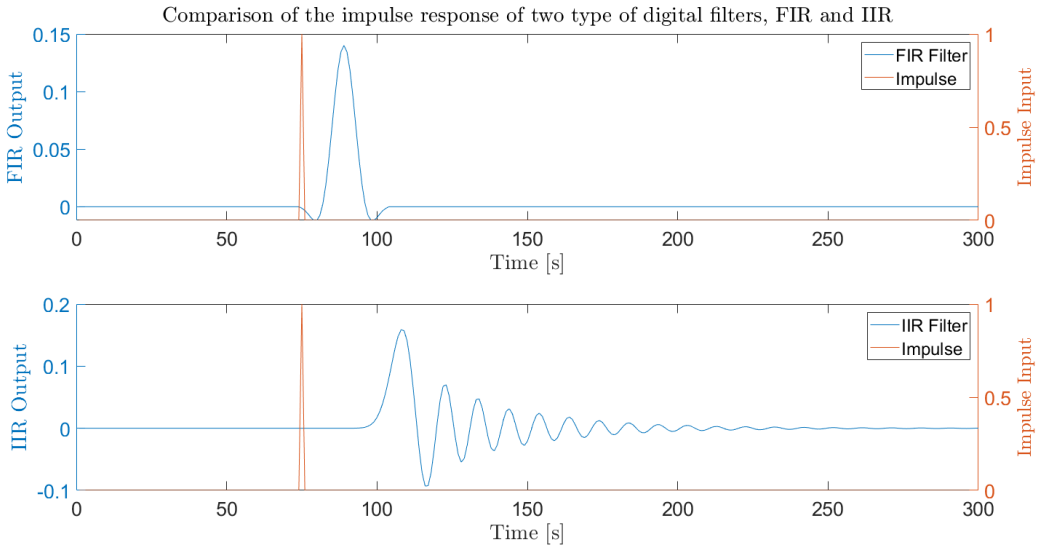

Fig. 3.4 Two graphs showing the impulse response for an FIR filter (top), and IIR filter (bottom). As there is no feedback, the FIR filter settles in a finite time, whereas the IIR filter oscillates with a decaying amplitude. This would technically continue indefinitely, but, after a certain time the oscillation would be small enough for a given application. Since the FIR filter has no feedback, and is the sum of a series of a finite number of inputs, the filter has to settle in a time given by the filter length and sampling rate.

Input	Filter 1 $[\frac{1}{2}\ \frac{1}{2}]$ Low Pass	Filter 2 $[\frac{1}{2}\ -\frac{1}{2}]$ High Pass
DC [1 1]	1	0
Nyquist $[1\ -1]$	0	1

Table 3.4 A table of the two simplest FIR filters and the resulting outputs for the inputs at a frequency at DC ($f = 0$) and Nyquist ($f_n = F_s/2$). Filter one is a low-pass filter (as it attenuates higher frequencies) whereas filter 2 is a high-pass filter (attenuates low frequencies).

summed. This multiplication is then repeated for each new value. The output y, is given by the transfer function $H(z)$, of the filter and the inputs x, as seen in equation 3.15a.

$$y = H(\mathrm{z})\, x \tag{3.15a}$$

$$y = \left(b_1 + b_2\, z^{-1} + b_3\, z^{-2} + \mathbf{...} + b_n\, z^{1-n}\right) x\,. \tag{3.15b}$$

As an example, two of the simplest FIR filters are those with the coefficients $[\frac{1}{2}\ \frac{1}{2}]$, and $[\frac{1}{2}\ -\frac{1}{2}]$. To understand these filters one must consider a series of inputs of two different frequencies, the first being DC, i.e. input values of [1 1], and the second being at the Nyquist frequency, i.e. input values of $[1\ -1]$. The FIR filter with coefficients $[\frac{1}{2}\ \frac{1}{2}]$ would output 1 for DC while outputting 0 for the Nyquist frequency, i.e. it attenuates the Nyquist frequency and lets DC through: a low pass filter (simple average). For the filter with coefficients $[\frac{1}{2}\ -\frac{1}{2}]$, the outputs would be the opposite, zero output for DC, and 1 for Nyquist, i.e. a high-pass filter. These are summarised in table 3.4.

The disadvantage of an FIR filter is that, for strong attenuations, they can require a large number of "taps", and therefore more memory and multiplications (computational power). For devices with low processing power, the system can struggle to process an FIR filter, and so an IIR filter would be preferable. The dsPIC, however, has a specialised DSP engine block, allowing it to efficiently compute an FIR filter.

The filter coefficients were generated for a low-pass filter with a zero at $\frac{1}{8}^{\text{th}}$ of the sampling frequency, allowing downsampling (or decimation) by a factor of four (without aliasing). The filter coefficients chosen are seen in appendix E, with the corresponding impulse response on the top graph of figure 3.4. Figure 3.6 shows the impulse response of the coefficients used in the dsPIC, as well as the transfer function of the filter. The lower graph shows a strong attenuation of more than -60 dB ($= 1 \times 10^{-3}$) for frequencies above $\frac{1}{8}^{\text{th}}$ of

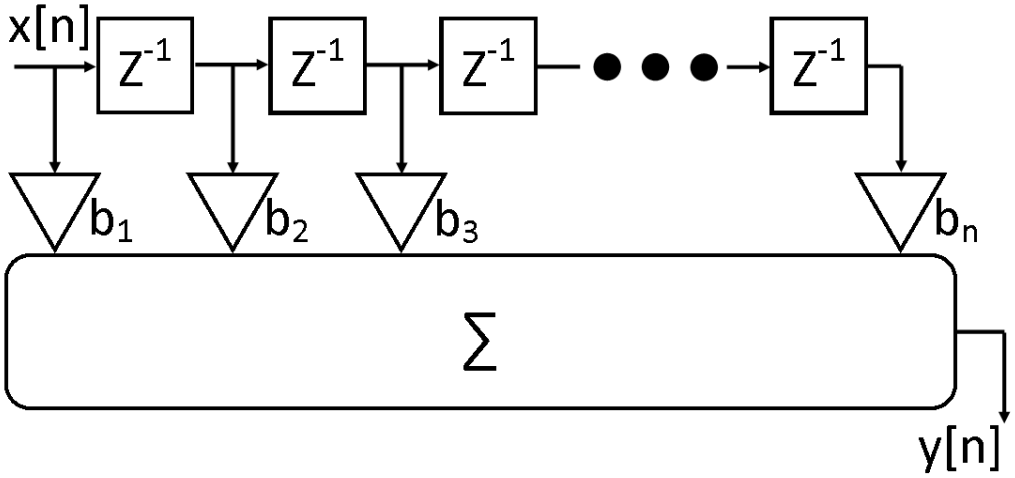

Fig. 3.5 A flow diagram showing how a digital FIR filter functions. The inputs, $x[n]$, pass into a delayed tap stage. The values at each stage are multiplied by the coefficients, b_m, and summed together. For the next discrete sample, each input moves to the next stage, and the new input is inserted. These new stages are then multiplied by the coefficients again, and summed to form the output $y[n]$.

the sampling frequency. The coefficients are padded with zeros at the end to have a total length of 32 (2^5) as the filter has to be of this length for the dsPIC to accept the coefficients.

White noise can be generated using MATLAB, and inserted through an FIR filter with the same coefficients used in the dsPIC. Figure 3.7 shows the simulated noise for the AD7195 at a data rate of 25 Hz after three decimation stages. Three decimation stages result in the downsampling of the data rate to $F_s = \frac{25}{4^3} = 0.39$ Hz. The RMS of the temperature variations can be calculated using the equation:

$$T_{\text{rms}} = \sqrt{\frac{1}{n}\sum_{i=1}^{n}(T_i - T_{\text{mean}})^2}\,, \tag{3.16}$$

where T_{rms} is the RMS noise of the temperature for n data points, T_i is the i^{th} temperature data point and T_{mean} is the mean temperature. Table 3.5 shows the RMS noise in μK of the undecimated and decimated data, calculated using equation 3.16. It is clear from the table that a higher gain results in a lower RMS noise. The table also displays the reduced noise after three stages of decimation which also clearly shows that decimation reduces the RMS

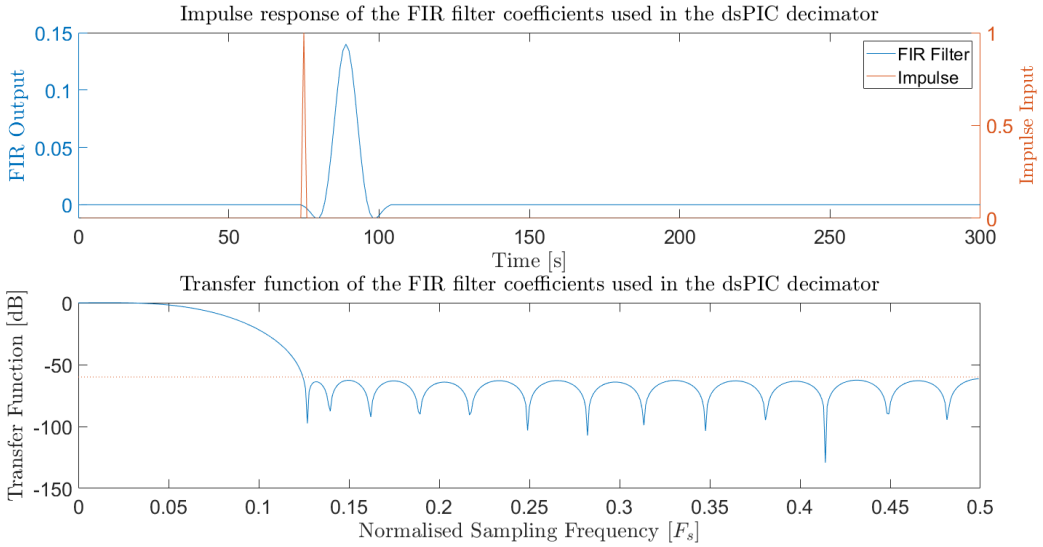

Fig. 3.6 Graph of the impulse response and the transfer function of the filter used in the dsPIC's decimator. It can be seen that the low pass filter is designed to remove frequencies above 0.125 of the sampling frequency. After downsampling by a factor of four, this filter design prevents any aliasing as frequencies above the new Nyquist frequency are attenuated.

noise in the system (as well as the data rate). The last column on the table displays the ratio of the two RMS values. It shows that the noise is reduced by a factor of almost 10. It also implies that decimating higher gains results in a more significant reduction of noise.

Table 3.6 shows the ratio of the RMS noise values from table 3.5 in relation to the value at a gain of 1. The values in table 3.6 show the same trend as observed in table 3.5, that is, increasing gain results in a lower noise, with an even larger reduction for the decimated data.

3.3 Performance

During initial testing of the AD7195 setup, it became clear that there had been an error in the initial schematic. Though everything in the system seemed to measure accordingly, it was noticed that the polarity of the input and reference were the wrong way around. This meant that, during DC measurements, the input was the opposite sign than expected: posing a particular problem for the reference input, as the input cannot be negative. Since the AD7195 knows that the logic will reverse the polarity, it takes this into account. However, if the reference is then connected in reverse to begin with, the system will always be measuring the wrong polarity and not work. The error was found to be the routing of the logic from the

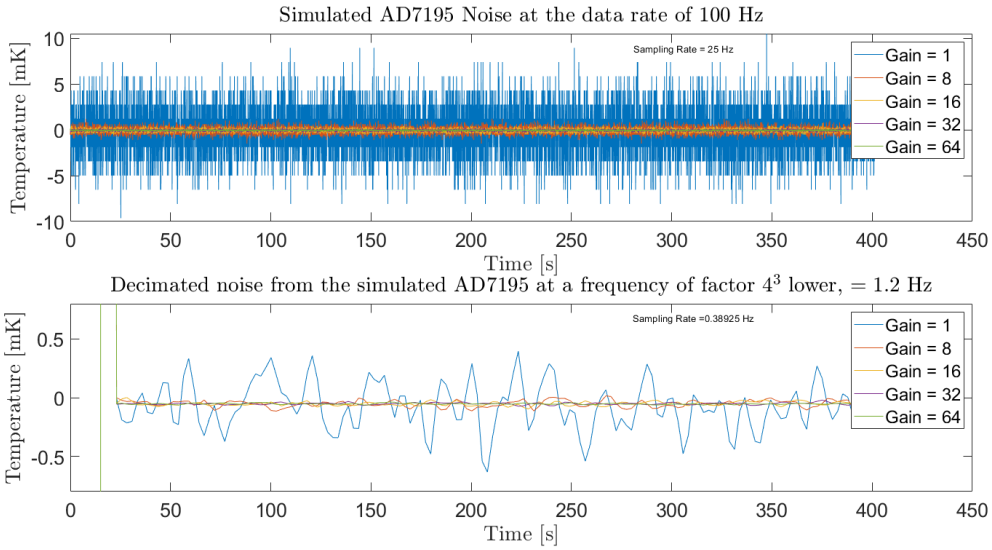

Fig. 3.7 Graphs showing the simulated noise of the AD7195 both before (top pane) and after (bottom pane) three decimation stages. This decimation results in a reduction of the sampling frequency from 25 Hz, to 0.39 Hz (a factor of 4^3). A clear reduction in RMS noise can be observed.

Gain	Undecimated RMS Noise [μK]	Decimated RMS Noise [μK]	Ratio of RMS Noise
1	2545	261	9.76
8	359	30	11.8
16	181	17	10.6
32	95	7.4	12.8
64	59	4.5	13.1

Table 3.5 A table of the undecimated and decimated noise after three stages (a data rate reduction of $4^3 = 64$). It shows a definite reduction in noise for all values of the gain, yet a stronger attenuation of noise at higher gains.

Gain	Ratio of Undecimated RMS Noise (Gain=1/Gain)	Ratio of Decimated RMS Noise (Gain=1/Gain)
1	1	1
8	7.1	8.6
16	14	15.2
32	26.7	35
64	43.3	58

Table 3.6 A table of the ratios of the RMS noise at the current quoted gain, relative to a PGA of 1, for both the decimated and undecimated data. It shows, again, that the noise of the decimated data is reduced more as gain increases.

AD7195 to the MOSFET gates. The tracks for the logic were wired to the wrong MOSFET (of the same type). This meant that the gate of one MOSFET had to be manually connected to the logic that was initially going to the other MOSFET gate. As a consequence, this process had to be done for all three sets of BS170s and BS250s. Though somewhat unsightly, this change proved successful, and the AD7195 began to values that were valid. The correct connections can be seen in figure 3.8.

The AD7195, like most digital integrated circuits, contains arrays of memory that dictate the settings of the device. For example, the AD7195 has nineteen 8-bit arrays, known as registers. They are split up as follows: communications (8-bit), status (8-bit), mode (24-bit), configuration (24-bit), data (24-bit), ID (8-bit), GPOCON (8-bit), offset (24-bit), and full scale (24-bit). Another example is that of the configuration registry, which has bits that allow the user to set: if chopping is enabled, if AC excitation is active, which channel inputs are to be used for data conversion, and the value of the gain. The mode register contains 10 bits, referred to as FS9, to FS0 (equivalent to the first 10 bits of the register, MR9 to MR0). These 10 bits allow the output data rate to be selected using equation 3.17.

$$\text{Output Data Rate} = \frac{\text{MLCK}}{1024}\frac{1}{N\,\text{FS}}\,, \tag{3.17}$$

where MLCK is the frequency of the master clock (≈ 4.92 MHz), N is the order of the sinc filter, and FS is the value of the 10 bit register in decimal. As an example, using the sin^4 filter ($N = 4$), with the values $FS = 1$, 49 or 1023, an output data rate of 1.22 kHz, 25 Hz and 1.2 Hz would be obtained.

The system was programmed with an FS of 49 (in decimal). An FS of this value is the equivalent of 25 Hz when using the sinc^4 filter, or 0.39 Hz, after three stages of the decimation filter. It was immediately evident that the levels of noise on the AD7195 output

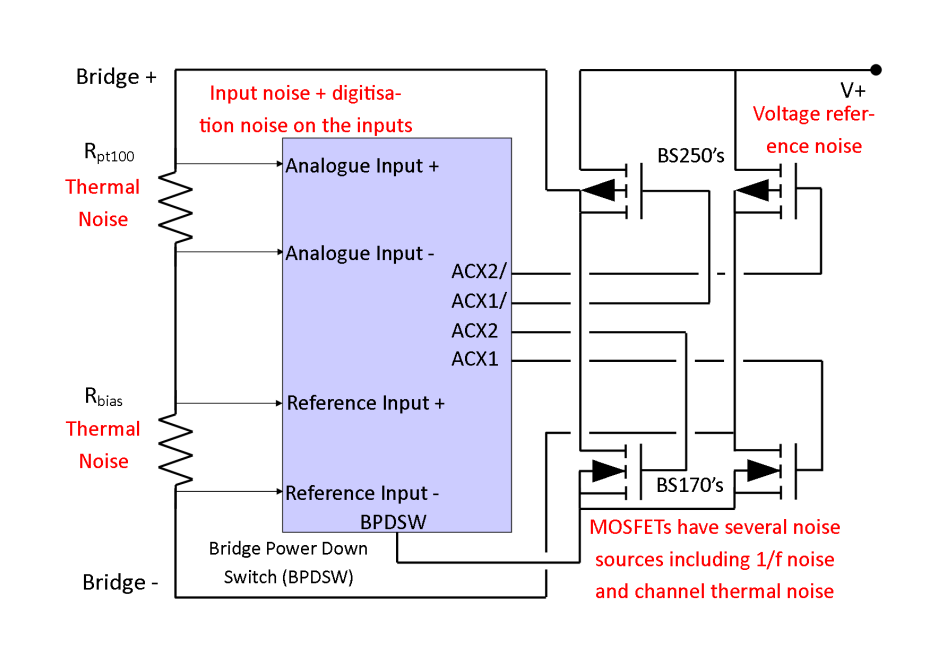

Fig. 3.8 A circuit diagram showing the full schematic for the AD7195, with corrected connections from the logic outputs, to the gates of the MOSFETs. Originally, the system had the logic going to the wrong gate of the same MOSFET type, resulting in the wrong polarity of bridge.

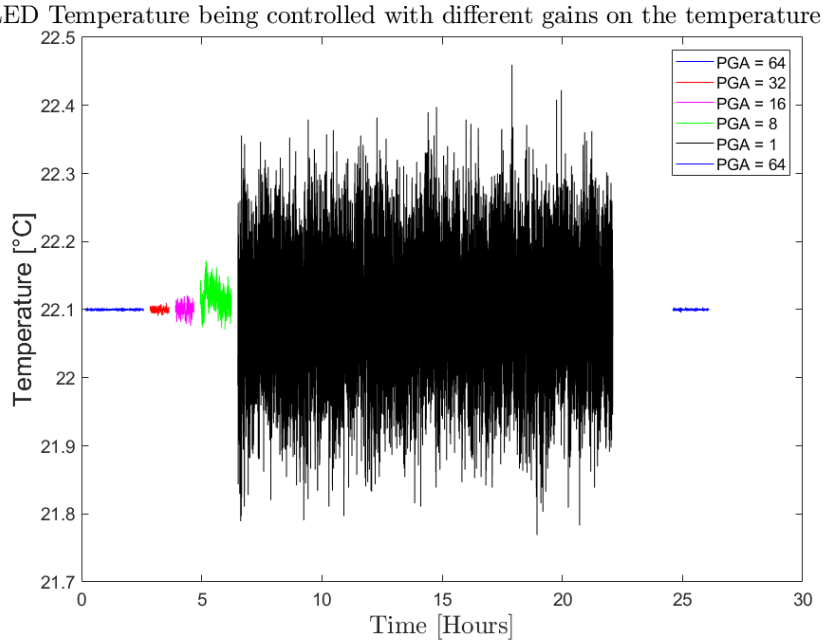

Fig. 3.9 A graph showing the measured noise in the AD7195 when running at 25 Hz (FS = 49). The noise is considerably higher than the theoretical values estimated previously by a factor of 16 to 32. An RMS noise of 0.96 mK, 3 mK, 8 mK, 16.6 mK and 83.6 mK for gains of 64, 32, 16, 8 and 1 respectively, was measured.

were much higher than previously estimated. The decimated data shown in figure 3.9 shows an RMS noise level of 0.96 mK at a gain of 64, and 83.6 mK at a gain of 1. This noise is a factor of 16.94 higher at a gain of 64 (32.84 at a gain of 1) than what was estimated in figure 3.3. The noise in the system, however, still reduces with increasing gain, implying that the input noise is the limit. The source of this discrepancy was never found, yet could have been due to the fundamental circuit design. There could be pick-up between tracks, generating increased noise levels on the inputs of the AD7195, as well as pick-up from the environment. During testing, many of the capacitor positions that were on the board were not used that could have potentially resulted in a noise-reduction. These positions were mainly grounding/decoupling capacitors. These explanations still indicate that the noise is external, but the fact that the noise is reduced on increasing the PGA would suggest that it is internal noise at low gains.

Of the entire system, the three temperatures that were considered the most necessary to control were those of the thermal shield (a shaped sheet of copper to isolate the outside environment and the silica mount), the LED, and the MEMS (which is also the approximate

temperature of the photodiodes). The control loops needed to be tuned and this was carried out using the Ziegler-Nichols tuning method [6]. Table 3.7 shows the PID coefficients that were obtained for each of the positions. Figure 3.10 shows the settling of this PID. The temperature took approximately 800s to settle while overshooting by 120 mK, despite the fact that it started only a few 10s of mK from the set point. Figure 3.11 shows the performance of the PID once it settles. It can be seen that the temperatures only vary by approximately ± 2 mK once settled. Allan deviation is a technique that is commonly used to compare the noise performance of measurements. Allan deviation averages a set of data to a series of increasing time constants and shows the RMS noise of that data set, if the sampling frequency was set at that time constant [104]. In this thesis, a similar technique is used as a means of comparing the noise performance of the device by calculating an RMS directly from the amplitude spectral density assuming that all amplitudes above the set bandwidth are removed. This assumption therefore means that the values presented in this thesis of RMS are for an ideal case using an ideal low-pass filter. Further, Allan deviation is typically shown on a graph in a log log plot with time on the x-axis whereas, the RMS throughout this Thesis have frequency on the x-axis. Figure 3.12 shows the amplitude spectral density and sensitivity of the settled data, showing an amplitude spectral density of 390 μK/$\sqrt{\text{Hz}}$ at 10 s, or an RMS of 39 μK. It is worth noting that the shape of the signal from the controlled system looks periodic, as seen in the ASD of the data: there are peaks at specific frequencies. These peaks could be the result of pick-up, or the interaction between PID systems. If only one temperature is being controlled, the periodic oscillation, seen in figure 3.11, smooths out and disappears. It was also noted that the amplitude of these oscillations also varied from week to week, potentially being explained by the cables being closer some of the time or different types of wires being used as the experiment is changed.

Position	K_p	K_i	K_d
Shield	90	40	10
LED	6	40	10
MEMS	6	40	10

Table 3.7 A table of the PID coefficients used in the system to control temperatures in the system. These were obtained using the Ziegler-Nichols tuning method.

Figure 3.13 shows the variations in temperature over almost 33 hours whilst using the PID controller. Though temperature variations are above 1 milliKelvin, they are still within acceptable levels, as the RMS noise level is less than 1 milliKelvin (except for the shield). Table 3.8 shows the RMS noise for each of the temperatures. It is clear that the shield, which

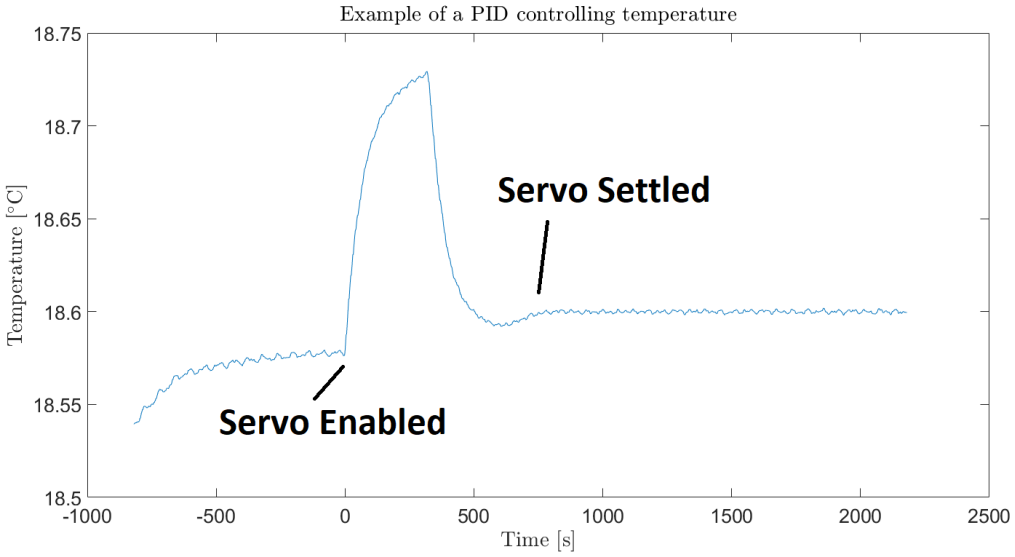

Fig. 3.10 A graph of the inner shield temperature settling after turning on the PID control system. It took approximately 800s to reach this setpoint, while overshooting by approximately 120 mK.

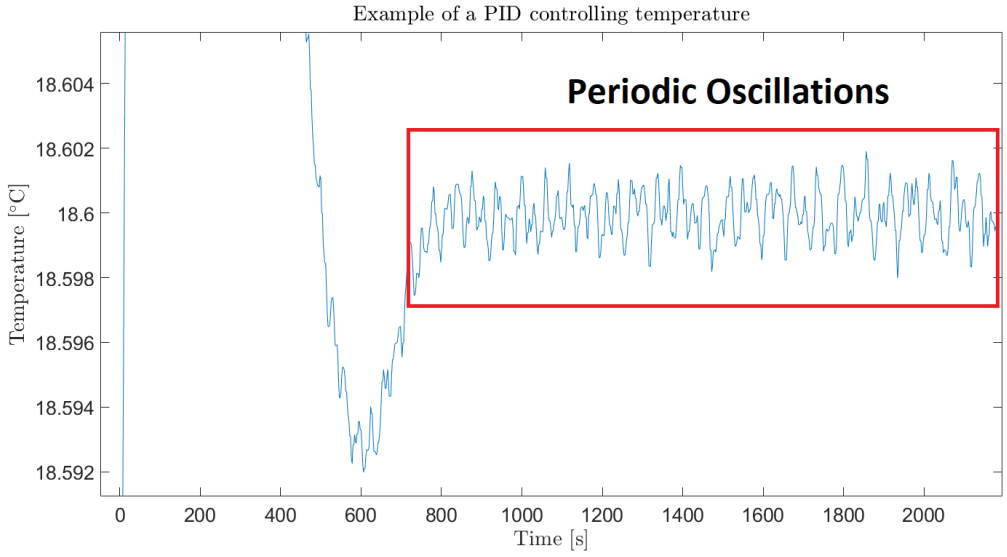

Fig. 3.11 Graph of the settled PID data. It shows maximum variations of ± 2 mK over the 10 minute period.

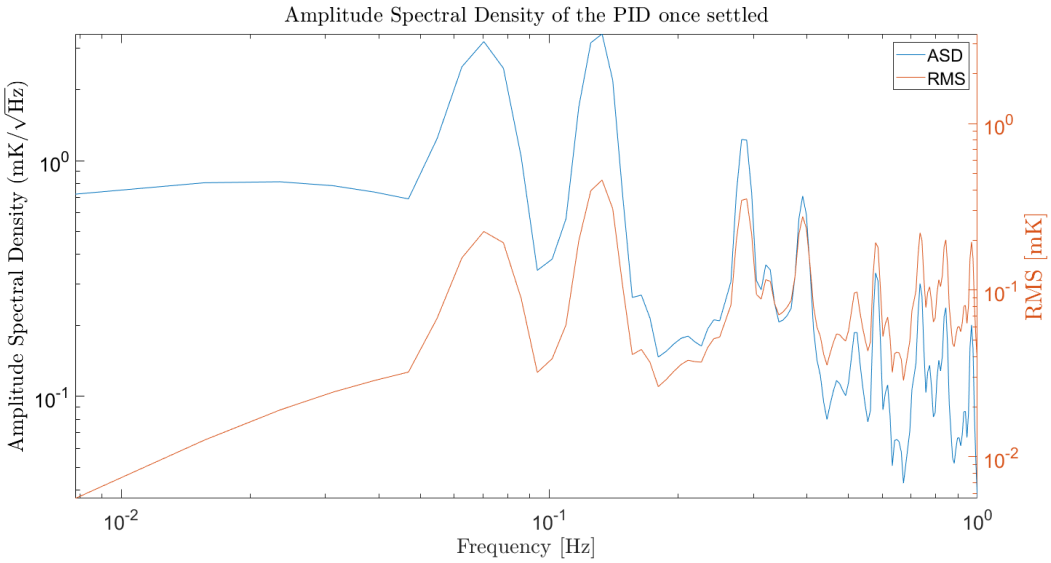

Fig. 3.12 Graph of an amplitude spectral density of the settled PID data. It can be seen that the device has an RMS sensitivity of 39 μK at 10 s.

Position	RMS Noise [mK]
Shield	1.9
LED	0.93
MEMS	0.75

Table 3.8 The resulting thermal RMS noise when implementing the PID controller on three positions in the system. The shield is controlled within a few mK RMS, whereas the other two positions are less than 1 mK RMS.

is closest to the outside, was the hardest to control, with a noise that was approximately twice as large as the other two temperatures. Note that the levels of noise for the LED and MEMS are close to the previous measurement which looked at the effect of PGA on the noise.

The amplitude spectral densities of the three temperatures can be seen in figure 3.14. It shows an amplitude spectral density of 0.74 mK/$\sqrt{\text{Hz}}$, 1.9 mK/$\sqrt{\text{Hz}}$ and 1.1 mK/$\sqrt{\text{Hz}}$, for the MEMS, Shield, and LED respectively. If averaged to 100s, a sensitivity of 74 μK, 190 μK and 110 μK could be obtained. Note, by averaging further, the temperature sensors noise would reduce and perhaps result in a better thermal control.

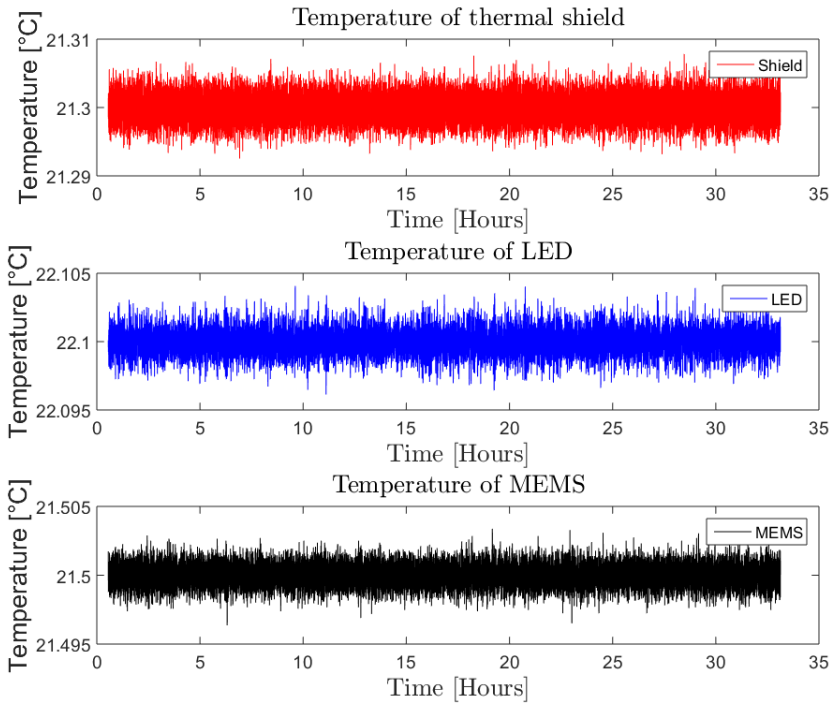

Fig. 3.13 Graphs showing the three temperatures in the system, the shield, the LED, and the MEMS. The temperatures can be seen to be controlled with an RMS noise of 1.9 mK, 0.93 mK and 0.75 mK, respectively. The control on the shield is poorer than the others, likely due to it being closer in proximity to outside variations in temperature.

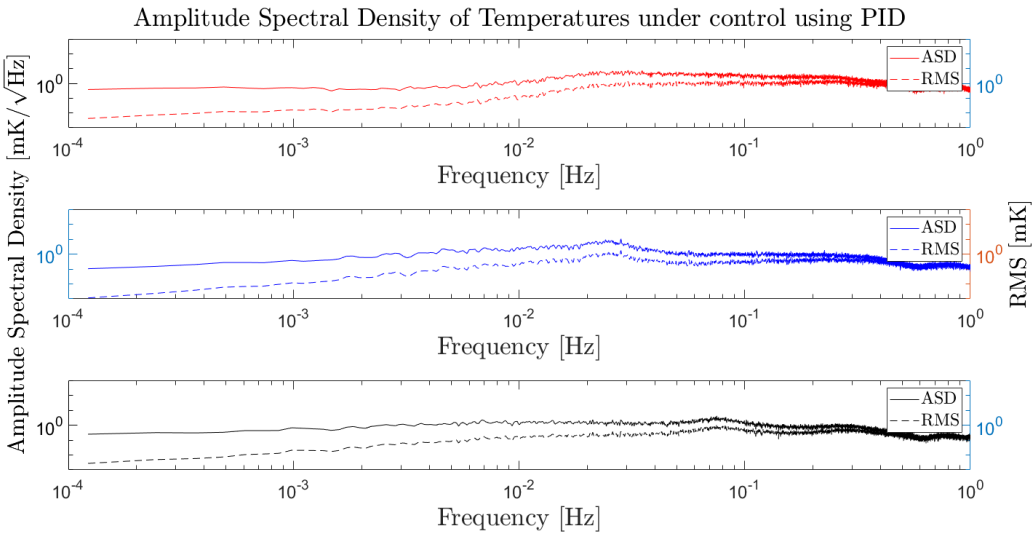

Fig. 3.14 Graph showing the amplitude spectral density and corresponding RMS for the three temperatures presented in figure 3.13. It shows an ASD of 0.74 mK/$\sqrt{\text{Hz}}$, 1.9 mK/$\sqrt{\text{Hz}}$ and 1.1 mK/$\sqrt{\text{Hz}}$, for the MEMS, Shield, and LED respectively. If the data was averaged to 100s, a sensitivity of 74 μK, 190 μK and 110 μK could be obtained.

3.4 Conclusion

To summarise, a low-cost, portable, temperature sensor and control was required to obtain the target sensitivity and allow the system to be taken out of the lab. Ideally the system required sub-milliKelvin control to obtain the target sensitivity of tens of μGal (the previous MEMS had a thermal sensitivity up to 25 μGal mK^{-1}). Here, using low-cost electronic components, it has been shown that temperatures can be controlled to within 0.7 mK to 2 mK. To obtain this level of control, three AD7195s were used, each to measure a temperature sensitive resistor (a Pt100). Once the value of temperatures were sampled and calculated, the system used a PID control loop to output a signal from a DAC. This voltage was then buffered and used to drive current through a resistor. It can also be seen that the PID that settled in approximately 800 s to the milliKelvin level. This settling occured while all three temperatures were under PID control. A necessary component in the system was the decimator, which lowered the sampling frequency of the data while reducing the noise. It utilised a low-pass FIR filter with a cut-off frequency at $\frac{1}{8}^{\text{th}}$ of the Nyquist frequency. This filter allowed the data to be downsampled by a factor of four while avoiding aliasing.

Chapter 4

Lock-in Amplifier

As previously mentioned, to obtain a value for the relative changes in the local acceleration of gravity, the relative displacement of the MEMS must be measured. The displacement measurement utilises the shadow sensor technique which is often implemented within the Gravitational Wave community, such as Advanced LIGO (aLIGO) [86], and its use has been suggested for a third generation of differential optical shadow sensors (DOSS) within the Laser Interferometer Space Antenna (LISA) collaboration [105] *. To further improve the performance of the displacement measurement, the shadow sensor was combined with the lock-in amplification technique. The LED is modulated at a known frequency, and the resulting variations in current from the photodiodes are demodulated to produce a DC signal proportional to the displacement of the proof mass. The modulation and demodulation allows for low-frequency noise and drift to be eliminated (or at least reduced). This chapter will discuss the shadow sensor and digital lock-in amplifier and compare the final performance to that of the expected noise model of the system. A displacement measurement will require a sensitivity of approximately one nanometre to obtain an acceleration sensitivity in the order of tens of μGal.

4.1 Shadow Sensor

A shadow sensor [106–109] relates to an experimental technique used to measure displacements by amplifying the difference in light (or shadow) over two photodiodes. A light source (in this case, an off-the-shelf LED) illuminates a mass on a spring system (the MEMS proof

*aLIGO uses the shadow sensor to monitor the vibrations of 600 mm long, and 400 μm wide silica fibres, which are used to suspend the interferometer mirrors. LISA uses a three dimensional shadow sensor to monitor the position of a test mass relative to the satellite. The position is then used in the drag-free feedback control loop.

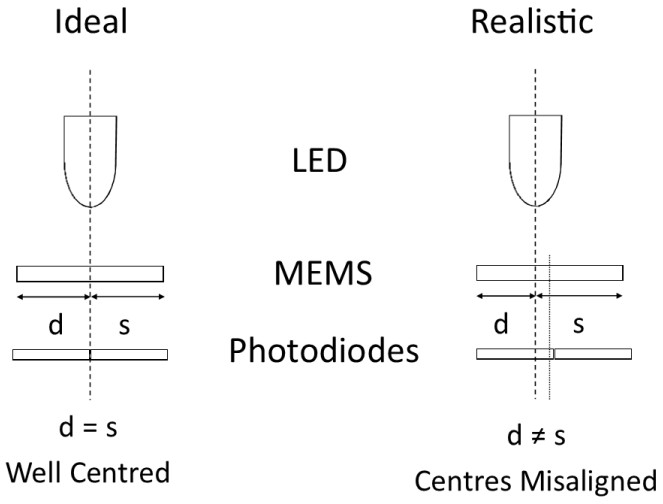

Fig. 4.1 A diagram depicting the comparison between the ideal set-up for a shadow sensor and the more realistic version. In reality, the centres of all components will be misaligned with each other. When the MEMS is then inserted into the system, it will have to be placed more on the side with a larger illumination (the side with the LED centre-line). The MEMS has to be placed on this side to attempt to achieve a signal closer to zero (by compensating for the excess light).

mass), creating a moving shadow behind it. This shadow is cast onto two photodiodes set up in a configuration that measures the difference in current from each diode. This difference in current is obtained by connecting one photodiode anode to another's cathode, and vice versa. By measuring the difference in current, rather than amplifying both phototdiodes individually, allows for larger gains during conversion to a voltage. A large gain on separate photodiode currents would result in the output being saturated, the term used when the output voltage reaches the supply voltage, and thus would limit the gain. Larger gains then allow for higher sensitivities, i.e. more volts per metre but would be a compromise on the dynamic range.

If the shadow was precisely in the middle of the photodiodes (with a perfectly symmetric intensity distribution), the photodiodes would have zero output, and therefore, it would be theoretically possible to amplify them by an infinite amount. However, being perfectly centred is not practical as there will always be a degree of misalignment between both, the LED and the photodiodes, and the LED to the MEMS. Figure 4.1 shows an example of how the system will likely be misaligned.

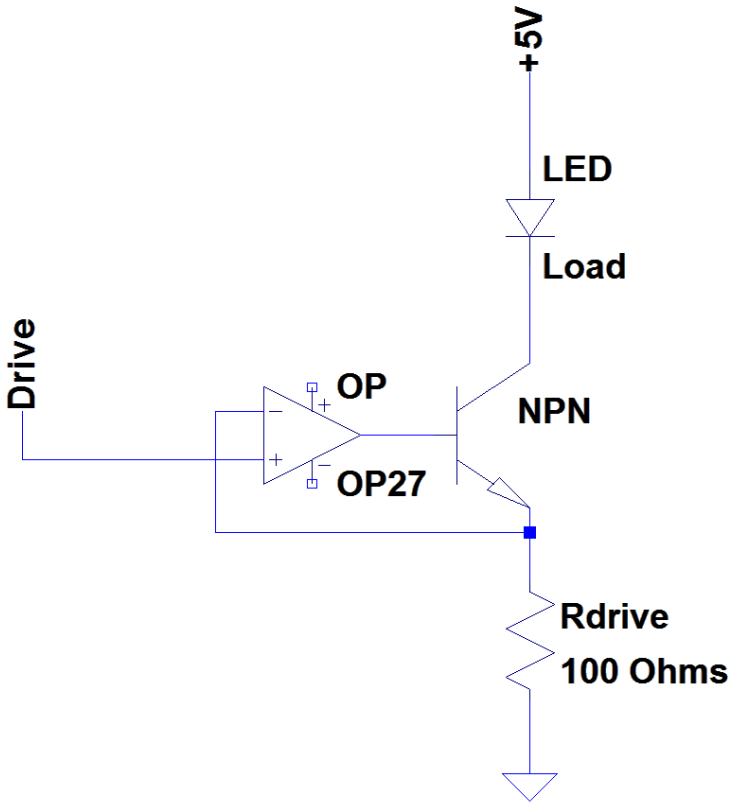

Fig. 4.2 A schematic of the circuit used to produce a stable current source. The drive voltage combined with the op amp ensures that the voltage across R_{drive} is fixed, and therefore, the current through it is also fixed. This is done by the op amp changing its output resulting in the conductance of the MOSFET also changing. The change in conductance always ensures the current through the resistor is the same, and therefore, the LED.

4.1.1 Drive and Readout

As the system uses the lock-in technique a modulated drive signal is required. The modulation is created using a current source (seen in figure 4.2) as opposed to a voltage source. A voltage source is where a voltage is attached directly to the LED through a resistor, as had been done previously by R. P. Middlemiss et al [83]. A current source was chosen as it was thought that changes in the LED impedance would alter the current passing through it, and therefore the light output of the LED. These changes would then be seen in the final signal as excess noise or drift in the displacement. In an attempt to remove this effect, the current source regulates the conductance of the MOSFET (as seen in figure 4.2) to ensure the current through the LED matches the drive voltage divided by the resistance of the resistor labelled R_{drive}.

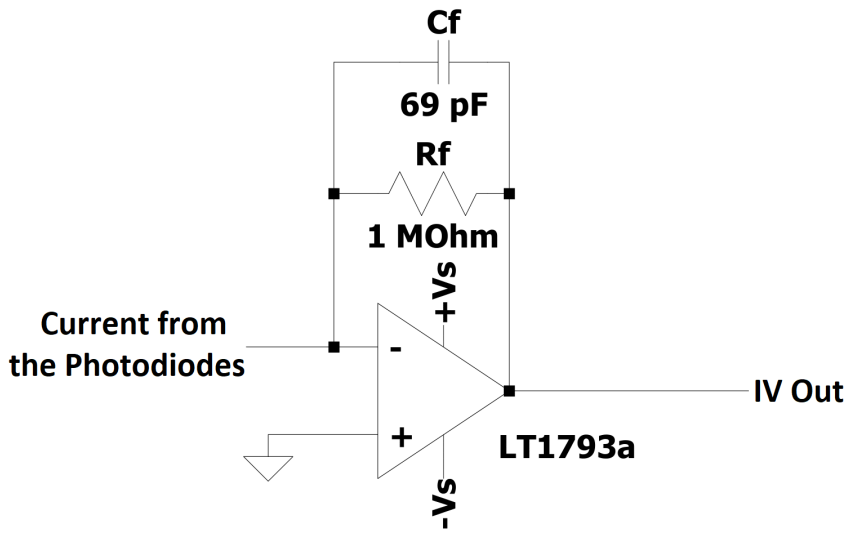

Fig. 4.3 A circuit diagram of the transimpedance amplifier used to convert the current from the split-photodiodes to a voltage. The values of the feedback components chosen were 69 pF and 1 MΩ which has a -3 dB cut-off at ≈ 2.3 kHz.

As with the system demonstrated by R. P. Middlemiss et al [1, 83]., a current-to-voltage amplifier is required to convert the current from the photodiodes to a voltage, which can then digitised. Previously, an off-the-shelf, Stanford Research Systems, SR570 current-to-voltage converter was used. As this device is significantly bulky, it was deemed necessary to replace it when creating the custom electronics board. A simple transimpedance amplifier was designed, with a feedback of $R = 1$ MΩ, and $C = 69$ pF. With the values of the feedback components: the cut-off frequency (-3dB) of $f_c \approx 2.3$ kHz is obtained. Figure 4.3 shows the transimpedance amplifier that was used to convert the current from the split-photodiode to a voltage. Despite the fact that the system modulates the LED at much lower than 2.3 kHz (The modulation frequency is approximately 120 Hz to 160 Hz), a cut-off this high was necessary due to the output from the DAC being similar to that of a square wave. If the cut-off frequency was not sufficiently large enough, the higher frequency components that are required to produce a square wave would also be attenuated. The attenuation of the high frequency components in a square-wave results in rounding of the waveform. This process will be expanded on further in the chapter.

Though initially the plan was to sample after the current-to-voltage converter, it became apparent that this would not be possible. The ADC, a Texas Instruments ASD1248 would not accept input voltages that are negative (relative to analogue ground). Therefore, it was deemed that a pseudo differential measurement was required. A pseudo differential measurement is achieved by summing a bias voltage onto the signal before sampling. This summed voltage is then connected to the positive input terminal, whereas, the negative input terminal is connected to the bias voltage only. This configuration results in the sample being equal to the difference between each terminal. Figure 4.4 displays the circuit required for the pseudo differential measurement as just described. U3 in the diagram was an INA105, precision unity gain differential amplifier which already contains four 25 kΩ resistor. The package (U3) was used as a summing amplifier which allows multiple voltages to be summed together with a positive gain, i.e. a non-inverting summing amplifier. The set-up can be modelled by considering one of the input voltages as grounded and then considering the resistor bridge that forms from this. It can be seen from this model that, the voltage at the positive terminal of the op amp would be equal to $V_+ = V_1 \frac{R_2}{R_1+R_2}$ when $V_2 = 0$. If $V_1 = 0$ is used, $V_+ = V_2 \frac{R_1}{R_1+R_2}$. If these two expressions are combined by considering non-zero input voltages, the expression $V_+ = V_1 \frac{R_1}{R_1+R_2} + V_2 \frac{R_2}{R_1+R_2}$ is obtained. Using the ideal op amp assumption that zero current flows into the inputs, i.e. $V_+ = V_-$, the relationship, $V_1 \frac{R_1}{R_1+R_2} + V_2 \frac{R_2}{R_1+R_2} = V_{out} \frac{R_{f1}}{R_{f1}+R_{f2}}$ is obtained. This can be rearranged to obtain equation 4.1.

$$V_{out} = \left(1 + \frac{R_{f2}}{R_{f1}}\right) \left[V_1 \frac{R_2}{R_1+R_2} + V_2 \frac{R_1}{R_1+R_2}\right] . \tag{4.1}$$

Equation 4.1 can be simplified by setting all resistances to an equal value. This gives $V_{out} = V_1 + V_2$, i.e. a non-inverting summing amplifier with unity gain. The buffers were achieved using a TL084 [110], quad package general purpose JFET operational amplifier.

The voltage is then sampled by the ADS1248 at rates up to 2 kHz. This ADC also contained a Programmable Gain Amplifier (PGA). The ADC was initially tested for the use of temperature sensing due to its ability to use an external reference. As with the AD7195, the ADS1248 is a $\Delta - \Sigma$ analogue-to-digital converter.

4.2 Digital Lock-in Amplifier

Lock-In Amplification is a powerful technique used to extract signals from noise [87]. These measurements are known as phase-sensitive since the output is sensitive to the phase difference between the reference and the signal. Lock-in amplifiers typically modulate a

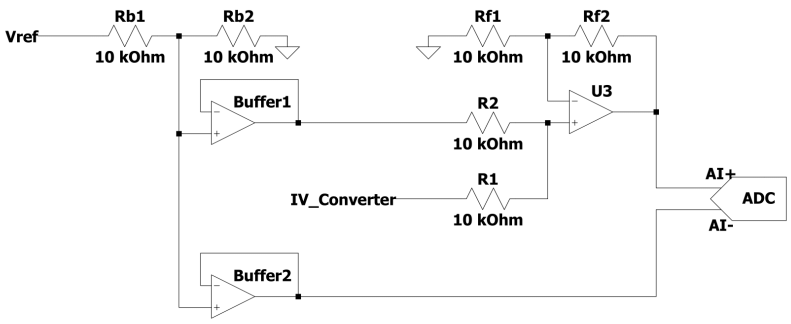

Fig. 4.4 A diagram of the circuit used to create a buffered bias voltage and sum the bias voltage and signal. This bias voltage is used to create a pseudo differential input for the ADS1248 as the inputs cannot be below analogue ground. The first stage in the circuit is a resistor bridge with equal valued resistors such that the voltage in the into buffer 1 is equal to half of the voltage reference. This voltage is then buffered using two unity gain amplifiers. One of the buffered voltages is directly connected to the negative input terminal, while, the other voltage is summed onto the signal from the current-to-voltage converter before being connected to the positive input terminal.

signal using a sinusoidal function. For this experiment, the LED is modulated, meaning it becomes brighter and then dimmer at a chosen reference frequency. If a signal of amplitude V_s, being modulated at a frequency of f_M is considered, then the modulated signal would appear in the form seen in equation 4.2.

$$V_M = V_s \cos(2\pi f_M t + \psi) \,, \tag{4.2}$$

where V_M is modulated signal at time (t) with a phase difference of (ψ) relative to the reference frequency. To demodulate, a lock-in amplifier then multiplies the input signal (V_M) by the reference signal, here equal to $V_r = \cos(2\pi f_M t)$. Removing any DC component is preferred before demodulation occurs. To understand why the DC component should be removed, first consider the demodulation of the equation 4.2, by multiplying by the reference frequency as seen in equation 4.3.

$$V_d = V_M V_r = V_s \cos(2\pi f_M t + \psi) \cos(2\pi f_d t) \tag{4.3a}$$

$$\equiv \frac{1}{2} V_s \left(\cos(2\pi t(f_M + f_d) + \psi) + \cos(2\pi t(f_M - f_d) + \psi)\right) \,. \tag{4.3b}$$

The demodulation process is effectively frequency beating, which results in a low frequency and high-frequency term. If the modulation frequency matches the demodulation frequency, i.e. $f_M = f_d$, the low frequency term becomes DC (i.e. $f = 0$ Hz), while, the higher frequency term becomes $f = 2\,f_M$. If the there was still a DC component before demodulation, i.e. $V_M = V_s \cos(2\pi\, f_M\, t + \psi) + V_o$, then, when multiplied by the reference frequency, an extra term arises equal to $V_o \cos(2\pi\, f_M\, t)$. This extra term appears as an oscillation with the same frequency as the modulation frequency. Another important reason to remove the DC component is that the measurement could begin to saturate, limiting the gain, and therefore, sensitivity of the system. The higher frequency term ($\cos(2\pi\, t(f_M + f_d) + \psi)$) can be filtered using a low pass filter, with a notch at the modulation frequency. A notch at the frequency f removes the f and $2f$ components. Once filtered, equation 4.4 is obtained.

$$V_{ip} = \frac{1}{2} V_s \cos(\psi) : \text{In-Phase.} \tag{4.4}$$

Note that the equation shows, as the phase delay changes, the output also changes. The equation, however, only shows the term for the in-phase component of the signal. The quadrature component of the signal is obtained by demodulating using the equation $\cos(2\pi\, f_d\, t + \frac{\pi}{2})$. The quadrature component can be seen in equation 4.5.

$$V_{oop} = \frac{1}{2} V_s \sin(\psi) : \text{Quadrature.} \tag{4.5}$$

The in-phase component is typically referred to as X, and the quadrature as Y. The magnitude, R, can be obtained by adding in quadrature as seen in equation 4.6.

$$R = \sqrt{X^2 + Y^2} = \frac{1}{2} V_s \sqrt{\cos^2(\psi) + \sin^2(\psi)} \tag{4.6a}$$

$$R = \frac{1}{2} V_s\,. \tag{4.6b}$$

The reason this technique is such a powerful method of extracting signals from noise is due to what it accomplishes in the frequency domain. The signal, with amplitudes in the frequency domain, are all shifted by both $-f_M$, and $+f_M$. For example, a frequency of 0 Hz becomes the modulation frequency after demodulation. A low-pass filter is also necessary after demodulation. It is important to note that the modulation and demodulation process does not reduce the noise in the system, but rather shifts the amplitudes in frequency space so low frequency noise can be filtered more effectively (as it is moved to higher frequency). If the system had high amounts of noise around the modulation frequency, this noise will

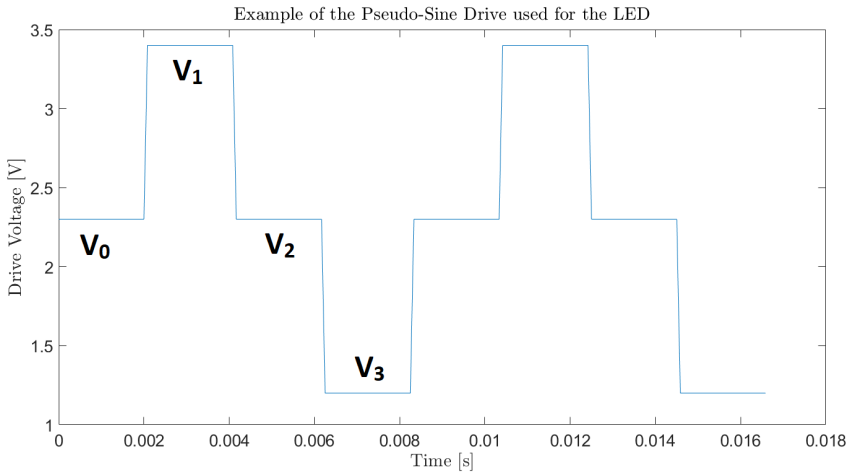

Fig. 4.5 A diagram depicting the shape of the pseudo sine wave used in the drive for the LED. It takes the form of a four point sine wave, i.e. middle - high - middle - low. The figure shows two cycles of the drive.

still be seen after demodulation and filtering (for a given bandwidth). Without the lock-in process, removal of the low-frequency noise would have required a filter with extremely long time constants, which would be impractical.

The digital lock-in amplifier used here features some notable differences to typical lock-in amplifiers as just described. It was decided that a 12-bit DAC ('TLV5616'), would be used to drive the LED. At the time, it was thought this system would use an LED modulated as a sine wave. However, due to the limited speed of the ADS1248, and therefore the limited modulation frequency as they are intrinsically linked, the decision was made to create a pseudo-sine wave. A pseudo-sine wave uses only four points per cycle, i.e. middle - high - middle - low. The pseudo-sine wave takes the form seen in figure 4.5, and was chosen over a simpler square wave so that information on both the in-phase and quadrature components can be calculated. DACs are not normally able to source large amounts of current; even tens of mA could be impractical and may cause significant variations in voltage, as the output from the DAC struggles to source or sink enough current. This limitation is why a simple buffer was fixed to the output of the DAC to allow for larger currents. The OP-amp used to buffer was the OPA2277. After testing with this simple drive, the decision was then made to use the current source described above and displayed in figure 4.2.

Despite the similarities between the digital lock-in amplifier and its analogue counterpart, the mathematics involved are simpler with the former. If only four points per cycle are considered, i.e. $\sin(0) = 0$, $\sin(\pi/2) = 1$, $\sin(\pi) = 0$, and $\sin(3\pi/2) = -1$, the system can be

demodulated by simple subtraction. That is, the in-phase component can be obtained by subtracting the fourth phase from the second phase, i.e. $V_d = V_1 - V_3 = \frac{1}{2}V_s + \frac{1}{2}V_s = V_s$, where V_n is the voltage at the $n^{th} + 1$ phase, $n = 0...3$. Similarly, the quadrature component can be calculated using $V_d = V_0 - V_2$. Interestingly, this digital method is capable of dealing with DC offsets on the input, as the simple subtraction removes the offset value as $V_1 = V_o + V_a$ and $V_3 = V_o - V_a$, therefore, $V_d = V_1 - V_3 = 2\,V_a$, where V_a is the amplitude of the oscillation, and V_o is the offset voltage.

The frequency of the LED drive is locked to the sampling frequency of the ADS1248. As there are four points per cycle of the sine wave, the drive frequency is $f_d = \frac{f_s}{4}$, where f_s is the sampling frequency of the ADS1248. Given that the ADS1248 can sample at a rate of 5 Hz to 2 kHz, the modulation frequency can then vary from 1.25 Hz to 500 Hz. Given that low frequency, or 1/f noise can couple from many places in this experiment, the lock-in amplifier is better suited with modulation frequencies higher than the corner frequency. The highest three sampling frequencies of the ADS1248 are: 640 Hz, 1 kHz and 2 kHz. During testing, it was noted the lock-in was being limited by the noise of the ADS1248, therefore, the lower rate of 640 Hz was chosen.

Post demodulation, the decimator (that was also used for decimating the temperatures as shown in chapter 3), was also be implemented here. This decimation was required to bring the higher data rates obtained from the ADS1248 to a more manageable level. Several stages were required to get the modulation frequency from 160 Hz to ≈ 1 Hz. Using four decimator stages would obtain the output data rate of $\frac{160}{4^4} = 0.625$ Hz.

4.3 Noise Model

4.3.1 Shadow Sensor

As with the previous noise model for the temperature sensors, noise can be picked up from many places such as: the electronics, pick-up (electromagnetic), and mains noise. Figure 4.2, as referenced previously, shows the circuitry that was required to modulate and drive an LED. It is quire clear that Johnson noise originates in several places, such as the resistors, LED, and the MOSFET. The DAC introduces quantisation noise, as well as noise from the voltage reference. Further types of noise from the LED would include: shot noise and relative intensity noise. Shot noise is a type of noise that originates from the unpredictable nature of light/electrons. i.e. the time when photons arrive at the photodiode is unpredictable and would appear as random noise. If we consider the photodiode as a counter for photons in

discrete time ranges, then photons from the LED would fill each of these bins non-uniformly and would appear as fluctuations in the current output. The effect is more easily observed at low light levels since if a few photons arriving later or earlier than expected would result in a larger relative change.

To understand the noise in the lock-in amplifier, three circuits have to be considered. The first is the drive circuit (figure 4.2), the second is the transimpedance amplifier circuit (figure 4.3) and lastly, the rest of the read-out circuitry (figure 4.4). The noise in the circuit is largely from Johnson noise on the resistors, but also includes a few other sources. The large number of OP amps used in circuitry would also introduce further noise sources. On-top of the circuits just mentioned, noise will be introduced by the LED in the form of shot noise. All of these noise sources will now be discussed.

LED Shot Noise

The spectral noise density of shot noise (in units of A/$\sqrt{\text{Hz}}$) can be calculated using the equation [111]:

$$\sigma_i = \sqrt{2\,q\,I}\,, \tag{4.7}$$

where q is the elementary charge of an electron ($q = 1.6 \times 10^{-19}$ C) and I is the current. This current density can be multiplied by a resistance R, and the square root of the bandwidth Δf, to convert it into an RMS voltage, i.e. $\sigma_{V_{rms}} = \sigma_i R \sqrt{\Delta f}$. In order to estimate the shot noise from the photodiodes, the nominal amount of current from the photodiodes must be calculated. This estimate should use the current from each photodiode, i.e. the total current before subtraction. The total current should be considered as the shot noise is not correlated, and therefore, would not cancel. As they cannot be cancelled, the shot noise values need to be summed in quadrature. As an estimate, the LED could be driven to 4 V at maximum, which is the equivalent of 40 mA of drive current. A typical LED, such as those used by R. P. Middlemiss, emit somewhere from 500 mcd to 1 cd in luminous intensity (for a drive of 20 mA, using values from the L-53SRC-C LED datasheet [112]). It can be seen from the graph of luminous intensity versus forward current (from the datasheet) that the intensity is linearly proportional to the forward current. This linear proportionality results in the LED emitting approximately $I_v = 1.5$ cd. Given that the LED is approximately 2 cm from the photodiodes that are 5 mm $\times$5 mm (length $\times$ width), a solid angle of $\Omega = 4.86$ mst can be

calculated. The candela is equal to $\frac{1}{683}$ W st^{-1} (by definition). Therefore, the total power on the photodiodes would equal 10.3 μW as seen in equation 4.8a.

$$\begin{aligned} P = I_v \Omega &= (1.5)(\frac{1}{683})(4.68 \times 10^{-3}) \\ &= 10.3 \ \mu\text{W} \ . \end{aligned} \tag{4.8a}$$

This calculation, however, assumes the only surface area that is illuminated by the LED is that calculated from the solid angle. Figure 4.6 shows a visualisation of the setup, highlighting the area created from the solid angle calculation. Clearly, light will also be covering the areas not included within the calculation using the solid angle. If we assume that the light on the photodiode has an equal intensity, then the total power of light can be found by multiplying by $\frac{4}{\pi}$, i.e. $P_T = 13.1$ μW. If this total power was entirely absorbed by the photodiodes, the current from the photodiodes can be calculated by multiplying by the spectral response of the photodiodes, i.e. $I = P S_s = (13.1 \times 10^{-6})(0.55) = 7.2$ μA. If the device were perfectly centred such that each photodiode had equal light, 3.6 μA of current would flow from each photodiode but cancel out to obtain 0 A.

A current equal to 7.2 μA is the equivalent of $\sigma_i = 1.52$ pA/$\sqrt{\text{Hz}}$ of shot noise. This value, though small, becomes more important as it is amplified by the current-to-voltage converters gain. This results in $\sigma_V = \sigma_i R_G = (1.52 \times 10^{-12})(1 \times 10^6) = 1.52$ μV/$\sqrt{\text{Hz}}$, where R_G is the feedback resistance of 1 MΩ. Although the ADS1248 is sampling at a minimum 640 Hz, with a bandwidth of 320 Hz, the noise actually has a bandwidth defined by the feedback on the current to voltage converter. This results in a bandwidth of 2.3 kHz, as this is the cut-off frequency of the current-to-voltage converter. Therefore, the RMS voltage noise that is seen by the input of the ADS1248 is equal to 72.3 μV.

LED Drive Circuitry

Before discussing the noise on the readout circuitry, the noise on the LED drive will be discussed. Note here that any noise in the circuit takes effect by changing the current through the LED and, therefore, the current from the photodiodes. It is known from the previous calculation that 40 mA going through the LED generates 7.2 μA from the photodiodes, i.e. $Q = \frac{7.2 \times 10^{-3}}{40} = 0.18$ mA$_{PD}$/A$_{LED}$, where Q is the conversion factor. It was therefore easier to consider the noise in the drive circuit as a current rather than voltage, as it allowed the noise to be converted into a current after the photodiodes.

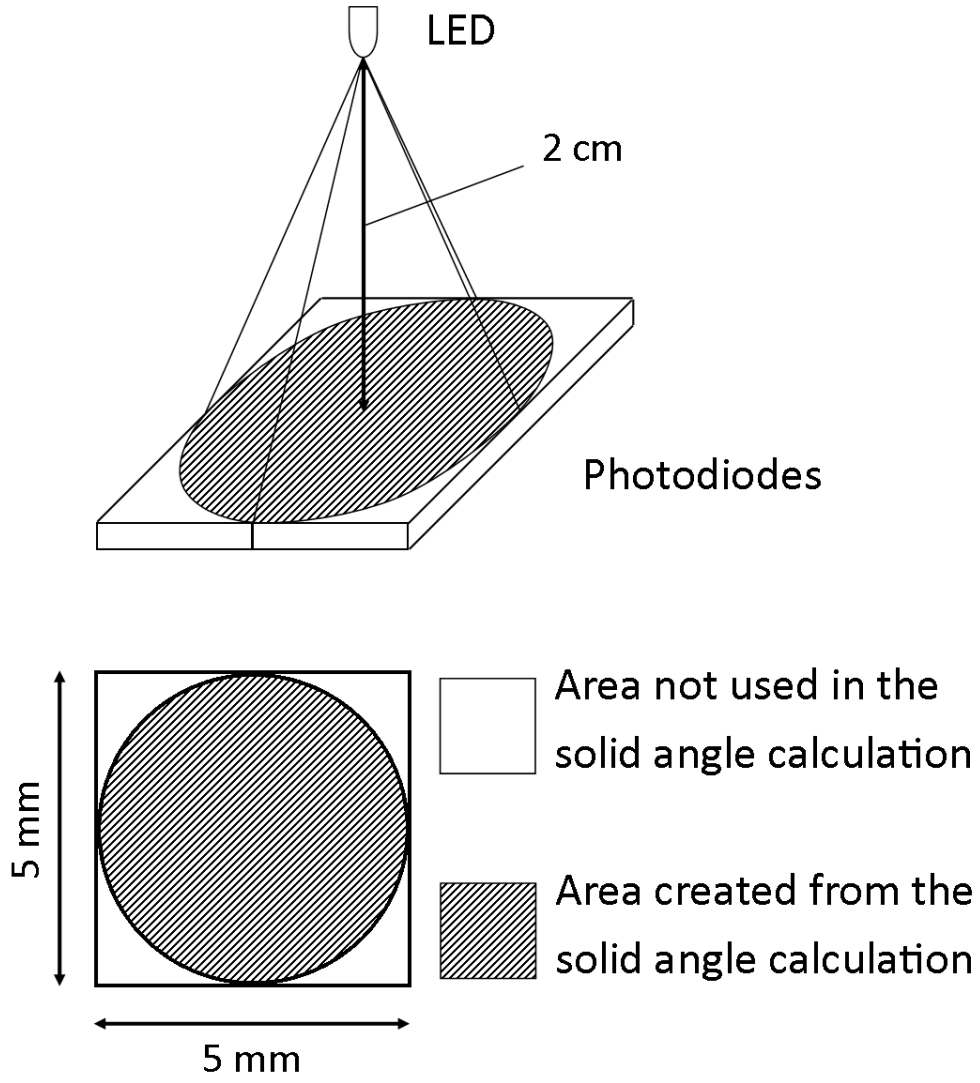

Fig. 4.6 Diagram of the photodiode and LED geometry, highlighting the area used in the solid angle calculation. Only the shaded area is included in the power calculation of 10.3 μW. This value can then be multiplied by $\frac{4}{\pi}$ to obtain the total power over both photodiodes.

The datasheets of transistors typical give a value for the noise as a noise metric, namely, the noise figure and noise factor. The noise factor is simply the change in signal to noise ratio (SNR) of the input to the output, i.e. $F = \frac{\text{SNR}_i}{\text{SNR}_o}$. The noise figure is the noise factor in decibels, i.e $NF = 10\log_{10}(F)$. As an example, the "ON Semi 2N3904TAR NPN Transistor" has a noise figure of approximately 3.5 dB at 640 Hz. This is the equivalent to stating the output SNR is the ratio of the input SNR over $10^{\frac{NF}{10}}$, i.e. $\text{SNR}_o = 0.45\,\text{SNR}_i$. This SNR means the input signal degrades by over half, relative to the noise. If we consider that the SNR is dictated by the noise from the resistor, DAC, and OP amp, then an estimate of noise equal to this SNR multiplied by $1/0.45 = 2.22$ can be obtained. It should be noted that the noise figure only degrades the current passing through the transistor, and therefore, this simplistic approach is a worst case-scenario.

The voltage reference (LTC6655) was used to source the current through the LED, regulated by the MOSFET. The data sheet specifies a voltage noise of approximately 50 nV/$\sqrt{\text{Hz}}$. Given that this voltage noise is through the drive resistor (equal to 100 Ω), a current noise can be calculated equal to 500 pA/$\sqrt{\text{Hz}}$.

The RMS quantisation error on the DAC is equal to $\Delta/\sqrt{12}$, i.e. the quantisation step over the square root of 12. Here, a 12-bit DAC with a reference voltage of 3 V has an RMS voltage noise equal to 211 μV, or 2.11 μA. Note that since the bandwidth is 2.3 kHz (from the filter), this is the equivalent of 44.1 nA/$\sqrt{\text{Hz}}$.

The Johnson noise can be calculated using equation 3.6a given in chapter 3. For a 100 Ω resistor, this is equal to 12.9 pA/$\sqrt{\text{Hz}}$. Similarly, the voltage and current noise of the buffer placed after the DAC can be found from their data sheet. .

Table 4.1 shows the noise sources from the current source LED drive, as well as their value, in terms of a noise density. It shows a clear dominant effect from the quantisation noise on the DAC. This 44.1 nA/$\sqrt{\text{Hz}}$ on the LED would result in 7.94 pA/$\sqrt{\text{Hz}}$ of noise from the photodiodes, however, if the effect of the noise degradation from the transistor is considered, an estimate of 17.63 pA/$\sqrt{\text{Hz}}$ is be obtained. Multiplying by the 1 MΩ feedback resistor and the square root of the bandwidth $\Delta f = 2.3$ kHz, obtains a voltage noise on the input of the ADC equal to 380 μV.

LED Readout Circuitry

The rest of the noise sources in the readout circuitry (figure 4.4) are listed in table 4.2. The table also includes the summed noise originating from the drive circuitry. It is important to note that using the full noise from the drive assumes that 100% of the noise propagates through the system. If the noise was correlated, as the shadow sensor is centred, the noise

Noise Source	Noise Type	Current Noise Density [pA/$\sqrt{\text{Hz}}$]
Drive Resistor	Johnson Noise (White)	12.9
Buffer Current Noise	White	0.5
Buffer Voltage Noise	White	0.03
Reference Noise	White	500
DAC Digitisation Noise	White	44100
Noise Figure	(Noise Metric)	$\times$2.22
Total		97902

Table 4.1 A table of the noise sources on the LED drive circuitry. Its clear that the digitisation noise (through the 100 Ω resistor) is the largest contributor to intensity fluctuations in the LED.

should cancel (at least partially). i.e. this is a worst-case scenario. The six resistors (Rb1, Rb2, R1, R2, Rf1 and Rf2) refer to the resistors used in the summing circuit, where the 1.5 μV is the incoherent sum of all six. Including the first OP-amp used to convert the current to a voltage, there are a total of four OP-amps used: one for the current-to-voltage converter, two as buffers, and one as the summing amplifier. Again, the 576 nV refers to the incoherent sum of all four. The table shows that the system should be limited by shot noise from the photodiodes given the assumptions made above. The estimations carried out would imply that the system should be dominated by the noise from the LED drive circuit, in particular, the digitisation noise from the DAC. This noise, averaged by the decimators, from a rate of 120 Hz to 0.625 Hz, would become $\approx$ 15.4 μV. To obtain this, first the expected noise reduction was obtained using the decimator simulation described in the previous chapter. From MATLAB, a factor of 25.15 was calculated when using four decimation stages. By dividing the starting RMS noise (387 μV), by this factor, the final noise of 15.4 μV was obtained. Changing the PGA of the system should not change the noise. The noise should not change as the PGA will not change the SNR of the external signal, and therefore, will not reduce the noise. If the system was dominated by noise from the ADC itself, then the PGA would make a difference.

4.3.1.1 Model of the Shadow Sensor Calibration

When using the system, a calibration must first be carried out to allow the voltage to be transformed to a displacement. Here, the objective is to calculate the change in output voltage due to a known change in displacement. This calibration allows future measurements to be converted into a displacement and, therefore, acceleration. Typically, the process is

Noise Source	Noise Type	RMS Voltage Noise [μV]
Feedback Resistor	Johnson (White)	6.17
Feedback Capacitor	Johnson (White)	7.75
Resistors	Johnson ($\times$6)	1.5
Input Noise (PGA@1,640Hz)	White	13.2
Digitisation Noise	White	0.063
Op Amp Input Voltage Noise	White ($\times$4)	0.576
Reference Noise	White	10
LED Drive Noise	White	380
Shot Noise	White	72.3
Total		387

Table 4.2 A table of the noise sources from the photodiode readout circuitry. The noise should be dominated by the digitsation noise from the LED drive, followed by the shot noise.

undertaken by first attaching a piece of silicon (or stationary MEMS) to a copper wire using wax. This copper wire is then connected to a micrometre stage that can move in the necessary direction for the calibration (as seen in figure 4.7). By moving the stage up/down in steps of 10 μm $\rightarrow$ 50 μm steps, a change in the output voltage is noted, and a value of the calibration is calculated (in V/m or more commonly mV/m).

Using what was calculated in the previous subsection, the LED outputs approximately 13.1 μW. If the entire system were perfectly centred there would be 6.55 μW of light on either side which therefore cancels. If a perfectly centred MEMS is considered, an estimate of the calibration can be made from the change in light over each side, for a given change in displacement. If the MEMS moves 0.5 mm for a photodiode of dimensions 5 mm $\times$5 mm, one side now has 2.5 mm^2 more light where the other has 2.5 mm^2 more shadow. With the starting arrangement having 7.5 mm^2 of light on either side, a displacement of 0.5 mm would therefore, create a geometry with 10 mm^2 of light on one side, and 5 mm^2 on the other, as visualised in figure 4.8. This movement is the equivalent of 2.62 μW as calculated in equation 4.9. This equation uses the total light over the photodiodes, and the relative change in light between either side given a displacement of MEMS. The equation also assumes the movement of the MEMS is equal to the change in shadow but will not be true given the arrangement.

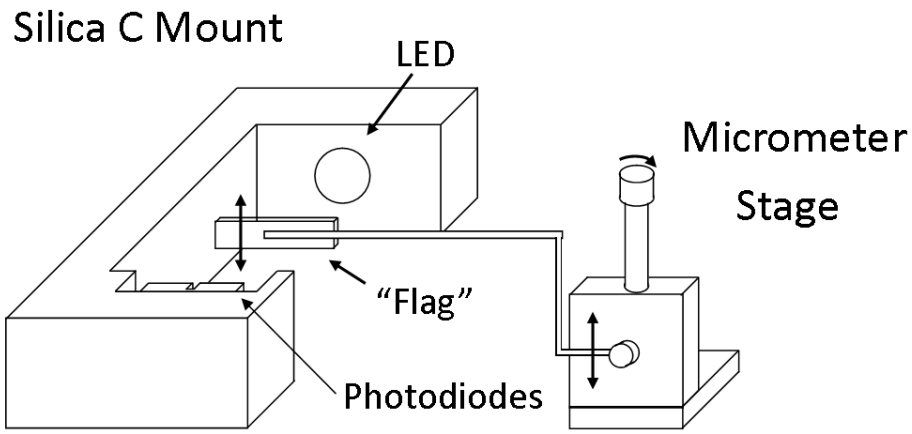

Fig. 4.7 A diagram showing the shadow sensor calibration technique. A small piece of silicon can be moved up and down using a micrometer stage by known amounts (typically 10 μm to 50 μm steps). This step results in a voltage change which, when divided by the step in metres, obtains a calibration.

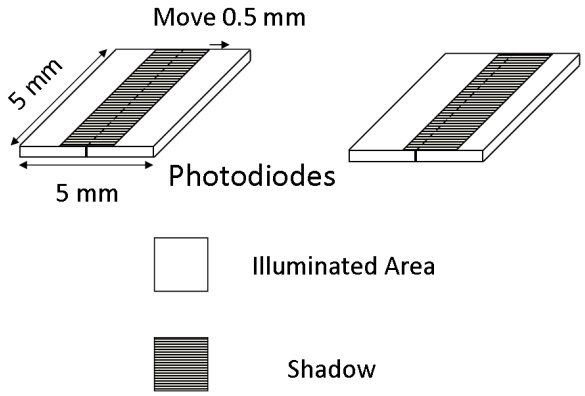

Fig. 4.8 A diagram depicting a moving shadow across the split photodiode. It visualises the concept used to calculate a theoretical calibration of the shadow sensor. If the shadow moves by 0.5 mm, and we know the total area and power of the light, the change in power can be calculated, and therefore, the change in voltage.

$$\Delta P = \frac{A_1}{A_T} P_T - \frac{A_2}{A_T} P_T \tag{4.9a}$$

$$= (13.1 \times 10^{-6}) \left[\frac{10}{25} - \frac{5}{25} \right] \tag{4.9b}$$

$$= 2.62 \ \mu\text{W} \ , \tag{4.9c}$$

where ΔP is the change in power from two photodiodes with an illuminated area A_1 and A_2, and total combined area A_T. A power of 2.62 μW results in approximately 1.44 μA of current. When amplified by the 1 MΩ feedback resistor, the current becomes 1.44 V. That is, a 0.5 mm displacement should result in $\approx$ 1.44 V which is an equivalent calibration of 2880 V m^{-1}.

4.3.2 Digital Lock-in Amplifier

It should be noted, again, that the lock-in demodulation does not reduce the total noise in the system, but rather shifts the noise around in the frequency domain, allowing for effective filtering. This shifting of amplitudes allows the removal of the low-frequency noise, which

is up-shifted to a higher frequency. From the expected 15.4 μV of noise and a calibration of 2880 V m^{-1}, a displacement noise of 1.5 nm (or 8.9 nm/$\sqrt{\text{Hz}}$ using 0.3125 Hz as the bandwidth) can be calculated. An amplitude spectral density of this value could be averaged to 281 pm RMS at 1000 s. This displacement is the equivalent of 4.4 μGal for a 2 Hz MEMS device, far better than required. These calculations, however, are likely to be inaccurate when also considering that the above calculation assumes the amplitude spectral density is white.

As the assumption that white-noise was the only type to exist in the system, a MATLAB script was created that simulated a more in-depth noise propagation through the lock-in amplifier. The script uses an input of the modulation frequency and amplitude of noise, both white and 1/f. However, since it is difficult to approximate the amount of 1/f noise in a given system, this functionality was not used.

Inputting 387 μV of white noise into the simulation obtains an RMS 11.9 μV, even lower than in the above calculation. This RMS was calculated at a sampling rate of 640 Hz for a total time of 1000 s, i.e. 640 kSamples. Figure 4.9 shows the randomly generated data after demodulation (160 Hz). Figure 4.10 shows the difference in the amplitude spectral densities for four of the stages during demodulation and filtering. The first stage shows a clear peak at the modulation frequency (160 Hz) with white noise. The second stage shows that, after demodulation, there is no change in the noise, except at the modulation frequency, which is to be expected, as the lock-in moves this amplitude to DC. The third stage is simply the downsampled second stage with no filtering or averaging. Again, this stage shows that there is no real change in noise, as the downsampling happens at a frequency which has been attenuated by the demodulation process. The final plot, after four decimation stages show a clear attenuation after 260 mHz. However, since there is no perfect transition between attenuation and no attenuation, this transition period includes frequencies slightly lower than the Nyquist to ensure rejection at the Nyquist. This simulation was processed 100 times to obtain the mean and RMS values for: the lock-in amplifier and the four decimation stages. It was noted that the when the fourth decimation stage had more noise, it did not necessarily correlate to more noise in the lock-in stage. Figure 4.11 shows a histogram of the RMS noise for both the lock-in stage (top graph), and the fourth decimation stage (bottom graph). A normal equal to 387 μV_{rms} can be observed showing that the random number generator varied slightly between iterations. After four stages of decimation, the normal became ≈ 11.7 μV_{rms} (close to the previously stated 11.9 μV) but varied up to 1 μV_{rms}, giving a reasonable limit on what level of noise reduction is expected from the decimation stages, i.e. the ratio of the starting and final noise ($387/11.7 = 33.1$). There are two main reasons why the noise reduction factor is slightly above what is calculated assuming an ideal low pass

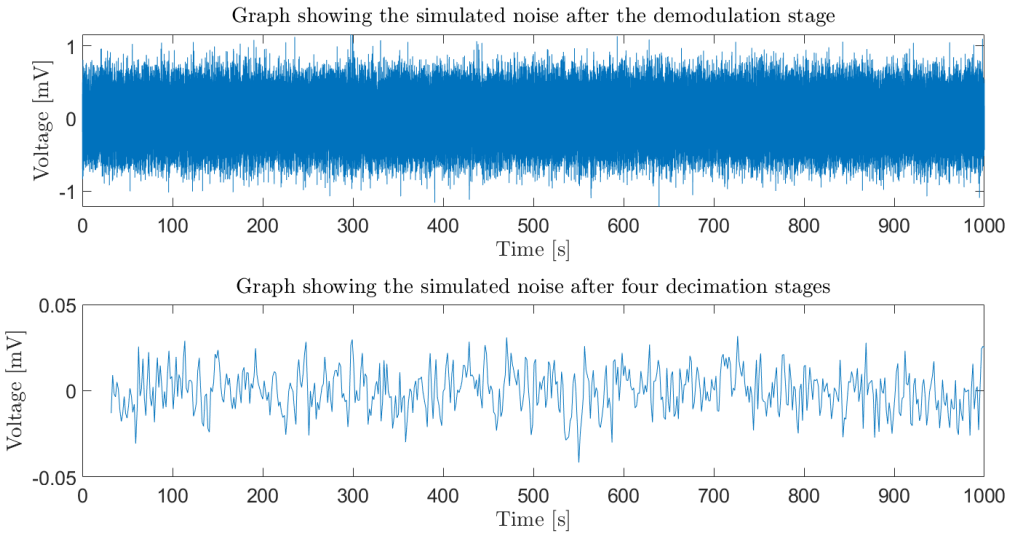

Fig. 4.9 A graph of the simulated data using a MATLAB script. The figure shows two plots; the top one is the data straight after demodulation of the lock-in amplifier (no filtering), while the bottom graph shows this data after the four stages of decimation. It is clear that the noise is reduced and, with the input RMS noise of 387 μV, a value of 11.9 μV is expected. The simulation was carried out using a sampling rate of 640 Hz up to 1000 s, i.e. 640 kSamples.

filter, i.e. the square root of the ratio of the starting Nyquist frequency to the final cut-off ($\sqrt{2\times 4^4} = \sqrt{512} = 22.6$). The first main reason is that the digital lock-in amplifier stage averages over two of the four cycle pseudo-sine wave, as two of the cycles are subtracted and then divided by two ($(V_s + V_o) - (V_o - V_s) = 2V_s$). This averaging results in an extra factor of $\sqrt{2}$ improvement in noise, for a final reduction of 32. The other reason was that the roll-off from the filter begins before 1/8th of the Nyquist frequency which would result in more attenuation. A value of 11.7 ± 1 μV_{rms} is the equivalent to 7.27 ± 0.62 nm/$\sqrt{Hz}$ (using a bandwidth of $0.625/2$), and therefore, could be averaged to 230 pm over 1000 s (3.6 μGal). For the target sensitivity, this should be more than enough.

4.4 Performance

By carrying out the calibration method previously described (figure 4.7), several voltage steps were obtained by moving the flag in 10 μm increments. These steps can be observed in figure 4.12, and can be used to calculate a calibration of 11.6 kV/m. This value is almost a factor of 5 larger than the estimated 2.88 kV/m. A point to note is that many calibrations have been carried out during this project, and since there were always changes to the set

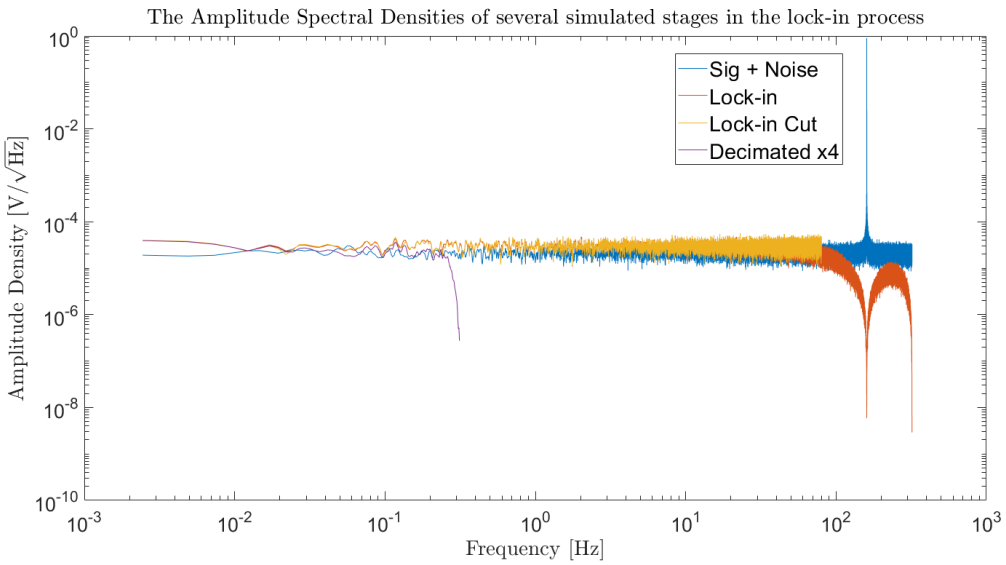

Fig. 4.10 Graph of the amplitude spectral density for the stages involved in the demodulating and decimation of the simulated data. The four stages shown are: the signal with white noise, the lock-in amplifier before downsampling and filtering, the lock-in after downsampling (still no filtering), and the fourth decimation stage. It can be seen that the amplitude spectral density does not increase when downsampling during demodulation. After four decimation stages the highest frequency present is 0.3125 Hz, i.e. half of the sampling rate.

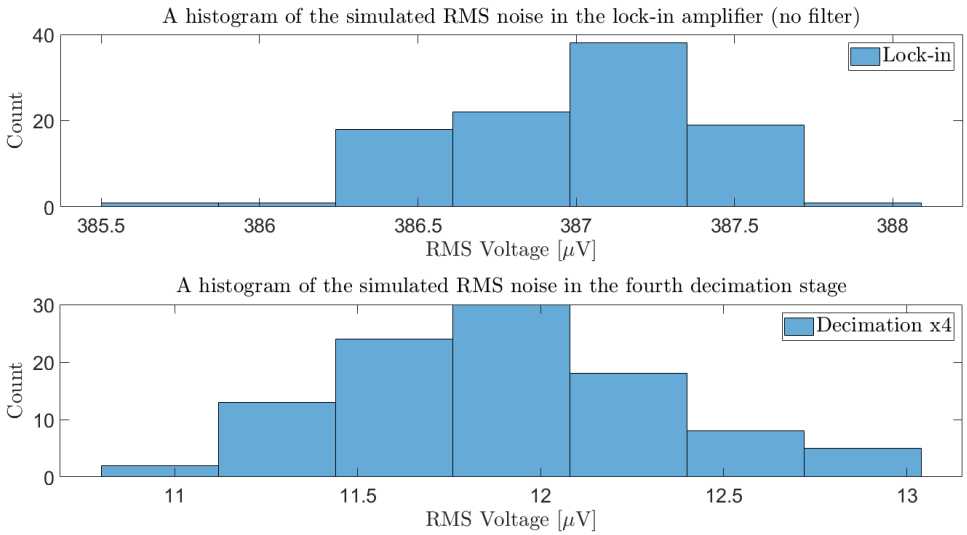

Fig. 4.11 Histograms for the simulated RMS values of the lock-in stage (top graph), and the fourth decimation stage (bottom graph). A non-Gaussian can be observed in both. The lock-in starts with a noise of approximately 387 μV_{rms}, reducing down to 11.7 μV_{rms} after four stages of decimation. It can also be see that the final noise after four stages decimation varies by approximately 1 μV_{rms}. This value gives a limit on what should be expected using the simulated noise.

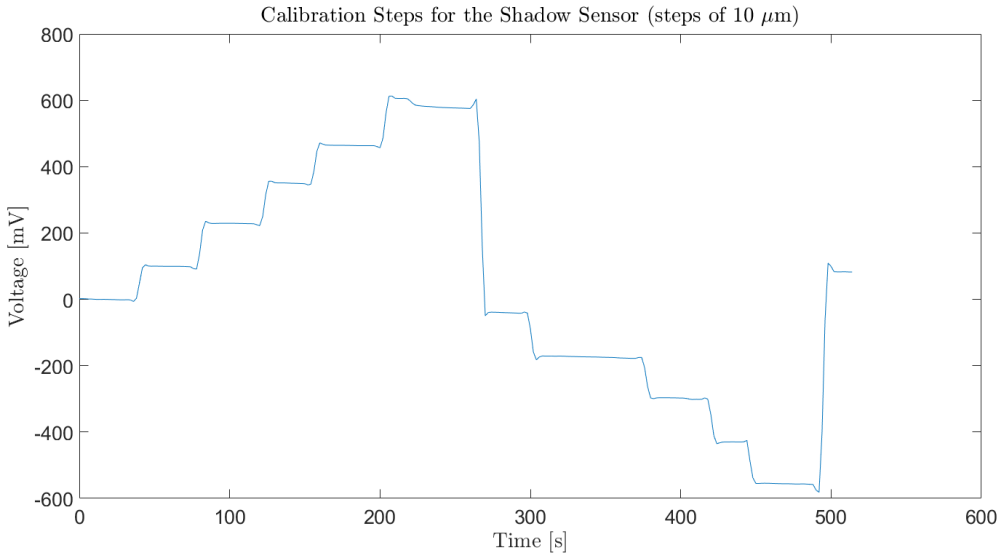

Fig. 4.12 Graph of the shadow sensor calibration. Here, five 10 μm steps are made to a flag in one direction, then reset to zero and repeated for the opposing direction. The total 50 μm movement causes a change in output of 580 mV. This results in the calibration value of 11.6 kV/m.

up, including the drive resistor and voltages, changes to the calibration value were always observed. The typical value for the calibration was approximately 8 kV/m. This value is still different from the theoretical value, likely due to the estimated value of light being emitted by the LED being inaccurate. Given the assumptions made to estimate the calibration, the value matches quite well with the measured value. The discrepancy between the calibration values is likely due to the assumptions involving the LED and PD system such as the intensity for a given current and the absorption value.

Initial testing started with the lock-in amplifier running at low frequency as the code for communication was being worked on by Mr David Loomes. This lock-in used the ADS1248 at a sampling rate of 5 Hz, and resulted in a lock-in output of 1.25 Hz. This frequency would never be used in the final device, but, still allowed noise analysis of the system. At the lowest sampling rate, the noise was limited by the reference voltage. It was then decided to replace the reference with a low-drift, low-noise precision LTC6655 voltage reference. As an example, the MAX6177 outputs at 3.3 V, with a noise of 10 μV_{RMS}, whereas the LTC6655 outputs at 3 V, with a noise of 2 μV_{RMS} (both specified between 10 Hz to 1 kHz).

Once the required code for the comms register for the ADS1248 was finalised by Mr. Loomes, work on the analysis of the system at higher frequencies began. Figure 4.13 shows the increase in noise from the ADS1248 as the sampling rate is increased from 20 Hz, to 40

Hz, to 80 Hz, and finally 160 Hz. It is worth noting this is the raw output from the ADS1248 without any decimation or averaging. The RMS noise increases from 9.6 μV, to 12.4 μV, to 19.4 μV, and finally 30.0 μV. These noise measurements are all higher than the stated values in the datasheet by a factor of 3 or 4, rising to a factor of just over 5 for the higher frequencies. It is still uncertain why this was, considering that these data rate tests were carried out with the internal reference and supply voltages as shown in the datasheet. It was, however, considered an adequate level of noise as, if the calibration was of order 5 kV/m, then this would be the equivalent of 6 nm without the lock-in amplifier or any averaging. If the theoretical improvement in noise of $\sqrt{4^4} = 16$ was obtained, then this noise would be closer to 0.4 nm, which, for a 2 Hz device, is 6.3 μGal.

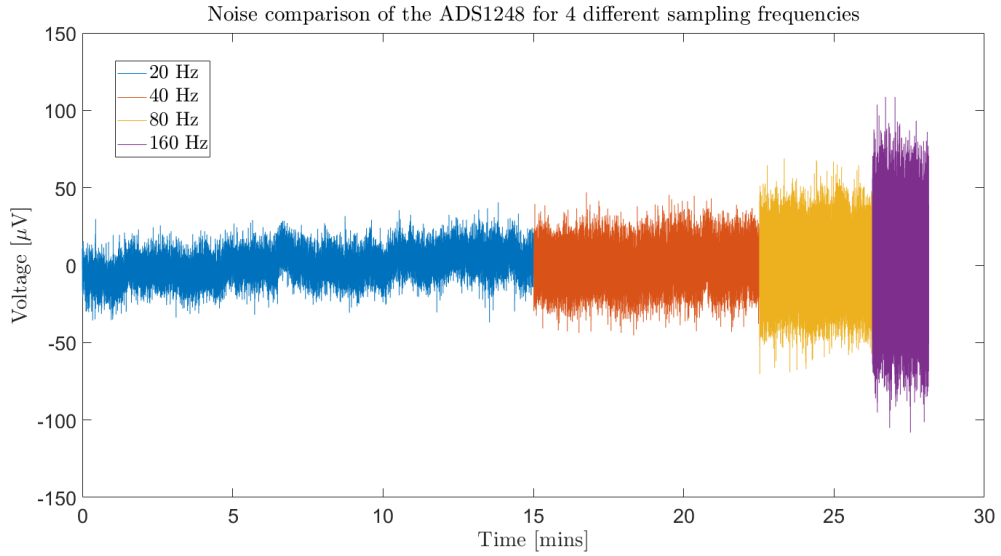

Fig. 4.13 A graph showing a noise comparison of four different sampling frequencies for the ADS1248. The rates 20 Hz, 40 Hz, 80 Hz and 160 Hz were tested and, as expected, noise increased as the sampling rate increased. The RMS noise for these tests were: 9.6 μV, 12.4 μV, 19.4 μV, and 30.0 μV. Note that this is the direct output from the ADS1248 and not utilising the lock-in or any averaging.

Figure 4.14 shows the noise at each PGA setting while the LED is on at a constant value (no modulation). At a PGA of 1, the noise is at its highest, 0.6 nm/$\sqrt{\text{Hz}}$. This noise reduces to 0.33 nm/$\sqrt{\text{Hz}}$ at a PGA of 2, 0.25 nm/$\sqrt{\text{Hz}}$ at 4, and finally 0.233 nm/$\sqrt{\text{Hz}}$ at a PGA of 8 and above.

Figure 4.15a shows the noise of the system while under temperature control for two different decimation stages using a MEMS with a resonant frequency of 10 Hz. It can be seen that the noise decreases as the data goes through more decimation. The RMS noise reduces

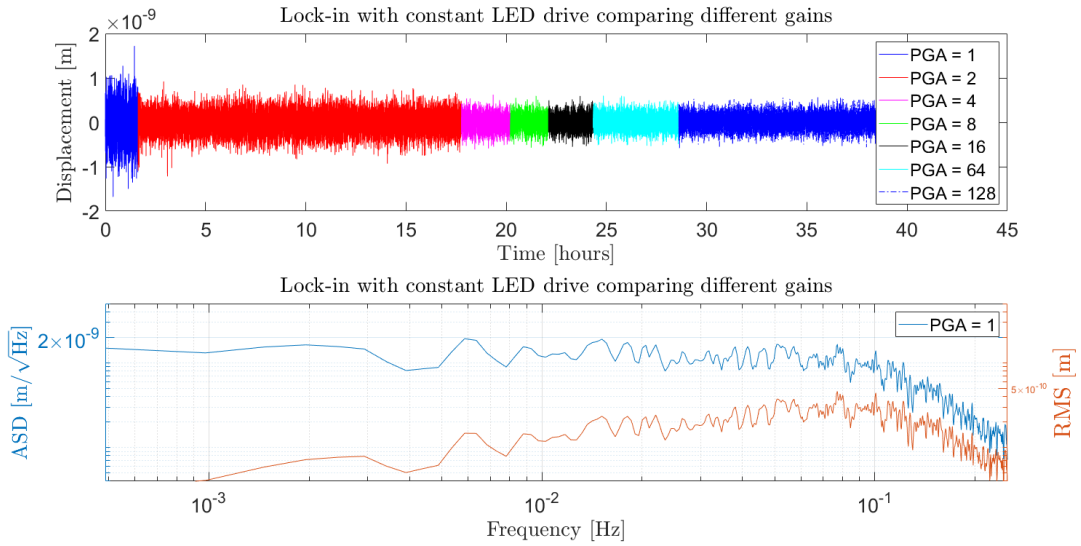

Fig. 4.14 Graph showing the noise from the digital lock-in amplifier using the ADS1248. The top graph shows the time series data for a PGA of 1, 2, 4, 8, 16, 64 and 128. A decrease in noise can be observed until a PGA of 8, where it remains constant. The initial noise at a PGA of 1 is 2 nm peak-to-peak, decreasing to 1 nm peak-to-peak at a PGA of 8 and above. The lower graph shows the corresponding amplitude spectral density and RMS noise for a PGA of 1. A value of just over 1 nm/$\sqrt{\text{Hz}}$ can be extracted which results in an RMS of 100 pm at 100 s

from 6.3 nm in stage 2, to 1.7 nm in stage 4, nearly a factor of four reduction (for a reduction of 4^2 in the sampling rate). This reduction in noise is close to the general rule, $\sqrt{F_1/F_2}$, i.e. the best reduction in noise possible is the square root of the ratio of downsampling. It should be noted that the lock-in output is at a rate of 120 Hz, and therefore, the second decimator stage is at 7.5 Hz, and the fourth, 0.47 Hz. Figure 4.15b shows the amplitude spectral density of the data discussed above. It can be seen that lock-in average 2 has a noise of 25 nm/$\sqrt{\text{Hz}}$, where stage 4 has a noise of 3.7 nm/$\sqrt{\text{Hz}}$, both at 100 s. This ASD means that, if the data were averaged to 100 s, a sensitivity of 2.5 nm and 0.37 nm for stages two and four respectively could be obtained.

The data in figures 4.14 and 4.15 was post-processed using regression analysis. Regression required the use of a MATLAB script ("Mregg") that correlates a series of chosen variables to the signal and then estimates their effect on it. The regression method and how it was used relating to data such as this will be discussed more in chapter 6. Using this method, figure 4.16 was obtained, showing data spanning over 33 hours. It shows a 6 nm variation, which is the equivalent of 14 nm/$\sqrt{\text{Hz}}$. If averaged to 1000 s, the noise would have an RMS

of 0.44 nm, or 6.95 μGal. This level of noise displays that the system should be able to measure the changes in gravity adequately.

4.5 Conclusion

A displacement sensitivity of a few nanometres was required to obtain the necessary acceleration sensitivity of the MEMS gravimeter. The system would also have to be low-cost, portable and lightweight. Here, a shadow sensor based upon the techniques developed in the gravitational wave community has been presented that can obtain sensitivities of 0.44 nm at 1000 s; an acceleration sensitivity of 6.95 μGal. To obtain this sensitivity, a digital lock-in amplifier was utilised on a custom electronics board. The microcontroller filtered the output from a digital based lock-in amplifier using a low-pass filter, followed by downsampling. This process was then repeated for a total of four stages to obtain a performance of 14 nm/$\sqrt{\text{Hz}}$. To obtain the target RMS, the data can be averaged up to one thousand seconds. Unfortunately, the noise is not entirely white and is, therefore, limited at low-frequency. This limitation results in a constant RMS sensitivity below 10 mHz.

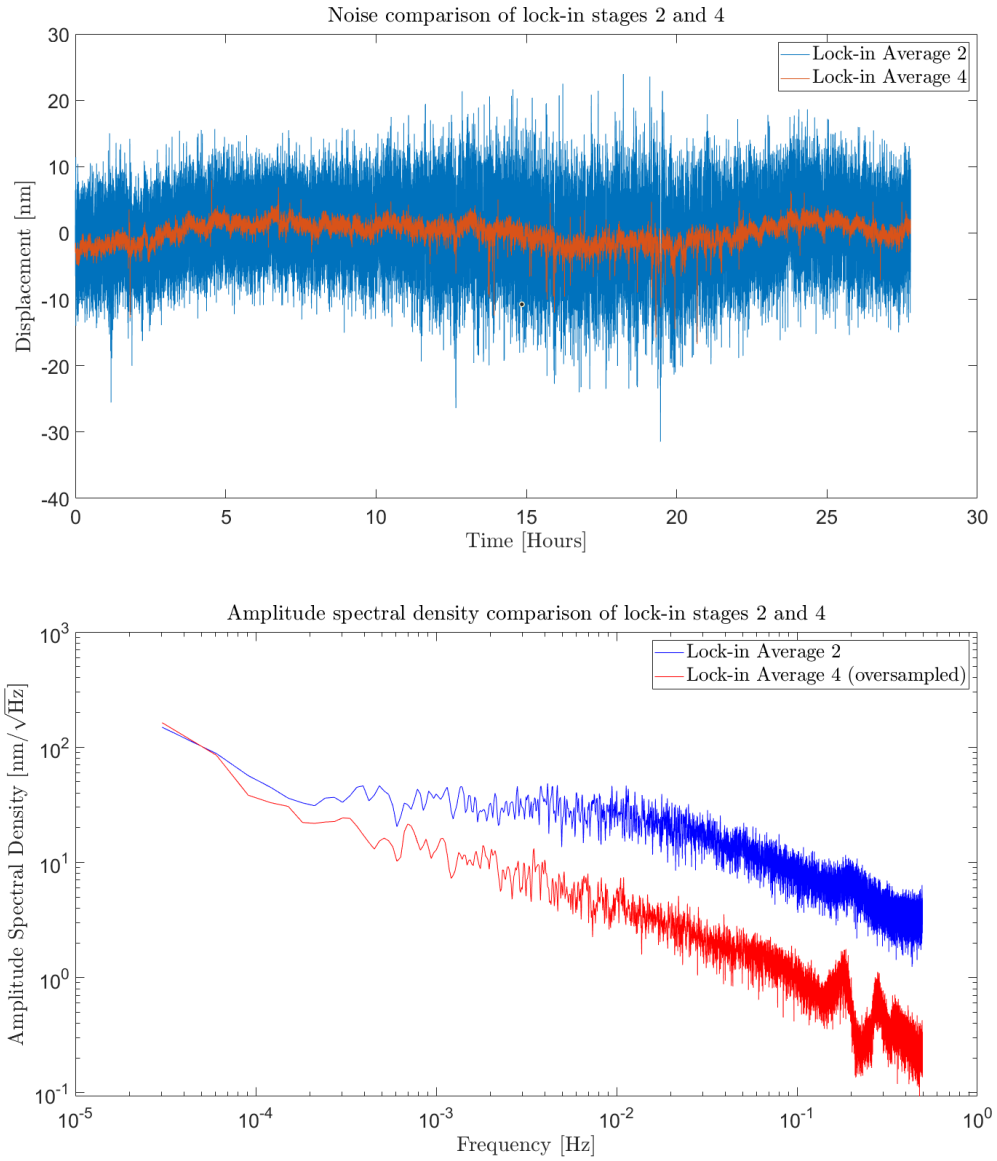

Fig. 4.15 Two graphs comparing the resulting noise from the 2nd and 4th lock-in stages. The top graph shows the 2nd and 4th lock-in stage as a time series. Clearly they both track each other but after two extra stages of decimation, the 4th stage has lower noise. The RMS is reduced from 6.3 nm to 1.4 nm. The bottom graph shows the amplitude spectral density of both sets of data. Note that the 4th decimation stage is now oversampled so both ASD's can be compared within in the same frequency range. Comparing the values at 100 s, stage 2 has a value of 25 nm/$\sqrt{\text{Hz}}$, whereas, stage 4 has a value of 3.7 nm/$\sqrt{\text{Hz}}$. This is an equivalent sensitivity of 2.5 nm and 0.37 nm, when averaged to 100 s.

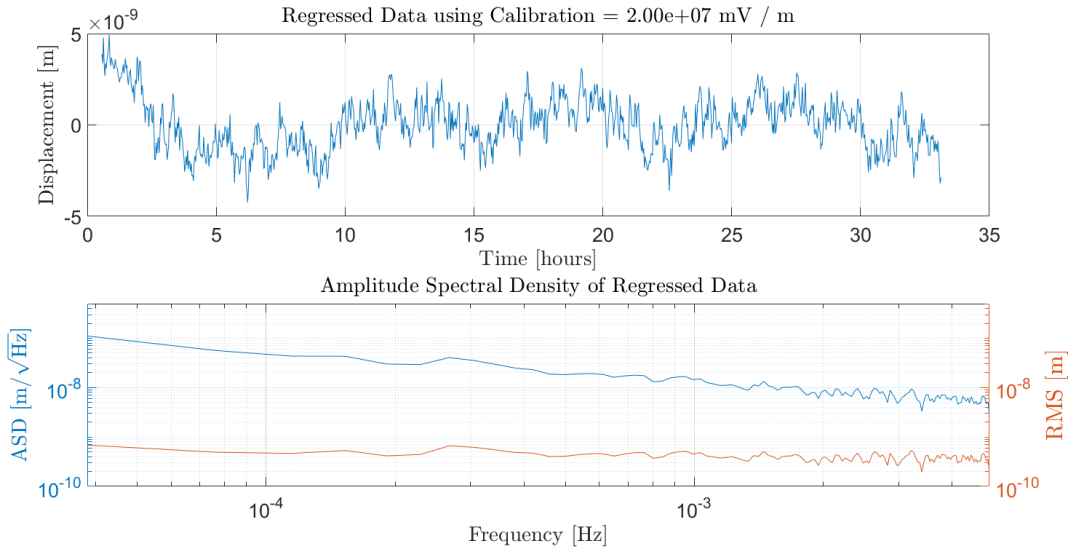

Fig. 4.16 Graph of the long term noise in the lock-in in amplifier after four decimation stages and regression. The top graph shows the time domain where the bottom graph shows the corresponding amplitude spectral and RMS. Variations of up to 6 nm can be seen in the time domain that correspond to an RMS of 0.44 nm at 1000 s.

Chapter 5

Tilt Sensor

5.1 Introduction

All gravimeters are sensitive to tilt, a MEMS gravimeter being no exception. Since the device is measuring changes in the acceleration of gravity, a change in tilt would appear as a change in the signal. It is as a result of this effect that a sensor was required that could accurately tilt to a sufficient level, allowing regression during post-processing. The system designed and tested for this project should have a sensitivity similar to the set-up used by R. P. Middlemiss et al., approximately 4.4 μGal/μRad in the most sensitive axis and 0.12 in the less sensitive axis. To achieve μGal performance, a tilt sensitivity of the order μRads would be required.

The sensor also needs to meet the overall criteria of being low-cost, lightweight and portable. In light of this, two sensors were tested, one of which was tested in two separate arrangements. Both sensors are electrolytic tilt sensors which function as bubble levels but with an electronic readout. The first of the tilt sensors to be tested was the 755-1129 high gain, dual axis, electrolytic tilt sensor from Jewell Instruments, utilising the 83162, dual channel, signal conditioning card. This device is not low-cost (more than several thousand pound sterling) but was still tested as a baseline sensor. The second sensor was the "SH50055-A-009" from Spectron Sensors, a single axis electrolytic tilt sensor, of which two were required for the system (perpendicular to each other). This device was lower cost than the Jewell Instruments device, approximately two hundred pound sterling each. Rather than using an off-the-shelf conditioning card for the tilt sensor from Spectron Sensors, custom electronics were designed for two tests to help keep the cost low. One of the tests utilised the dsPIC33E for excitation and sampling, whereas the other test used an AD7195, specialised for bridge measurements and the temperature measurements in chapter 3.

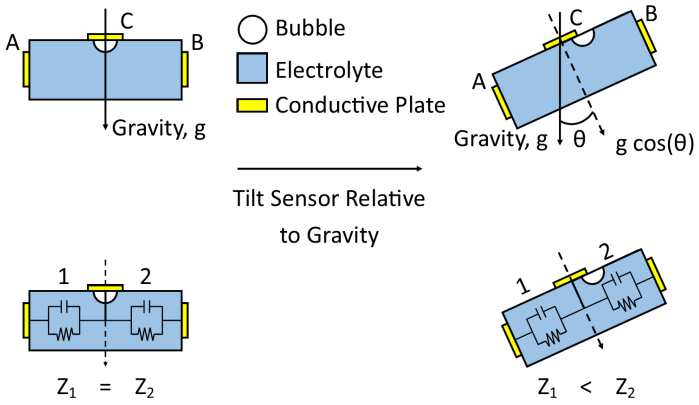

Fig. 5.1 A picture showing how an electrolytic tilt sensor functions as it is tilted away from vertical. The bubble inside the channel moves upwards as it is tilted away from gravity, causing a decrease in impedance on the side the bubble moves away from. The other side with more of the bubble increases in impedance as the bubble will be less conductive than the electrolyte. The difference in impedance between these two sides relates to the angle at which it is tilted, relative to gravity. Note that the sum of the two impedances should be constant.

5.2 Design

5.2.1 Jewell Instruments Sensor

The high-gain, dual-axis 755-1129 electrolytic tilt sensor [113], from Jewell Instruments was initially chosen to be tested. To operate the sensor, an expensive 83162 dual-channel signal conditioning card was also required.

As stated before, electrolytic tilt sensors function as bubble levels but with an electronic readout. The position of the bubble is measured using three electrodes, two drive plates and one pick-off plate. As the device is tilted away from gravity, the bubble moves towards one side, changing the relative impedance between the side plates and the centre plate. It is this relative change in impedance between between plates that is measured and converted into an angle. Figure 5.1 shows an approximation to how the inside of an electrolytic tilt sensor channel functions as it is tilted away from the maximum of gravity.

The channels in the electrolytic tilt sensor can be modelled as two sets of RC circuits, in series from one side of the sensor to the other (plates A and B are known as the drive plates). The centre point (plate C) of the sensor is a pickoff plate. By exciting a voltage across the bridge, and measuring the change in impedance, a value for the angle can be determined. There is, however, one issue, in that the sensors are not compatible with DC voltages. A DC voltage would deteriorate the electrolytic solution, degrading the sensors functionality. Over time, this effect would stop the device from functioning, and thus AC excitation is required for any measurements made. In the case of the Jewell Instruments sensor, the conditioning card generates an AC excitation drive and handles the demodulation of the output to a DC voltage.

5.2.2 Spectron Sensors

Due to the costly nature of the Jewell Instruments sensor, work was carried out to find, design, and test a new, lower cost system. This new system also required the design of custom circuitry to further reduce the costs. It was found that Spectron had a single axis electrolytic tilt sensor (SH50055-A-009 [114]) for less than two hundred pounds.

5.2.2.1 Internal ADC set-up

Since the tilt sensors were not compatible with DC excitations, a circuit that would have AC excitation was necessary. It was noted that the dsPIC has an internal ADC that could sample considerably faster than the external ADCs on the custom electronics board, and thus, would be used to sample the tilt sensor output. One issue is that the internal ADC can only sample one channel at any given moment. In light of this, a method to combine both axes would be necessary.

The internal ADC was ideal as it contained several bi-directional I/O ports that could be updated when a new sample was obtained by the internal ADC, allowing an AC signal to be produced for the sensors. When a new value was sampled, the microcontroller would then store the value and change the output pins in anti-phase. Rather than waiting for the code to come to a specific point to check if the internal ADC had sampled, the system utilised an interrupt. This interrupt stops the microcontroller where it is in the code to give priority to the internal ADC. This process allows for a high sampling and AC excitation rate. One downside to the internal ADC was that it has a limited bit depth (12-bits) which could limit the sensitivity. The AC excitation has the form of a square wave similar to the lock-in amplifier drive. Since the system has to measure two axes with one input, the microcontroller

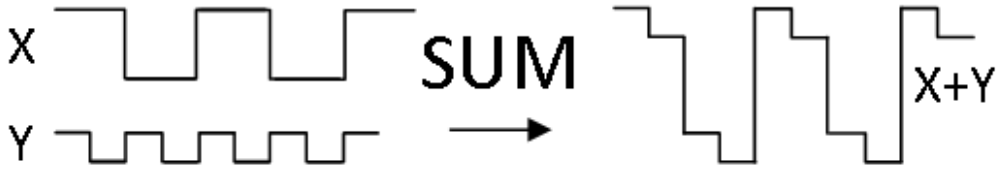

Fig. 5.2 A diagram showing an example of two drive waveforms, for two tilt sensors and the resulting wave when summed. One is at twice the frequency of the other so that, when summed, both axes can be demodulated digitally. This summation allowed two axes to be sampled with a single channel ADC.

outputs two frequencies, one twice the frequency of the other. These two frequencies are then summed together. Figure 5.2 shows the result of two square waves summed together, where one has a frequency twice of the other. It is evident from the figure that the amplitude of each of these frequencies can be extracted by assessing the differences between phases [115]. The amplitude of each frequency can be extracted mathematically by first considering a square wave split into four phases. The lower frequency square wave goes from high-high-low-low, while the higher frequency square wave goes from high-low-high-low. With this, it can be seen that the value of the lower frequency, V_l, and higher frequency, V_h, can be calculated from the value at each phase, V_n, where $n = 1,2,3,4$ using the equations 5.1a and 5.1b.

$$V_l = V_1 + V_2 - (V_3 + V_4) \tag{5.1a}$$

$$V_h = V_1 + V_3 - (V_2 + V_4)\ . \tag{5.1b}$$

Initial designs of the excitation circuitry utilised a buffer on the digital outputs, followed by a high pass filter to ensure no DC component remained. This high-pass had a cutoff frequency of 0.7 Hz. The excitation was then connected to either side of the sensor, where one side is anti-phase to the other. The output of the tilt sensor was then high passed again, before being buffered and summed to the other axis. To ensure that the voltage was between ground and $+V_{\text{ref}}$, half of the reference voltage was also summed onto the signal. The circuit diagram for this can be seen in figure 5.3 and shows the circuitry for a single axis. In the figure, Tilt + and Tilt - refer to the drive used to excite the tilt sensor. Since an AC signal

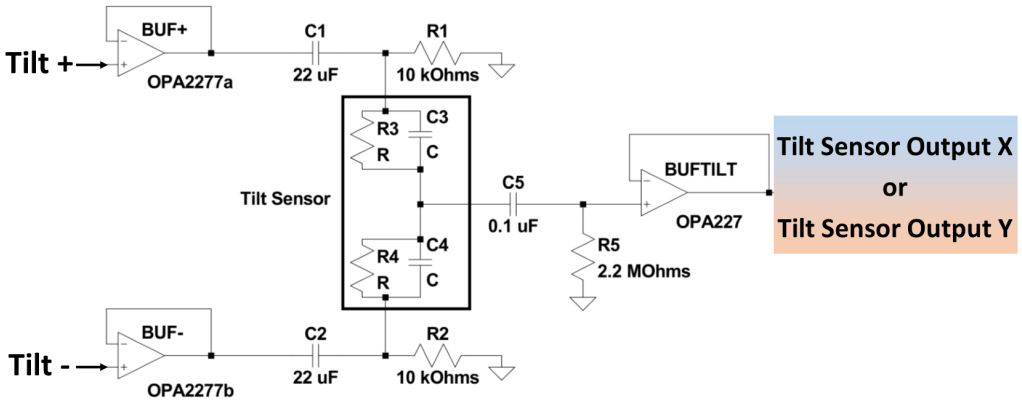

Fig. 5.3 Schematic of the drive used to measure one axis of the Spectron tilt sensor. Digital outputs from the dsPIC in antiphase are both high-pass filtered (to ensure no DC), and passed into the tilt sensor. The pickoff plate is then passed through another high-pass filter and buffered. This process is then repeated for the other axis of measurement and summed together in figure 5.4

is being used to excite the tilt sensor, Tilt + and Tilt - switch from high to low relative to each other. Two of these circuits are required for 2-axis tilt sensing, with one at twice the frequency of the other. Since the dsPIC33E only has one ADC channel, the signals have to be summed together and each component extracted digitally. To sum each of the axes together, the circuit in figure 5.4 was used.

5.2.2.2 AD7195 Set-up

Following initial testing of the Spectron tilt sensors using the internal ADC of the dsPIC, it was thought that lower noise could be obtained using the AD7195's that had been used for temperature sensing. The AD7195, made for measuring resistor bridges and strain gauges, was also ideal for measuring the electrolytic tilt sensor. The AD7195 allows for AC excitation, which is necessary for running the sensor. It was thought that the AD7195 would obtain a better performance than the internal ADC, due to it's much larger bit-depth (24-bits compared to 12-bits of the internal ADC).

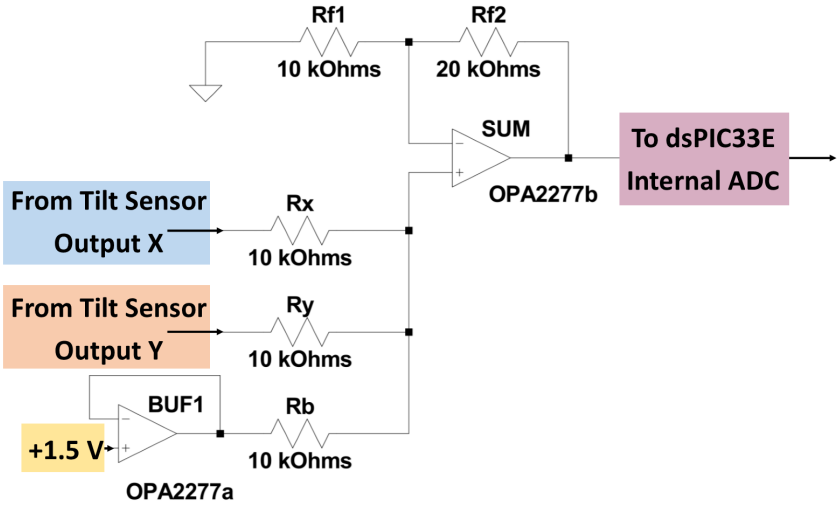

Fig. 5.4 Schematic of the circuit used to combine both tilt sensor axis signals (from two sets of figure 5.3), including a bias voltage to ensure the input to the dsPIC is above ground. The circuit is a non-inverting summing amplifier, as used with the lock-in amplifier, but with three voltages being summed together. This means an R_{f2}, with a value twice of the other resistors, had to be used to obtain unity gain (see equation 4.1).

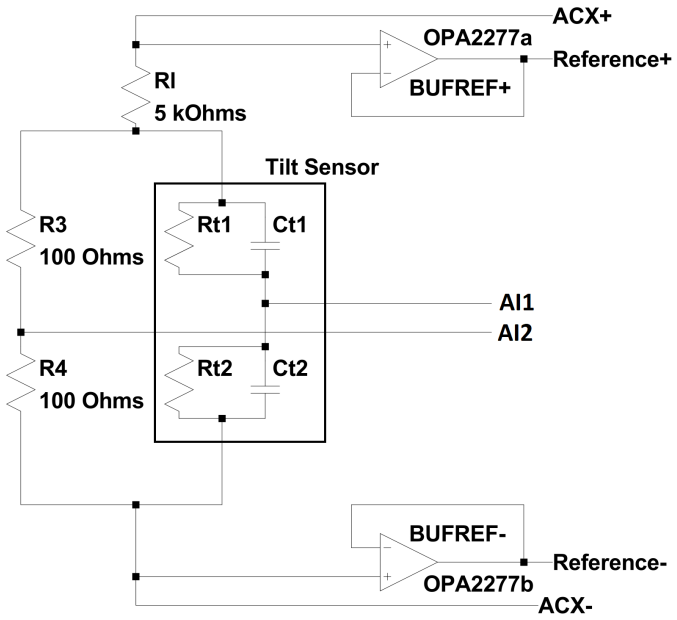

Fig. 5.5 Schematic of the tilt sensor (from Spectron Sensors) as part of a Wheatstone bridge, measured using the AD7195. Above the Wheatstone bridge is a current limiting resistor (*Rl*). The reference voltage for the AD7195 is obtained from the entire circuit and buffered by an OPA2277.

Additionally, it was decided to turn the sensor (a half bridge) into a full Wheatstone bridge which should have less noise. Since a full bridge has an output of zero when balanced, this would also allow for higher gain settings. This change was accomplished by using two extra resistors of a similar impedance to half of the tilt sensor, as seen in figure 5.5. The impedance of the tilt sensor at 1 kHz was found to be $\approx 100\ \Omega$ *. To reduce the total current in the circuit, a current limiting resistor was used with a value of 5 kΩ. With a resistance of at least 5 kΩ, the maximum current was of an order of a milliampere. The limiting resistor was thought necessary as the voltage reference that supplies the bridge cannot supply large amounts of current and so would introduce noise. The reference voltage for the AD7195 is taken over the entire circuit, i.e. the excitation voltage. Since the AD7195 has input buffers on the analogue inputs but not for the reference, extra buffers are required (OPA2277a/b in figure 5.5). ACX+/- is the AC drive obtained using the MOSFET arrangement as seen in figure 3.2 from chapter 3.

*This measurement was carried out by simply putting a known resistance in series with the tilt sensor and driving an AC signal

Due to the nature of the electrolytic tilt sensors, the code for the AD7195 was changed during testing to ensure AC excitation was always enabled. This change involved altering the line of code that sets the config register's bits relating to ACX and CHOP to be always on, i.e. "config.chop = 1;" and "config.acx = 1;" [99]. This change ensures, during boot-up of the microcontroller, that the bridge is set to AC as soon as possible, and thus does not require any input from a computer before any damage occurs to the tilt sensor.

5.3 Noise Model

5.3.1 Jewell Instruments

Due to most of the circuitry being supplied commercially for this product (the 755-1129 Miniature Tilt Sensor from Jewell Instruments), the theoretical noise is almost entirely from stated values in datasheets. The datasheet [113] specifies a resolution of < 0.1 μRad, with a repeatability of 1 μRad.

The conditioning card (Model 83162 Dual-Channel Signal Conditioning Card) outputs a voltage proportional to the tilt, in a range of ± 8000 μRad, with a calibration of 0.1 μRad/mV while on high gain, or 1 μRad/mV while on a low gain. The output, however, is limited to a range of -16 V to $+16$ V at a high gain, while a low gain would vary from -8 V to $+8$ V. The upper limit of the voltage on both gains is still too high for being sampled by the ADS1248 and would likely have to be limited to ± 3 V, i.e. ± 300 μRad on high gain, and ± 3000 μRad on a low gain. It should be noted that as the signal would be measured by the ADS1248 on the dsPIC33E board, extra noise could be introduced. However, the ADS1248 should only introduce 1.1 μV_{rms} or 1 nRad and thus can be ignored [116].

Additional sources of error for the tilt measurements can also be caused by the temperature sensitivity of the device. It is specified that the output will vary up to ± 3 μRad/K, and 0.04 %/K of full scale. For a peak-to-peak oscillation of 5 mK, an angle of approximately 7.5 nRad would be expected given the stated sensitivity.

5.3.2 Spectron Sensor

5.3.2.1 Internal ADC Setup

Table 5.1 shows the summarised noise for the drive circuit (figure 5.3) and the summing circuit (figure 5.4). The table includes thermal noise, both resistive and capacitive, as well as voltage noise from OP-amps, and the reference. The datasheets and other documentation

for the dsPIC33E family of microcontrollers lack information on the internal ADC, and thus the input noise could not be found. Instead, the digitisation noise was used. Though the internal ADC has sampling rates up to 1.1 MHz, it comes with a corresponding limited bit depth, 10 bits for speeds up to 1.1 MHz or 12 bits for speeds up to 500 kHz. The RMS digitisation noise is equal to: RMS $= \frac{q}{\sqrt{12}}$ [117], where q is the least significant bit (LSB), i.e. $q = \frac{V_{\text{range}}}{2^{\text{no.bits}}-1}$. For a 10 bit analogue-to-digital converter, for a voltage range of 3 V, this results in an RMS noise of 847 μV, whereas a 12 bit system has an RMS noise of 211 μV. The table shows the value for the 12 bit system, as this is the planned operation of the ADC. The table shows that, for a 12 bit system, an RMS noise of 220 μV would be expected. This 220 μV is dominated by the digitisation noise (assuming no further input noise on the ADC), and is the equivalent to 1.07 μRad, given the calibration of 1 mV/arcsecond (0.21 mV/μRad) given from the Spectron datasheet. This noise is within the specifications required for measuring gravimetry signals and could be improved further by averaging (the decimator as discussed in chapters 3 and 4). Given the output data rate of up to 50 kHz, 4 stages of the decimator would obtain a factor of 19.4 of an improvement in noise while reducing the data rate to a more usable 195 Hz. This noise improvement would mean the 1.07 μRad would become 55 nRad. This noise is lower than necessary, but would be ideal for regression purposes.

The temperature sensitivity of the internal ADC is not stated by the datasheet. This is problematic for estimating thermal effects. The datasheet for the tilt sensor states a sensitivity of 0.6%/K, which is the equivalent of 6000 ppm/K. Typically, resistors and capacitors can have thermal coefficients of a few hundred ppm, however, it is important to note that if, for example, R5 from figure 5.3 were to change in temperature, this would merely cause the cut-off frequency to change slightly. This would have a negligible effect given that the excitation is at a frequency of 50 kHz or more. The same can be said for R1 and R2 in the figure, as well as the corresponding capacitors, C1, C2 and C5. Similarly, the op amps BUF+/BUF- and BUFTILT (from figure 5.3) only state a thermal coefficient for the offset voltage. This should not effect the measurement unless the temperature changes were at a similar frequency to the drive. Figure 5.4 has several resistors that can change with temperature: Rx, Ry, Rb, Rf1 and Rf2. It is worth noting that, if Rf1 and Rf2 both change by the same temperature, and have the same thermal coefficient, then the gain equal to $G = 1 + \frac{R_{f2}}{R_{f1}}$ would not change. Similarly, if all the resistors (Rx, Ry and Rb) were to change with the same thermal coefficient, then the final result would be identical, that is $V_o = G\left(\frac{V_x+V_y+V_b}{3}\right)$.

An issue arises in the circuit when there is a non-uniformity of the heating between components, which, in this case, would result in a worst case scenario, with the largest temperature coefficients effecting the output. This would be dominated by changes on the tilt

Source	RMS Noise Voltage [μV]
Spectron Drive Circuit	
BUF+ (OPA2277a)	186
BUF- (OPA2277b)	186
BUFTILT (OPA227)	186
C1	0.0137
C2	0.0137
C5	0.293
R1	2.88
R2	2.88
R5	42.6
Tilt Sensor[†]	0.287
Sum	62.126
Spectron Summing Circuit	
Drive Stage X	62.126
Drive Stage Y	62.126
Bias Voltage (+1.5 V)	4.2
BUF1 (OPA2277a)	186
Summing Amplifier (OPA2277b)	186
Rx	2.88
Ry	2.88
Rb	2.88
Rf1	2.88
Rf2	4.07
Voltage Reference	4.2
Digitisation (12-bit)	211
Sum	220 μV = 1.07 μRad

[†]This is the thermal noise created from the impedance of one side of the tilt sensor

Table 5.1 A table of the noise contained within the spectron sensor electronics. The first set of numbers are for the tilt sensor drive for just one axis. The second includes the sum of all the noise from the drive and the final summing stage.

sensor itself, since it has a coefficient of 6000 ppm/K. Since typical resistors have temperature coefficients of the order 100's ppm/K, the tilt sensors coefficient would dominate. Therefore, we can consider just the temperature coefficient of the tilt sensor to estimate the expected tilt sensitivity of the set-up. This calculation can be made by estimating at what angle the system is from gravity followed by the expected change in the output for the stated sensitivity. If the system was levelled to a vertical displacement of 10 μm (the smallest division of the micrometers) over a baseline of 28 cm, the system would be 35.7 μRad from vertical gravity. If it is then assumed that the tilt sensor, which is subject to environmental temperature changes, could change by 200 milliKelvin in a well insulated room, the change in the output of the tilt sensor would simply be the angle, 35.7 μRad times 6000 ppm/K multiplied by 0.2 K, i.e. 42.8 nRad. This is under the most ideal case. If the vertical displacement was instead 50 μm and the temperature varied by 2 K, the output would be expected to change by 2 μRad which is not insignificant. From this calculation it should therefore be noted that, to obtain the target sensitivity of tens of μGal, the temperature of the tilt sensor should not vary by a few Kelvin, unless the system can be centred better than 50 μm.

5.3.2.2 AD7195 Setup

Table 5.2 shows the noise from the circuitry used for measuring tilt via the AD7195. The noise is dominated by the input noise at low gains, while at a high gain of 64 the noise will become dominated by the buffers on the input as the gain reduces the input noise (which is the dominant effect at low gains). At a PGA of 1, an RMS of 23.08 μV would be expected. Using the calibration of 1 mV/arcsecond, this is the equivalent of 112 nRad. With a data rate of approximately 1.2 kHz (as chopping is enabled), three stages of decimation would reduce this to 18.75 Hz, while reducing the noise by a factor of 9.26. This noise reduction would result in 112 nRad reducing to 12.1 nRad. This result shows that the AD7195 should have lower noise than the internal ADC setup.

The temperature sensitivities of the electronics are similar to that of the electronics used in the internal ADC set-up. The AD7195 has a gain temperature sensitivity of 1 ppm/K and an offset error of $\pm$100/gain which is several orders of magnitude lower than the specified values for the Spectron sensor (0.6% K^{-1} [114]). This means that the system's temperature sensitivity should be dominated by the tilt sensor (SH50055-A-009) at 6000 ppm K^{-1} which should be at least an order of magnitude larger than any resistor values in the circuit.

Source	RMS Noise Voltage [μV]
Spectron AD7195 Circuit	
Sensor	0.091
Rl	0.644
R3	0.091
R4	0.091
BUFREF+	5.87
BUFREF-	5.87
AXC+/AXC-	1.202
Input Noise (PGA = 1)	21.5
(PGA = 64)	0.6
Digitisation	0.052
Sum, PGA = 1	23.08 μV = 112 nRad

†This is the thermal noise created from the impedance of one side of the tilt sensor using a frequency of 5 kHz.

Table 5.2 Noise from the tilt sensor electronics when in use with the AD7195. Noise is dominated by the input noise of the ADC, and will benefit from increasing the gain (PGA) of the system.

5.4 Performance

5.4.1 Jewell Instruments

A calibration allows the conversion of the measured voltage into an angle. Figure 5.6 shows the steps made by moving a micrometre stage 50 microns up and down over a baseline of 28 cm on the short axis and 47 cm on the long axis, i.e. an angle of 179 μRad (short axis) and 106 μRad (long axis). The top graph shows a change of 390 mV, or 0.46 μRad/mV for the short axis. The long axis measured a change of 225 mV, i.e. 0.47 μRad/mV. These calibrations are half of the expected value that is given in the datasheet for the device (1 μRad/mV). This results in twice the voltage for a given change in angle (i.e. twice as sensitive).

Using the calibrations above, data for the tilt sensors were plotted for over 19 hours and shown in figures 5.7a and 5.7b. After regression, both graphs show a variation of up to ± 1 μRad. The second plot on each of the figures shows the amplitude spectral density in $\mu\text{Rad}/\sqrt{\text{Hz}}$, and the corresponding RMS (obtained by multiplying the ASD with the square root of the frequency). As an example, if averaged to 100 seconds, a sensitivity of 100 nRad could be achievable as the ASD is 1 $\mu\text{Rad}/\sqrt{\text{Hz}}$. A comparison can only be made to

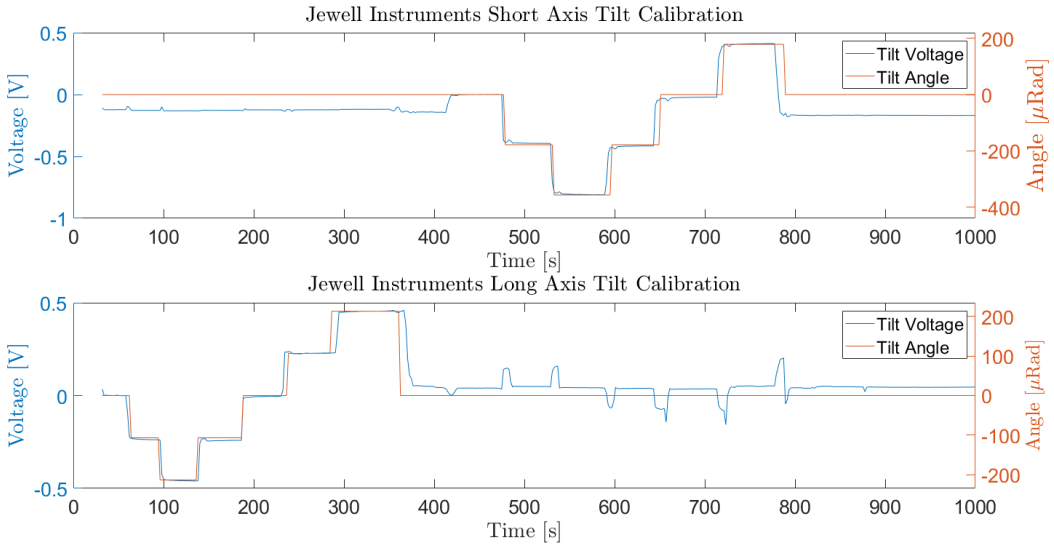

Fig. 5.6 Two graphs showing the calibration steps in the Jewell Instruments setup. The plots show a change of 390 mV for the short axis, and 225 mV for the long axis (for a step of 179 μRad and 106 μRad, respectively). These are the equivalent of 0.46 μRad/mV and 0.47 μRad/mV for the top and bottom axes, respectively. Both of these are approximately half of the specified value of 1 μRad/mV, which results in approximately twice the sensitivity (twice the voltage is obtained for a given change in angle).

the values specified in the datasheet, as it is a commercial product. The datasheet specifies a resolution of < 0.1 μRad and repeatability equal to 1 μRad. The figure shows that the product can achieve resolutions < 0.1 μRad given enough averaging and is repeatable within 1 μRad over the time period measured here (19 hours). The measurement sensitivity is also likely limited by the output of the tilt sensor conditioning card and sensor, not the ADS1248.

5.4.2 Spectron Sensors

5.4.2.1 Internal ADC Setup

As before, a calibration was carried out for the Spectron sensors. A similar calibration to the Jewell Instruments sensor was obtained of 0.49 μRad/mV and 0.44 μRad/mV (from a voltage change of 365 and 220 mV) for each axis. Both of these values are approximately twice the values given by the datasheet (0.21 μRad/mV) for the device "SH50055-A-009" electrolytic tilt sensor. This discrepancy is likely explained by the system using custom electronics, as opposed to a commercial conditioning card. For example, it could be that the company's conditioning card uses a different drive voltage.

Using the measured calibration, data for approximately 19 hours was obtained. The graphs in figures 5.8a and 5.8b show variations larger than that of the Jewell Instruments. The figures have variations of up to 2 μRad, resulting in an ASD of 3 μRad/$\sqrt{\text{Hz}}$, which corresponds to an RMS of 300 nGal at 100 s (three times larger than the Jewell Instruments).

5.4.2.2 AD7195

A calibration was also carried out on the set-up using the AD7195, resulting in a value of 0.2381 μRad/μV (750 μV for a 50 micron vertical step). For testing the sensor with the AD7195, only a single axis was measured so that two could still be used as temperature sensors.

The calibration was followed by noise tests using the programmable gain amplifier (PGA) that is built into the ADC. It was seen that the noise decreased as the PGA was increased, showing that the noise at low gain was dominated by the input noise of the ADC. This improvement in performance can be seen in figure 5.9 and shows a decrease in noise until a PGA of 32 is reached. The PGA of 64 and 128 both show no improvement, and even appears to increase in noise. The reason behind this will be discussed later in this chapter.

Another representation of the performance using the AD7195 for different gains can be seen in the ASD and sensitivity plots shown in figure 5.10. It can be seen at a PGA of 1 the amplitude spectral density is 1.25 μRad/$\sqrt{\text{Hz}}$. If averaged to 100 s, this could obtain a

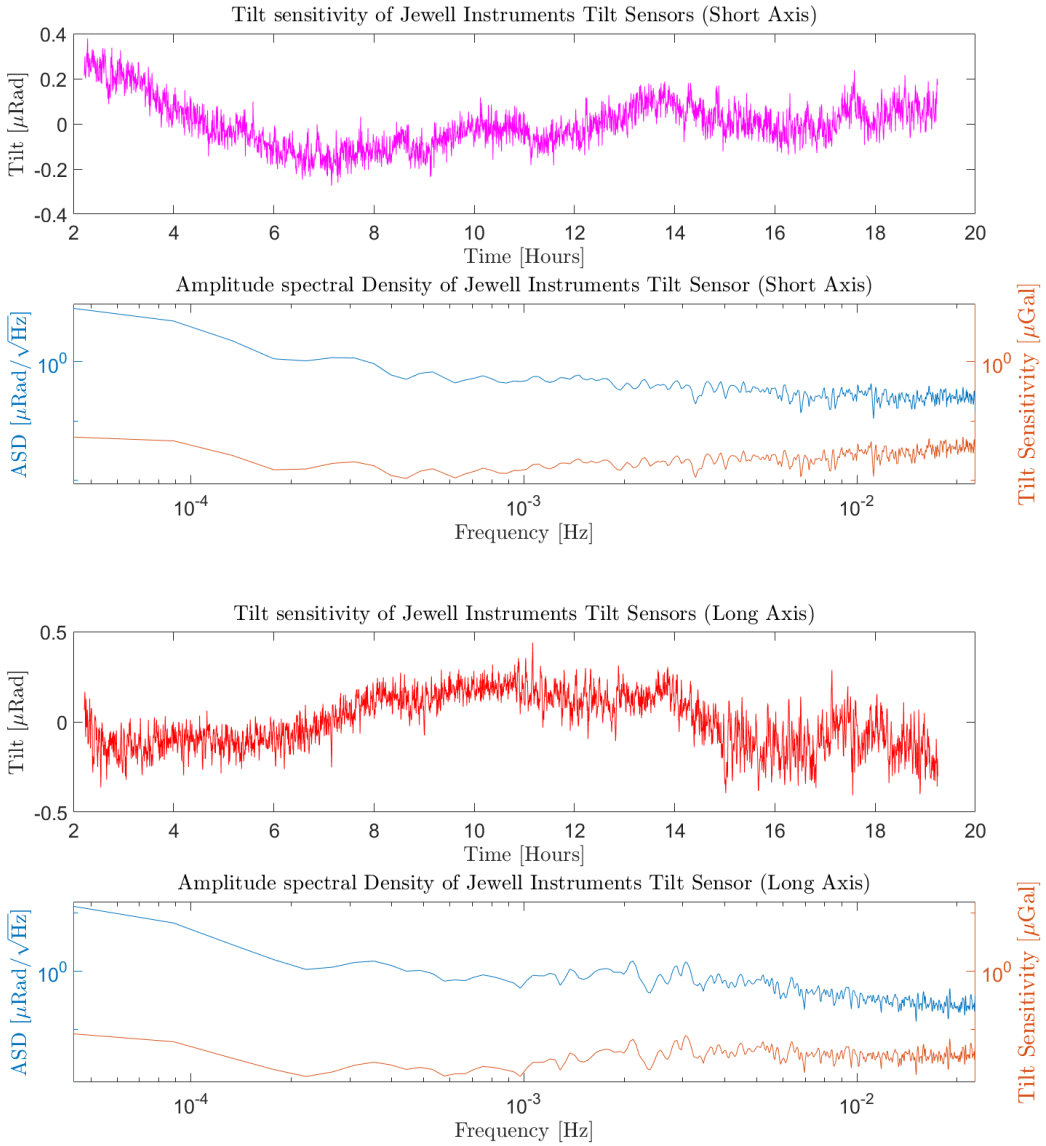

Fig. 5.7 Two sets of plots showing the tilt sensor data in the time domain (1st and 3rd panes) and the ASD (2nd and 4th panes). The 1st and 2nd panes show data for the short axis and the 3rd and 4th panes is data for the long axis. A tilt sensitivity of approximately 1 μRad/$\sqrt{\text{Hz}}$ can be seen. This is the equivalent to approximately 100 nRad at 100s. This sensitivity is the same for both axes.

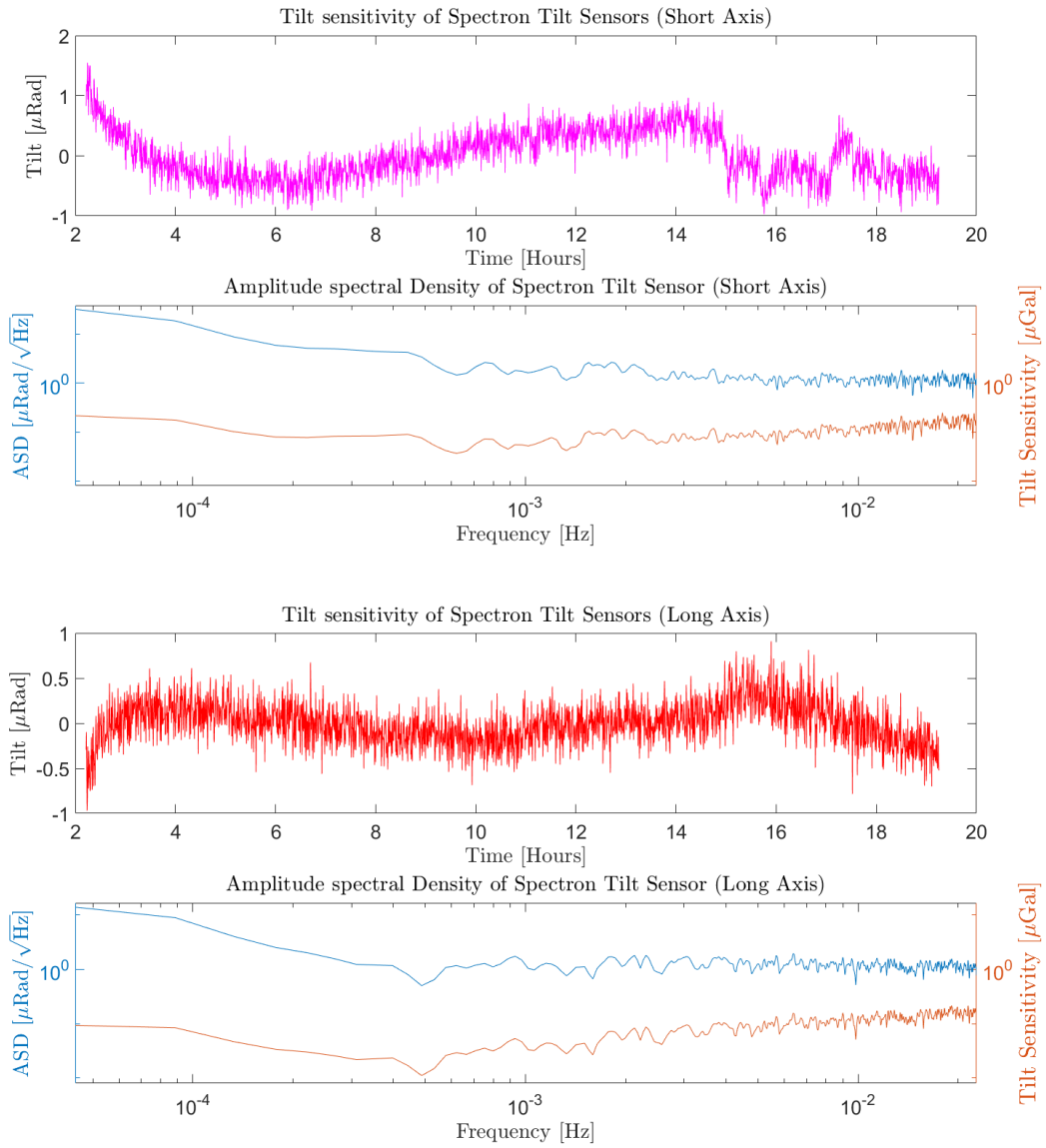

Fig. 5.8 Two sets of graphs showing the tilt data from the Spectron sensor using the internal ADC. The 1st and 3rd panes show data in the time domain where the 2nd and 4th panes show the ASD. Panes 1 and 2 are for the short axis while panes 3 and 4 are the long axis. Both axes show an amplitude spectral density of 3 μRad/$\sqrt{\text{Hz}}$, or, 300 nRad at 100s. For the Spectron Sensors, two separate devices were used, one for each axis that were then summed together for the internal ADC to sample.

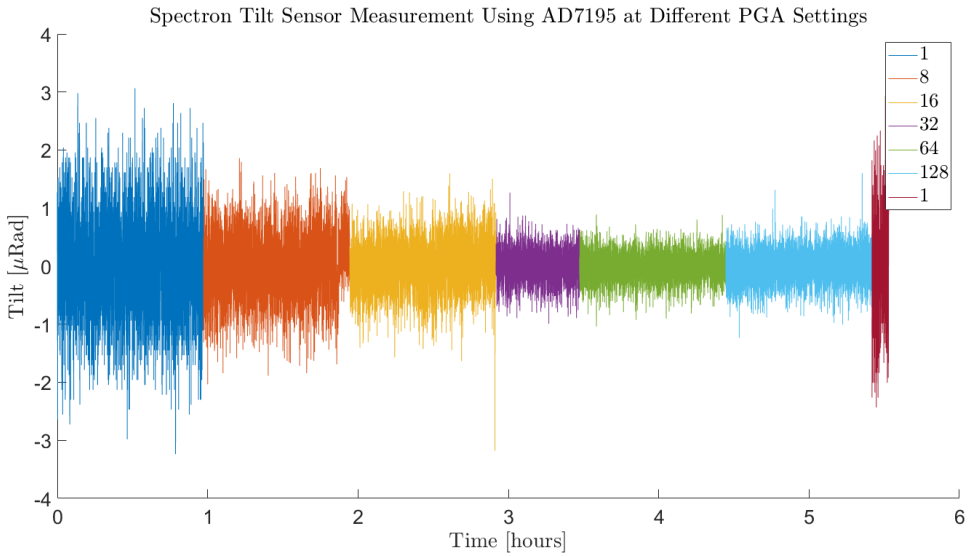

Fig. 5.9 Graph of the noise from the Spectron sensor using the AD7195 readout as a function of the PGA setting. It shows a clear decrease in noise as the PGA is increased, until a gain of 32 where this trend stops. At these higher gains no further improvement is observed.

sensitivity of 0.141 μRad. Increasing the PGA also decreases the noise to a value of 0.138 μRad/$\sqrt{\text{Hz}}$, or 15 nRad at 100 s. However, it can be seen that the noise above 100 mHz is not lowered by the PGA. This noise, however, can be averaged over and removed.

Microseismic Noise

The origin of increased noise above 100 mHz looked familiar to microseismic noise that has also been seen in the MEMS device. It was this observation that was followed by a comparison of the data, at a high PGA, to a local seismometer station at Eskdalemuir, Scotland, UK, approximately 92 km from the University of Glasgow. This comparison can be seen in figure 5.11, and shows a similarity in the low frequency noise over the course of five days. Both plots have similar amplitude changes, with figure 5.12 highlighting the amplitude spectral density at three distinct moments in time during the measurement. The amplitude and frequency of the microseismic peak change over time with a clear secondary peak seen at ≈ 0.16 Hz. However, there is the primary microseismic peak that is expected below 100 mHz, which cannot be seen due to it being weaker in amplitude. It was thought that the tilt sensor has a transfer function that naturally cuts off frequencies below 100 mHz due to the bubble being heavily damped. This transfer function can be simplistically seen

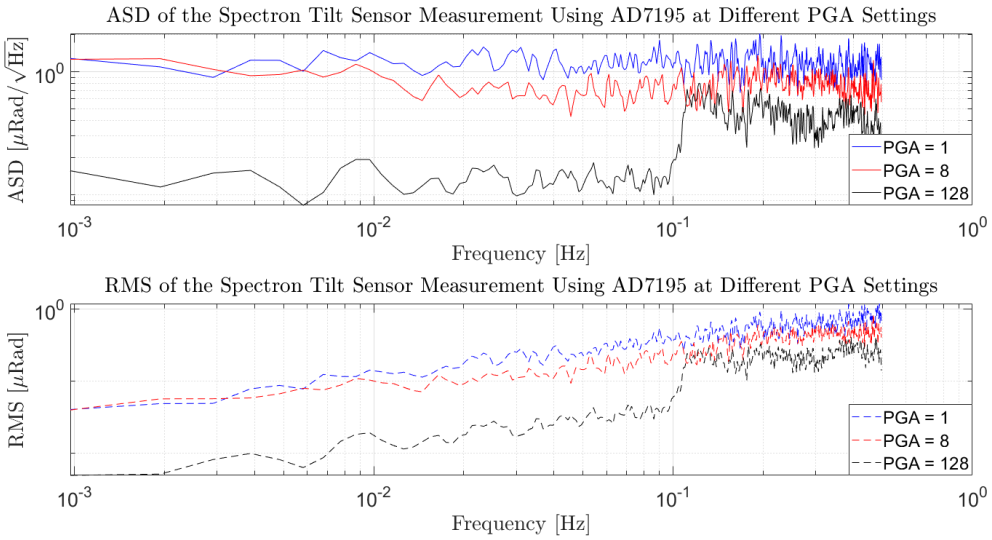

Fig. 5.10 Graphs of the amplitude spectral density from the Spectron tilt sensor using the AD7195 (upper plot) and the corresponding RMS (lower plot). The top plot shows an ASD of 1.25 μRad/$\sqrt{\text{Hz}}$ at the lowest PGA, going down to 0.138 μRad/$\sqrt{\text{Hz}}$ at a PGA of 128. The lower plot shows an RMS of 0.141 μRad at 100 s, for a PGA of 1 and 15 nRad at 100 s. At the higher gain setting a clear peak above 100 mHz appears.

as a highpass filter, with a cut-off frequency at around 100 mHz (see appendix F for more details on the transfer function of the device).

From the data presented, it is clear that the Jewell Instruments and Spectron sensor (using the AD7195) obtained the best results. With a sensitivity of 15 nRad at 100 s, the AD7195 allowed the microseismic peak to be observed, demonstrating that it had the superior sensitivity. Since the system is limited by microseismic noise, better sensitivities require averaging over this frequency range, i.e. average with a time constant of at least 10 s.

5.5 Conclusion

The maximum tilt sensitivity of the MEMS has been measured to be 4.4 μGal/μRad [83], requiring the development of a tilt sensor with μRad precision. This chapter has shown the design and testing of such a tilt sensor, with affordability as its main goal. To reach this goal, three set-ups were tested. The first sensor tested was the the high gain dual axis 755-1129 electrolytic tilt sensor from Jewell Instruments. This sensor obtained an amplitude spectral density of 1 μRad/$\sqrt{\text{Hz}}$ which costs upwards of 2 thousand pounds. The second and third set-ups both used the SH50055-A-009 single axis electrolytic tilt sensor from Spectron

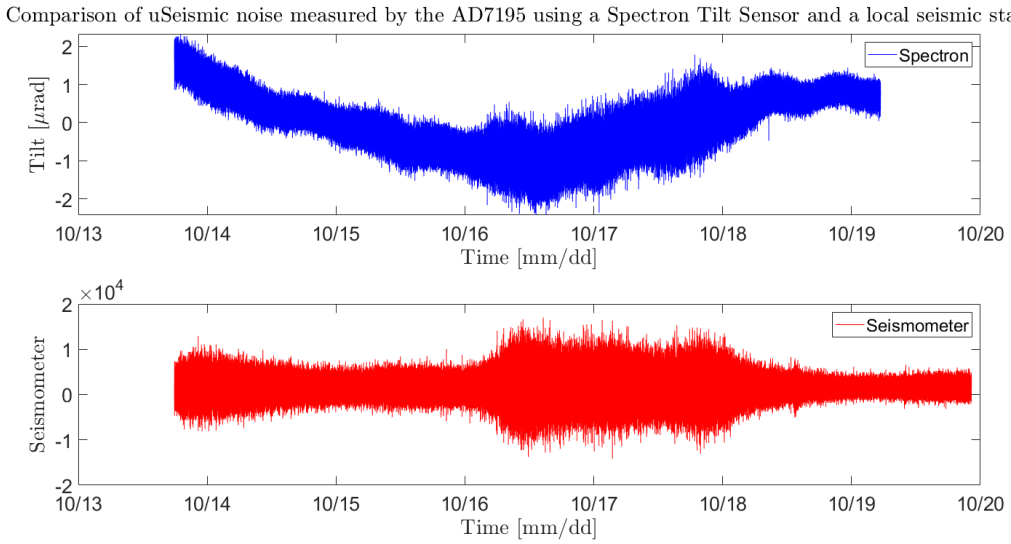

Fig. 5.11 A graph showing a comparison of the tilt data obtained using the Spectron sensors and AD7195 to a local seismic station at Eskdalemuir, Scotland, UK. It can be observed that they both have a similar amplitude which changes over time. Figure 5.12 shows the amplitude spectral density at three points during the measurement.

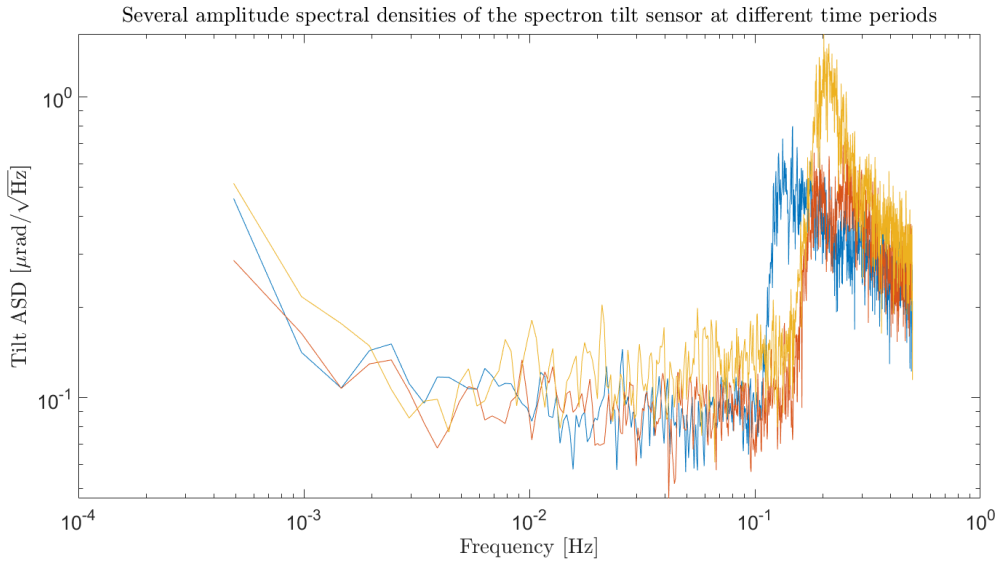

Fig. 5.12 A graph of the amplitude spectral density of the Spectron sensors using the AD7195 at three moments in time during the measurement from figure 5.11. It shows the secondary microseismic peak moving from 160 mHz to 210 mHz. The primary peak cannot be observed due to it having a weaker amplitude than the secondary.

Device	Cost [£]	Sensitivity [μRad/$\sqrt{\text{Hz}}$]
Jewell Instruments	3000	1
Spectron Sensor (Internal ADC)	200	3
Spectron Sensor (AD7195)	200	0.15 (PGA = 128)

Table 5.3 Table showing the summary of each of the set-up arrangements for measuring tilt. Although Jewell Instruments does have a lower noise when using a PGA of 1 for the AD7195 setup, the AD7195 can obtain even better sensitivities while being over an order of magnitude cheaper.

Sensors which costs approximately £200 per axis. The second set-up used the dsPIC33E internal ADC and custom electronics to give a sensitivity of 3 μRad/$\sqrt{\text{Hz}}$. The third set-up used the AD7195 $\Delta\Sigma$ ADC from Analog, achieving a sensitivity of 0.15 μRad/$\sqrt{\text{Hz}}$. This was enough to observe a clear microseismic peak at 0.16 Hz. This final set-up can obtain and RMS of 141 nRad when averaged to a 100 s. Table 5.3 shows the summary of these results, highlighting that the sensor from Spectron Sensors was at least a factor of 10 times cheaper than the Jewell Instruments set-up but with improved sensing performance.

Chapter 6

Field Prototype

6.1 Introduction

This thesis has detailed the design, development and testing of a low-cost and lightweight system capable of measuring temperatures, tilt and displacements with the aim of its use with a MEMS gravimeter. So far, individual systems have been introduced, described and their results presented. The displacement sensor shown is capable of measuring down to 0.44 nm when averaged over a 1000 s. This displacement sensitivity allows changes in the acceleration of gravity to be measured to ten μGal, which is in-line with the target sensitivity of the device. To obtain this level of accuracy, the temperature sensors had to measure and actuate with an accuracy of 0.75 mK RMS. Another important variable to monitor is the tilt of the device. The sensors presented obtained a sensitivity of 15 nRad RMS when averaged over 100 s [106], also conforming to the necessary performance of the device. This chapter will discuss the aforementioned sub-systems as a custom electronics board that was created and tested for this project. Following details of the electronics board, the realisation of the MEMS gravimeter as a field-portable device will be demonstrated. To show this, data from two successful out-of-the lab measurements will be discussed, namely, a measurement of the change in gravity from the top and bottom of a lift shaft, and a measurement of the change in gravity between two separate altitude points while going up a local hill range. The final result that will be shown is the measurement of the Earth Tides using the new miniaturised system and the comparison of this to the original measurement made by R. P. Middlemiss et al [1].

6.2 Electronics Board

6.2.1 Board Layout

To fit all of the electronic components, a four-layer custom electronics board was designed (with the help of Mr David Loomes), fabricated (by the company European Circuits Ltd), tested and improved. The layout of the top and bottom layer of the board can be seen in figure 6.1. Most of the components were populated on the top layer of the board (partially carried out by European Circuits Ltd) while the other three layers were used for routing, the analogue ground and the analogue supply voltages. A photo of the board is shown in figure 6.2.

For external connections, four Weidmuller B2L 3.50 Series 3.5mm Pitch Straight Pluggable Terminal Block, 14 way were used. Added to this, is a Hirose FX10A-120P/12-SV171 stacking board connector to allow the printed board to be connected to the microcontroller (dsPIC33E) starter kit. This connector had to be placed on one of the corners so that the USB connectors on the starter kit would face outwards.

The first design of the electronics board had several issues that only came to light after production. Two such issue were that, (a) the MOSFET gates (used in the temperature sensor) were connected the wrong way round, (b) the ADS1248's were powered in a way that did not allow voltages to be sensed that were below analogue ground. Overall, the board provided the performance that was required, and has been described throughout this thesis. The board gave acceptable performance for the: displacement sensor, temperature sensors and actuators, and tilt sensors [106]. The inability to input signals below analogue ground to the ADS1248 required the design and testing of extra circuitry as discussed in chapter 4. The MOSFET issue, however, only required the re-soldering of the gates. This re-soldering involved swapping the positions that the gates connected to for the same MOSFET type.

6.2.2 Miniaturised Platform

The custom electronics board was a significant milestone for this project, but more advancements were necessary, in particular, the vacuum housing which the MEMS is stabilised inside. To be able to take the device into the field, many changes to the experimental apparatus had to be made in order to meet the required criteria. This is particularly evident when considering that, previously, the system was attached to the inside of a vacuum chamber with the approximate dimensions of 1 metre in diameter and 1.5 metres tall. Clearly, the development of a portable platform and vacuum system would be required to test the system

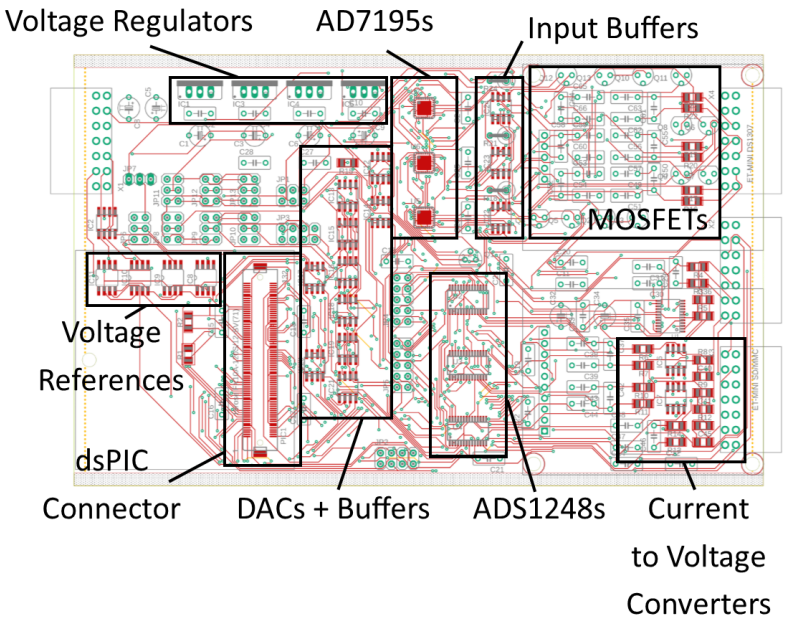

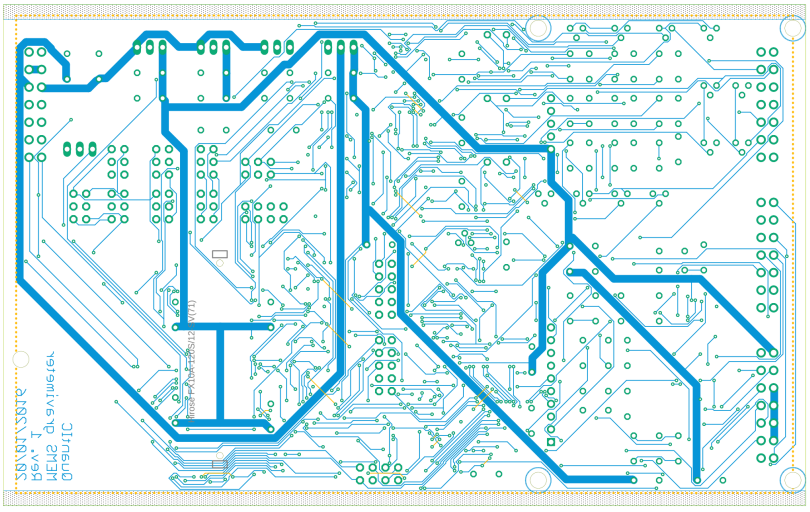

02/03/2019 21:47 f=1.60 C:\Users\Steven\Documents\EAGLE\projects\David Loomes\v3\Gravimeter.brd

Fig. 6.1 Two schematics showing the top layer (top image) and bottom layer (bottom image) of the four layer custom electronics board. The top layer contains most of the necessary electronic components for running the system, many of which are annotated in the image. The bottom layer consists entirely of tracks and vias.

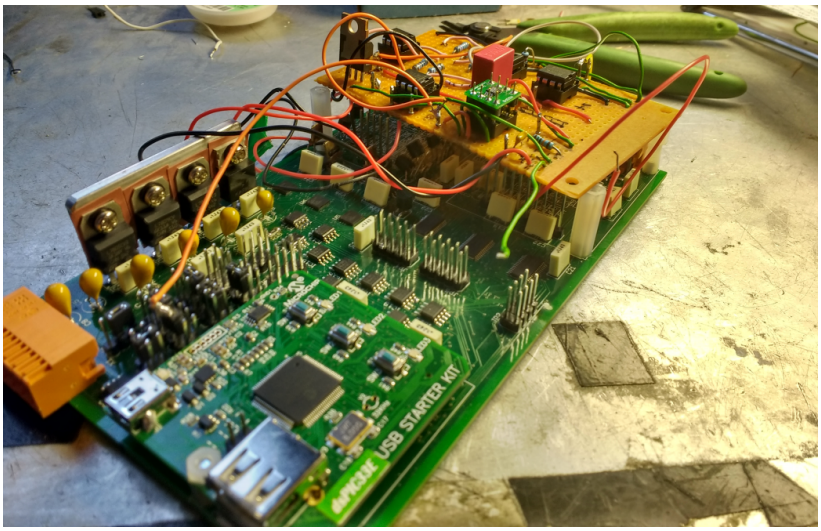

Fig. 6.2 A photograph of the populated electronics board that was designed and tested to bring the system from the lab into the field. A temporary satellite board that was used to solve the issues with the ADS1248 can be seen in the far side. This satellite board was later replaced by a simple copper board.

in the field. Two iterations of a portable platform were designed and tested, the first being larger and heavier than the second.

The platforms were both similar in design and just varied by size. Each of the platforms consisted of a stiff metal plate which had a small vacuum tank, micrometer legs (for changing the tilt), batteries and electronics board connected to it. The first system was made from a 30 cm by 47 cm by 0.8 cm aluminium plate with three holes in a triangle pattern to fit micrometer legs. This triangular arrangement of micrometer legs allowed for the tilt to be changed on both axes. The plate also had the batteries attached from which the system would be powered, initially using two 12 V lead-acid batteries and, later, two 8 V lithium-ion batteries (due to their reduced size).

For the vacuum system, a steel cube was purchased from Caburn MDC Vacuum Systems (E-CU250-6). The steel cube measured approximately 12.7 cm and weighed around 8 kg (not including flanges). The purchased cube required a flange for each of the faces. These flanges could contain electronic connectors or a glass window, or neither. The system was designed to include a getter pump. A getter pump is a passive way of maintaining a vacuum. It functions similarly to a catalytic converter, whereby a surface can adsorb particles inside the chamber such that any out-gassing or leaks can be, at least partially, negated. After using a getter for extended periods, it is recommended to condition the surface again by heating the getter to several hundred degrees for a set amount of time while actively pumping.

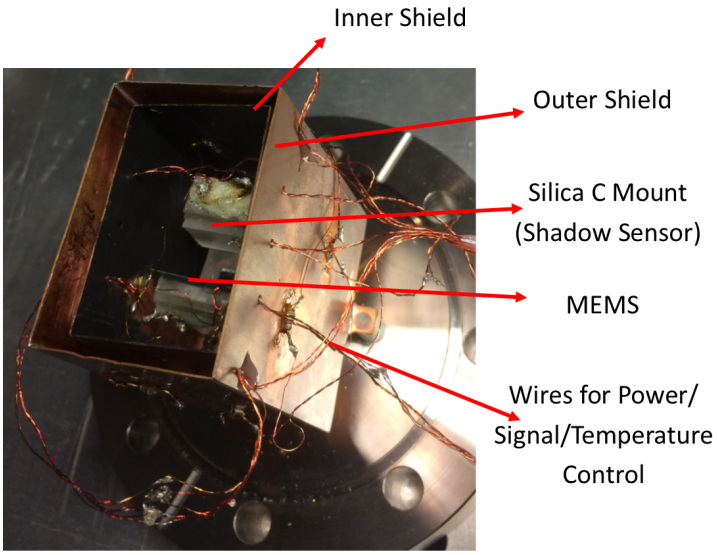

Fig. 6.3 A photograph showing the inside of the large vacuum cube. The silica C can be seen with both the inner and outer shields. The Macor spacers are not visible here as they are beneath the silica C.

This process forces any adsorbed particles on the surface to be released. During activation and conditioning of the getter pump, the system must be maintained at vacuum so that any particles that are released, are then removed from the system. Inside of the cube was a multilayer shield system for thermal isolation and control. This isolation consisted of two layers of copper separated from the steel cube using Macor spacers, Macor being a trademarked glass-ceramic used for its low thermal conductivity. The inside of the inner shield then contained the silica C which can be seen in figure 6.3. The vacuum cube was attached to the aluminium platform via three bolts, tightened from the other side of the plate.

Though the new system was somewhat portable, it was still considered too bulky to be practical, and thus further improvements had to be made. The first adjustment was the purchase of a smaller vacuum cube (E-CU150-6) from the same company. This cube was approximately 7 cm and weighed approximately 1.36 kg (not including the flanges). This change was particularly necessary as it would then allow for a smaller aluminium plate, decreasing the overall size and more importantly the weight. The newer plate was a 30 cm by 30 cm by 1 cm aluminium plate, again with the same triangular arrangement of micrometer legs. Using the lithium-ion batteries rather than lead-acid also allowed for a further decrease

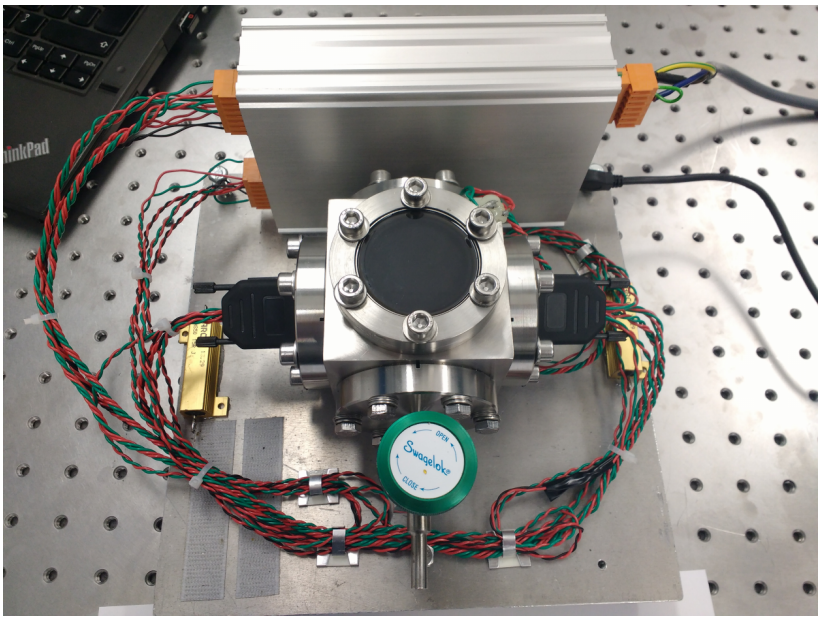

Fig. 6.4 A photograph of the 2nd miniaturised platform for taking the MEMS into the field. The system now measures 30 cm $\times$30 cm $\times$15 cm, and weighs approximately 10 kg, a much more convenient size and weight. Future work would be carried out after this project to further miniaturise the device.

in weight. One other change was not to use the getter. This was removed as maintaining a vacuum for short term measurements was not as important. To add to this, the getter introduced a significant amount of weight and bulk. This new system can be seen in figure 6.4. There was not enough space to fit a well-designed copper shield, therefore a piece of copper foil was formed into a rectangular prism shape that could be slipped over the silica C.

6.3 Lift Measurement

6.3.1 Method

The first step in field-testing of the gravimeter was to measure the change in gravity while travelling up and down in a lift. By making repeated measurements at the bottom and top of an elevator shaft (a difference of 20.73 m), the altitude dependence of gravity can be measured. An estimate of the change in acceleration from gravity can be calculated using the free air effect which is equal to $\Delta g_{FA} = -0.3086$ mGal m^{-1}. Using 20.73 m for the change in altitude, the expected change in gravity from the free-air effect alone would be equal to -6.3973 mGal. A diagram can be seen in figure 6.5 which depicts the experiment

and the local terrain. Typically measurements of gravity require a correction to be made. The Bouguer correction is the correction applied to measurements of gravity by considering the effect from an infinite slab of an assumed density. The free-air effect assumes that the device is surrounded by air and not ground/rock while increasing in altitude. The Bouguer anomaly takes into account that as measurements are made at increasing altitudes, it is more likely there still exists rock/ground that acts to increase the acceleration due to gravity. Since the Bouguer correction normally results in a higher absolute value of gravity as altitude increases, the change in gravity from one point to another is reduced. The Bouguer correction is important as the lower measurement was 9 m below ground. The effect from taking measurements below ground result in a correction that is of the opposite sign and twice what it would have been above ground (as stated by H.O. Seigel [118]). The effect is doubled because, as the sensor is moved below ground level, there is now less of the material below the sensor and that material is now placed above the sensor (doubling the effect), i.e. the infinite slab is removed from below the sensor and placed above. The general equation for the Bouguer correction [22] Δg_B:

$$\Delta g_B = +2\pi\rho GH \ , \tag{6.1}$$

where ρ is the mean density of the infinite slab, G is the gravitational constant and H is the thickness of the slab.

Since the publishing of the paper [2], measurements have been made using a LaCoste and Romberg g meter at same locations as this experiment. The measurement was made with the help of Bridgeporth. The commercial gravimeter gave an average difference of 4.969 mGal. Given that the commercial gravimeter is properly calibrated with an error of approximately 10 μGal, an estimate of the correction can be made. By comparing to the free-air effect, there must be a Bouguer correction of 1.43 mGal. Using equation 6.1, this would require an average slab density of 1900 kg m^{-3}. Considering that the lift shaft is expected to have material only covering one side, with a density that could be similar to concrete (2400 kg m^{-3}) which will likely be reinforced with reinforcing steel, surrounding by an unknown type of rock or mineral that could vary from 2000 kg m^{-3} to 3000 kg m^{-3}, a lower value is believable.

The small cube and platform, using a MEMS with a resonant frequency of 8.4 Hz, was first brought to the bottom of the lift shaft and placed onto the hard floor. The measurement was not carried out inside the lift itself in order to remove accelerations caused by the lift shaking as people walked nearby. After settling for 30 s, the system was put back into the lift and taken to the top of the lift shaft where a second measurement was taken on the

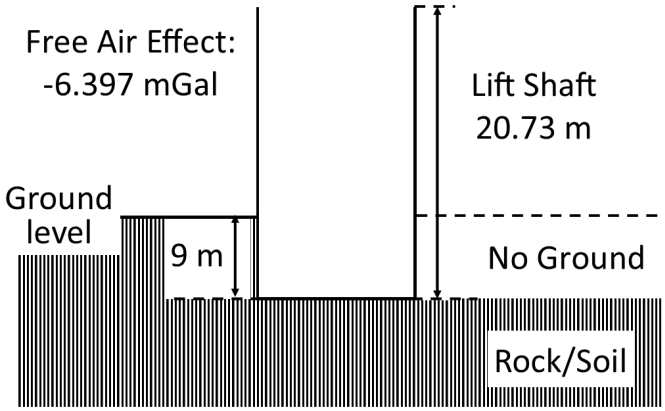

Fig. 6.5 A diagram depicting the lift measurement while showing the local terrain. It can be seen that the bottom of the lift is partially covered by ground on one side, resulting in the need for a correction of the expected signal.

concrete floor outside the lift shaft. This process was then repeated several times at the top and bottom of the building. Figure 6.6 shows a picture of one of the tests in the lift before it was realised that excess noise was being produced by leaving the gravimeter in the lift. The figure highlights several pieces of the necessary equipment for running the experiment including the batteries, electronics board, tilt sensor, laptop, aluminium platform and vacuum cube. The data then had to be post-processed to remove the remaining drift that was present in the data due to poor thermal control at the time.

6.3.2 Results

The lift measurement was carried out several times. It was evident that measurements taken while inside of the lift were noisier compared to those taken on the harder ground just outside. Figure 6.7 shows the data from a set of measurements at a sampling rate of 1 Hz with no further downsampling or averaging. The figure shows a total of four measurements, two at the top of the building, and two at the bottom. The average change was 4.57 mGal between the measurements, with a standard deviation in each measurement of 0.330 mGal, 0.326 mGal, 0.288 mGal, and 0.321 mGal (shown as error bars in the graph). Given the sampling rate of 1 s, these standard deviations are the equivalent to 0.330 mGal/$\sqrt{\text{Hz}}$, 0.326 mGal/$\sqrt{\text{Hz}}$, 0.288 mGal/$\sqrt{\text{Hz}}$, and 0.321 mGal/$\sqrt{\text{Hz}}$. It is clear that the measured value from the MEMS gravimeter is close to the commercial gravity meter (4.969 mGal). The difference between

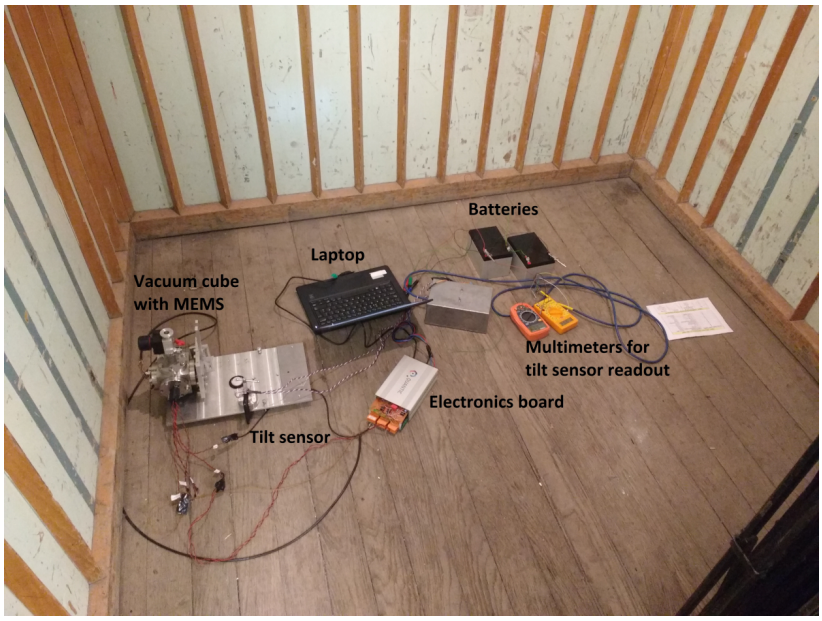

Fig. 6.6 A photograph of the lift measurement experiment set-up highlighting some of the necessary pieces of equipment including the batteries, electronics board, tilt sensor, laptop, aluminium platform and vacuum cube.

these measurements could be due to a poor calibration of the MEMS gravimeter. An error in the calibration of 10% could easily be true.

6.4 Field Test

6.4.1 Method

Following the successful lift measurements, it was decided that the next step was to take the system outdoors. Close to the University of Glasgow is the Campsie hill range, with convenient road access most of the way up. This access allowed a measurement to be taken using the large cube and platform due to it having two layers of thermal isolation in the form of copper shields, which should give the device better performance when controlled. The system was brought to the bottom of the hill (point A on figure 6.8) for the first measurement, followed by another measurement that was a 10 minute drive up the hill (point B on figure 6.8). After the measurement at the top, the device was then taken back to the starting position and another measurement taken. Each measurement required the device to be taken out of the vehicle, levelled, and the MEMS left to settle as data was gathered for up to 10 minutes.

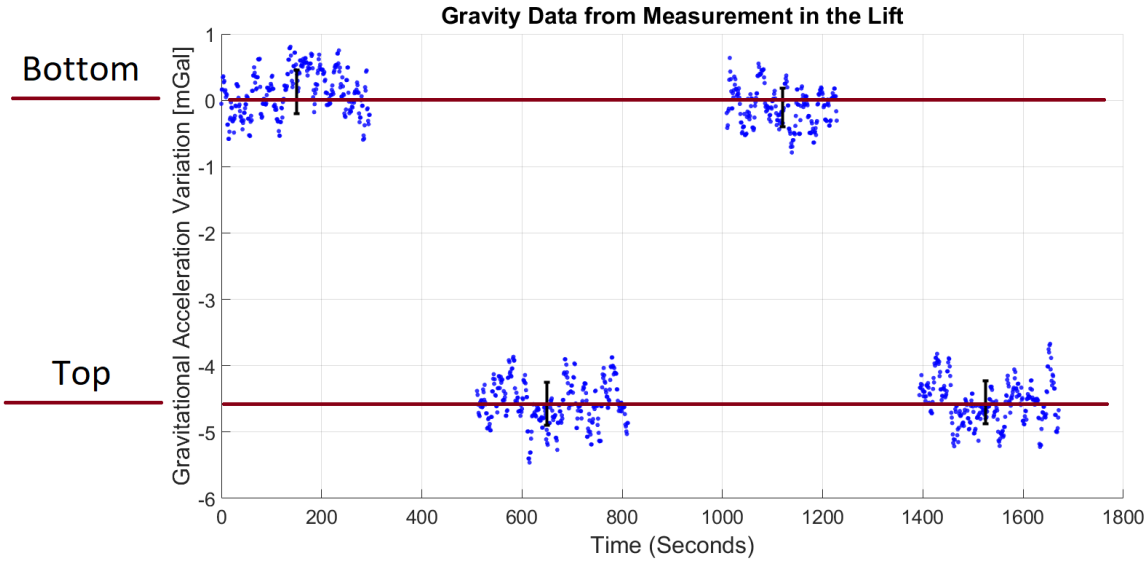

Fig. 6.7 A graph showing the data obtained from the lift tests after regression [2]. The measurements show a clear pattern with respect to the position of the gravimeter in the lift shaft. Note that the time in-between measurements have been removed, as the lift causes the MEMS to become excited. Also seen are the error bars showing the standard deviation of the measurement at that position.

The tilts were also monitored during the measurements so that adjustments could be made if excessive drift was observed.

To ensure the MEMS device survived any damage during transit, the system was placed upside-down; a method tried and tested to be the most robust form of transporting the device. This mode of transport forced the proof mass to lean against the top of the frame, which combined with the fact that the upwards direction has less displacement for the MEMS to travel, reduces the stress in the system and therefore, increases the robustness. To further increase the robustness of the system, a MEMS with a frequency of 8.4 Hz was chosen. Figure 6.9 shows the set-up at the top of the hill. It was expected that the measurement would be noisier than the lift due to the difficulty in controlling the temperature of the system while it was outside. The reason it was expected to be more difficult to control was there are much larger temperature changes associated with being outside. The wind would also cause vibrations in the MEMS, producing spikes in the data output.

The total altitude change was 259 m (from the approximate altitudes of 73 m and 332 m, which were obtained by looking at topographic maps). Figure 6.8 shows the positions on a map that were used for this measurement. An estimate of 79.9 mGal is expected when using just the free-air. This value, as before, requires a Bouguer correction. To reiterate the

Bouguer correction, as the user ascends a hill, they are still on solid terrain as opposed to ascending into the air. This extra mass acts downwards and decreases the expected signal. Using equation 6.1 from before, the estimate of 32.6 mGal can be made given that the composition of the Campsies is predominately basalt [119]. One issue with this calculation is the assumption that the infinite slab extends in all directions. To make a more accurate correction, a pyramidal shape for the slab can be considered, which results in a value that is approximately 40% of the original, i.e. 13 mGal. These values give an expected range for the measurement to be from 47.3 mGal to 66.9 mGal.

6.4.2 Results

It became immediately apparent during testing that there was excess noise in the system. This noise was not in the form of white noise, but as large spikes in the lock-in output, and was very likely caused by the MEMS being excited. It was realised that the system was being excited by the wind. The wind was an easy problem to at least reduce. Simply placing a box around the plate during measurements allowed the system to be safer from any wind effects.

To begin the analysis, a linear drift was removed as the device has some intrinsic drift. Figure 6.10 shows the regressed data. A signal of 45 mGal was measured, compared to the lower expected value of 47.3 mGal. The plot shows error bars for each stage of the measurement, with a standard deviation of 2.6 mGal and 2.7 mGal for the measurements made at the lower elevation, and 3.6 mGal at the higher elevation. The data was sampled at a frequency of 0.5 Hz with no further downsampling or averaging. By far the largest contributor to the excess noise (the standard deviations were approximately $10\times$ what was measured in the lift) was the temperature control and the wind. Both the LED and MEMS varied in temperature by nearly 75 mK over the course of the experiment. This variation was both short term and long term. Clearly any future measurements have to obtain significantly better thermal control.

6.5 Tides

From the night on the 8th of April 2018, the miniaturised system was left gathering data using a MEMS device with a resonant frequency of 2.5 Hz. The small cube and platform were placed in the basement of the Physics Building, due to the temperature stability of the room and its isolation. The system was put under vacuum, levelled, and the temperature controllers activated. This process required all of the sub-systems as described in chapters 3, 4, and 5.

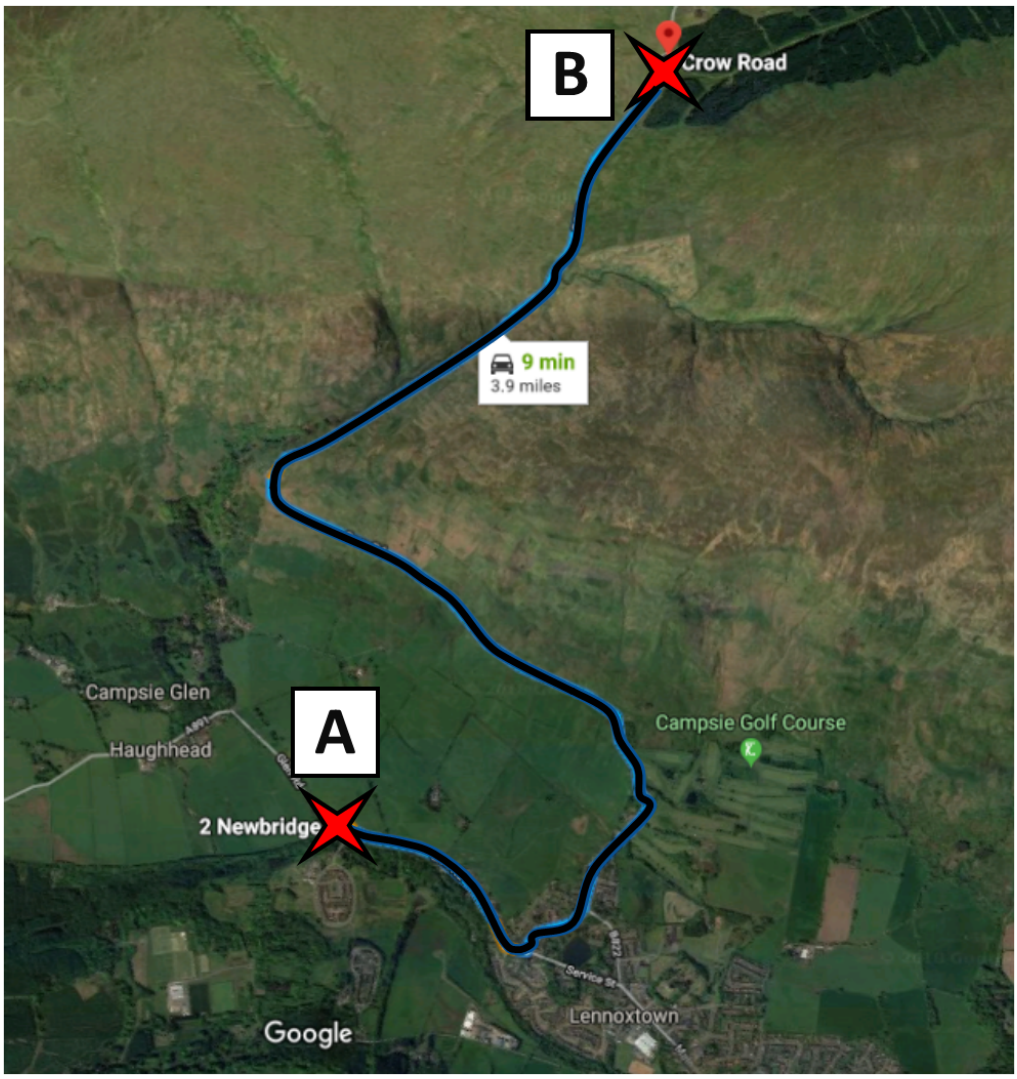

Fig. 6.8 An image from Google maps marking the measurement sites. The approximate height at the lower position was 73 m, ascending to 332 m at the topmost position. A signal between 47.3 mGal to 66.9 mGal was expected, taking the Bouguer effect into account. *Image taken from www.maps.google.com*

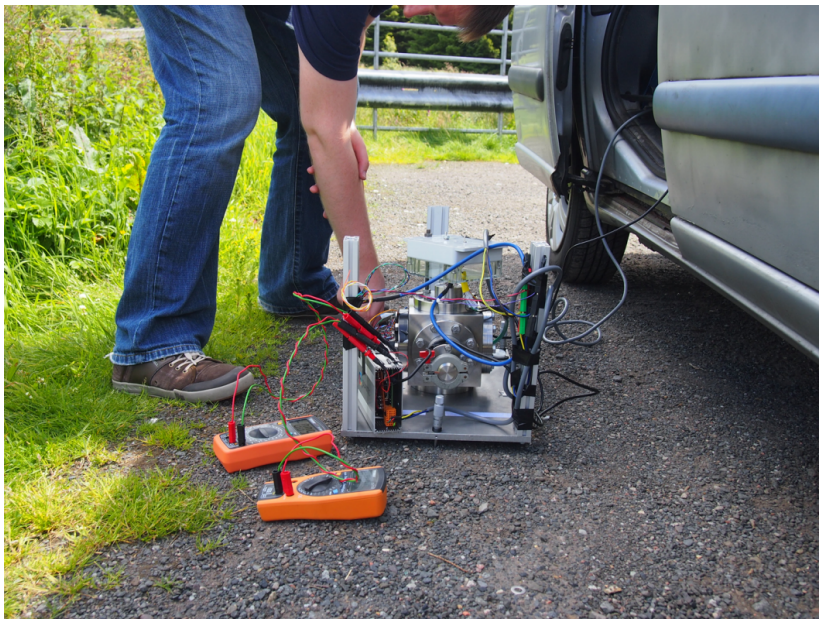

Fig. 6.9 A photograph showing the experimental set-up for the measurements at the Campsies Hill Range using the large cube set-up due to it having two thermal shield. All the necessary equipment was attached to the aluminium plate seen in the image, aside from the batteries (out of the image) and the voltmeters to allow for easier feedback from the tilt sensor for levelling.

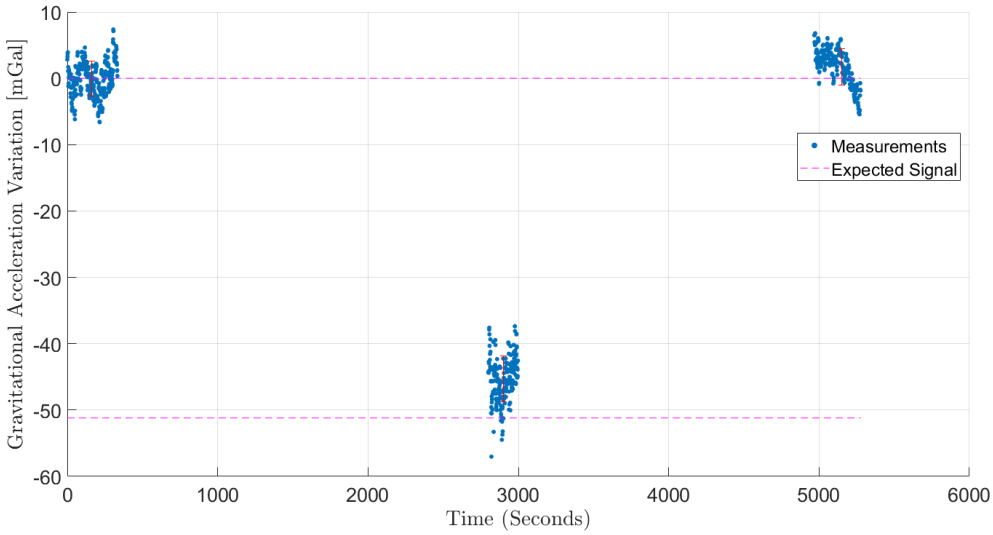

Fig. 6.10 A graph of the data gathered from the Campsies measurement [2]. It shows a change of 45 mGal, compared to the expected value of 47.3 mGal (assuming a Bouguer correction of 32.6 mGal). The error bars shown in the plot relate to the standard deviations of the data taken at each position. The standard deviation was calculated to be 2.6 mGal $\rightarrow$ 3.6 mGal.

The sub-systems, namely the digital lock-in amplifier, the temperature sensors and PIDs, and the tilt sensors were logging data for up to 101 hours using the dsPIC33E. After about a week of measurements, post-processing began. It was evident that during the experiment, the LED and shield temperature varied considerably. This variation can be seen in figure 6.11. The figure shows the lock-in amplifier data after four decimation stages against each of the three temperatures, noting that no obvious Earth tide signal can be observed. Both the LED and the shield vary by up to 50 mK while the MEMS is controlled within 2 mK. Both the LED and shield are more susceptible to changes in temperature. The likely reason for the poor thermal control on the LED was the location of the temperature sensor and heater. Although the temperature sensor was close to the LED, the heater was approximately 1 cm away through the silica. This would result in slow response times for the PID, especially when under vacuum, making it harder to control. The shield, however, is closer to the outer environment, and thus, is more likely to vary. The graph clearly shows a similarity in shape between both the LED and shield temperature to the lock-in data. As previously described in chapter 4, regression is a technique to calculate the correlation between multiple variables (a series of dependant variables). Regression is often used in econometrics [120] and was used in the work previously done by R. P. Middlemiss et al [2, 1, 83]. A regression tries

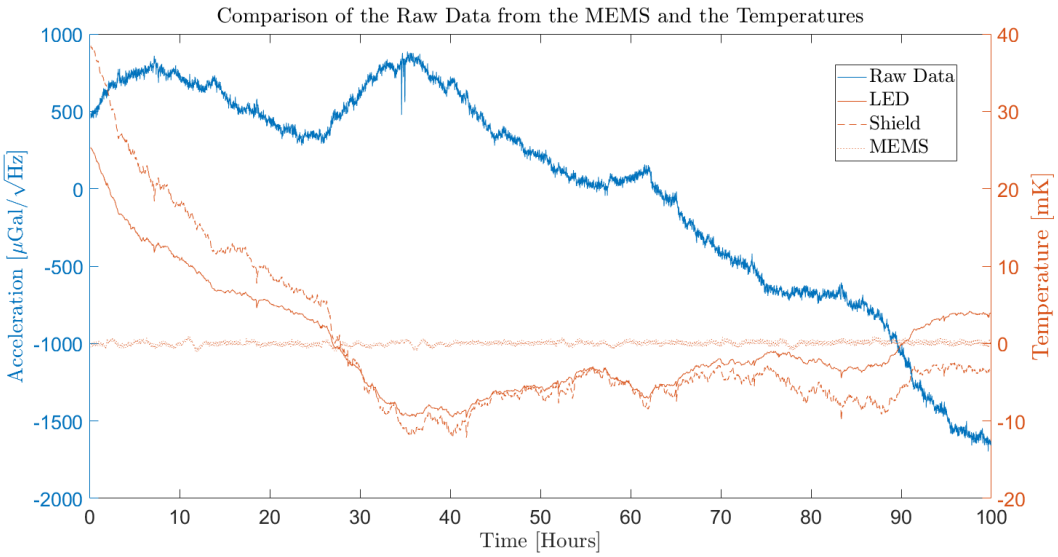

Fig. 6.11 A graph showing the raw data from the lock-in amplifier after four stages of decimation against the three measured temperatures (LED, MEMS and shield). A clear similarity in shape can be seen between the LED, shield and lock-in output. A regression was required to understand which data was correlated.

to minimise the sum of the square residuals of a given fit function, i.e. a regression carries out a least squares fit between each of the co-variables and the main variable. Given such a technique, the correlation coefficient from all measured quantities (three temperatures and two tilts) could be calculated.

The basis of a multi-variable regression is that a series of dependant variables X_i change the mean value of the dependant variable Y, given the partial regression coefficients β_i [120]. This description leads to equation 6.2.

$$Y = \beta_1 X_1 + \beta_2 X_2 + \beta_3 X_3 + \ldots + \beta_n X_n \, . \tag{6.2}$$

Given that the measurement will likely contain an offset, X_1 is equal to unity (a constant dependency on that partial regression coefficient throughout the measurement). Similarly, for this application, X_2 relates to the linear drift in the system, and therefore, is the equivalent of the time variable t. The other X terms relate to the three temperatures and two tilts. Substituting these terms into the previous equation, equation 6.3 is obtained. This equation is the regression relationship specific to this application and choice of regression variables.

$$Y = \beta_{\text{Offset}} + \beta_{\text{drift}} t + \beta_{\text{LED temp}} T_{\text{LED temp}} + \beta_{\text{MEMS temp}} T_{\text{MEMS temp}} + \beta_{\text{shield temp}} T_{\text{shield temp}} + \beta_{\text{tilt X}} \theta_{\text{tilt X}} + \beta_{\text{tilt Y}} \theta_{\text{tilt Y}} \,. \tag{6.3}$$

To obtain the regression coefficients, the MATLAB script "Mregg" was used [121]. This script simply requires the regression variables to be input. The output takes the form of an array with the length equal to the number of regression variables. These regression variables can then be multiplied with the respective variable and summed together. This summed value is then subtracted from the data, leaving the regressed data. A set of correlation coefficients are obtained in terms of μGal/unit, where "unit" is variable dependant. For example, "unit" would be Kelvin for the temperatures (or mK). Table 6.1 shows the resulting correlation coefficients from this experiment. Though perhaps not obvious from table 6.1, the linear drift and LED temperature end up contributing the most to the measurement. The reasons for the temperature sensitivities have already been discussed at length, however, the reasons behind the drift have not. Though it is not known for certain, one of the main reasons could be that the LED is ageing, resulting in it producing less light for a given current over time. This would produce the linear trend seen throughout all measurements. It is worth noting that drift is not exclusive to this device but is also found in commercial gravimeters such as the CG-6 discussed in chapter 1. The CG-6 drifts by up to 200 μGal/day which is not that different from the 640 μGal/day measured here. It is also worth noting that the correlation coefficient for the MEMS temperature seems particularly low. This can easily be explained by how well the PID was operating for the MEMS. Since the MEMS temperature just appears as white noise with no drift, a regression cannot distinguish changes in the temperature with changes in the output from the lock-in, therefore, the coefficient would appear as zero. If the MEMS temperature also changed over time, a more accurate value for the coefficient could then be obtained.

A fit function can be calculated from each correlation coefficient and the corresponding variable data (i.e. $\beta_i X_i$). These fits were plotted and can be seen in figure 6.12 alongside the raw data from before. It is clear that once these fits are subtracted from the raw data, the graph will appear different in shape. As already noted, the linear drift and LED temperature are the largest contributors for variations. Figure 6.13 is obtained by subtracting the sum of all fits from the raw data [122]. Figure 6.13 shows the regressed data alongside the expected tide signal in the time domain (top graph), as well as the amplitude spectral density and RMS (bottom graph). The theoretical tide signal was generated using the software called "TSoft" [123]. To use "TSoft", the latitude and longitude of the measurement's position (Glasgow),

Coefficient Term	Correlation Coefficient, β
β_1 Offset	1353 μGal
β_2 Drift	-641.7 μGal/day
β_3 LED Temp	57 μGal/mK
β_4 MEMS Temp	0.16 μGal/mK
β_5 Shield Temp	7.7 μGal/mK
β_6 Tilt X	-3.2 μGal/mV
β_7 Tilt Y	98 μGal/mV

Table 6.1 A table showing the regression coefficients for the data gathered that was started on the 8th of April. Though difficult to see given the different variables, the linear drift and LED temperature coefficients gives the largest effect for the experiment. With a correlation coefficient of 57 μGal/mK, a change of 40 mK would result in an acceleration change of 2280 μGal. Likewise, over 101 hours, the linear drift reaches a correction of 2700 μGal by the end of the data.

combined with the date, are required, however, it is worth noting that the loading from the water tides has been ignored as they only contribute approximately 5% of the total signal. The regressed data does appear to follow the predicted tides well. The lower graph shows the ASD with a sensitivity of 180 μGal/$\sqrt{\text{Hz}}$ at 125 s, which is the equivalent to an RMS of 13 μGal at 1000 s.

To understand if the signal seen was caused by the Earth tides, and not by other random fluctuations, a cross correlation between the measurement and the theoretical tide data was calculated. To do this correlation, a function in MATLAB called "corrcoef" was used. By inputting the measurement and a theoretical tide signal, the script calculated a correlation coefficient of $R = 0.541$. This value on its own does not give too much information, therefore, a technique known as random permutation statistics, which is a type of Monte Carlo simulation, was used to obtain a value for the confidence in the measurement. The method requires the measured data to be randomly permuted 1000+ times [124, 125], and the resulting correlation coefficient of each set of data to be noted. The histogram seen in figure 6.14 was obtained by permuting the data 10000 times while running the "corrcoef" script on each set. The histogram shows a standard deviation of 0.0127, i.e. a system with the noise from this experiment has a correlation coefficient of 0.0127 when randomly shuffled. This means that an $R = 0.541$ is equal to $0.541/.0127 = 42.6\sigma$ from the centre of such a histogram. 42.6σ is an extremely high level of confidence. It is the equivalent of a $< 1.7 \times 10^{-250}$ chance that the measurement was in-fact just random noise, lending confidence to the notion that the signal seen was caused by the Earth tides.

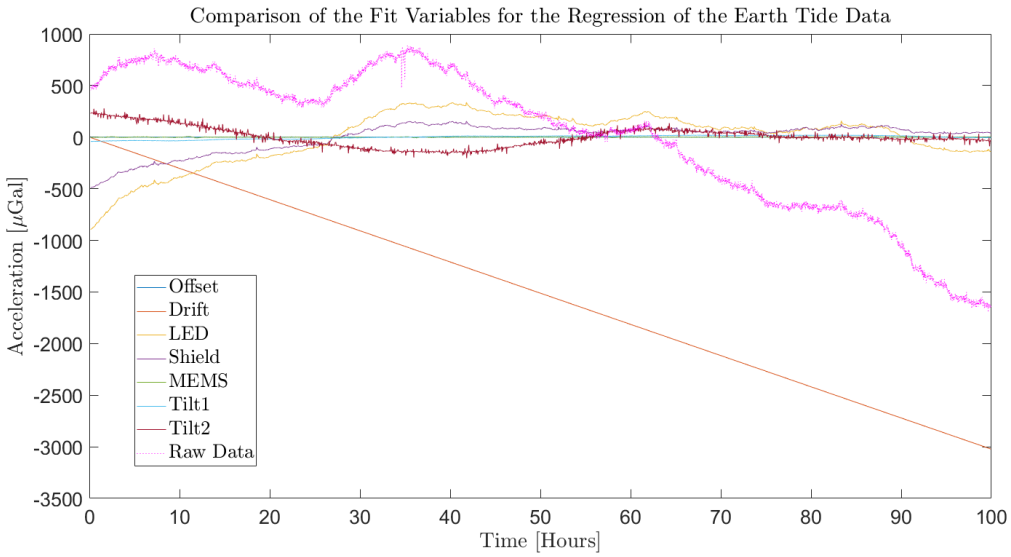

Fig. 6.12 A graph showing each of the fit functions obtained using the correlation coefficients (from the regression) and the dependant variables. It is clear that subtracting these fits from the raw data will drastically change its shape, the largest contributor of which is the linear drift and LED temperature.

As a comparison, the original data as reported by R. P. Middlemiss et al. [83] obtained a confidence of 114σ with an RMS of 30 μGal at 1000 s. The data presented in this thesis, shows a confidence lower than the original work (42.6 σ as opposed to 114 σ), but is likely due to this measurement containing less of the Earth tide signal (smaller time period), and therefore, is more likely that random permutations will mimic the theoretical tide signal. Even though the sigma reported here is lower than that of R. P. Middlemiss et al., the miniaturised system has been shown to have a better performance when averaged to 1000 s, 13 μGal compared to 30 μGal.

6.6 Conclusion

This chapter set out to combine the sub-systems which were described in chapters 3, 4 and 5. The chapter has highlighted the custom electronics board and several portable platforms. With the platforms and electronics board, several out-of-the-lab experiments have been described and their results presented. The first experiment carried out measured the change in gravity from the bottom and top of a lift shaft. From a 20.73 m change in altitude, a signal equal to 4.57 mGal was obtained. This is compared to the value of 4.969 mGal that was measured by

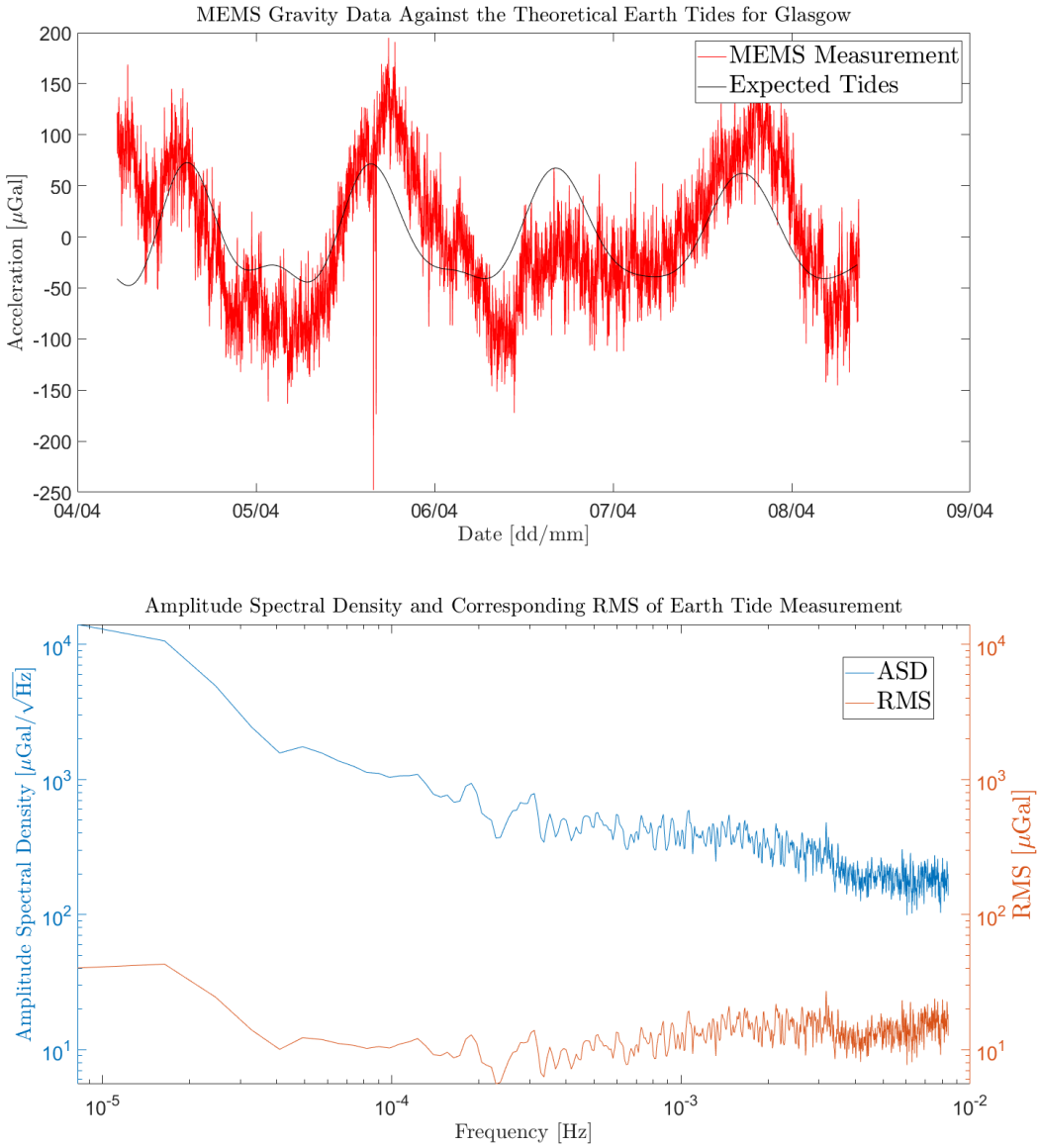

Fig. 6.13 Two graphs showing the regressed data measured by the miniaturised platform against the theoretical tide data (top graph) and the ASD and RMS of the measurement (bottom graph). A clear similarity in shape between the regressed data and the theoretical tide signal can be observed. The measurement is the equivalent of 180 μGal/$\sqrt{Hz}$ at 125 s. This is the equivalent to an RMS of 13 μGal at 1000 s.

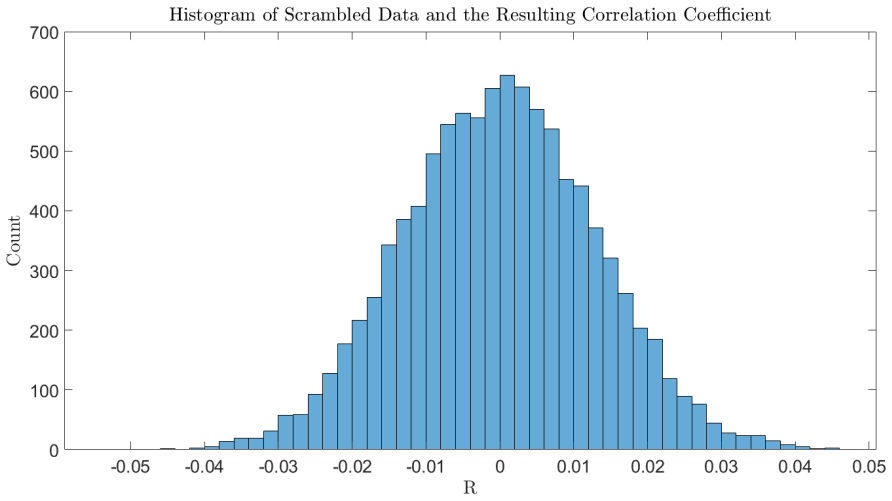

Fig. 6.14 A histogram showing the distribution of correlation coefficients generated from randomly shuffling the measured data. The distribution shown gives a standard deviation of 0.0127. Comparing this standard deviation to the correlation coefficient of the original data (0.541), a confidence of 42.6 σ can be calculated.

a commercial gravimeter (LaCoste and Romberg g meter). The lift measurements made in this thesis obtained a standard deviation of approximately 0.3 mGal as compared to 0.01 to 0.02 mGal that is stated in the user manual for the LaCoste and Romberg g meter. These tests were following by measuring the change in the acceleration due to gravity while ascending a local hill range, known as the Campsies. From a change in altitude of 259 m, a change in acceleration of 45 mGal was measured. This value is close to the lower limit of the theorised 47.3 mGal, which was calculated using a Bouguer anomaly of 32.6 mGal. The final of the measurements was the detection of the Earth Tide signal using the miniaturised platform and electronics board. The result from this measurement can be seen in figure 6.13 and shows a clear similarity between measurement and theoretical tide. The figure shows an RMS of 13 μGal over 1000 s, compared to 30 μGal from the original measurement as reported by R. P. Middlemiss [83]. To confirm that the system did measure the Earth Tides, a cross correlation between the measurement and the theoretical Earth Tide was calculated and compared to a series of permutated data sets. This process gave a confidence of 42.6σ, compared to 114σ from the original as reported by R. P. Middlemiss.

Chapter 7

Improvements, Future Work and Conclusion

7.1 Summary and Conclusions

The design, modelling and testing of an electronics platform has been presented in this thesis. The necessary techniques, testing and analysis to miniaturise a MEMS-based gravimeter have been outlined. This device, named "Wee-g", is lightweight, low-cost and portable, three attributes of the most significance to the field of gravimetry. These qualities render "Wee-g" an industry disruptive technology that could revolutionise the gravimetry sector. Potential buyers and funding bodies required proof that the device was not a lab-bound research interest but a feasible new technology capable of being commercially distributed. The system had to be removed from the lab, tested, and demonstrate that the device can take accurate measurements in the field.

The MEMS gravimeter presented in this PhD project has been shown to measure the Earth Tides with an RMS of 13 μGal when averaged to 1000 s. The system was also shown to be able to measure real changes in gravity when ascending a local hill range with a standard deviation of 2.6 mGal as well as changes in gravity when ascending in a lift with a standard deviation of approximately 300 μGal, showing promise for the MEMS's future commercial use. As a comparison, the RMS reported in this thesis (13 μGal) is a factor of three better than the original set-up as reported by R. P. Middlemiss (40 μGal [83]) when both are averaged to 1000 s. To compare the sensitivity of the device to real signals, changes in gravity of 45 μGal have been shown as 'clear precursors' to a volcanic eruption in the Canary Islands in 2011 [126].

The platform required the development of a portable vacuum system that could be adjusted for tilt, as well as the design and testing of a custom electronics board. An electronics board was necessary to control temperatures to the milliKelvin level to mitigate the temperature sensitivity of the Young's Modulus in the MEMS. The value of this sensitivity was simulated to be 115 μGal mK^{-1} using ANSYS and Solidworks models. It has been shown that the system can control temperatures within an RMS noise of 0.75 mK (an ASD of 0.74 mK/$\sqrt{\text{Hz}}$). Two other temperatures were also shown to be controlled in parallel with an ASD of 1.9 mK/$\sqrt{\text{Hz}}$ and 1.1 mK/$\sqrt{\text{Hz}}$. To obtain sub-milliKelvin control, an ADC from Analog Devices (AD7195) was used in a half-bridge configuration, utilising a ratiometric four-wire measurement. The actuation on the temperature was achieved using a DAC and buffer to output a voltage over a resistor. To further decrease the noise, the dsPIC33E microcontroller from Microchip was used to implement digital filters.

The board had to be able to measure nanometre level displacements in the proof-mass, providing a precision of tens of microGal. The board was shown to measure displacements of 0.63 nm RMS when averaged to 1000 s; which allows ten microGal sensitivity. To sense below a nanometre, an optical shadow sensor and digital lock-in amplifier was developed. A noise model was formulated to compare the final performance to what was expected in the system. It became apparent that there was a lot of excess noise in the system compared with what was expected. Measurements indicated that the excess noise originates from the LED (for the long term noise) and ADC, ADS1248 (for short term noise). The dsPIC33E was required for a series of digital filters (created with the aid of Mr. David Loomes) that reduced noise and the sampling rate. From the filters, a displacement sensitivity of 14 nm/$\sqrt{\text{Hz}}$ was obtained. Unfortunately, since the noise was not white and increased at lower frequencies, the measurement was limited to 0.44 nm RMS regardless of filtering. By comparing the performance of the MEMS gravimeter to the Scintrex CG-6 Autograv™Gravity Meter (discussed in chapter 1), it can be seen that the MEMS is approximately 10 times worse in accuracy. However, the MEMS gravimeter will be at least an order of magnitude lower in cost, size and mass making it a disruptive technology in the gravimeter industry.

Finally, the board has also proven capable of measuring changes in tilt to within a microRadian, allowing for precision levelling of the system. For a baseline tilt measurement, a dual axis electrolytic tilt sensor was used with a dual channel conditioning card (both from Jewell Instruments). The baseline measurement gave a sensitivity of 1 μRad/$\sqrt{\text{Hz}}$. This set-up was followed by two different configurations using a lower-cost electrolytic tilt sensor from Spectron Sensors. Both of these set-ups required different circuits to be designed and tested to replace the costly conditioning card. The first experiment using the Spectron's

tilt sensor obtained a sensitivity of 3 μRad/$\sqrt{\text{Hz}}$ compared to just 0.15 μRad/$\sqrt{\text{Hz}}$ for the second. The first experiment used the built-in ADC to the dsPIC33E microcontroller and a half-bridge but was noted to be noisy, and so, the AD7195 that had been used for temperature sensing was tested in a full-bridge configuration. This full-bridge was shown to have superior performance and was a factor of 10 lower in cost. Tilt sensing was required due to the gravimeter only sensing in one axis, and therefore, any changes in tilt would reduce the component of gravity measured. A larger effect, however, is due to the geometry of the MEMS only using three flexures. Only having three flexures (rather than four) results in an asymmetric restoring force, which causes excess sensitivity to changes in tilt.

The performance just stated has allowed the device to be tested in the field, proving that "Wee-g" was no longer lab-bound. Each sub-system discussed reduced the dimension of the "Wee-g" gravimeter from a fridge-freezer to just 30 cm wide by 30 cm deep by 15 cm high. The first out-of-the-lab experiment was measuring the change in gravity when ascending in a lift. This measurement obtained a change in acceleration due to gravity of 4.57 mGal with an average standard deviation of approximately 0.300 mGal. A value of 4.969 mGal was measured using a commercial gravimeter (LaCoste and Romberg g meter). The second field test was a measurement of the change in gravity while ascending a local hill range. The expected signal was approximately 47.3 mGal when using the lower limit, calculated by using a value of 32.6 mGal for the Bouguer anomaly. The measurement showed a change in gravity of 45 mGal with a standard deviation of 2.6 mGal $\rightarrow$ 3.6 mGal, close to the lower limit. A final measurement was then shown where an Earth Tide signal could be observed with a significance of 42.6σ. A platform of these characteristics will open up the field of gravimetry to a vast array of applications that have previously been impossible including; drone-based gravimetry and array-based gravimetry which are only two such examples of an ever-growing list of possibilities for the MEMS gravimeter.

7.2 Improvements

As with many projects, the deadlines put in place with regard to funding meant that sub-systems could not be continuously improved upon. This is evidenced by the fact that some components were made to work within an adequate standard without further improvements; it did not matter as long as they served their purpose. As an example, most of the noise in each of the sections outlined in chapters 3, 4 and 5 were above the expected value and the sources of the noise could have been located and reduced. However, since the noise was at the level that was required, it was acceptable to move on to the next stage of development.

This chapter will outline some of the possible improvements that could have been made throughout the project.

7.2.1 Displacement Sensor

After significant testing, it was found that the ADC used for sampling the lock-in based shadow sensor was not ideal. Firstly, the ADS1248 had been connected in a way that would not allow any voltages below ground, meaning a bias voltage always had to be summed on for a differential measurement. An obvious solution would be editing the board design such that the power supply was ± 2.5 V, therefore allowing the measurements of voltages below ground. Further to this, a new ADC would be preferable that could obtain higher sampling rates without increased noise. One such ADC that could have been used was the ADS1263, an eight-channel ADC that has only 2.45 μV_{rms} at a sampling rate of 2400 Hz, compared to the ADS1248's 32.3 μV_{rms} at 2000 Hz. The ADS1263 can also reach sampling frequencies of 38.4 kHz, with a noise of 103.6 μV_{rms}, though reducing the sampling rate to 19.2 kHz results in a noise of 8.7 μV_{rms}.

The introduction of a ratiometric measurement was another possible alteration to the shadow sensor set-up. This ratiometric measurement would be analogous to that of the temperature sensor, however a photodiode monitoring the power output of the LED would replace the use of a bias resistor. In it's current form, the LED directly illuminates the photodiodes with the MEMS in-between. A beam splitter was tested in-between the MEMS and the LED which would reflect approximately half of the light onto a single planar photodiode. This arrangement would allow the monitoring of the output power from the LED, consequently allowing the calculation of the ratio of the split photodiode to the total power. Unfortunately, any attempt at this arrangement resulted in much higher noise and more drift, even though several different bond methods were tested. One method was the use of Ceramabond, a ceramic paste that, when oven baked, becomes hard. Another method was to use a type of wax that was used for temporary bonding between surfaces, as it could be warmed up and removed (and was the preferred method as it was not permanent). Finally, Araldite, a binary epoxy that when mixed, cures over 24+ hours. The results of these tests were inconclusive, and so it was decided to dismiss the use of beam splitters. These failures could be as a result of the beam splitter reflecting some of the light, i.e. the signal from the photodiodes. If the system were limited by the light intensity, removing some of this light would only serve to increase noise relative to signal. The inconsistencies with the use of beam splitters could have also been due to reflections from the silica C. The introduction of anti-reflective black paint was an attempt to minimise this, but to no avail.

During LED testing, it would have been ideal had there been the time to shop around in search for a better performing LED, particularly in light of the fact that a significant issue arose when the LED was modulated. Since the LED drive (used for modulation) has been tested for its stability, the LED has to be the cause of the long term noise.

7.2.1.1 Temperature Sensor

Better performance of the temperature sensors could be obtained by increasing the PGA. A factor N increase in the PGA did not reduce the noise by a factor of N, therefore, a simple change that could have been implemented was changing the platinum resistor for one with ten times the resistance (i.e. swap the Pt100 for a Pt1000). Even with the increase in the input resistance (and therefore voltage), a PGA of up to 8 could still be used to obtain better performance. The signal could also be multiplied using a voltage amplifier which would then negate the need for the internal PGA. A voltage amplifier still increases the noise on the signal, but if the system was still limited by the AD7195 input noise better performance would be obtained. Another option would be to decrease the bias resistors resistance, however, this would be more difficult as the type of resistors used for the bias resistor have a thermal coefficient of 50 ppb/K, which makes it difficult to find smaller resistance versions without an increase in cost. Further improvement in the performance could then be made given the previous alterations are successful. In particular by experimenting with a lot of the grounding/decoupling capacitors that were not used but should have been. These decoupling capacitors could have reduced the noise on the measurement by removing higher frequency amplitudes. As with the shadow sensor, a better ADC could have been found though none have been seen thus far.

7.2.1.2 Tilt Sensor

Improvements on the tilt sensor will only be considered for the set-up using the AD7195 (the final arrangement outlined in Chapter 5). As the tilt sensor set-up utilised the AD7195, similar improvements just mentioned for the temperature sensor could be applied here. Since the arrangement still used a bias voltage as the reference, the drifting seen in figure 5.11 could be a real effect. The drifting was most likely not temperature related as the temperature had drifted continuously by almost 0.2 K in one direction whereas the tilt drift changed direction. As the system at high gains was limited by seismic noise, averaging can be used to remove this. The system could also be mounted on a seismic isolation platform to obtain a

new noise spectra, where it would likely be limited by the input noise of the ADC as with the temperature sensing set-up.

7.2.1.3 Field Tests

Although the field tests had been successful, it would always be better to obtain more data points, allowing a better estimate of the repeatability. A significant issue doing this was how time consuming the process was. The Campsies measurement for example required several people (including someone who could drive) to be free for an afternoon (though a full day would be preferable). It was also noted that the temperatures were not controlled properly during this measurement requiring improvements to be made to the set-up. These measurements had also been carried out using the large cube platform and there could be an argument made for testing the smaller cube. For one, since it is smaller, it has a lower thermal mass which should allow for better temperature control.

Though measurements in the lift could be taken in a few hours, excess noise (via excitation of the MEMS) had been seen due to people walking and closing doors nearby. These effects required the tests to be carried out when no-one was around (i.e. the weekend). The excess noise was worse at the higher altitude as the measurement was made on a mezzanine floor. The excitation of the MEMS was worse still if the measurement was made in the lift shaft. An obvious solution would be to use a vibration isolation platform for better performance.

7.2.2 Electronics Board V2.0

Originally, work was carried out in improving the board design, with the plan of ordering a new electronics board, "V2.0". In the end, the system was not ordered as progress had been made on other systems such as a field programmable gate array (FPGA). The newer board design had almost been finalised which included fixing of the previous boards mistakes and several major changes. One of the major changes was the replacement of the ADS1248 with the AD7768-8, an eight-channel simultaneous sampling, delta-sigma analogue to digital converter. The ADC would have been able to reach 256 kSPS per channel without an increase in noise. As a comparison, the AD7768-8 could reach a noise level of 7.83 μV_{rms} at a sampling rate of 256 kSPS when using the Sinc5 filter whereas the ADS1248 at best obtains 32.3 μV_{rms} at 2 kSPS. Depending on what was limiting the measurement, a higher sampling rate could lower the noise further as the modulation frequency is further away from 1/f noise. The faster ADC could have been used to modulate the LED with more points per cycle to better imitate a sine-wave. A sine-wave would allow for better filtering as a

bandpass filter could be used. The supply of ± 2.5 V was also used on the ADC rather than 0 V $\rightarrow$ 5 V which would allow measurements of inputs that were below ground (which would be needed for a high-pass filter). Since the AD7768-8 has no internal PGA, the LTC6912, a digital PGA was introduced. Even though the system had the ± 2.5 V supply, the electronics used to produce the biased differential measurement were also added to this design for future proofing. A minor change to the board was the addition of connections to all the second channels in the AD7195 temperature sensors. These additions were done to allow for twice the number of temperature/tilt measurements but would require they sampled at half the rate. The voltage references were also replaced with the LTC6655 that had been used up to now. The system also required the addition of ± 2.5 V for the IC power supplies. The DACs were also removed and replaced with three DAC8004, a 16-bit quad-channel digital to analogue converter. One of these DACs was reserved for the LED current drive and three buffered outputs. Another major alteration was the replacement of the dsPIC33E starter kit connector with a 100-pin PIM connector. This PIM connector negates the need for a starter kit and instead connects to a smaller board which contains the dsPIC33E module. This was placed on the centre of the board to be free up space that before had to be left empty for the starter kit. Having more space where the starter kit used to be also allows for another Weidmuller connector to be attached. The schematic of the second iteration of the board can be seen in appendix B.

7.3 Future Work

This project was created to develop a field-portable MEMS gravimeter from what was a lab-bound device which used a vast array of equipment to function. Due to the success presented in the preceding chapters, further projects have been funded. This section will highlight some of the future work relating to MEMS gravimeter technology that have or have yet to start.

7.3.1 Drone based Gravimetry

Gravimetry thus far has always been undertaken using bulky equipment that weighs up to 10 kg, and that costs upwards of £100,000. Consequently, gravimeters have never been applied to drones, quad-copters or any other such platforms. The MEMS gravimeter is set to be only a few 100 grams, introducing a world of possible applications. British Petroleum (BP) and

the Defence Science and Technology Laboratory (DSTL) are two of the major companies expressing an interest in the implementation of gravimeters on drones.

7.3.1.1 British Petroleum

BP have expressed an interest in replacing some of the aerial surveys that previously were obtained by low-flying light aircraft. The elimination of requiring a piloted platform would consequently eliminate the risks involved, particularly from the low-flying aspect. The lower costs involved with the removal of a pilot was also seen to be desirable by the company. The funded project would involve developing the MEMS technology that would allow the device to be flown on a fixed-wing, unmanned aerial vehicle. This fixed-wing UAV, the "Prion Mk3", has a wingspan of 3.8 m and a length of 3 m. The drone would be used to undertake unmanned aerial gravimetry surveys in search of oil and gas. The Prion has a range of over 1000 km, and can hold a maximum payload of 15 kg for up to 8 hours.

7.3.1.2 Defence Science and Technology Laboratory (DSTL)

DSTL has also expressed an interest in using the gravimeters similarly to BP: applying them to unmanned aerial vehicles. More specifically, they have displayed an interest in the detection of man-sized tunnels that are deeper than 2 m underground. This project would demonstrate the operational feasibility of rapid and passive acquisition of subterrain structure.

7.3.2 Newton-g Project

NEWTON-g, or "**New to**ols for terrai**n g**ravimetry" is a project submitted to the third FET-Open Research and Innovation Actions call. The project proposes to shift the paradigm in terrain gravimetry by creating the first "gravity imager" using the wee-g. The project aims to improve the currently poor level of knowledge of spatiotemporal changes in the characteristics and distribution of subsurface fluids (such as magma). Up to now, high-cost and bulky operating features have severely limited the field use of gravimeters. As the wee-g MEMS is a low-cost, lightweight and portable gravimeter, these issues may have been resolved. By creating a vast grid array of these devices around Mt Etna (Italy), the frequent gravity fluctuations can be monitored for scientific study. This study can be used to address critical societal issues, including sustainable energy management (i.e. hydrocarbons and geothermal), management of water resources, and the assessment of volcanic eruptions.

7.3.3 Future of wee-g

In order to begin the projects noted above, further adjustments must be made to the MEMS gravimeter discussed in this thesis, as well as further testing and refining. The future work seeks to shrink the device further, with assistance sought from the company "Kelvin Nano-Technology (KNT)" that works from the James Watt Nanofabrication Centre (JWNC). They will fabricate up to 40 MEMS, with a new design. These MEMS would include four flexures and a set of electrostatic combs that can be used as a displacement sensor (replacing the shadow sensor). Once the design of the MEMS becomes finalised, the MEMS will then be packaged into a standard MEMS package by the company "Optocap". This standard package and a prototype of the new MEMS design can be seen in figure 7.1. The new capacitive combs require different circuitry to be designed and tested. They require multiple high-speed AC signals that are out of phase, allowing the extraction of the relative overlap between combs. This extraction then allows a measurement of the displacement to be taken (or at least changes in displacement).

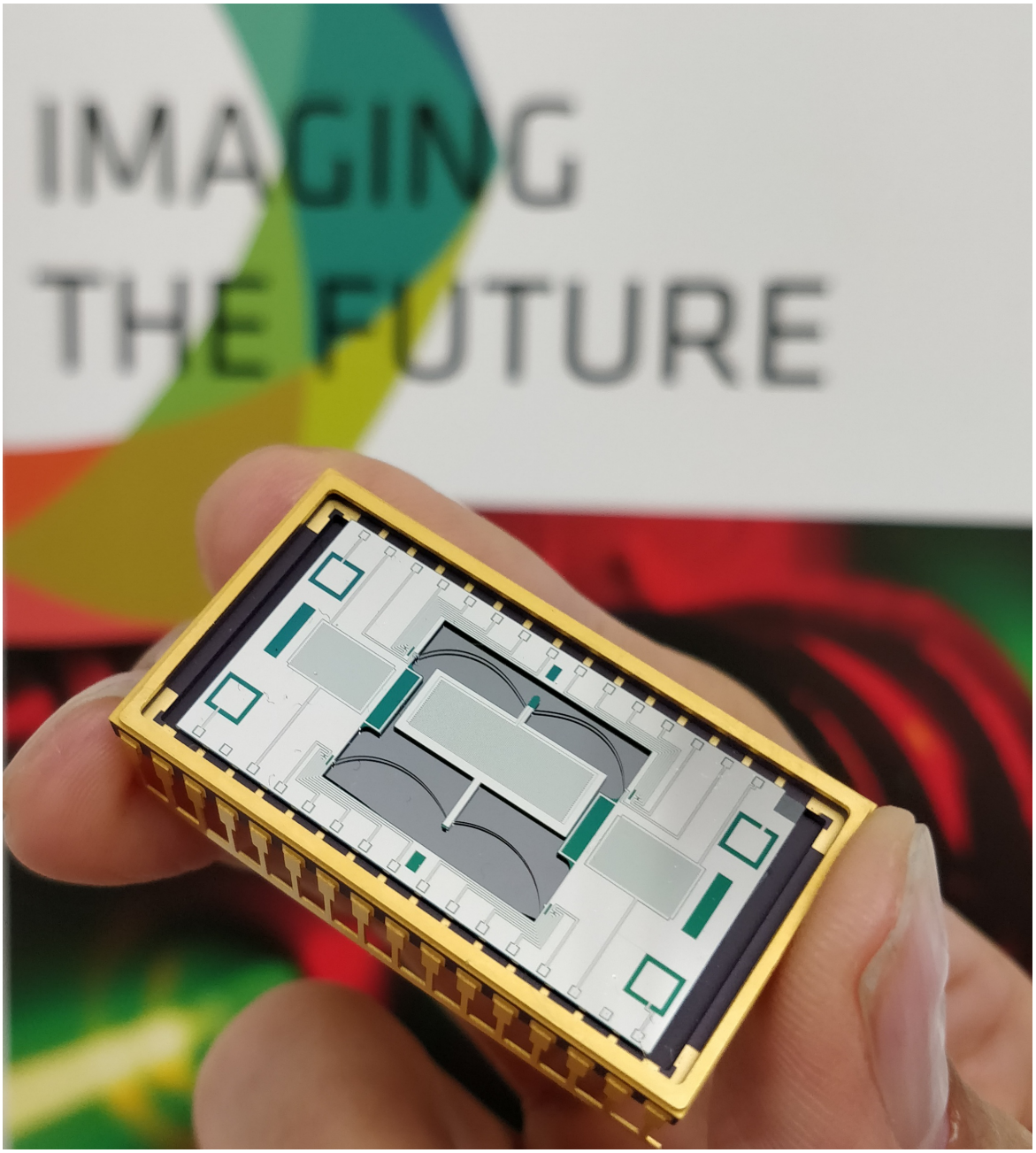

Fig. 7.1 Photograph of a new prototype MEMS inside a standard MEMS package from "Optocap". Future packages will be sealed off with a lid. The system requires new circuity to operate.

References

[1] R. P. Middlemiss, A. Samarelli, D. J. Paul, J. Hough, S. Rowan, and G.D. Hammond. The First Measurement of the Earth Tides with a MEMS Gravimeter. *Nature*, 531(1):614, 2016.

[2] R. P. Middlemiss, S. G. Bramsiepe, R. Douglas, J. Hough, D. J. Paul, S. Rowan, and G. D. Hammond. Field tests of a portable MEMS gravimeter. *Sensors (Switzerland)*, 17(11):1–12, 2017.

[3] K. Toland, A. Conway, L. Cunningham, G. Hammond, J. Hennig, S. Hild, J. Hough, R. Jones, E. Momany, L. Perri, S. Rowan, and A. Cumming. Development of a pulling machine to produce micron diameter fused silica fibres for use in prototype advanced gravitational wave detectors. *Classical and Quantum Gravity*, 35(16):165004, jul 2018.

[4] T. H. K. Barron, J. G. Collins, and G. K. White. Thermal expansion of solids at low temperatures. *Advances in Physics*, 29(4):609–730, aug 1980.

[5] M. A. Hopcroft, W. D. Nix, and T. W. Kenny. What is the young's modulus of silicon? *Journal of Microelectromechanical Systems*, 19(2):229–238, apr 2010.

[6] P. Suryawanshi and S. Karad. A comparative analysis of various tuning methods for pid control and their effects on the performance of a temperature control system. 07 2004.

[7] I. Newton. *The Principia*. Prometheus Books, 1995.

[8] A. J. Romaides, J. C. Battis, R. W. Sands, A. Zorn, D. O. Benson, and D. J. DiFrancesco. A comparison of gravimetric techniques for measuring subsurface void signals. *Journal of Physics D: Applied Physics*, 34(3):433–443, 2001.

[9] D. K. Butler. Microgravimetric and gravity gradient techniques for detection of subsurface cavities. *Geophysics*, 49(7):1084 – 1096, 1984.

[10] G. Barnes and J. Barraud. Imaging geologic surfaces by inverting gravity gradient data with depth horizons. *Geophysics*, 77(1):G1–G11, 2012.

[11] H. Rim and Y. Li. Advantages of borehole vector gravity in density imaging. *GEOPHYSICS*, 80(1):G1–G13, jan 2015.

[12] R. Yu. Gulenok, V. I. Isaev, V. Yu. Kosygin, G. a. Lobova, and V. I. Starostenko. Estimation of the oil-and-gas potential of sedimentary depressions in the Far East and West Siberia based on gravimetry and geothermy data. *Russian Journal of Pacific Geology*, 5(4):273–287, 2011.

[13] G. Kaufmann. Geophysical mapping of solution and collapse sinkholes. *Journal of Applied Geophysics*, 111:271–288, dec 2014.

[14] J. G. Paine, S. M. Buckley, E. W. Collins, and C. R. Wilson. Assessing Collapse Risk in Evaporite Sinkhole-prone Areas Using Microgravimetry and Radar Interferometry. *Journal of Environmental & Engineering Geophysics*, 17(2):75–87, 2012.

[15] J. Fernández, A. Pepe, M. P. Poland, and F. Sigmundsson. Volcano Geodesy: Recent developments and future challenges. *Journal of Volcanology and Geothermal Research*, 344:1–12, 2017.

[16] G. Williams-Jones and H. Rymer. Detecting volcanic eruption precursors: a new method using gravity and deformation measurements. *Journal of Volcanology and Geothermal Research*, 113(3-4):379–389, 2002.

[17] M. Battaglia, J. Gottsmann, D. Carbone, and J. Fernández. 4D volcano gravimetry. *Geophysics*, 73(6):WA3, 2008.

[18] D. Carbone, M. P. Poland, M. Diament, and F. Greco. The added value of time-variable microgravimetry to the understanding of how volcanoes work. *Earth-Science Reviews*, 169(April):146–179, 2017.

[19] H. Rymer and G. Williams-Jones. Volcanic eruption prediction: magma chamber physics from graveity and defromaton measurements. *Geophysical Research Letters*, 27(16):2389–2392, 2000.

[20] J. Pánisová and R. PaŠteka. The use of microgravity technique in archaeology: A case study from the St. Nicolas church in pukanec, slovakia. *Contributions to Geophysics and Geodesy*, 39(3):237–254, 2009.

[21] N. Haskins. Book Review - A Field Guide to Geophysics in Archaeology. *Archaeological Prospection*, 62(December 2009):61–62, 2010.

[22] W. Torge. *Gravimetry*. Walter de Gruyter, 1989.

[23] J. R. Smallwood. Maskelyne's 1774 schiehallion experiment revisited. *Scottish Journal of Geology*, 43(1):15–31, apr 2007.

[24] J E. J. Physical geodesy. by w. a. heiskanen and h. moritz. pp. ix + 364, and numerous diagrams. w. h. freeman and co., san francisco and london, 1967. price 100s. *Geological Magazine*, 104:302, 06 1967.

[25] M. N. Nabighian, M. E. Ander, V. J. S. Grauch, R. O. Hansen, T. R. LaFehr, Y. Li, W. C. Pearson, J. W. Peirce, J. D. Phillips, and M. E. Ruder. Historical development of the gravity method in exploration. *GEOPHYSICS*, 70(6):63ND–89ND, nov 2005.

[26] G. A. Good. *Sciences of the earth: an encyclopedia of events, people and phenomena*. Garland Publishing, 1998.

[27] P. Hariharan. *Basics of Interferometry, Second Edition*. Elsevier, 2007.

[28] K. J. Stephens and C. Wauthier. Satellite geodesy captures offset magma supply associated with lava lake appearance at masaya volcano, nicaragua. *Geophysical Research Letters*, 45(6):2669–2678, mar 2018.

[29] L. Field, J. Blundy, R. A. Brooker, T. Wright, and G. Yirgu. Magma storage conditions beneath dabbahu volcano (ethiopia) constrained by petrology, seismicity and satellite geodesy. *Bulletin of Volcanology*, 74(5):981–1004, feb 2012.

[30] R. Rummel, W. Yi, and C. Stummer. GOCE gravitational gradiometry. *Journal of Geodesy*, 85(11):777–790, aug 2011.

[31] D. P. Chambers, J. Wahr, and R. S. Nerem. Preliminary observations of global ocean mass variations with GRACE. *Geophysical Research Letters*, 31(13), jul 2004.

[32] B. D. Tapley, S. Bettadpur, J. C. Ries, P. F. Thompson, and M. M. Watkins. GRACE measurements of mass variability in the Earth system. *Science*, 305(5683):503–505, 2004.

[33] S. Swenson, D. Chambers, and J. Wahr. Estimating geocenter variations from a combination of GRACE and ocean model output. *Journal of Geophysical Research: Solid Earth*, 113(B8), August 2008.

[34] R. Pail, S. Bruinsma, F. Migliaccio, C. Förste, H. Goiginger, W. Schuh, E. Höck, M. Reguzzoni, J. Martin Brockmann, O. A., M. Veicherts, T. Fecher, R. Mayrhofer, I. Krasbutter, F. Sansò, and C. C. Tscherning. First GOCE gravity field models derived by three different approaches. *Journal of Geodesy*, 85(11):819–843, oct 2011.

[35] G. Dufréchou, R. Martin, S. Bonvalot, and S. Bruinsma. Insight on the western mediterranean crustal structure from GOCE satellite gravity data. *Journal of Geodynamics*, 124:67–78, feb 2019.

[36] G. Ramillien, F. Frappart, and L. Seoane. Application of the regional water mass variations from GRACE satellite gravimetry to large-scale water management in Africa. *Remote Sensing*, 6(8):7379–7405, 2014.

[37] R. Xiao, X. He, Y. Zhang, V. G. Ferreira, and L. Chang. Monitoring groundwater variations from satellite gravimetry and hydrological models: A comparison with in-situ measurements in the mid-atlantic region of the United States. *Remote Sensing*, 7(1):686–703, 2015.

[38] W. Torge. *Geodesy*. Walter de Gruyter, 2012.

[39] R. D. Marcus. Learning 'under fire': Israel's improvised military adaptation to hamas tunnel warfare. *Journal of Strategic Studies*, 0(0):1–27, 2017.

[40] D. Richemond-Barak. *Underground Warfare*. Oxford University Press, jan 2018.

[41] S. B. Ziauddin. Superpower underground: Switzerland's rise to global bunker expertise in the atomic age. *Technology and Culture*, 58(4):921–954, 2017.

[42] T. Cozzens. History underfoot: Secret world war ii underground bunkers and tunnels mapped. Jan 2012.

[43] P. Deery. Heritage report: The cold war goes underground: The kelvedon hatch nuclear bunker, 1952-92. *Labour History*, (78):198, 2000.

[44] L. Parfitt and L. Wilson. *Fundamentals of Physical Volcanology*. Wiley-Blackwell, 2008.

[45] G. Shaffer. Long-term effectiveness and consequences of carbon dioxide sequestration. *Nature Geoscience*, 3(7):464–467, jun 2010.

[46] M. Sugihara, K. Nawa, Y. Nishi, T. Ishido, and N. Soma. Continuous gravity monitoring for CO2 geo-sequestration. *Energy Procedia*, 37:4302–4309, 2013.

[47] X. Wang, H. Li, and Y. Han. Pre-seismic gravity anomalies before Linkou Ms6.4 earthquake by continuous gravity observation of Crustal Movement Observation Network of China. *Geodesy and Geodynamics*, 8(2):120–124, 2017.

[48] A. Witze. Gravity signals could speedily warn of big quakes and save lives. *Nature*, nov 2017.

[49] JP. Montagner, K. Juhel, M. Barsuglia, JP. Ampuero, E. Chassande-Mottin, J. Harms, B. Whiting, P. Bernard, E. Clévédé, and P. Lognonné. Prompt gravity signal induced by the 2011 tohoku-oki earthquake. *Nature Communications*, 7(1), 2016.

[50] J. K. Warren. *Evaporites*. Springer International Publishing, 2016.

[51] D. Powers. Evaporites, casing requirements, water-floods, and out-of-formation waters: Potential for sinkhole developments. 01 2000.

[52] A. Ozdemir. Sinkhole susceptibility mapping using logistic regression in karapınar (konya, turkey). *Bulletin of Engineering Geology and the Environment*, 75(2):681–707, aug 2015.

[53] A. J. O Jenkins, D. Messfin, and W. Moon. Gravity modelling of salt domes and pinnacle reefs. *J. Can. Soc. Expl. Geophys.*, 19(1):51–56, 1983.

[54] J. L. Chen, C. R. Wilson, J. C. Ries, and B. D. Tapley. Rapid ice melting drives earth's pole to the east. *Geophysical Research Letters*, 40(11):2625–2630, jun 2013.

[55] G. Xu. *Sciences of geodesy - I: Advances and future directions*. Number June. 2010.

[56] M. Feissel-Vernier, O. de Viron, and Karine Le Bail. Stability of VLBI, SLR, DORIS, and GPS positioning. *Earth, Planets and Space*, 59(6):475–497, 2007.

[57] P. Bird. An updated digital model of plate boundaries. *Geochemistry, Geophysics, Geosystems*, 4(3), 2003.

[58] A. Freise and K. A. Strain. Interferometer techniques for gravitational-wave detection. *Living Rev. Relativity*, 13(1), 2010.

[59] W. Bich, G. D'Agostino, A. Germak, and F. Pennecchi. Reconstruction of the free-falling body trajectory in a rise-and-fall absolute ballistic gravimeter. *Metrologia*, 45(3):308–312, may 2008.

[60] Micro-g LaCoste. *FG5 Brochure*.

[61] Micro-g LaCoste. *FG5*.

[62] Scintrex. *CG-6 AutoGrav Data Sheet*.

[63] Scintrex. *CG-6 AutoGrav Brochure*.

[64] Scintrex. *CG-5 AutoGrav Data Sheet*.

[65] S. Yang. Special issue on BioMEMS. *Biomedical Engineering Letters*, 2(2):69–70, 2012.

[66] D. Lindner. Microsystems for Chemical and Biological Applications. *MRS Bulletin*, 26(04):333–336, apr 2001.

[67] R. S. Shawgo, A. C. R. Grayson, Y. Li, and M. J. Cima. BioMEMS for drug delivery. *Current Opinion in Solid State and Materials Science*, 6(4):329–334, 2002.

[68] J. Bouchaud, B. Knoblich, H. Tilmans, F. Coccetti, and A. El Fatatry. RF MEMS roadmap. *Proceedings of the 37th European Microwave Conference, EUMC*, (October):1141–1144, 2007.

[69] H. A. C. Tilmans, W. De Raedt, and E. Beyne. MEMS for wireless communications: &lquot;from RF-MEMS components to RF-MEMS-SiP&rquot;. *Journal of Micromechanics and Microengineering*, 13(4):S139–S163, 2003.

[70] S. J. Park, I. Reines, C. Patel, and G. M. Rebeiz. High-Q RF-MEMS 46-GHz tunable evanescent-mode cavity filter. *IEEE Transactions on Microwave Theory and Techniques*, 58(2):381–389, 2010.

[71] M. Bakri-Kassem and R. R. Mansour. High power latching RF MEMS switches. *IEEE Transactions on Microwave Theory and Techniques*, 63(1):222–232, 2015.

[72] S. Middelhoek. Celebration of the tenth transducers conference: The past, present and future of transducer research and development. *Sensors and Actuators, A: Physical*, 82(1):2–23, 2000.

[73] L. M. Roylance and J. B. Angell. A batch-fabricated silicon accelerometer. *IEEE Transactions on Electron Devices*, 26(12):1911–1917, 1979.

[74] H. V. Allen, S. C. Terry, and D. W. De Bruin. Accelerometer systems with built-in testing. *Sensors and Actuators: A. Physical*, 21(1-3):381–386, 1990.

[75] STMicroelectronics. *LSM6DSL Data Sheet*.

[76] D. K. Shaeffer. MEMS inertial sensors: A tutorial overview. *IEEE Communications Magazine*, 51(4):100–109, 2013.

[77] D. Hollocher, X. Zhang, A. Sparks, S. Bart, W. Sawyer, P. Narayanasamy, C. Pipitone, J. Memishian, H. Samuels, S. Ng, R. Mhatre, D. Whitley, F. Sammoura, M. Bhagavat, C. Tsau, K. Nunan, M. Judy, M. Farrington, and K. Yang. A very low cost, 3-axis, mems accelerometer for consumer applications. In *SENSORS, 2009 IEEE*, pages 953–957, Oct 2009.

[78] X. Zou, P. Thiruvenkatanathan, and A. A. Seshia. A seismic-grade resonant mems accelerometer. *Journal of Microelectromechanical Systems*, 23(4):768–770, Aug 2014.

[79] R. Xu, S. Zhou, and W. J. Li. Mems accelerometer based nonspecific-user hand gesture recognition. *IEEE Sensors Journal*, 12(5):1166–1173, 2012.

[80] Y. Shi, Y. Zhao, H. Feng, H. Cao, J. Tang, J. Li, R. Zhao, and J. Liu. Design, fabrication and calibration of a high-g MEMS accelerometer. *Sensors and Actuators A: Physical*, 279:733–742, aug 2018.

[81] S. Bhattacharya, A. Krishna, D. Lombardi, A. Crewe, and N. Alexander. Economic MEMS based 3-axis water proof accelerometer for dynamic geo-engineering applications. *Soil Dynamics and Earthquake Engineering*, 36:111–118, may 2012.

[82] R. P. Middlemiss, S. G. Bramsiepe, R. Douglas, S. Hild, J. Hough, D. J. Paul, A. Samarelli, S. Rowan, and G. D. Hammond. Microelectromechanical system gravimeters as a new tool for gravity imaging. pages 1–15, 2018.

[83] R. P. Middlemiss. *Practical MEMS Gravimeter*. Phd thesis, The University of Glasgow, 2016.

[84] G. Cella, V. Sannibale, R. Desalvo, S. Márka, and A. Takamori. Monolithic geometric anti-spring blades. *Nuclear Instruments and Methods in Physics Research, Section A: Accelerators, Spectrometers, Detectors and Associated Equipment*, 540(2-3):502–519, 2005.

[85] Britannica Academic, Encyclopædia Britannica. *Haber-Bosch process*.

[86] N. A. Lockerbie and K. V. Tokmakov. A 'Violin-Mode' shadow sensor for interferometric gravitational wave detectors. *Measurement Science and Technology*, 25(12), 2014.

[87] D. P. Blair and P. H. Sydenham. Phase sensitive detection as a means to recover signals buried in noise. *Journal of Physics E: Scientific Instruments*, 8(8):621–627, 1975.

[88] Femto. *LIA-MVD-200-L Data Sheet*.

[89] Keithley, A Tektronix Company. *Keithley 2000 Multimeter Data Sheet*.

[90] Hewlett Packard. *HP 33120A Signal Generator Data Sheet*.

[91] Stanford Research Systems. *SR570 Current Preamplifier Data Sheet*.

[92] Stanford Research Systems. *SR560 Preamplifier Data Sheet*.

[93] National Instruments. *NI M Series 6229 Analogue to Digital Converter Device Specifications*.

[94] G. H. Keulegan and M. R. Houseman. Temperature coefficient of the moduli of metals and alloys used as elastic elements. *Bureau of Standards Journal of Research*, 10(3):289, March 1933.

[95] J. V. Malik, K. D. Jindal, Vinay Kumar, Vipin Kumar, Arun Kumar, Kh. S. Singh, and T. P. Singh. Effect of temperature on photonic band gaps in semiconductor-based one-dimensional photonic crystal. *Advances in Optical Technologies*, 2013:1–8, 2013.

[96] K. A. Vinogradova, L. A. Nikulina, S. S. Braslavskii, E. A. Solovieva, K. D. Mynbaev, V. I. Nikolaev, A. E. Romanov, and V. E. Bougrov. Temperature stability of colored led elements. *Materials Physics and Mechanics*, 18(2):143–147, 2013.

[97] P. H. Lee, J. H. Chou, and H. C. Tseng. Thermal stability of high-power leds analyzed with efficient nondestructive methodology. *IEEE Transactions on Device and Materials Reliability*, 13(3):401–406, 2013.

[98] Kingbright. *T-1 3/4 (5mm) SOLID STATE LAMP Datasheet*.

[99] Analog Devices. *AD7195 Data Sheet, http://www.analog.com/media/en/technical-documentation/data-sheets/AD7195.pdf*.

[100] L.-R. Trevisanello, M. Meneghini, G. Mura, C. Sanna, S. Buso, G. Spiazzi, M. Vanzi, G. Meneghesso, and E. Zanoni. Thermal stability analysis of high brightness LED during high temperature and electrical aging. In Ian T. Ferguson, Nadarajah Narendran, Tsunemasa Taguchi, and Ian E. Ashdown, editors, *Seventh International Conference on Solid State Lighting*. SPIE, sep 2007.

[101] G. Vasilescu. *Electronic Noise and Interfering Signals*. Springer, 2005.

[102] Maxim Integrated. *MAX6177 High-Precision Voltage References with Temperature Sensor*.

[103] Labfacility. *Platinum Sensing Resistors - Thin Film (Pt100 and Pt1000 Ohm)*.

[104] D. W. Allan. Statistics of atomic frequency standards. *Proceedings of the IEEE*, 54(2):221–230, Feb 1966.

[105] A. Zoellner, E. Hultgren, and K. Sun. Integrated differential optical shadow sensor for modular gravitational reference sensor, arxiv:1302.1623, 2013.

[106] S. G. Bramsiepe, D. Loomes, R. P. Middlemiss, D. J. Paul, and G. D. Hammond. A high stability optical shadow sensor with applications for precision accelerometers. *IEEE Sensors Journal*, 18(10):4108–4116, 2018.

[107] A. Zoellner, S. Tan, S. Saraf, A. Alfauwaz, D. DeBra, S. Buchman, and J. A. Lipa. Differential optical shadow sensor for sub-nanometer displacement measurement and its application to drag-free satellites. *Optics Express*, 25(21):25201, oct 2017.

[108] N. A. Lockerbie and K. V. Tokmakov. Quasi-static displacement calibration system for a “violin-mode” shadow-sensor intended for gravitational wave detector suspensions. *Review of Scientific Instruments*, 85(10):105003, 2014.

[109] N. A. Lockerbie, K. V. Tokmakov, and K. A. Strain. A source of illumination for low-noise ‘violin-mode’ shadow sensors, intended for use in interferometric gravitational wave detectors. *Measurement Science and Technology*, 25(12):125111, 2014.

[110] Texas Instruments. *TL08xx JFET-Input Operational Amplifiers, http://www.ti.com/lit/ds/symlink/tl082.pdf*.

[111] B. Schiek. *Noise in High-Frequency Circuits and Oscillators*. Wiley-Interscience, 2006.

[112] Kingbright. *T- 1 3/4 (5mm) SUPER BRIGHT LED LAMPS - L-53SR SUPER BRIGHT RED*.

[113] Jewell Instruments. *Model 755-High-gain , 756-Mid-range Miniature Tilt Sensors*.

[114] Spectron Sensors. *Electrolytic Tilt Sensors - SH50050 Ceramic Series*.

[115] W. B. Powell. *The Electrolytic Tilt Sensor*. Sensors Magazine.

[116] Texas Instruments. *ADS1248 Data Sheet*.

[117] W. Kester. Mt-001 tutorial taking the mystery out of the infamous formula , " snr = 6 . 02 n + 1 . 76 db , " and why you should care by. 2009.

[118] H. O. Seigel, I. Brcic, and P. Mistry. A guide to high precision land gravimeter surveys. *Scintrex Limited*, 222(1):1–122, 1995.

[119] F. Whyte and J. G. MacDonald. Lower carboniferous vulcanicity in the northern part of the clyde plateau. *Scottish Journal of Geology*, 10(3):187–198, October 1974.

[120] D. N. Gujarati. *Basic Econometrics*. McGraw-Hill, New York, 4th edition edition, 2004.

[121] J. Penny. Numerical methods using matlab, 2e. https://uk.mathworks.com/matlabcentral/fileexchange/2305-numerical-methods-using-matlab-2e. Online; accessed 18-June-2019.

[122] A. Prasad, S. G. Bramsiepe, R. P. Middlemiss, J. Hough, S. Rowan, G. D. Hammond, and D. J. Paul. A portable MEMS gravimeter for the detection of the earth tides. In *2018 IEEE SENSORS*. IEEE, oct 2018.

[123] M. Van Camp and P. Vauterin. Tsoft: graphical and interactive software for the analysis of time series and earth tides. *Computers & Geosciences*, 31(5):631–640, June 2005.

[124] P. Legendre. *Numerical Ecology*, volume 24. Elsevier, 2nd edition.

[125] R. P. Fender and M. A. Hendry. The radio luminosity of persistent x-ray binaries. *Monthly Notices of the Royal Astronomical Society*, 317(1):1–8, September 2000.

[126] S. Sainz-Maza Aparicio, J. Arnoso Sampedro, F. Gonzalez Montesinos, and J. Martí Molist. Volcanic signatures in time gravity variations during the volcanic unrest on el hierro (canary islands). *Journal of Geophysical Research: Solid Earth*, 119(6):5033–5051, June 2014.

Appendix A

Commonly Used Gravity Units

There are various units used to quantify gravitational acceleration. In this thesis units of *Gal* (or more specifically μGal) will generally be used to quantify gravitational acceleration. This is not an S.I unit (1 Gal is equivalent to 1 cm s^{-2}), but it is widely used by the geophysics community. Another commonly used unit is 'g', where 1g = 9.81 m s^{-2}. Since acceleration sensitivity can be different at different frequencies, device sensitivity is most commonly quoted in units of acceleration/$\sqrt{Hz}$. In other words, this is the acceleration sensitivity in an integration time of 1 second. Table A.1 shows some common conversion between these units.

Gal	**SI**	**g**
1000 Gal	10 m s^{-2}	1 g
100 Gal	1 m s^{-2}	10^{-1} g
10 Gal	10^{-1} m s^{-2}	10^{-2} g
1 Gal	10^{-2} m s^{-2}	10^{-3} g
10^{-1} Gal	10^{-3} m s^{-2}	10^{-4} g
10^{-2} Gal	10^{-4} m s^{-2}	10^{-5} g
10^{-3} Gal	10^{-5} m s^{-2}	10^{-6} g
10^{-4} Gal	10^{-6} m s^{-2}	10^{-7} g
10^{-5} Gal	10^{-7} m s^{-2}	10^{-8} g
10^{-6} Gal	10^{-8} m s^{-2}	10^{-9} g
10^{-7} Gal	10^{-9} m s^{-2}	10^{-10} g
10^{-8} Gal	10^{-10} m s^{-2}	10^{-11} g
10^{-9} Gal	10^{-11} m s^{-2}	10^{-12} g

Table A.1 Gravitational Acceleration Unit Conversions

Appendix B

Electronics Board Schematics

B.1 Electronics Board Version 1.0

The following pages contain the schematic for the only custom electronics board that was designed and tested for this project.

Processor module and power supplies

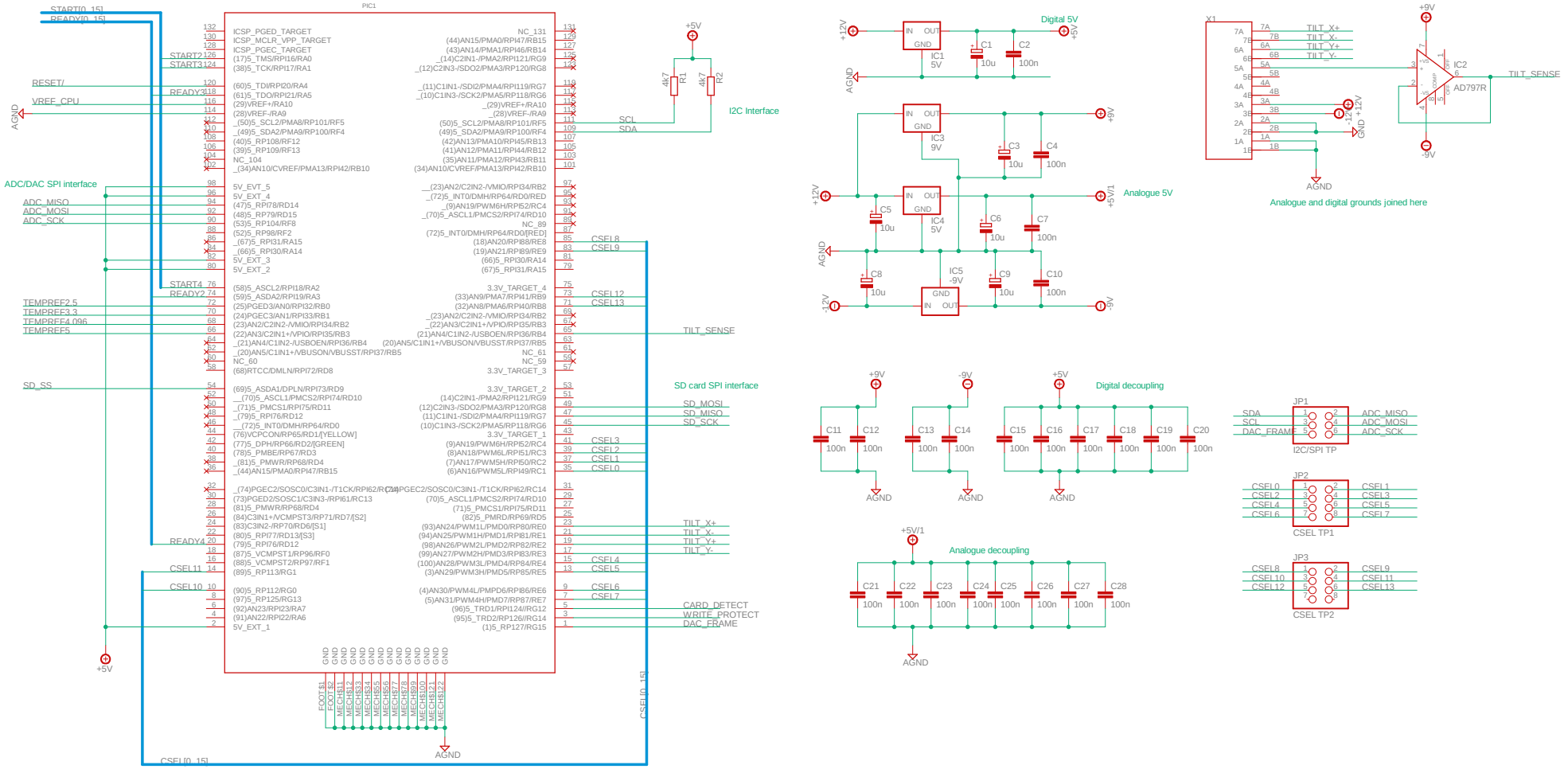

AD7172-2 A to D Converter

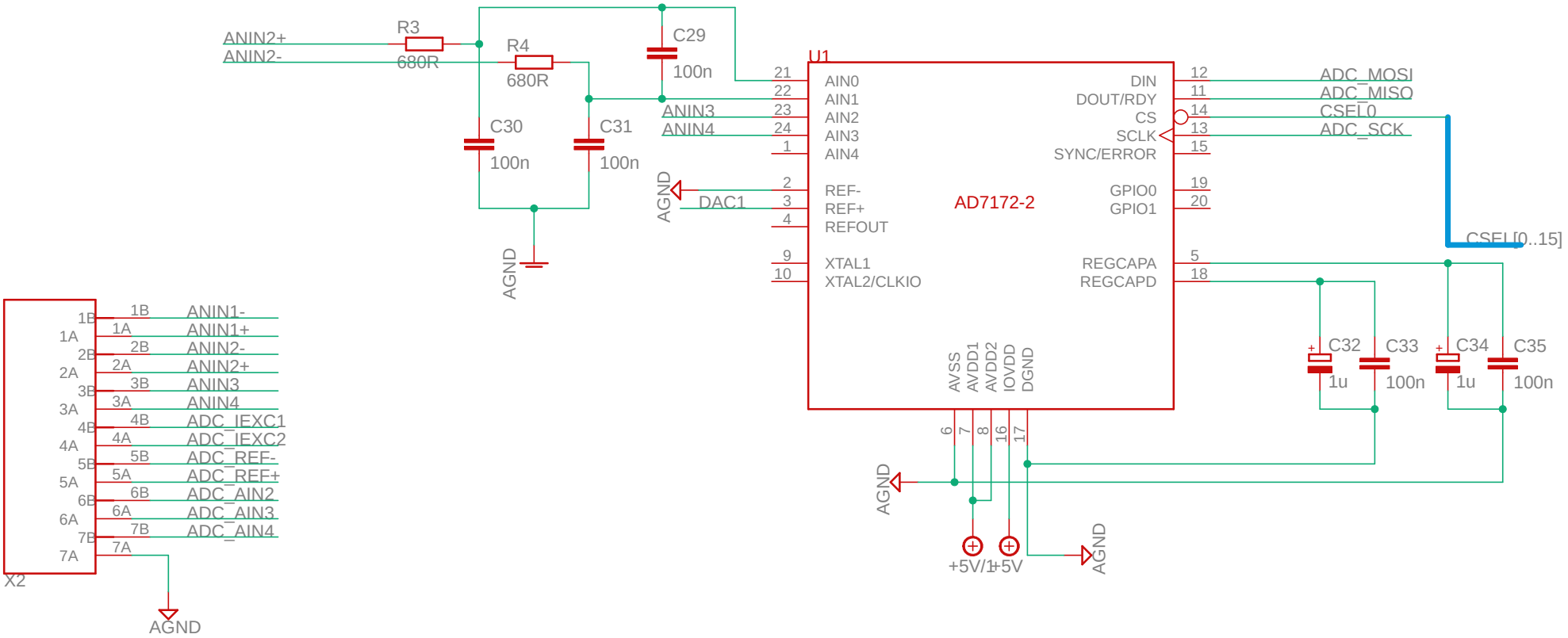

I to V converters + ADS1248 A to D converters

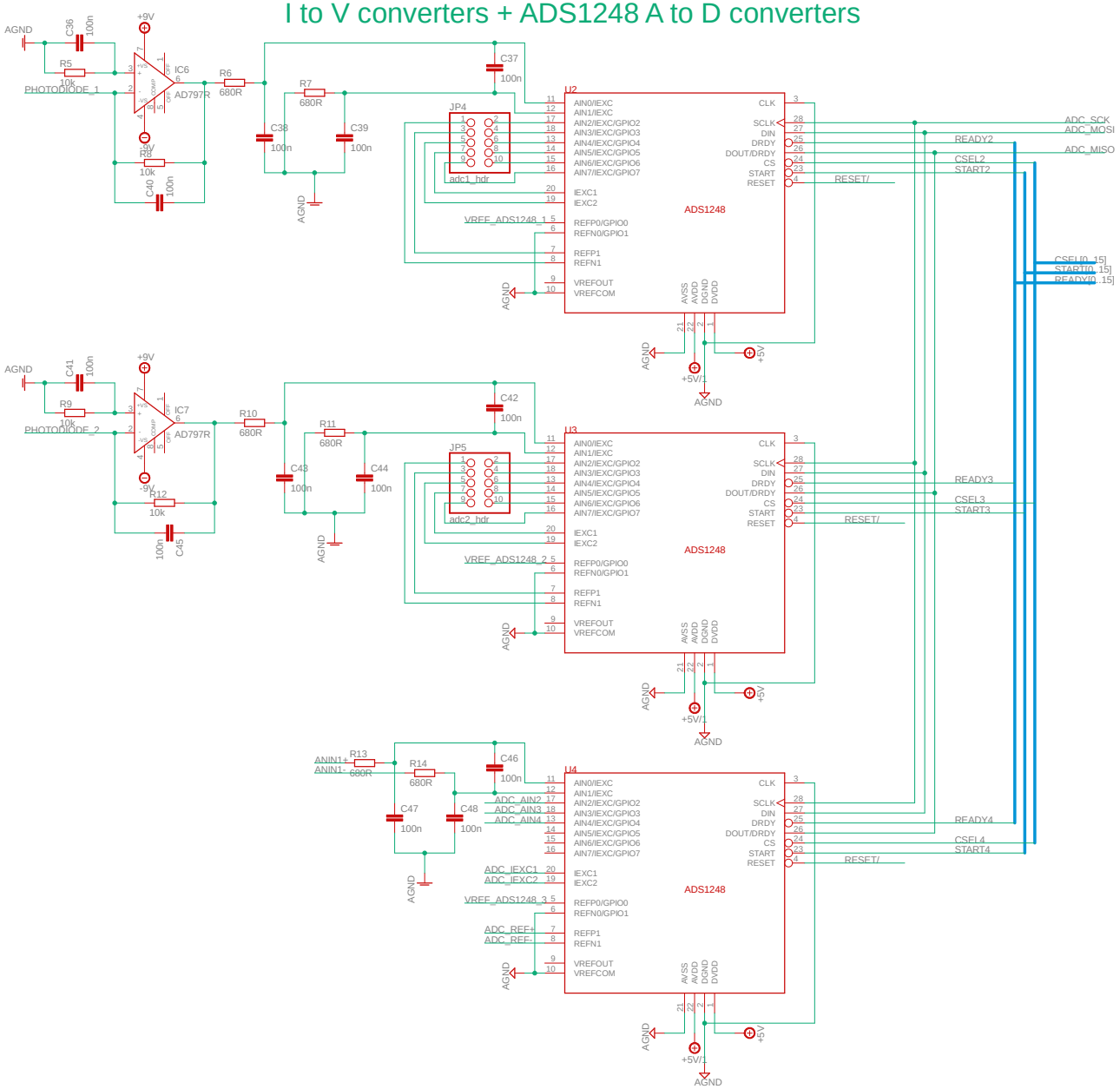

D to A converters, 2.5 Vref, LED drive

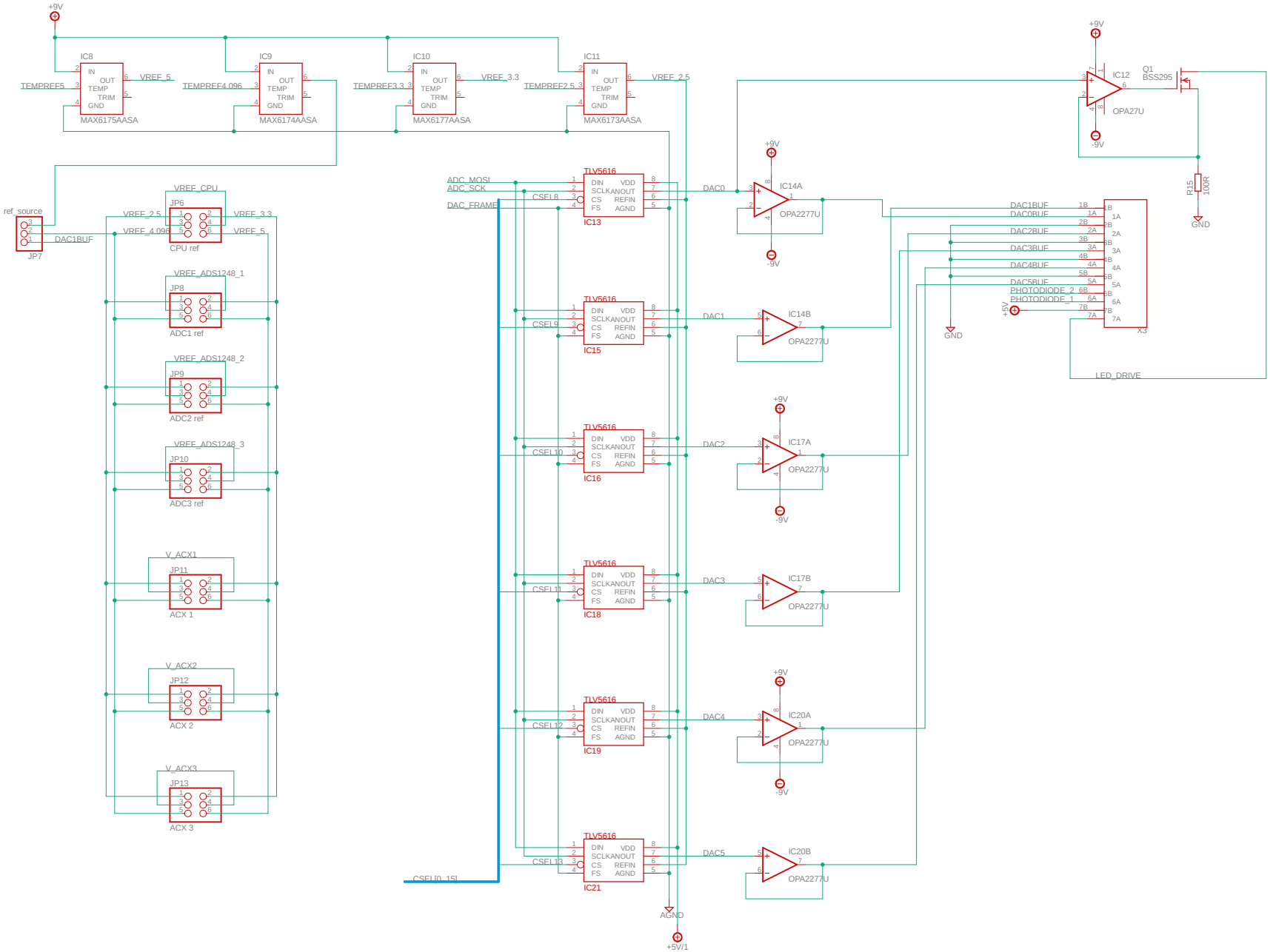

AD7195 temperature measurement

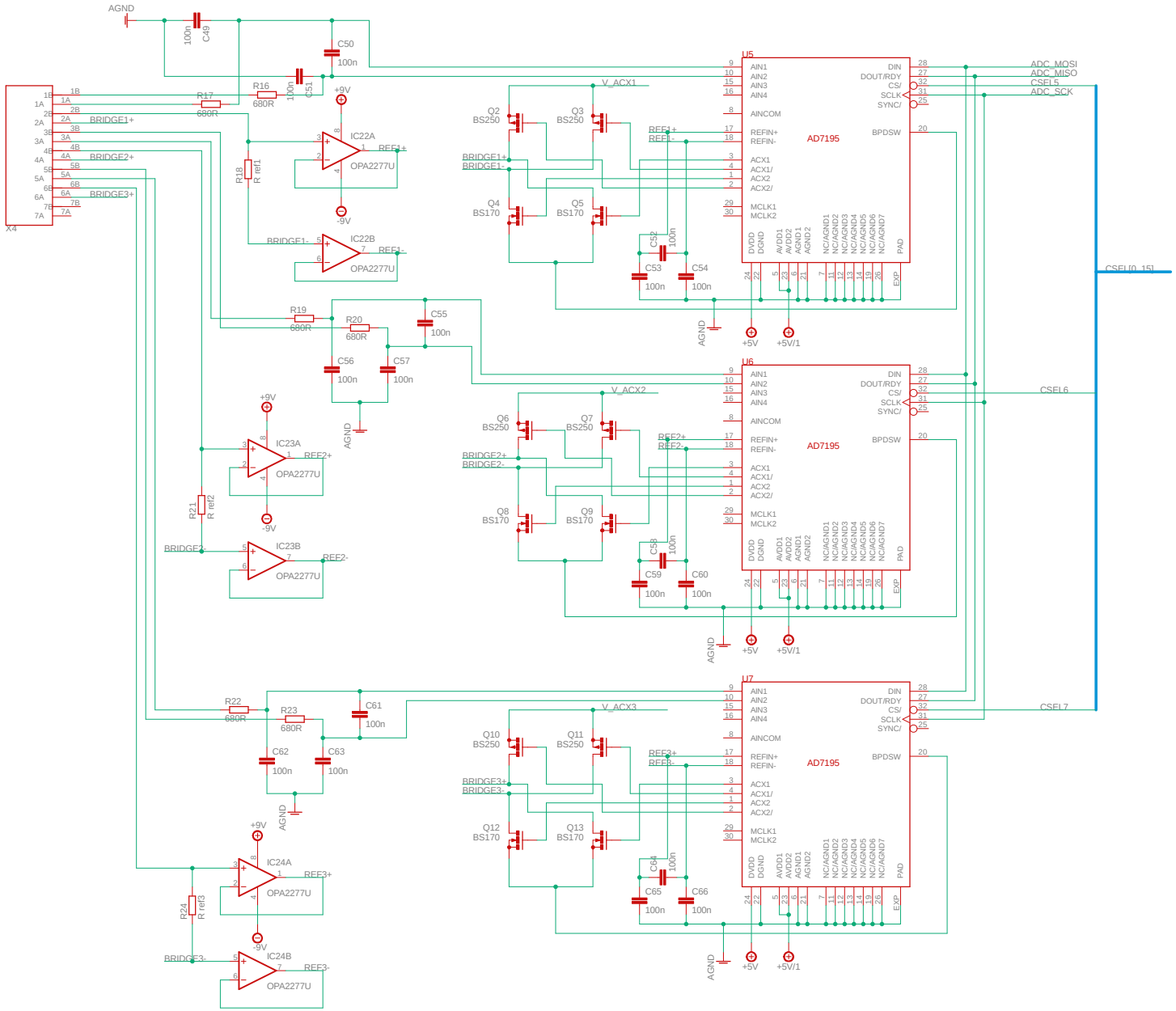

GPS module, clock-calendar and SD-RAM interface

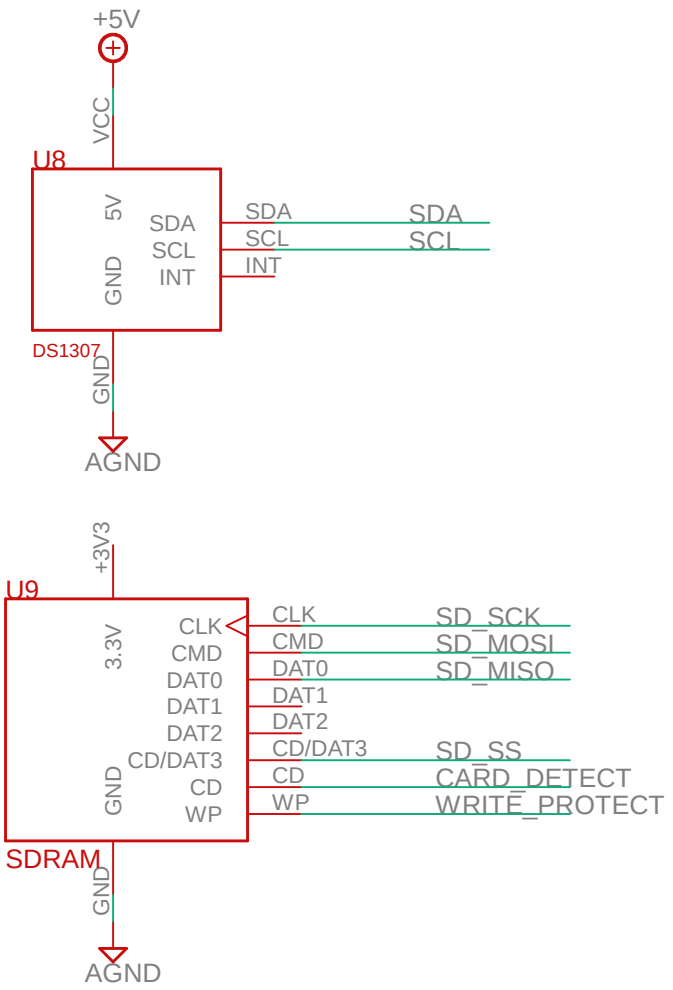

B.2 Electronics Board Version 2.0

The following pages contain the schematic of the planned second version of the custom electronics board. This board was never fabricated.

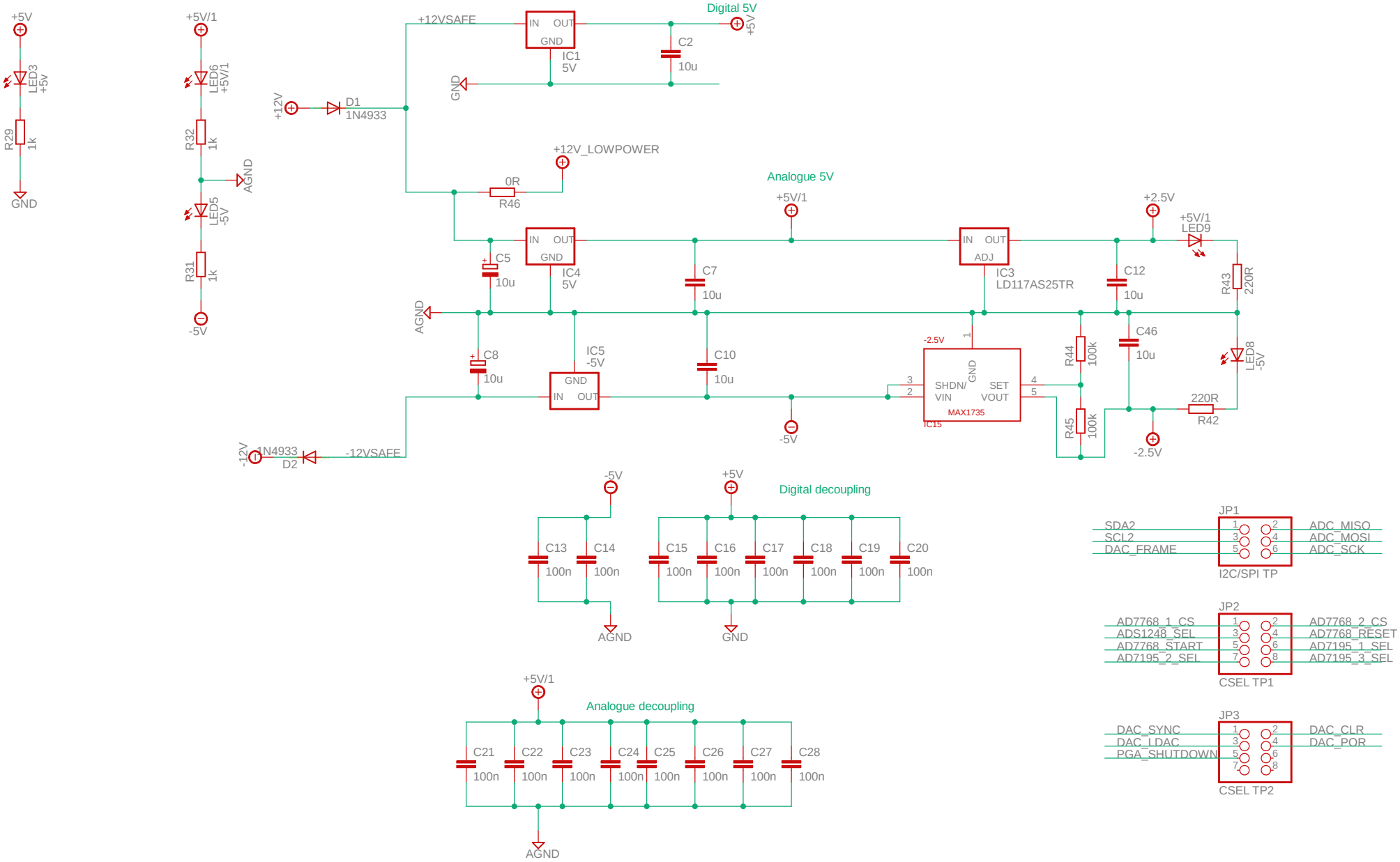
+5V
LED3
+5V
R29
1k
GND
+5V/1
LED6
+5V/1
R32
1k
AGND
LED5
-5V
R31
1k
-5V
+12VSAFE
IN OUT
GND
IC1
5V
C2
10u
Digital 5V
+5V
GND
+12V
D1
1N4933
+12V_LOWPOWER
0R
R46
Analogue 5V
+5V/1
IN OUT
GND
IC4
5V
C5
10u
C7
10u
AGND
C8
10u
IC5
-5V
GND
IN OUT
C10
10u
-5V
-12V
1N4933
D2
-12VSAFE
IN OUT
ADJ
IC3
LD117AS25TR
+2.5V
+5V/1
LED9
C12
10u
R43
220R
C46
10u
LED8
-5V
-2.5V
R44
100k
R45
100k
-2.5V
GND
SHDN/
VIN
SET
VOUT
MAX1735
IC15
220R
R42
-2.5V
-5V
+5V
Digital decoupling
C13
C14
100n
100n
AGND
C15
C16
C17
C18
C19
C20
100n
GND
+5V/1
Analogue decoupling
C21
C22
C23
C24
C25
C26
C27
C28
100n
AGND
JP1
SDA2
SCL2
DAC_FRAME
ADC_MISO
ADC_MOSI
ADC_SCK
I2C/SPI TP
JP2
AD7768_1_CS
ADS1248_SEL
AD7768_START
AD7195_2_SEL
AD7768_2_CS
AD7768_RESET
AD7195_1_SEL
AD7195_3_SEL
CSEL TP1
JP3
DAC_SYNC
DAC_LDAC
PGA_SHUTDOWN
DAC_CLR
DAC_POR
CSEL TP2

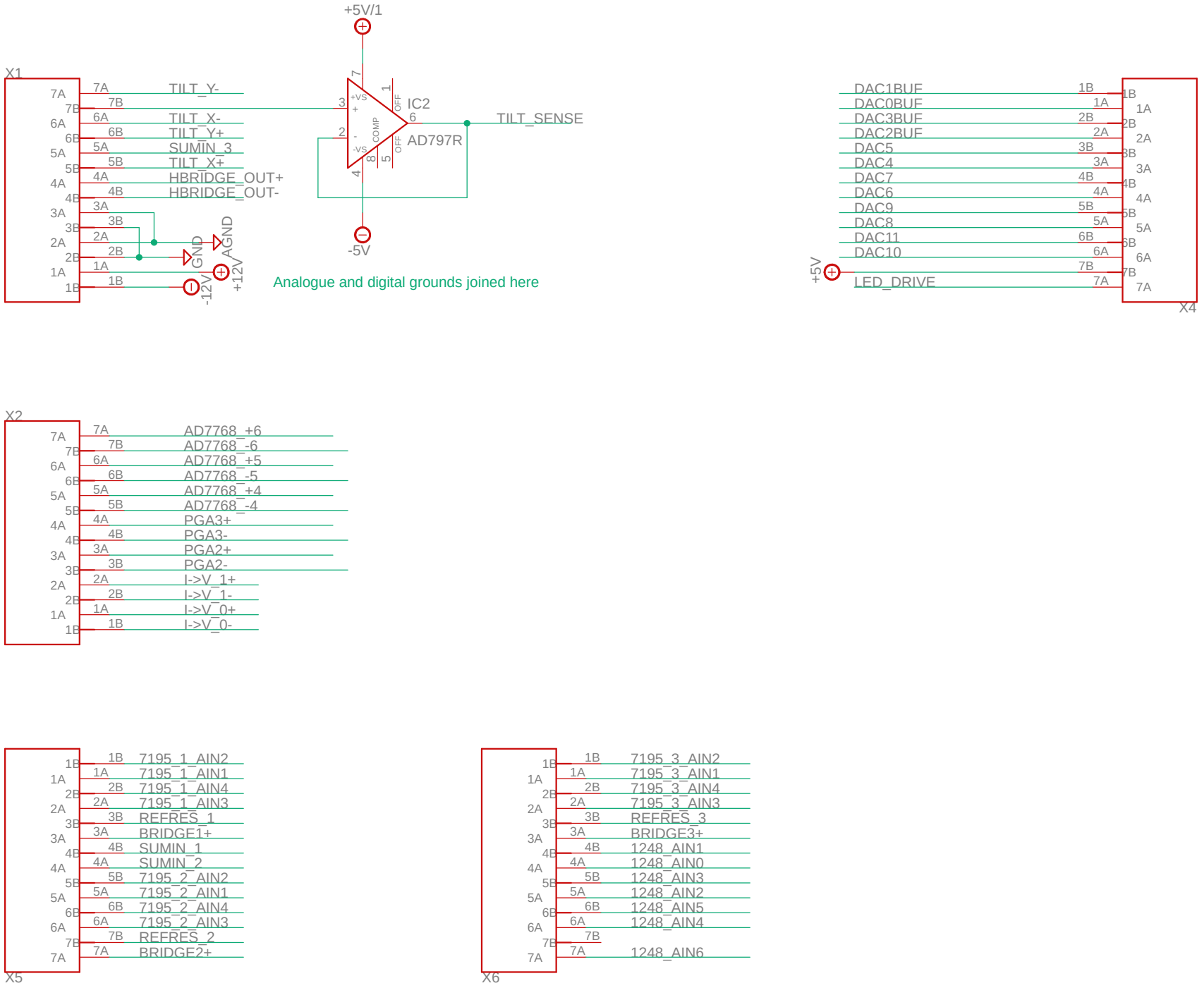
X1
7A TILT_Y-
7B
6A TILT_X-
6B TILT_Y+
5A SUMIN_3
5B TILT_X+
4A HBRIDGE_OUT+
4B HBRIDGE_OUT-
3A
3B
2A
2B
1A
1B
GND
AGND
-12V
+12V
+5V/1
-5V
IC2
AD797R
TILT_SENSE
Analogue and digital grounds joined here
DAC1BUF
DAC0BUF
DAC3BUF
DAC2BUF
DAC5
DAC4
DAC7
DAC6
DAC9
DAC8
DAC11
DAC10
LED_DRIVE
+5V
X4
X2
AD7768_+6
AD7768_-6
AD7768_+5
AD7768_-5
AD7768_+4
AD7768_-4
PGA3+
PGA3-
PGA2+
PGA2-
I->V_1+
I->V_1-
I->V_0+
I->V_0-
X5
7195_1_AIN2
7195_1_AIN1
7195_1_AIN4
7195_1_AIN3
REFRES_1
BRIDGE1+
SUMIN_1
SUMIN_2
7195_2_AIN2
7195_2_AIN1
7195_2_AIN4
7195_2_AIN3
REFRES_2
BRIDGE2+
X6
7195_3_AIN2
7195_3_AIN1
7195_3_AIN4
7195_3_AIN3
REFRES_3
BRIDGE3+
1248_AIN1
1248_AIN0
1248_AIN3
1248_AIN2
1248_AIN5
1248_AIN4
1248_AIN6

Processor module and power supplies

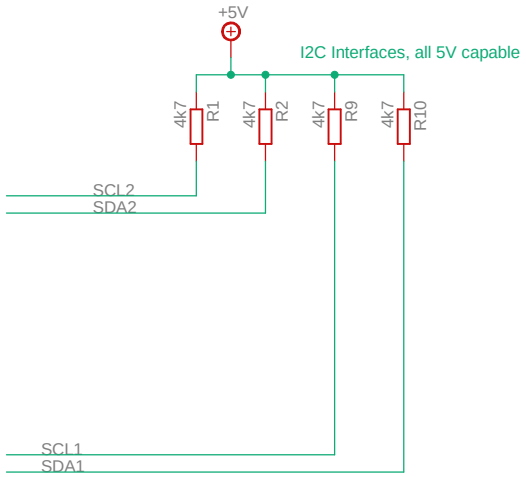

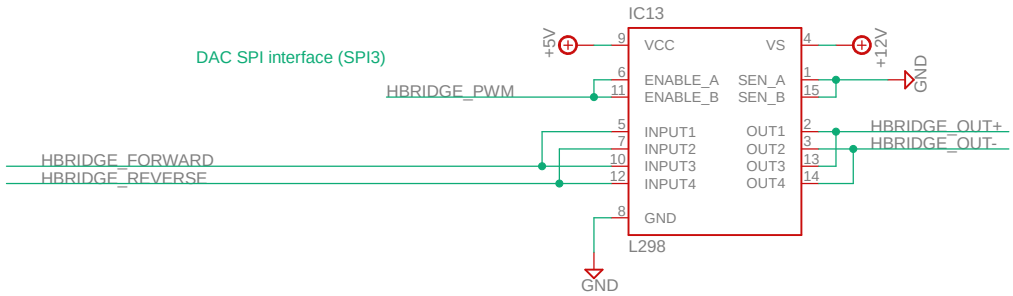

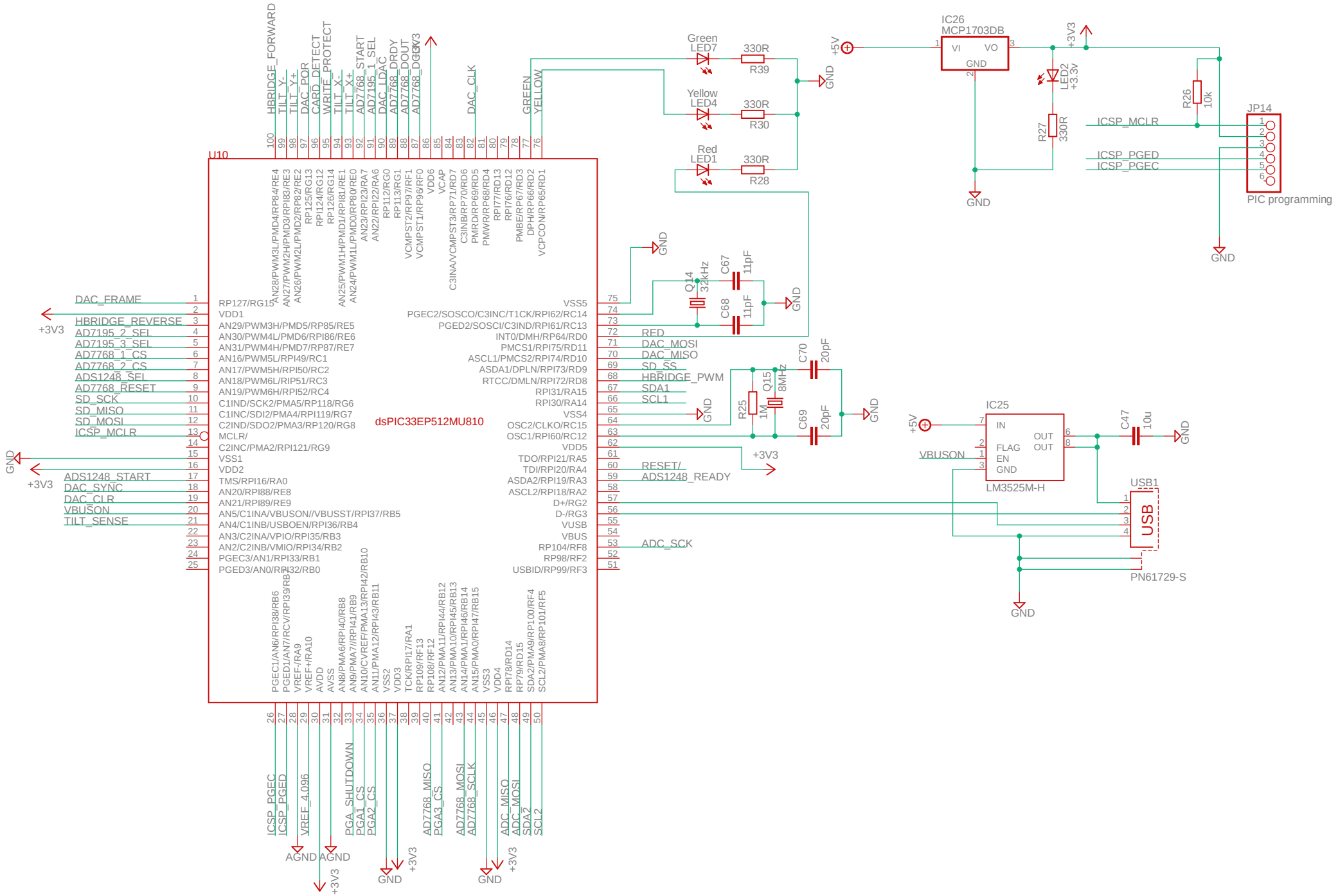
U10
dsPIC33EP512MU810
HBRIDGE_FORWARD
TILT_Y-
TILT_Y+
DAC_POR
CARD_DETECT
WRITE_PROTECT
TILT_X-
TILT_X+
AD7768_START
AD7195_1_SEL
DAC_LDAC
AD7768_DRDY
AD7768_DOUT
AD7768_DIN
+3V3
DAC_CLK
GREEN
YELLOW
Green LED7
Yellow LED4
Red LED1
330R
R39
R30
R28
GND
+5V
IC26
MCP1703DB
VI
VO
GND
LED2 +3.3v
R27
R26
10k
ICSP_MCLR
ICSP_PGED
ICSP_PGEC
JP14
PIC programming
Q14
32kHz
C67
11pF
C68
C70
20pF
C69
Q15
8MHz
R25
1M
RED
DAC_MOSI
DAC_MISO
SD_SS
HBRIDGE_PWM
SDA1
SCL1
RESET/
ADS1248_READY
ADC_SCK
IC25
LM3525M-H
IN
FLAG
EN
OUT
VBUSON
C47
10u
USB1
USB
PN61729-S
DAC_FRAME
HBRIDGE_REVERSE
AD7195_2_SEL
AD7195_3_SEL
AD7768_1_CS
AD7768_2_CS
ADS1248_SEL
AD7768_RESET
SD_SCK
SD_MISO
SD_MOSI
ICSP_MCLR
ADS1248_START
DAC_SYNC
DAC_CLR
VBUSON
TILT_SENSE
ICSP_PGEC
ICSP_PGED
VREF_4.096
PGA_SHUTDOWN
PGA1_CS
PGA2_CS
PGA3_CS
AD7768_MISO
AD7768_MOSI
AD7768_SCLK
ADC_MISO
ADC_MOSI
SDA2
SCL2
AGND

I to V converters + ADS1248 A to D converters

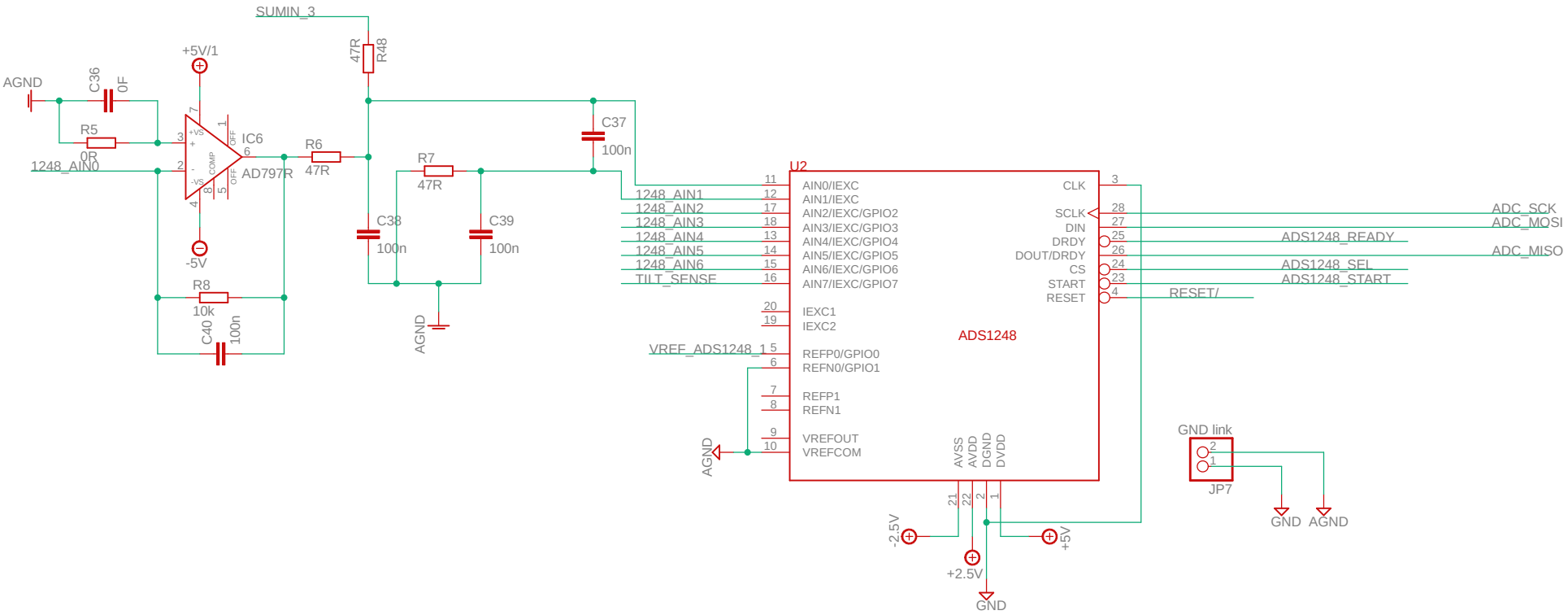

D to A converters, 2.5 Vref, LED drive

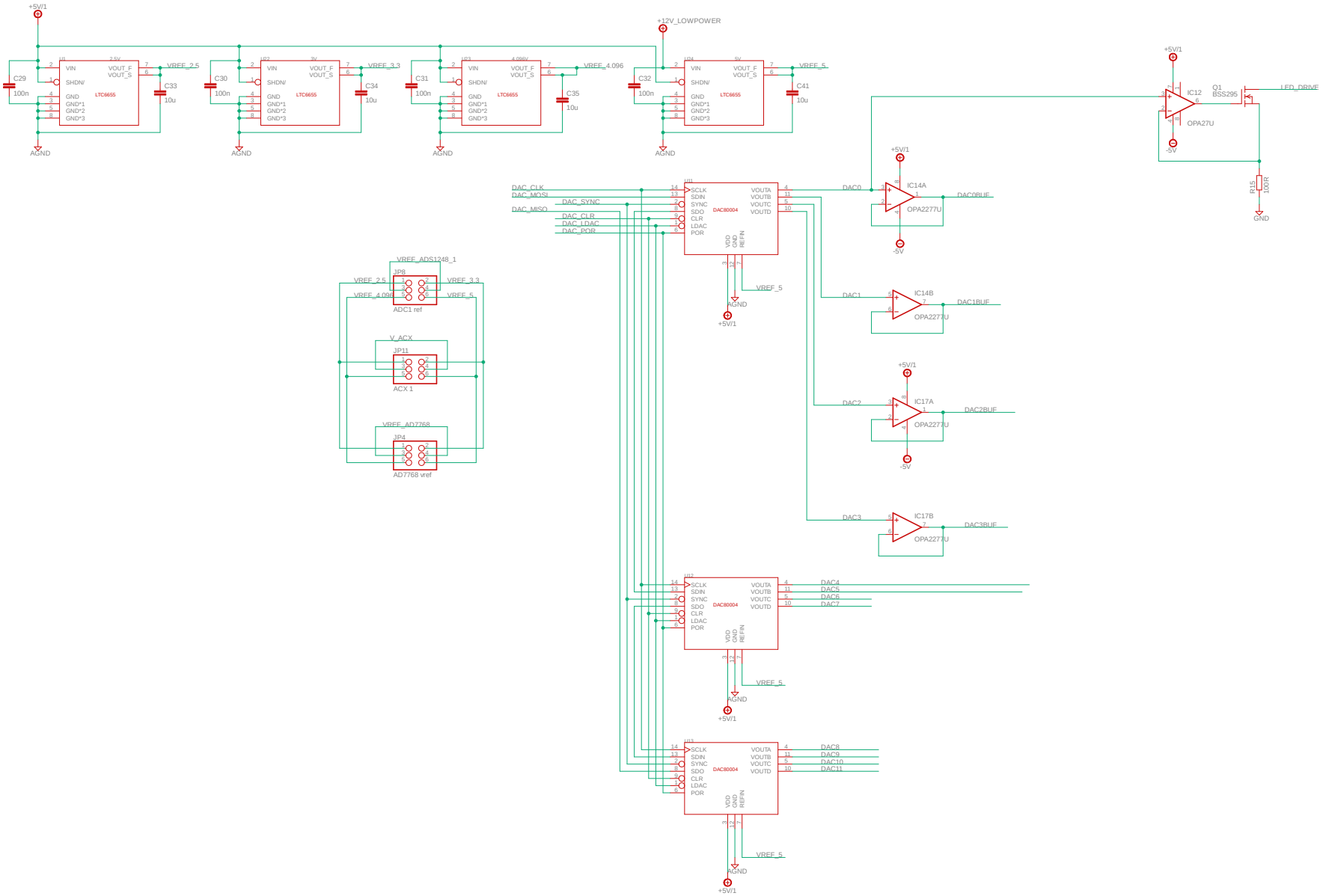

AD7195 temperature measurement

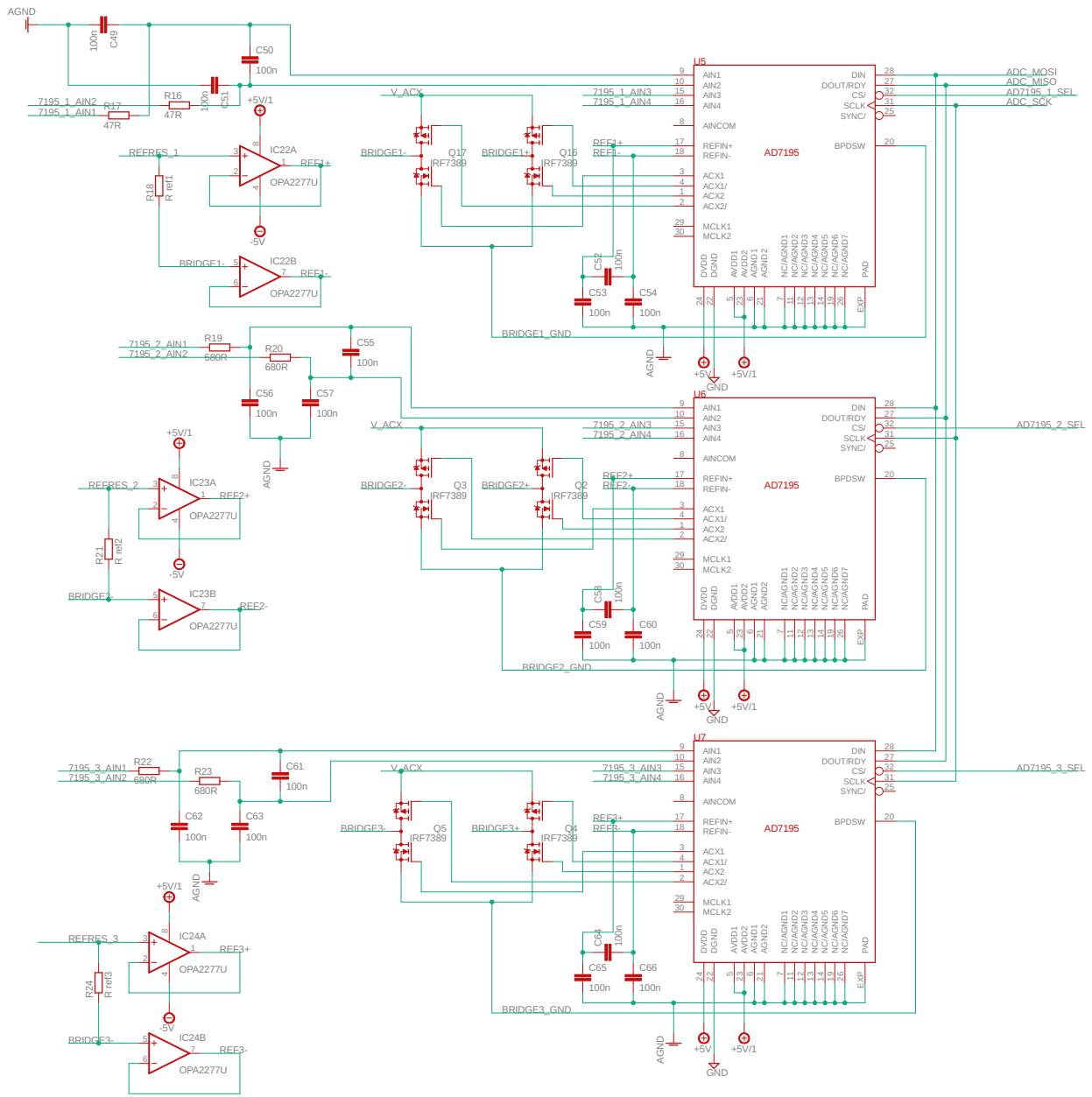

GPS module, clock-calendar and SD-RAM interface

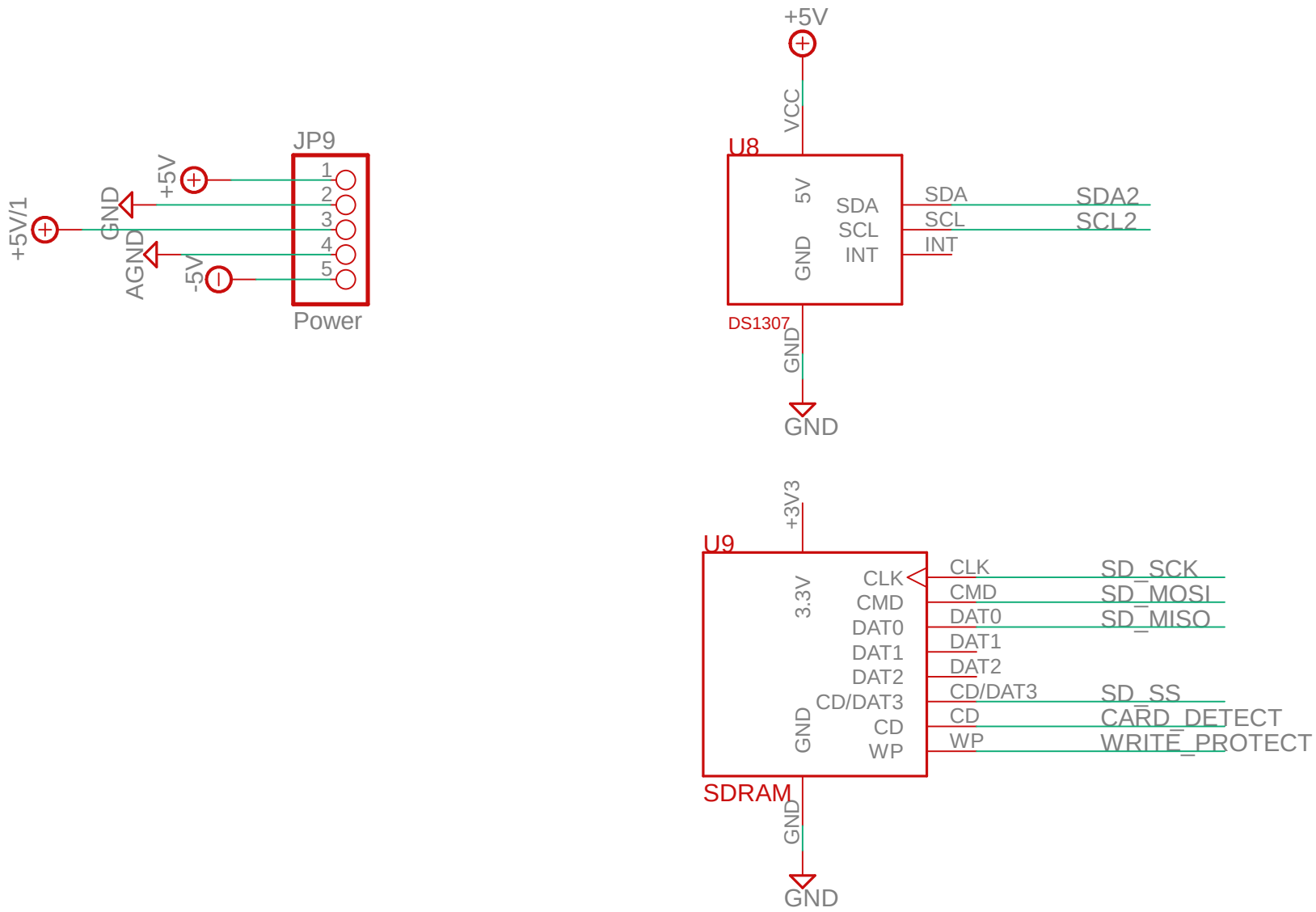

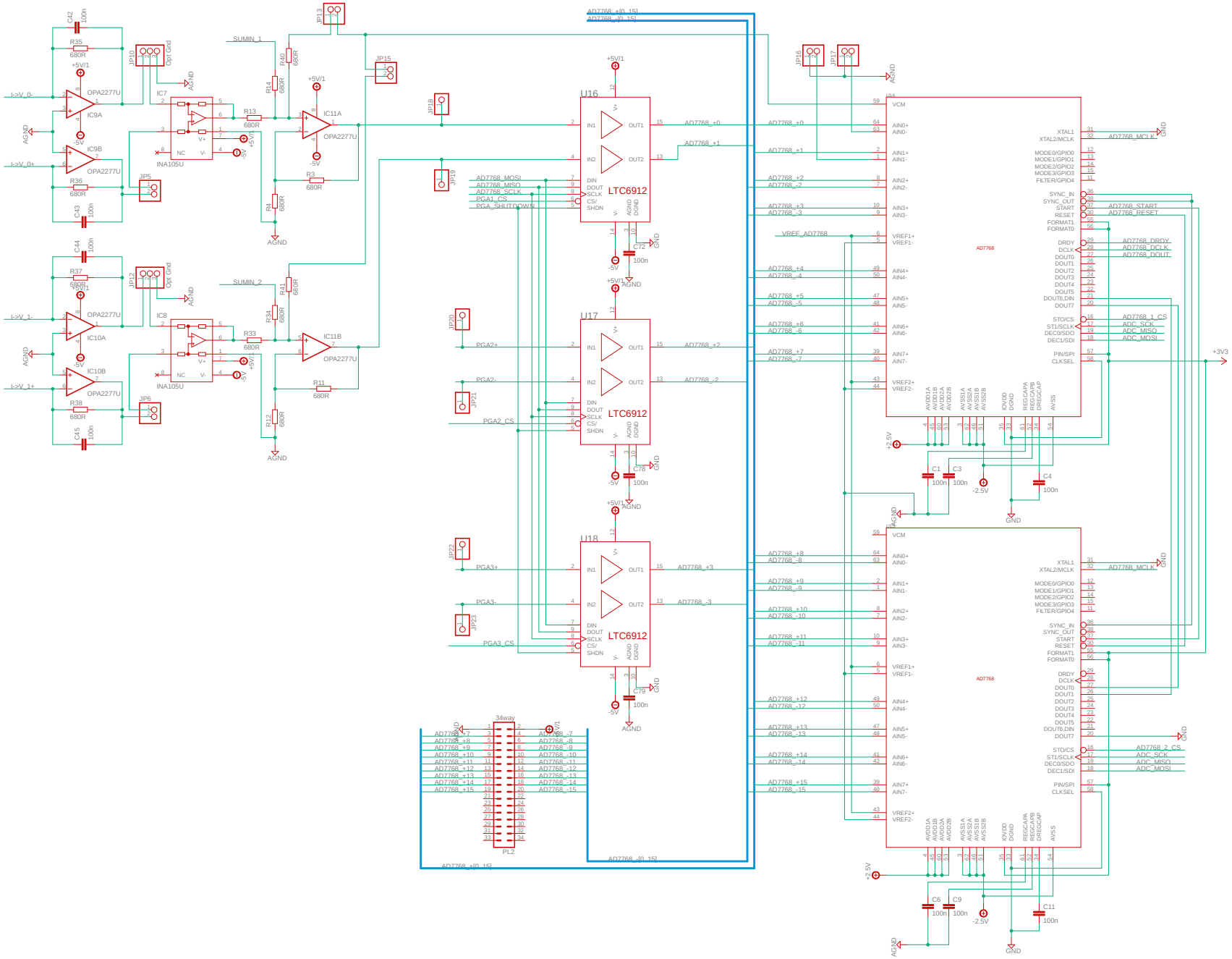
I->V_0-
I->V_0+
I->V_1-
I->V_1+
OPA2277U
INA105U
LTC6912
AD7768
AD7768_MOSI
AD7768_MISO
AD7768_SCLK
PGA1_CS
PGA_SHUTDOWN
PGA2_CS
PGA3_CS
AD7768_MCLK
AD7768_START
AD7768_RESET
AD7768_DRDY
AD7768_DCLK
AD7768_DOUT
AD7768_1_CS
AD7768_2_CS
ADC_SCK
ADC_MISO
ADC_MOSI
VREF_AD7768
+3V3
+2.5V
-2.5V
-5V
+5V1
AGND
GND
34way

Appendix C

Aliasing

Aliasing is an effect that occurs when a signal is not sampled enough times during a cycle. The Nyquist frequency is the highest frequency that can be sampled for a given sampling rate. The Nyquist frequency is equal to half of the sampling frequency, i.e. $F_n = \frac{F_s}{2}$. This relationship can be understood better when observing the digitising of an analogue signal below and above the Nyquist frequency. Digitisation can be observed in figure C.1. The figure shows when the signal is at a frequency of 0.1 F_s and 0.25 F_s, it is digitised correctly and its frequency clear. When sampling at double the sampling frequency, a clear sinusoidal can be observed but note that only two samples exist per cycle of the wave. Since only two samples exist in one wave, it becomes harder to draw a comparison between the digitised signal and analogue signal. It now becomes clear why a flat DC signal is observed when sampling at the same frequency of the signal. Having only one point per cycle results in the same position always being sampled which looks like a level.

Following the examples given, if an analogue signal that has a frequency above the sampling rate is digitised, it would appear as a lower frequency oscillation. Just like when sampling at exactly the frequency of the signal, the same process occurs when the analogue signal has a frequency of NF_s, where N is a positive integer. Given this knowledge frequencies higher than the Nyquist frequency are folded towards the frequency range of 0 Hz to F_n. This mapping effect is visualised in figure C.2, showing that a horizontal line can be drawn from higher analogue frequencies to the resulting digitised frequency. The figure shows the example that if a signal that is 0.85 of the sampling frequency is digitised, the sampled signal would be 'observed' with a frequency of $0.15F_s$.

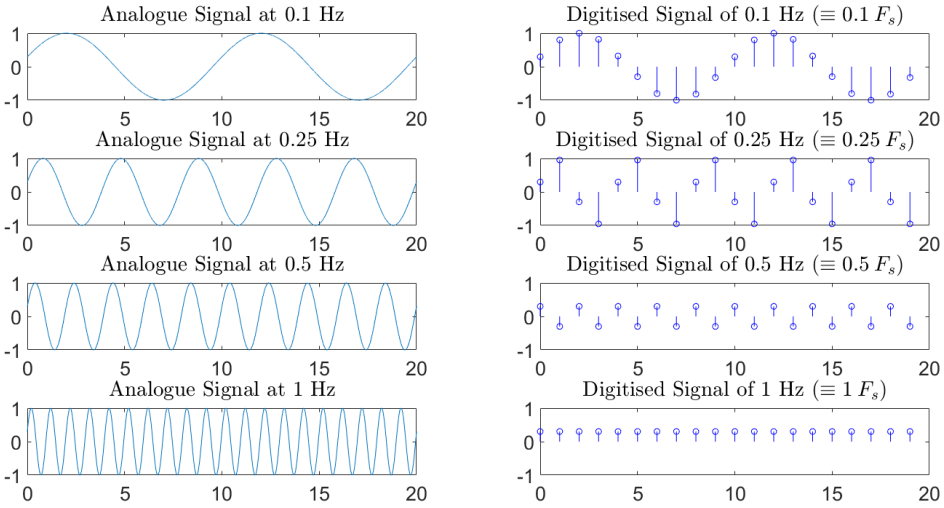

Fig. C.1 A series of graphs comparing how a signal of different frequencies, relative to the sampling frequency, is digitised. Given the sampling rate of 1 Hz, the four analogue signals shown here have a frequency of 0.1 Hz, 0.25 Hz, 0.5 Hz, and 1 Hz. The lowest three frequencies are sampled successfully however the 1 Hz signal appears as a DC signal.

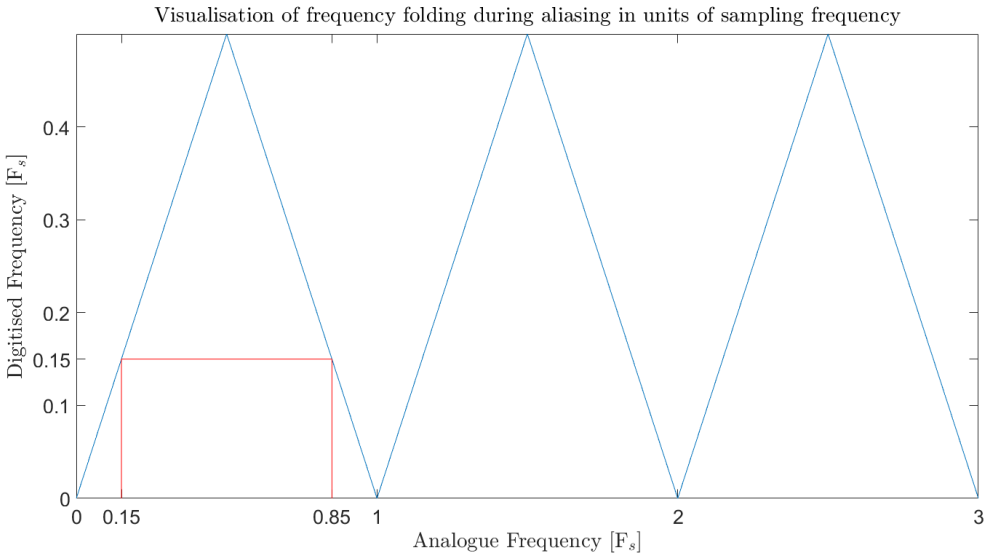

Fig. C.2 A graph depicting how the frequency of an analogue signal is mapped when digitised. Only if the analogue frequency is between 0 and the Nyquist frequency (F_n), is it digitised correctly. The effect of mapping to DC can also be seen for an analogue frequency of NF_s, as the line drawn would go to a frequency of zero.

Appendix D

Derivations of Equations used for Gravimeters

D.1 Absolute Gravimeters

D.1.1 Pendulum Gravimetry

To obtain an equation for a pendula based gravimeter, figure 1.6 should be considered. The figure shows a pendulum with a mass of m experiencing the force of vertical gravity F_g. This force causes a torque (an angular force) that acts to rotate the mass relative to the fixed point at the top. This torque will always be towards the lowest position, shown as a dashed outline in the figure. Torgue is defined as the cross product of the pointing vector and the force vector, obtaining the equation:

$$\Gamma = L F_g \sin(\theta) \,, \tag{D.1}$$

where $F_g = m\,g$ and L is the length from the fixed point to the mass. Substituting the term for F_g into previous equation obtains:

$$\Gamma = L m\, g \sin(\theta) = I\,\ddot{\theta} \,, \tag{D.2}$$

where $\ddot{\theta}$ is the angular acceleration and I is the moment of inertia of the pendulum. I is equal to mL^2 for a point mass, this obtains equation D.3b.

$$L\,m\,g|\sin(\theta) = L^2\,m\ddot{\theta}\ , \tag{D.3a}$$

$$\ddot{\theta} = \frac{g}{L}\sin(\theta)\ . \tag{D.3b}$$

For a small angle pendulum $\sin(\theta) \approx \theta$, noting that for an oscillating system $\ddot{\theta} = \omega_0^2\,\theta$, where ω is the angular resonant frequency. ω is equal to $\frac{2\pi}{T}$ where T is the oscillation period. Substituting these into equation D.3b obtains equation D.4a.

$$(\frac{2\pi}{T})^2\theta = \frac{g}{L}\theta\ ,$$

$$T = 2\pi\sqrt{\frac{L}{g}}\ . \tag{D.4a}$$

Equation D.4a shows that the oscillation period for a pendulum at small angles is purely dependant on the length of the pendulum L and the acceleration due to gravity g. This can be rearranged to equation D.5 which allows the absolute value of the acceleration due to gravity to be calculated.

$$g = \frac{4\,\pi^2 L}{T^2}\ . \tag{D.5}$$

Not all measurements are perfect and will always have an error associated with them. If the period is perturbed by ΔT and the length by ΔL, there would be a resulting error in measured value of gravity, $g + \Delta g$. Using these statements obtain equation D.6a

$$(g+\Delta g)(T+\Delta T)^2 = 4\pi^2(L+\Delta L)$$

$$g\,T^2 + 2T\,\Delta T\,g + (\Delta T)^2\,g) + \Delta g\,T^2 + 2\Delta g\,\Delta T\,T + (\Delta T)^2\,\Delta g = 4\pi^2 L + 4\pi^2\Delta L\ . \tag{D.6a}$$

By ignoring the higher order error terms in equation D.6a and noting that $4\pi^2 L = g T^2$, equation D.7a is obtained.

$$\begin{aligned} \Delta g\, T^2 &= 4\pi^2 \Delta L - 2\, T\, g\, \Delta T \\ \implies \left(\frac{\Delta g}{g}\right) &= \left(\frac{\Delta L}{L}\right) - \left(\frac{2\,\Delta T}{T}\right) . \end{aligned} \tag{D.7a}$$

Equation D.7a shows how the error in the calculated value of gravity changes with a given error in length and period.

D.2 Free Fall Gravimetry

An object in free fall in a gravitational field will follow Newtons Second Law of motion equated to the force from gravity as seen in equation D.8.

$$m\, g = \frac{G\, M_E\, m}{r^2} , \tag{D.8}$$

where g is an acceleration of the mass m in a gravitational field from the mass M_E at a distance of r from the centre of mass. G is the gravitational constant $= 6.67 \times 10^{-11}$ m^3 kg^{-1} s^{-2}. It follows that the object will also follow equation D.9.

$$\begin{gathered} g = \frac{\mathrm{d}v}{\mathrm{d}t} , \\ \therefore \\ \int g\, \mathrm{d}t = \int \mathrm{d}v , \\ \therefore \\ g\, t + c = v , \end{gathered}$$

where v is the velocity after time t at a constant acceleration of g. c is the integral constant. Note that when $t = 0$, $v = c$, i.e. $c = v_0$ (the initial velocity). This yields equation D.9

$$v = v_0 + g\, t . \tag{D.9}$$

Further to equation D.9, as v is defined as seen in equation D.10, equation D.11a and be obtained,

$$v = \frac{\mathrm{d}z}{\mathrm{d}t} \,, \tag{D.10}$$

$$\int v \,\mathrm{d}t = \int \mathrm{d}z \,,$$

where

$$\begin{aligned} v &= v_0 + g\,t \,, \\ \int v_0 + g\,t \,\mathrm{d}t &= \int \mathrm{d}z \,, \\ v_0\,t + \frac{1}{2} g\,t^2 + c &= z \,. \end{aligned} \tag{D.11a}$$

Similar to above, when $t = 0$ and $z = c$ then $c = z_0$. Equation D.11a becomes:

$$z = z_0 + v_0\,t + \frac{1}{2} g\,t^2 \,. \tag{D.12}$$

Rearranging equation D.12 obtains:

$$g = 2\,\frac{(z - z_0) - v_0\,t}{t^2} \,. \tag{D.13}$$

For a **free fall gravimeter**, a mass is continuously dropped while having its position and time are recorded. Since equation D.13 has two unknown variables, the initial velocity (v_0) and initial position (z_0) at least three positions and times are required. To obtain an equation for calculating g, a series of relationships for the difference in positions and velocities are first noted:

$$\begin{aligned} z_3 - z_1 &= \dot{z_0}\,[t_3 - t_1] + \frac{g}{2}\,\left[t_3^2 - t_1^2\right] \,, \\ z_2 - z_1 &= \dot{z_0}\,[t_2 - t_1] + \frac{g}{2}\,\left[t_2^2 - t_1^2\right] \,. \end{aligned}$$

Rearranging the equation above for $\dot{z_0}$ obtains:

$$\dot{z_0} = \frac{(z_2 - z_1) - \frac{g}{2}\,(t_2^2 - t_1^2)}{t_2 - t_1} \,. \tag{D.15}$$

Substituting equation D.15 into other equation obtains:

$$z_3 - z_1 = \frac{(z_2 - z_1)(t_3 - t_1) - \frac{g}{2}\,(t_2^2 - t_1^2)(t_3 - t_1)}{t_2 - t_1} + \frac{g}{2}\,(t_3^2 - t_1^2) \,.$$

Again by rearranging, the following can be obtained:

$$g = 2\,\frac{(z_3 - z_1)(t_2 - t_1) - (z_2 - z_1)(t_3 - t_1)}{(t_3^2 - t_1^2)(t_2 - t_1) - (t_2^2 - t_1^2)(t_3 - t_1)}\,.$$

Factorising the bottom line and taking the common factors results in:

$$g = 2\,\frac{(z_3 - z_1)(t_2 - t_1) - (z_2 - z_1)(t_3 - t_1)}{(t_3 - t_1)(t_2 - t_1)(t_3 - t_2)}\,, \tag{D.16}$$

where z_n and t_n are the n^{th} value of position and time respectively. It can be seen from equation D.16, that with accurate enough time and length measurements, the absolute value of the gravitational acceleration can be calculated. In reality, however, many more points than three are used during such measurements for an increase in accuracy.

D.2.1 Symmetric Rise and Fall Gravimetry

Similar to the free fall gravimeter, a **Symmetric Rise and Fall Gravimeter** throws a mass up to an apex point where it then starts to free fall. This trajectory is governed by:

$$z = z_0 + v_0\,t + \frac{1}{2}\,g\,t^2\,. \tag{D.17}$$

Time is measured for the mass to return to a set location, i on its way down. If the mass is thrown at some initial velocity v_0 then the time taken to reach the apex is $t_a = -\frac{v_0}{g}$. By substituting these into the equations for velocity and position, the following relationships are obtained:

$$v = g\,(t - t_a) \tag{D.18a}$$

$$z = z_0 + \frac{g}{2}\left(t^2 - 2\,t_a\,t\right)\,. \tag{D.18b}$$

Noting that during the period of time before reaching the apex, ($t < t_a$), $v = -t\,g$, where g is negative, therefore v is positive, i.e. upwards. For $t > t_a$ then v is negative, i.e. downwards. Due to the symmetry of the trajectory, the velocity of the mass at position i has a velocity

of the same magnitude but opposite sign while at the other side of the apex, i.e. $v_1 = -v_2$. Consider $v_1 - v_2$,

$$\begin{aligned} v_1 - v_2 &= 2\,v_1 \,, \\ 2\,v_1 &= 2\,g(t_1 - t_a) \,. \end{aligned}$$

Since t_1 to t_a is half of the time from either side of one position:

$$\implies 2\,(t_1 - t_a) = \frac{2\,v_1}{g} = \Delta t_i \,. \tag{D.20}$$

Now consider the difference in position and velocities squared at two different positions 1 and 2 on the trajectory and the position either side of the apex.

$$\begin{aligned} v_2^2 - v_1^2 &= (g(t_2 - t_a))^2 - (g(t_1 - t_a))^2 \,, \\ &= g^2 \left([t_2 - t_a]^2 - [t_1 - t_a]^2 \right) \,, \\ &= g^2 \left(t_2^2 - t_1^2 - 2\,t_2\,t_a + 2\,t_1\,t_a \right) \,, \\ &= g^2 \left([t_2^2 - t_1^2] + 2\,t_a\,[t_1 - t_2] \right) \,, \end{aligned} \tag{D.21a}$$

$$\begin{aligned} z_2 - z_1 &= \left([z_0 + \frac{g}{2}(2\,t_a\,t_2 - t_2^2)] - [z_0 + \frac{g}{2}(2\,t_a\,t_1 - t_1^2)] \right) \,, \\ &= \left([\frac{g}{2}(2\,t_a\,t_2 - t_2^2)] - [\frac{g}{2}(2\,t_a\,t_1 - t_1^2)] \right) \,, \\ &= \frac{g}{2} \left([t_1^2 - t_2^2] + [2\,t_a\,t_2 - 2\,t_a\,t_1] \right) \,, \\ &= \frac{g}{2} \left([t_1^2 - t_2^2] + 2\,t_a [t_2 - t_1] \right) \,. \end{aligned} \tag{D.22a}$$

It can be observed from equations D.21a and D.22a that:

$$\begin{aligned} v_2^2 - v_1^2 &= 2\,g\,(z_2 - z_1) = 2\,g\,\Delta z \,, \\ &= \frac{g^2}{4} \left(4\,[t_2^2 - 2\,t_2\,t_a] - 4\,[t_1^2 - 2\,t_1\,t_a] \right) \,, \\ &= \frac{g^2}{4} \left(4\,[t_2 - t_a]^2 - 4\,[t_1 - t_a]^2 \right) \,. \end{aligned}$$

Noting from equation D.20:

$$= \frac{g^2}{4}\left(\Delta t_2^2 - \Delta t_1^2\right) .$$

Rearranging for g obtains:

$$g = \frac{8\Delta z}{\Delta t_2^2 - \Delta t_1^2} . \tag{D.24}$$

It can be seen from equation D.24 that for a symmetric rise and fall gravimeter, two measurement positions (with two timings each on the arc) are adequate to infer the acceleration of gravity.

D.3 Relative Gravimeters

D.3.1 Relative Pendulum Gravimetry

To understand how a relative measurement works, first take the ratio of equation D.5 for two separate measurements. i.e.

$$\frac{g_2}{g_1} = \frac{T_1^2}{T_2^2} . \tag{D.25}$$

If g_1, the gravity at position 1 is known, a value for g_2, the value of gravity at position 2 can be calculated from the oscillation periods alone, T_1 and T_2. Given that:

$$\frac{g_2}{g_1} = \left(\frac{T_2 - (T_2 - T_1)}{T_2}\right)^2 ,$$
$$\frac{g_2}{g_1} = \left(1 - \frac{T_2 - T_1}{T_2}\right)^2 .$$

By multiplication of g_1 and expansion of the square:

$$g_2 = g_1 + g_1\left(-2\,\frac{T_2 - T_1}{T_2} + (\frac{T_2 - T_1}{T_2})^2\right) ,$$
$$\implies \Delta g_{1,2} = g_2 - g_1 = g_1\left(-2\,\frac{T_2 - T_1}{T_2} + (\frac{T_2 - T_1}{T_2})^2\right) . \tag{D.27a}$$

Noting from equation 1.16 that the change in gravity can be obtained without any calibration and with solely the oscillation period at two positions. If we differentiate equation D.25 we can observe how the error in the measurement varies with the oscillation periods.

$$\mathrm{d}g_2 = 2\,g_1 \left(\frac{2\,T_1\,\mathrm{d}T_1}{T_2^2} - \frac{T_1^2\,T_2}{T_2^3} \right) . \tag{D.28}$$

Dividing equation D.28 by g_2 a term for the relative error of the g_2 is obtained:

$$\frac{\mathrm{d}g_2}{g_2} = 2 \left(\frac{\mathrm{d}T_1}{T_1} - \frac{\mathrm{d}T_2}{T_2} \right) . \tag{D.29}$$

D.3.2 Spring Balance and Zero Length Spring

The system shown in figure 1.10 is in equilibrium when the opposing torques equal, i.e. equation D.30.

$$\Gamma_{cs} + \Gamma_{ms} = \Gamma_g \, , \tag{D.30}$$

where Γ_{cs}, Γ_{ms} and Γ_g are the torques for the counter spring, measuring spring and gravity respectively. The torque from gravity is given by the cross product of the force from gravity and the point vector a, $F_g = m\,g$ at a distance a from the pivot point. Therefore the torque is given by the relationship, $\Gamma = m\,g\,a\,\sin(\alpha+\delta)$ where α is the angle between the suspended mass and the origin of the counter spring and δ is the angle between the counter spring origin and the z plumbline. g is the acceleration due to gravity. These variables are depicted in figure 1.10. The major opposing torque to gravity is the counter spring, Γ_{cs}. This spring would have an opposing force of $F_{cs} = -k\,\Delta L$, with $\Delta L = L - L_0$. Here, L is the current length of the counter spring with an original length L_0. k is the spring constant equal to $\omega_0^2\,m$. The resulting torque at a distance b from the pivot would be, $\Gamma_{cs} = k\,L - L_0\,b\,\sin(\Theta)$ where, from trigonometry, $\sin(\Theta) = \frac{d}{L}\,\sin(\alpha)$.

$$\Gamma_g - \Gamma_{cs} = 0 = m\,g\,a\,\sin(\alpha+\delta) = k\,(L-L_0)\,b\,\frac{d}{L}\,\sin(\alpha) \, . \tag{D.31}$$

It can be seen that for a given change in the angle alpha (measured by the measuring spring), a change in gravity can be obtained, i.e.

$$m\,a\,\sin(\alpha+\delta)\,\mathrm{d}g + \mathrm{d}\alpha \left(m\,g\,a\,\cos(\alpha+\delta) - k\,b\,d\,\frac{L-L_0}{L}\,\cos(\alpha) \right) - k\,b\,d\,\frac{L_0}{L^2}\,\sin(\alpha)\,\mathrm{d}L = 0 \, .$$

From trigonometry again:

$$L^2 = b^2 + d^2 - 2\,b\,d\,\cos(\alpha)\ .$$

By implicit differentiation and rearranging:

$$\mathrm{d}L = \frac{b\,d}{L}\,\sin(\alpha)\,\mathrm{d}\alpha\ .$$

Substitute this into previous equation and rearrange:

$$\frac{\mathrm{d}\alpha}{\mathrm{d}g} = \frac{m\,a\,\sin(\alpha+\delta)}{\frac{b\,d}{L}\left(k\,\frac{L-L_0}{L}\,\cos(\alpha) + k\,b\,d\,\frac{L_0}{L^2}\sin^2(\alpha) - m\,g\,a\,\cos(\alpha+\delta)\right)}\ . \tag{D.32}$$

Equation D.32 shows the relationship between a change in gravity and the effect on α. It can be seen that given a calibration, a change in gravity can be calculated if the change in angle α is measured (via the measuring spring for example). The calibration can be obtained from measuring the spring for a known signal. An important note to make is if the device is a zero-length spring, $L_0 = 0$ then equations D.31 and D.32 become:

$$m\,g\,a\,\sin(\alpha+\delta) - k\,b\,d\,\sin(\alpha) = 0\ , \tag{D.33a}$$

$$\frac{\mathrm{d}\alpha}{\mathrm{d}g} = \frac{m\,a\,\sin(\alpha+\delta)}{k\,b\,d\,\cos(\alpha) - m\,g\,a\,cos(\alpha+\delta)}\ .$$

Noting from equation D.33a:

$$d = \frac{m\,a\,\sin(\alpha+\delta)}{k\,b\,\sin(\alpha)}\,g\ .$$

Substituting this into previous equation, rearranging and noting the trigonometric identity $\sin(X \pm Y) = \sin(X)\,\cos(Y) \pm \cos(X)\,\sin(Y)$ obtains:

$$\frac{\mathrm{d}\alpha}{\mathrm{d}g} = \frac{\sin(\alpha+\delta)\,\sin(\alpha)}{\sin(\delta)}\,\frac{1}{g}\ . \tag{D.34}$$

Appendix E

Decimator Filter Coefficients

The dsPIC33E required the use of an FIR filter that removes higher frequency noise. The removal of the higher frequency content was required as it allowed the output data rate to be downsampled before saving. This downsampling was achieved using an FIR, low-pass filter with a zero (notch) at $1/8^{\text{th}}$ the sampling frequency. Having the zero at $1/8^{\text{th}}$ the sampling rate allows the data rate to be reduced by a factor of 4 without aliasing. The coefficients used in the FIR take the form of an array of 32 numbers that have several zeros padded onto the end so that the array was a power of 2 (for system reasons). The coefficients can be seen in table E.1.

Coefficients: $b_1\ b_2\ b_3\ ...\ b_n$							
-0.0013	-0.0032	-0.0061	-0.0093	-0.0118	-0.0118	-0.0075	0.0027
0.0194	0.0421	0.0685	0.0954	0.1186	0.1344	0.1400	0.1344
0.1186	0.0954	0.0685	0.0421	0.0194	0.0027	-0.0075	-0.0118
-0.0118	-0.0093	-0.0061	-0.0032	-0.0013	0	0	0

Table E.1 A table showing the coefficients used in the FIR filter for decimation. Coefficients generated have a cutoff at $1/8^{\text{th}}$ of the sampling frequency to allow for a reduction in the sampling rate of 4. Coefficients read left to right, top to bottom. Note the extra padding at the end with zeros as the microcontrollers decimator work with powers of 2, here 32 coefficients.

Appendix F

Transfer Function of the Spectron Tilt Sensors

During testing of the Spectron Tilt Sensor (SH50055-A-009) with the AD7195, the secondary μSeismic peak was observed, with no apparent primary peak. There were two reasons thought of as to why no primary peak was seen. The first was quite simply that the primary peak was much weaker (an order of magnitude) than the secondary and thus the base level of noise was too high for this to be seen. The other was that the tilt sensor was acting as a natural high-pass filter and, therefore, the transfer function was attenuating the primary peak.

Given the second idea as to why no secondary peak was seen, the signal from the tilt sensor was measured while using a piezo stage to accelerate the device at different frequencies with a known maximum displacement. The displacement of the oscillations were obtained using a camera that had been created to measure the width of silica fibres and could output pictures and videos [3]. A screen capture of the process is showing figure F.1 which shows the calibration (figure F.1a), the piezo stage at its furthest left position (figure F.1b) and the piezo stage at its furthest right position (figure F.1c).

From the maximum displacement and frequency, the maximum velocity and acceleration can be calculated using equations F.1, F.2 and F.3.

$$s = s_m \sin(\omega t) \,, \tag{F.1}$$

$$v = \mathrm{d}s/\mathrm{d}t = \omega s_m \cos(\omega t) \,, \tag{F.2}$$

$$a = \mathrm{d}v/\mathrm{d}t = -\omega^2 s_m \sin(\omega t) \,, \tag{F.3}$$

(a) An image of the calibration taken using the silica fibre profiler. The image shows a silica fibre of a known width, which allows the pixel width to be obtained. This then allows later images to be calculated as a displacement.

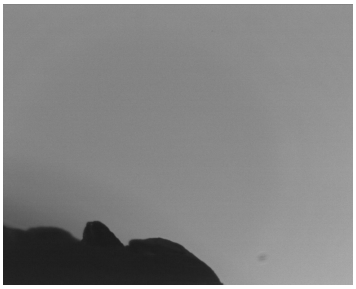

(b) An image of the piezo stage at its furthest left position. This can be compared to figure F.1c to obtain the maximum displacement of the piezo stage.

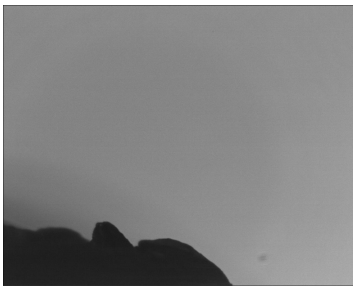

(c) An image of the piezo stage at its furthest right position. Comparing to figure F.1b allows the number of pixels moved to be extracted and converted into a meaningful displacement using the calibration.

Fig. F.1 Three images taken from the video output of the silica fibre imager [3]. The first allowed a calibration of the pixel width to be calculated. Using the calibration, the total change in displacement was calculated using the change in pixels between the two images in panes (b) and (c).

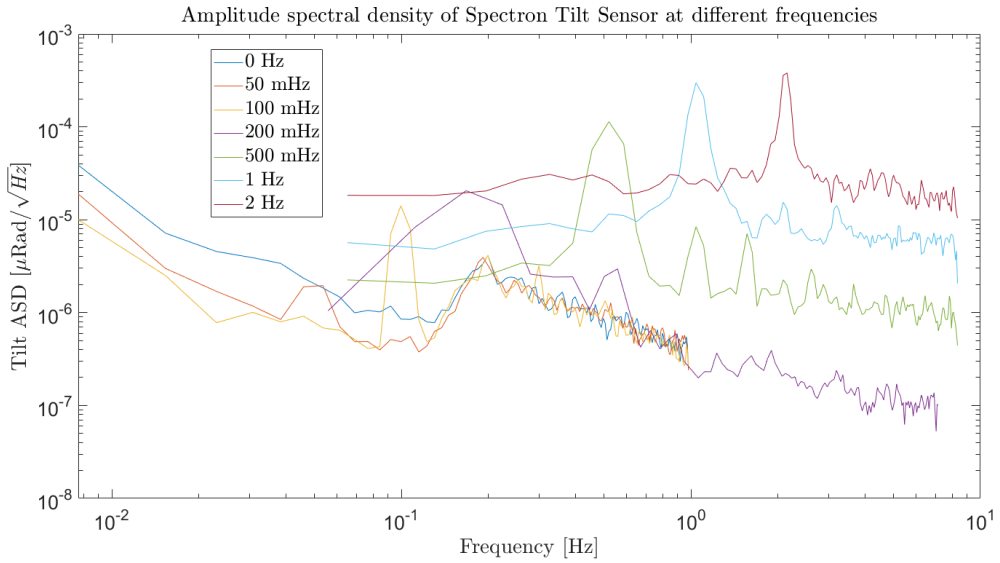

Fig. F.2 A graph showing the amplitude spectral density for the tilt sensor while driven by a piezoelectric stage at different frequencies. It shows a clear trend that the lower frequencies have a lower amplitude. This statement, however, is deceptive as the maximum velocity and acceleration from the piezo stage increase as the frequency increases. This is why the transfer function which is shown in figure F.3 is a better standard

where s, v and a are the displacement, velocity and acceleration with a maximum displacement of s_m. ω is the angular frequency of the oscillations equal to $\omega = 2\pi f$ where f is the frequency. Given that the device was measured to be moving 16.47 μm for the frequencies 0 Hz, 50 mHz, 100 mHz, 200 mHz, 500 mHz, 1 Hz and 2 Hz, the velocities and accelerations seen in table F.1 were obtained. Also in this table is the RMS noise from each of the frequencies. The table shows, as the frequency increases, the noise also increases. Figure F.2 shows the amplitude spectral densities of these measurements, showing a clear decrease in amplitude of the peak as the frequency gets lower. The figure shows that the velocity drops off sharply at low frequencies which would explain why the primary peak was not observed.

Stating that the lower frequencies have a smaller amplitude, however, is deceptive because as the frequency increases, the maximum velocity and acceleration also increase (displacement is a constant as measured). Therefore, a plot of RMS noise over the acceleration (or velocity) is a better standard for comparison. Figure F.3 shows the transfer function as an acceleration.

Frequency	Maximum Velocity [μm s^{-1}]	Maximum Acceleration [μm s^{-2}]	RMS Noise [μRad]
0 Hz	0	0	0.449
50 mHz	10.35	6.502	0.387
100 mHz	15.52	14.63	0.922
200 mHz	20.70	26.01	1.878
500 mHz	51.74	162.6	9.068
1 Hz	103.5	650.2	36.41
2 Hz	207.0	2601	46.49

Table F.1 A table of the maximum velocity, acceleration and RMS noise for different piezo frequencies using the spectron tilt sensor and AD7195. These were obtained by accelerating the tilt sensor using a piezo electric stage at different frequencies.

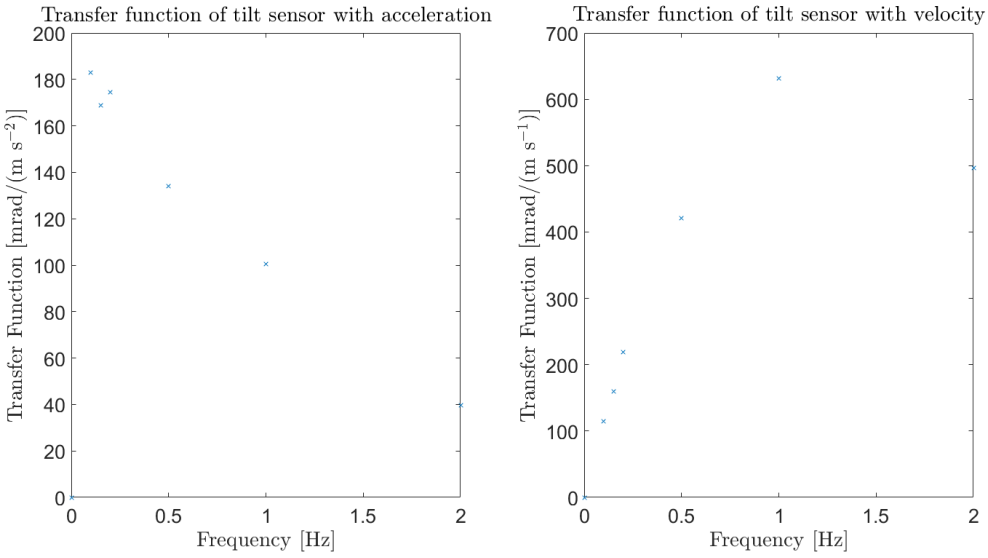

Fig. F.3 Two graphs of the Spectron tilt sensor's transfer function. The sensors were driven by a piezoelectric stage at distinct known frequencies. The maximum displacement was then measured using a silica fibre profiler allowing the velocities and accelerations of each frequency to be calculated. The RMS noise of each frequency was then calculated and divided by the acceleration for one transfer function (left) and velocity (right).

Appendix G

Delta-Sigma Converters

One type of analogue to digital converter that has been used extensively throughout this project is the delta-sigma ($\Delta\Sigma$) converter. Figure G.1 shows a basic flow diagram for a delta-sigma converter of the first order. An analogue signal passes through a differential amplifier which has an output leading to an integrator (i.e. a summing stage). This summed value is then compared to a reference voltage using a simple 1-bit ADC which has an output that can only go zero or one. This digital signal also then pulses a 1-bit DAC which connects to the inverting terminal of the first differential amplifier. This process in the frequency domain shapes the noise of the system to high frequencies, allowing for more effective filtering.

Consider three cases, one where the analogue signal is small relative to the voltage reference, one where the signal is half of the voltage reference, and the final case where the signal is almost equal to the voltage reference. In the case where the signal is small relative to the reference voltage, the integrator will take a long time before it cumulates into a significant enough voltage to cause the comparator to go high. This example would therefore mostly have an output of zeros with a very occasional one (no ones if the input was zero or below, i.e. railing). If the input signal was almost equal to the voltage reference, then the output would almost entirely be made of ones with the occasional zero. It may now also be evident that if the signal was equal to half of the voltage reference, then the output would be 50% ones and 50% zeros. Contextually it can easily be understood from these experiments that the input analogue signal can be measured with better accuracy than if a 1-bit ADC would have been used on its own. This improvement, however, requires a substantial sampling rate to get enough samples to be able to average effectively.

A simulation of a $\Delta\Sigma$ ADC was carried out using MATLAB. Here each of the stages was represented digitally. The script first creates a random input value that has a specific level of

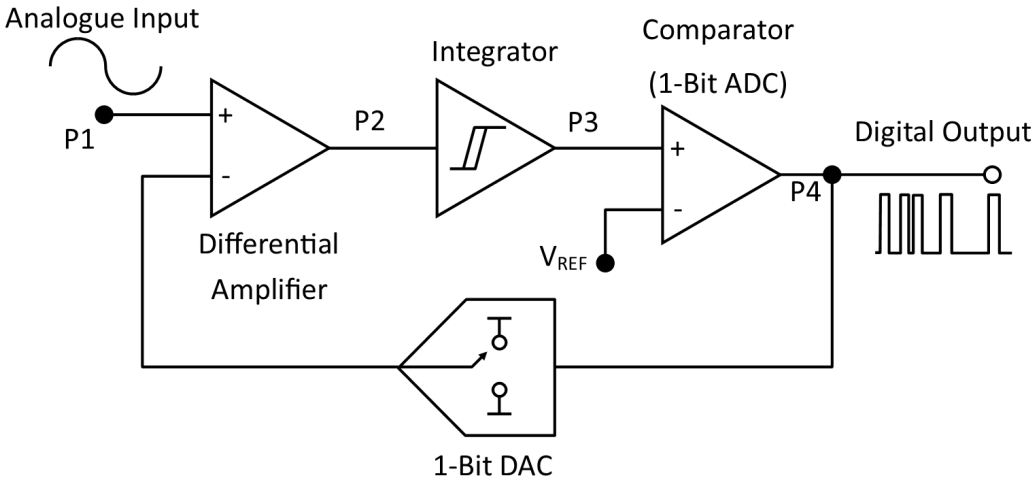

Fig. G.1 A basic flow diagram for delta-sigma analogue to digital converters. An analogue signal passes through a differential amplifier which has an output leading to an integrator (i.e. a summing stage). This summed value is then compared to a reference voltage using a simple 1-bit ADC which has an output that can only go 0 or 1. This digital signal also then pulses a 1-bit DAC which connects to the inverting terminal of the original differential amplifier.

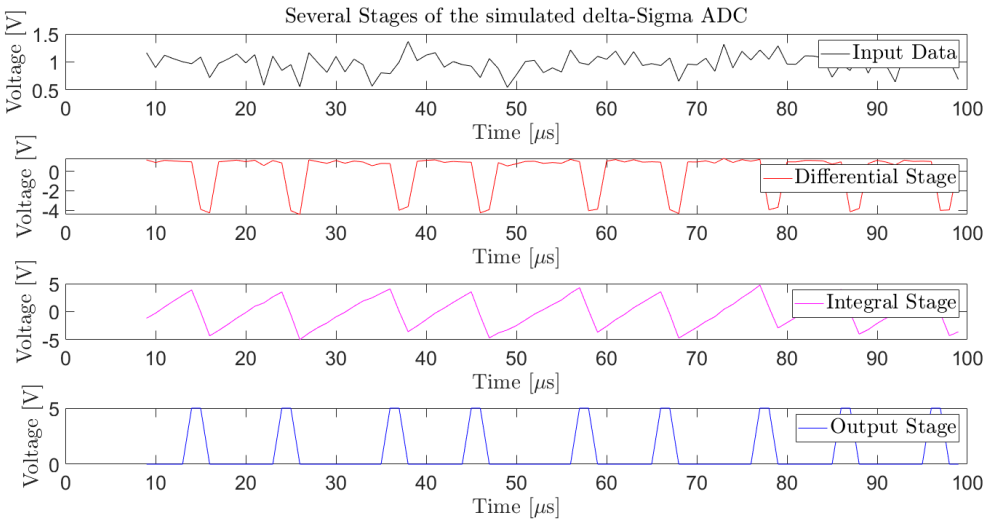

Fig. G.2 A series of graphs showing each stage of the simulated ΔΣ ADC. The first graph shows randomly generated noise with a specific RMS. The second graph shows the output of the differential amplifier. The series of sudden dips in the graphs is when the previous output of the final stage was unity. The third graph shows the summing stage, which can be seen trending upwards until the previous output becomes one which helps reset the integral. The final graph is the output of the 1-bit ADC, or, the comparator which when above half of the voltage reference is one and when below, is zero. This digital value is also used to create the inverting terminal value of the differential amplifier via the use of a 1-bit DAC. The final graph is shown as a voltage, but is stored as zeros or ones (which can be scaled based on the voltage reference).

random noise, this value then has the voltage reference subtracted if the last digital output was a one, and zero if the last digital output was zero. After taking the difference, the value is added to a summing stage which has its new value compared to half the value of the voltage reference. If the value is greater than the reference, the output is a one, if it is less then it is a zero. This digital output is both saved, as well as used for the next iteration of the differential amplifier. Figure G.2 shows a series of graphs, each showing a stage of the described flow diagram. It can be seen that as the system iterates, the summing stage slowly grows until above the comparator criterion which then outputs a one. This one is also then used to create an analogue value which subtracts from the next differential amplifier value. The subtraction allows the integral to effectively be reset, allowing it to grow and so on.

To also check if the simulation was working, an input signal which slowly went from zero to the voltage reference was used to show the rate at which the output is zero. Figure G.3 shows this test. Though the graphs are both a simple straight line, it does prove that

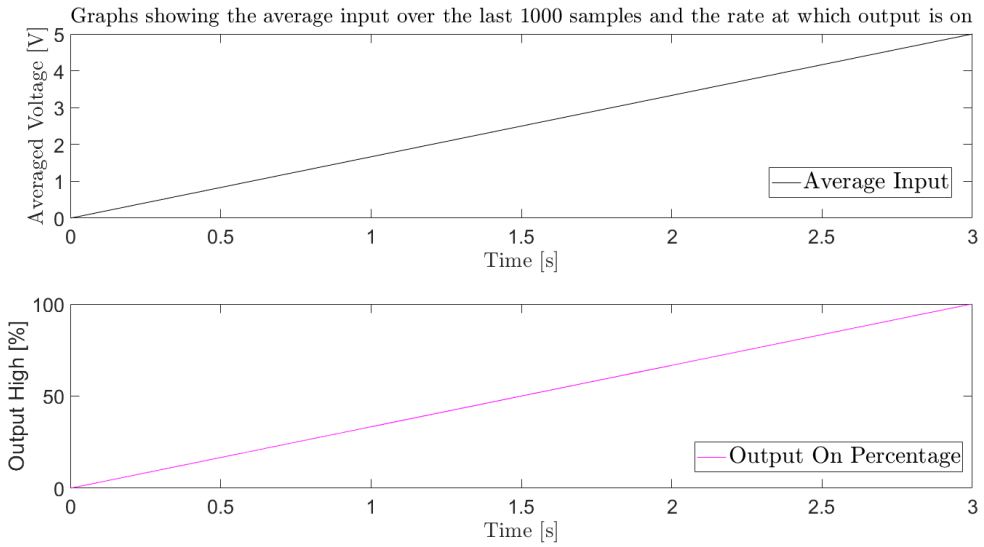

Fig. G.3 Two graphs showing the rate at which the digital output is one relative to an input which varies from zero to the voltage reference. It shows a clear linear trend towards the output being one, 100% of the time as the voltage trends to the voltage reference.

as the voltage approaches the voltage reference, the number of times the digital output is one approaches 100%. This trend is the expected behaviour, noting that if the output was averaged when it was high 100% of the time, the result would show that the value was at the voltage reference.

Following the previous test, simple white noise was introduced into the input with a mean value between zero and the voltage reference ($V_{\text{mean}} = 1$ V, $V_{\text{rms}} = 0.2$ V). These are also the values used in figure G.2. The output from this figure was then filtered twice using an FIR filter with a -3 dB point at 0.045 of the sampling frequency, i.e. 0.09 of the Nyquist frequency. After each of the stages of filtered, the data was downsampled by a factor of 8. Figure G.4 shows two graphs; the first shows the input data versus the two stages of filtering. The second graph shows the amplitude spectral density of the data shown in the first but with the ASD of the output of the comparator (scaled with the voltage reference). It can be seen straight away that once filtered, the output of the 1-bit ADC had a mean value equal to the input, but, had less noise. The second stage of filtering can be seen to have even less noise than the first. In this simulation, the total down-sampling from the comparator to the second stage was 64. The system was simulated with a sampling rate of 1 MHz. Therefore the final output data rate was 15.6 kHz. The RMS noise was reduced from 200 mV to 41 mV after a single stage of filtering and 13 mV after two. This change is an improvement of almost a factor of

15.4. If we consider that the filter had its first notch at 0.045 of the sampling frequency, and there was a factor of eight in down-sampling between stages of filtering, it would be expected that the notch of the second filter is at a frequency of, $f_{\text{notch}} = 0.045\,F_s/8 = 5.625$ kHz, i.e. ideally an improvement of $\sqrt{F_s}/\sqrt{0.045\,F_s/8} = 13.3$. This value is lower than what was obtained in the simulation as it assumes the only frequencies attenuated are the ones after the notch frequency. Clearly frequencies before this are also attenuated (though less) and thus would result in even lower noise.

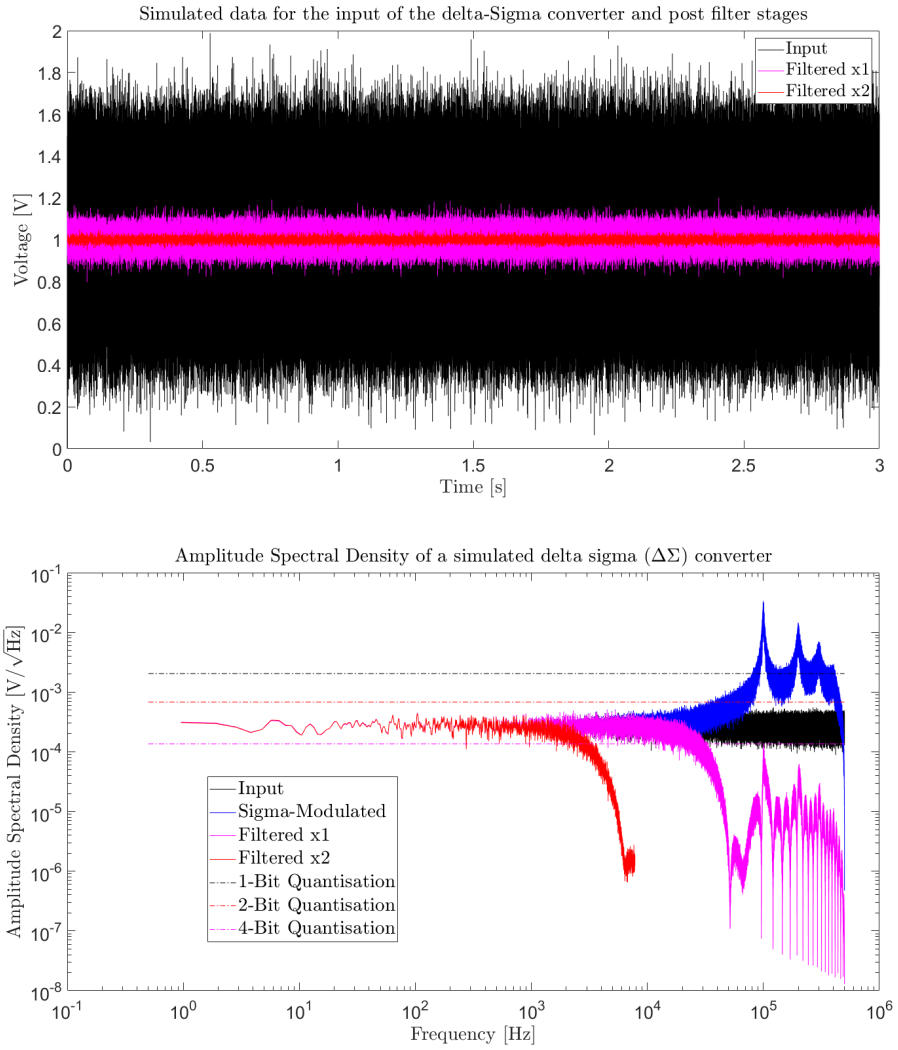

Fig. G.4 Two graphs showing the time domain and amplitude spectral density for different stages in the simulated ΔΣ ADC. The first graph shows the reduction in noise from the input after one and two filtering stages. A clear reduction in noise can be observed even after one stage. The second graph shows the amplitude spectral density of different stages in the simulation. The sigma-modulated data has large peaks at high frequency due to noise shaping but can be removed with effective filtering. As this is filtered, the bandwidth of the system is reduced which results in the lower noise.